博士論文

Study of Higgs boson decays to tau pairs at the International Linear Collider

（国際リニアコライダーにおけるヒッグスボゾンのタウ対崩壊の研究）

川田　真一

広島大学大学院先端物質科学研究科
量子物質科学専攻

2016 年 2 月

目次

１．主論文

Study of Higgs boson decays to tau pairs at the International Linear Collider

（国際リニアコライダーにおけるヒッグスボゾンのタウ対崩壊の研究）

川田真一

２．公表論文

A study of the measurement precision of the Higgs boson decaying into tau pairs at the ILC

Shin-ichi Kawada, Keisuke Fujii, Taikan Suehara, Tohru Takahashi, Tomohiko Tanabe

The European Physical Journal C, **75**:617, pp 1 - 11 (2015)

３．参考論文

(1) **A conventional positron source for international linear collider**

Tsunehiko Omori, Tohru Takahashi, Sabine Riemann, Wei Gai, Jie Gao, Shin-ichi Kawada, Wanming Liu, Natsuki Okuda, Guoxi Pei, Junji Urakawa, Andriy Ushakov

Nuclear Instruments and Methods in Physics Research Section A, **672**, pp 52 - 56 (2012)

(2) **Feasibility study of the measurement of Higgs pair creation at a photon linear collider**

Shin-ichi Kawada, Nozomi Maeda, Tohru Takahashi, Katsumasa Ikematsu, Keisuke Fujii, Yoshimasa Kurihara, Koji Tsumura, Daisuke Harada, Shinya Kanemura

Physical Review D, **85**, 113009, pp 1 - 7 (2012)

(3) **Development of an intense positron source using a crystal-amorphous hybrid target for linear colliders**

Y. Uesugi, T. Akagi, R. Chehab, O. Dadoun, K. Furukawa, T. Kamitani, S. Kawada, T. Omori, T. Takahashi, K. Umemori, J. Urakawa, M. Satoh, V. Strakhovenko, T. Suwada, A. Variola

Nuclear Instruments and Methods in Physics Research Section B, **319**, pp 17 - 23 (2014)

(4) **Blocking positive ion backflow using a GEM gate: experiment and simulations**
P. Gros, K. Fujii, T. Fusayasu, Y. Kato, S. Kawada, M. Kobayashi, T. Matsuda, O. Nitoh, A. Sugiyama, T. Takahashi, J. Tian, T. Watanabe, R. Yonamine
Journal of Instrumentation, **8**, C11023, pp 1 - 8 (2013)
Proceedings of MPGD2013 (3rd International Conference on Micro Pattern Gaseous Detectors)

(5) **Spatial resolutions of GEM TPC. A novel theoretical formula and its comparison to latest beam test data**
R. Yonamine, K. Fujii, K. Ikematsu, A. Ishikawa, T. Fusayasu, P. Gros, Y. Kato, S. Kawada, M. Kobayashi, T. Matsuda, O. Nitoh, R. D. Settles, A. Sugiyama, T. Takahashi, J. Tian, T. Watanabe
Journal of Instrumentation, **9**, C03002, pp 1 - 15 (2014)
Proceedings of MPGD2013 (3rd International Conference on Micro Pattern Gaseous Detectors)

(6) **Higgs Boson Decays to Tau Pairs at the ILC with ILD Detector**
Shin-ichi Kawada, Keisuke Fujii, Taikan Suehara, Tohru Takahashi, Tomohiko Tanabe
JPS Conference Proceedings, **1**, 013013, pp 1 - 4 (2014)
Proceedings of APPC12 (12th Asia Pacific Physics Conference)

主論文

Study of Higgs boson decays to tau pairs at the International Linear Collider

Shin-ichi Kawada

Graduate School of Advanced Sciences of Matter
Hiroshima University

2016

Abstract

The most of constituents of matter and the interaction among them accessible by current experiments are well described by the Standard Model of particle physics. The Standard Model is based on the gauge principle, which require the invariance of the theory under the local gauge transformation. However, the gauge principle requires that the masses of particles should be zero which is obviously not realized in nature. Therefore, it is necessary to introduce a mechanism to give a mass to each elementary particle after constructing the model based on the gauge principle. The Higgs mechanism is introduced as the mass generation mechanism in the Standard Model, using the idea of spontaneous symmetry breaking. The idea of the Higgs mechanism was proposed in 1964 and the Standard Model based on the idea was established in 1973. Since then, the Standard Model has been extensively tested and shown its validity except for the existence of the last piece, the Higgs boson, a particle predicted by the Higgs mechanism.

On July 4th, 2012, the discovery of a Higgs-like particle was reported by the experiments at the Large Hadron Collider (LHC). The Standard Model has completed by the discovery of the Higgs boson, however, there are still many unsolved questions which the Standard Model cannot provide the answer, such as the existence of dark matter, dark energy, baryon number asymmetry, and so on. These problems indicate that there should be phenomena beyond the Standard Model and investigation of the Higgs boson through the precise measurement is a key to understand unsolved questions.

In the Standard Model, the coupling constants of matter fermions and gauge bosons to the Higgs boson is proportional to the their masses. On the other hand, if there is new physics beyond the Standard Model, the coupling deviates from the Standard Model prediction. The deviation depends on the new physics beyond the Standard Model, but is estimated to be $O(\%)$ in many models. Therefore, the precision of a few percent or less is required to shed light on a signal of new physics concealed in the coupling constants.

The International Linear Collider (ILC) is a planned next-generation high energy linear collider to explore particle physics. The ILC uses high energy interaction of elementary particles, electrons and positrons, which provides an ideal opportunity to measure the properties of Higgs boson very precisely.

In this study, we will discuss the Higgs boson decaying into tau lepton pairs ($h \to \tau^+\tau^-$) at the ILC. In order to evaluate the measurement accuracy of the process of Higgs boson decaying into tau pairs at the ILC, we need the simulation as realistic as possible. There are some studies using e^+e^- collisions, however, these studies did not considered the realistic backgrounds, or based on an obsolete Higgs boson mass. Therefore, it is necessary to study the measurement precision of Higgs boson decaying into tau pairs at the ILC with considering realistic backgrounds and realistic detector model. The purpose of this study is to provide the reference performance of the ILC for measuring Higgs boson decaying into tau pairs as the primary information to phenomenological studies.

In this thesis, studies of the Higgs boson decaying into tau pairs at the ILC with the center-of-mass energies ($\sqrt{s}$) of 250 GeV and 500 GeV are presented, assuming a mass of Higgs boson of 125 GeV, beam polarizations of electron and positron of $P(e^-, e^+) = (-0.8, +0.3)$, and integrated luminosities of 250 fb^{-1} for $\sqrt{s} = 250$ GeV and 500 fb^{-1} for

$\sqrt{s} = 500$ GeV. The sets of $\sqrt{s}$ and integrated luminosity are based on the nominal running scenario of the ILC. First, the Monte-Carlo (MC) samples of signal and background events were generated for possible all production processes at $\sqrt{s}$ of 250 GeV and 500 GeV. These generated MC samples were processed with the detailed detector simulation assuming the International Large Detector (ILD) model, which is one of the detector concept planned for the ILC. The hadron backgrounds from $\gamma\gamma$ interactions, in which photons produced by the beam–beam interaction were also considered. After the MC generation and detector simulation, the algorithms of tau lepton clustering, lepton finding, and jet clustering were applied to reconstruct the events properly. Then, the analysis for background rejection and optimization was performed. This optimization was performed aiming to maximize statistical signal significance. The processes of $e^+e \to q\bar{q}h$, $e^+e \to e^+e\ h$, and $e^+e \to \mu^+\mu\ h$ were analyzed at $\sqrt{s} = 250$ GeV, and $e^+e \to q\bar{q}h$ and $e^+e \to \nu\bar{\nu}h$ were analyzed at $\sqrt{s} = 500$ GeV. After the optimization, the measurement precision for the production cross section times the branching ratio was estimated.

In addition to the evaluation with the nominal ILC running scenario, an evaluation with a possible luminosity upgrade scenario was performed. In the luminosity upgrade scenario, the statistics of 2000 fb ^{1} at $\sqrt{s} = 250$ GeV and 4000 fb ^{1} at $\sqrt{s} = 500$ GeV are assumed. With considering this running scenario, the precision for production cross section times the branching ratio will reach 1.0%. We also estimated the precisions of the branching ratios by using the production cross section, which can be independently measured by the ILC experiment, and this study. The expected precision for the branching ratio will be 3.6% with the nominal running scenario, and will reach 1.4% with the luminosity upgrade scenario.

In conclusion, we showed that the expected precisions for the production cross section times the branching ratio and the branching ratio is 1% level with the possible luminosity upgrade running scenario. This study provides the primary reference performance of the ILC, which could be used as the input to the phenomenological studies on physics beyond the Standard Model.

Contents

List of Figures

List of Tables

1 Introduction

1.1 Particle Physics

Particle physics is a study of searching for ultimate elements of matter and interactions among them, one of the fundamental question which mankind have had since the dawn of history. As a results the endeavor for over thousands of years, today, we have a theory called the "Standard Model".

In the Standard Model, the interactions between elementary particles are described by the gauge principle, which requires the Lagrangian is invariant under the local gauge transformation. The strong interaction among quarks is described by the invariance under $SU(3)_C$ transformation [1–4], known as the Quantum ChromoDynamics (QCD). The electroweak interaction is described by the invariance under $SU(2)_L \otimes U(1)_Y$ transformation [5–7], known as Glashow-Weinberg-Salam model. The gauge principle requires the massless vector bosons as mediators of the interactions. In addition, all matter fermions must be massless to preserve gauge invariance, which is clearly not realized in the real world. There are many massive fermions such as electrons, muons, quarks, etc., and the weakness of the weak interaction is believed to be due to the massive gauge boson. On the other hand, it is well verified that the gauge theory describes interactions among matters once we allow massive gauge bosons and fermions. All these results indicate that one must construct the interaction among matters by the gauge principle and introduce a mass generation mechanism to fit them to the real world.

The Higgs mechanism was introduced [8–12] as the mass generation mechanism with the idea of spontaneous symmetry breaking [13, 14], and that predicts the existence of a massive scalar boson, the Higgs boson. The framework of the Standard Model consisting of the gauge principle and the Higgs mechanism was constructed in 1973. Until 2012, all particles except for the Higgs boson were discovered, and most of experimental results were consistent with the Standard Model.

As for the search for the Higgs boson, the LEP experiments at the CERN [15] set its lower mass limit of 114.4 GeV in 2003 [16]. The region of 162 GeV to 166 GeV were excluded by CDF experiments and D0 experiments in 2010 [17]. The multi-parameter analysis of the Standard Model preferred relatively low mass Higgs boson with 87^{+35}_{26} GeV as the most probable mass with the Standard Model parameters [18].

The Large Hadron Collider (LHC) at the CERN started operation of proton–proton collisions with the center-of-mass energy ($\sqrt{s}$) of 7 TeV in 2010. On July 4th, 2012, the discovery of a Higgs-like particle was announced by the ATLAS and the CMS experiments [19, 20] at the LHC with the mass of about 125 GeV. The Standard Model framework was completed by this discovery. As a result of this historical discovery, the Nobel prize in physics was awarded to Francois Englert and Peter W. Higgs in 2013 "for the theoretical discovery of a mechanism that contributes to our understanding of the origin of mass of subatomic particles, and which recently was confirmed through the discovery of the predicted fundamental particle, by the ATLAS and CMS experiments at CERN's Large Hadron Collider" [21].

However, the completion of the Standard Model does not mean the end of particle physics. The Standard Model is not the theory for describing everything. Certainly, the

Standard Model can explain most of experimental results, however at the same time, the Standard Model has some problems or cannot provide the answer to some results.

One example is that the Standard Model cannot explain the existence of dark matter and dark energy. In the latest results, the Universe consists of matter, dark matter, and dark energy. The composition ratio of the Universe is 4.9% of matter, 26.8% of dark matter, and 68.3% of dark energy, respectively [22]. We only know about 5% of our Universe, and remaining components are unknown. Another example is that the Standard Model cannot provide the reason of matter dominance of the Universe. It is considered that the equal numbers of particles and antiparticles were created at the beginning of the Universe. During the evolution of the Universe, particles survived from pair annihilations with their antiparticles partners. However, we have not found the explanation of this matter–antimatter asymmetry.

In addition, the Standard Model itself has theoretical issues. The mass of the Higgs boson is known to be unstable against the quantum correction. In other words, one need unnaturally fine tuning of $O(10^{-14})$ in the Standard Model parameter to keep the Higgs boson mass around 100 GeV. It is called the naturalness problem. The naturalness problem is related with the mechanism of the spontaneous symmetry breaking which happens at 100 GeV energy scale. The Standard Model describes the electromagnetic force, weak force, and strong force, but does not include the gravity. So that it will not be applicable to very beginning of the Universe where the gravitational interaction, or equivalently structure of space-time, becomes negligible for particle interactions.

Therefore, new physics beyond the Standard Model is necessary to explain these unsolved questions. Many possibilities for physics beyond the Standard Model has been proposed, such as the supersymmetric model or the composite model. and all models predict signatures beyond the Standard Model in experimental studies.

In the Standard Model, the coupling constants of matter fermions and gauge bosons to the Higgs boson are proportional to the masses of particle. If there is new physics beyond the Standard Model however, the coupling constant will deviate from the Standard Model prediction. The deviation depends on models beyond the Standard Model, but is estimated to be small in many models. For example, it is estimated to be at the few percent level if there is new physics at the scale of around 1 TeV [23].

The ATLAS and the CMS are also searching for new physics. However the LHC uses the proton–proton collision. Since a proton is a composite object made of quarks and gluons, a reaction of proton–proton collision is very complicated. Thus, it is difficult to measure the Higgs boson precisely with the proton–proton collision due to large background contaminations even if the production rate is large.

1.2 The International Linear Collider

The International Linear Collider (ILC) is proposed as a next-generation electron–positron collider for high energy physics experiment. The electron–positron collision provides us cleaner environment than the proton–proton collision, and it is possible to measure the properties of Higgs boson precisely. The Technical Design Report (TDR) of the ILC has been published in 2013 [24–28]. In TDR, the basic objective of the ILC, physics target,

detectors and its performance, technologies for construction, are summarized. Details of the ILC are summarized in the ILC TDR, and will discuss in Chapter 3. In this section, we will focus on the Higgs boson physics at the ILC.

1.3 Higgs Production at the ILC

The cross section of the Higgs production as a function of $\sqrt{s}$ is shown in Figure 1.3.1. The major diagrams of Higgs production are shown in Figure 1.3.2.

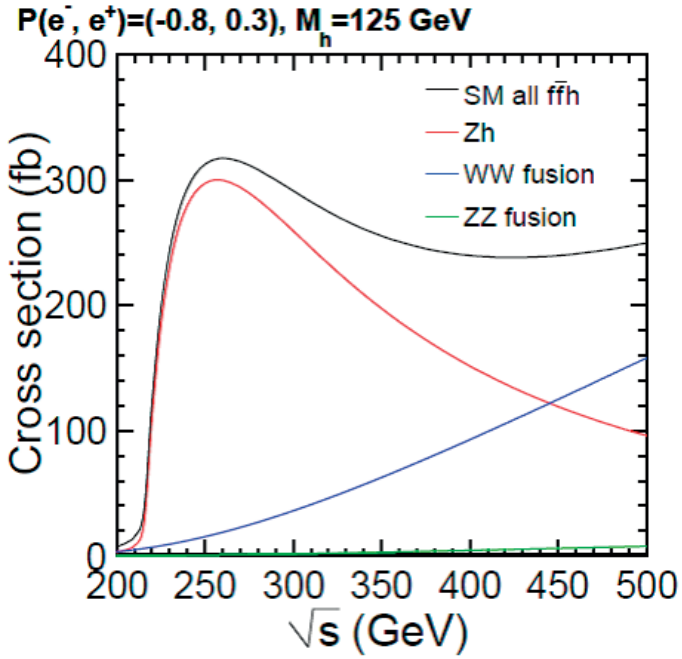

Figure 1.3.1: Cross sections of Higgs production processes as a function of $\sqrt{s}$ [25]. A Higgs mass of 125 GeV and a beam polarization combination of $P(e^-, e^+) = (-0.8, +0.3)$ are assumed in this plot.

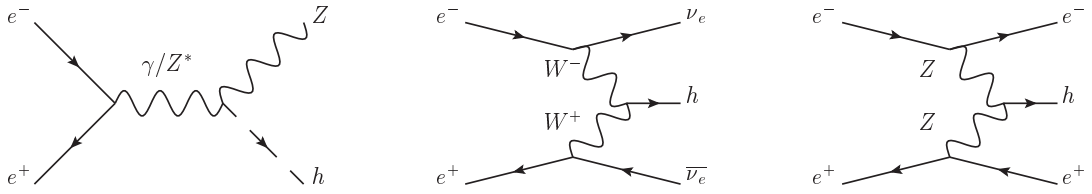

Figure 1.3.2: The diagrams of Higgs production processes. Left: $e^+e^- \to Zh$ (Higgs-strahlung), middle: $e^+e^- \to \nu_e\overline{\nu_e}h$ (WW-fusion), right: $e^+e^- \to e^+e^-h$ (ZZ-fusion).

Measurements of the Higgs boson coupling constants with fermions and gauge bosons can be performed via Higgs-strahlung process at $\sqrt{s} = 250$ GeV, while the contributions from W and Z boson fusion processes is not large enough for the measurements. At $\sqrt{s} = 500$ GeV, the WW-fusion process is the most dominant Higgs production process.

1.4 Higgs Coupling Studies at the ILC

In this study, we discuss the Higgs couplings. The quantities we can directly obtain from the experiment are the production cross section times the branching ratio. Thus, the process of interests can be categorized as $\sigma_{Zh} \times \mathrm{BR}(h \to X\overline{X})$, $\sigma_{\nu\bar{\nu}h} \times \mathrm{BR}(h \to X\overline{X})$, where σ_{Zh}, $\sigma_{\nu\bar{\nu}h}$ are the cross section of Higgs-strahlung, WW-fusion, respectively, and X denotes b, c, g, W, Z, τ, μ. The production cross sections and branching ratios are related with parameter of the Standard Model as;

$$\sigma_{Zh} \times \mathrm{BR}(h \to X\overline{X}) = \sigma_{Zh} \cdot \frac{g^2_{hX\overline{X}}}{\Gamma_T}$$
$$\sigma_{\nu\bar{\nu}h} \times \mathrm{BR}(h \to X\overline{X}) = \sigma_{\nu\bar{\nu}h} \cdot \frac{g^2_{hX\overline{X}}}{\Gamma_T},$$

where Γ_T is the Higgs total width, and $g_{hX\overline{X}}$ is the coupling constants of the Higgs boson to X [29]. In the case of tau decay in Higgs-strahlung process,

$$\sigma_{Zh} \times \mathrm{BR}(h \to \tau^+\tau^-) = \sigma_{Zh} \cdot \frac{g^2_{h\tau\tau}}{\Gamma_T}.$$

In the ILC experiment, the production cross section via Higgs-strahlung process can be measured independently so that the branching ratio can be extracted. Since the total width is a common factor for all decay modes of the Higgs boson, it is possible to evaluate relative consistency of the coupling constants. In addition, the total width can also be measured independently via WW-fusion in the ILC experiments [29], therefore, it is possible to evaluate the absolute value of the constants as well.

1.5 Higgs Boson Decays to Tau Pairs

In this study, we will discuss the Higgs boson decaying into tau lepton pairs ($h \to \tau^+\tau^-$) at the ILC. This channel will be a good probe for testing of new physics effects in the coupling between Higgs boson and a fermion, because;

1. the mass of the tau lepton from the Higgs mechanism has been measured with good precision, while the masses of the quarks such as b quark has uncertainty from the QCD effect, so that the results of the measurement can be compared with the theoretical prediction with small uncertainty,

2. tau is the heaviest lepton and has larger branching ratio than muon or electron, which allows smaller statistical uncertainty.

1.5.1 New Physics Effect

The coupling constants will deviate from the Standard Model prediction if there is new physics beyond the Standard Model. The deviation depends on the new physics model, but is estimated to be $\sim O(\%)$ by many models beyond the Standard Model. In this

section, we will discuss typical examples of the new physics and its effect to the Higgs boson decaying into tau pairs.

Composite models assume that the Higgs boson is a bound state of the fundamental fermions with a compositeness scale f [25]. In this model, the deviation of Higgs couplings to gauge bosons and fermions is predicted as

$$\frac{g_{hxx}}{g_{h_{\rm SM}xx}} \simeq 1 \pm O(v^2/f^2), \tag{1.5.1}$$

where v is the vacuum expectation value of the Higgs field ($\sim$ 246 GeV), which will be introduced in Section 2. In the minimal composite Higgs model [30], for example, it is estimated to be

$$\frac{g_{h\tau\tau}}{g_{h_{\rm SM}\tau\tau}} \simeq 1 - 3\%(1\ {\rm TeV}/f)^2, \tag{1.5.2}$$

for tau lepton. If $f = 1$ TeV, the deviation is about 3%.

Another example is two Higgs doublet models (THDM) [31]. These models assume an extended Higgs sector and there will be five physical Higgs bosons, which are usually referred as h, H^0, $H^\pm$, and A. The two vacuum expectation values v_1 and v_2 satisfy the equation of $v_1^2 + v_2^2 = v^2$. The β is a parameter defined as $\tan\beta \equiv v_2/v_1$. The supersymmetric model (SUSY) is a type of THDM, which is one of the most attractive candidate for physics beyond the Standard Model [32–34]. SUSY models potentially solve the naturalness problem, include dark matter candidates and only known possibility which could be extended to incorporate the gravitational interaction. In general, SUSY models have number of input parameters so that deviation from the Standard Model can be either large or small depending on the models as well as parameters. One example given in Ref. [25], originally studied in Refs. [35, 36], shows that

$$\frac{g_{h\tau\tau}}{g_{h_{\rm SM}\tau\tau}} = 1 + 2.5\%, \tag{1.5.3}$$

for tau lepton, assuming $\tan\beta = 5$, $m_A = 1$ TeV and heavy two top squark masses of 857 GeV and 1200 GeV. These examples show typical deviations of the coupling constant of the Higgs boson with the tau lepton of about a few percent, which implies the required precision for the measurement as a probe of physics beyond the Standard Model.

1.5.2 LHC Prospects

At the LHC experiments, the process of Higgs boson decaying into tau pairs will be measured using proton–proton collision. This decay has been studied by the ATLAS and the CMS experiments, who reported a combined signal yield consistent with the Standard Model expectation, with a combined observed significance at the level of 5.5σ [37–39]. According to Refs. [25, 40], it would be measured by $\sim$ 12% at the $\sqrt{s} = 14$ TeV LHC with accumulated 300 fb ^{1} data. The HL-LHC accumulates 3000 fb ^{1} at $\sqrt{s} = 14$ TeV, and it would be measured by $\sim$ 9%. Thus, the LHC experiment may not have sufficient sensitivity for new physics described in previous section. On the other hand, previous studies show that the measurement at the ILC can be an order of a few percent and that the measurement at the ILC plays crucial role even after or the same time with the LHC experiments.

1.6 Purpose and Contents of This Thesis

In this thesis, we will discuss the Higgs boson decaying into tau lepton pairs at the ILC. There are some studies of measuring this channel using e^+e collision [41, 42]. However, these studies did not take into account some of the relevant background processes [42] or based on a Higgs boson mass hypothesis which differs from the observed value. Therefore, we need more realistic evaluation to prove the performance of the ILC.

For these reasons, we evaluated the measurement precision of Higgs boson decaying into tau pairs at the ILC by using a detailed detector simulation assuming a Higgs mass of 125 GeV. The purpose of this study is to give a reference performance of the ILC capabilities by a realistic simulation study based on the accelerator and the detector proposed in the ILC TDR [24–28] together with its running scenario published recently [43, 44].

The contents of this paper are organized as follows. A brief overview of the Standard Model is described in Section 2. In Section 3, we describe the ILC and the ILD detector concept, followed by the analysis setup in Section 4. The event reconstruction and selection at center-of-mass energies of 250 GeV and 500 GeV are discussed in Sections 5 and 6. Section 7 describes the prospect of the measurement precision assuming an ILC running scenario, followed by the summary in Section 8.

2 The Standard Model of Particle Physics

2.1 Brief Summary of the Standard Model

There are 17 elementary particles in the Standard Model, which are the six quarks (u: up, d: down, c: charm, s: strange, t: top, b: bottom), six leptons (e: electron, ν_e: electron neutrino, μ: muon, ν_μ: muon neutrino, τ: tau, ν_τ: tau neutrino), four gauge bosons (γ: photon, g: gluon, W: W boson, Z: Z boson), and one Higgs boson h. The gauge principle describes the interactions; electromagnetic interaction, weak interaction, and strong interaction, by requiring the Lagrangian is invariant under the gauge transformations. The Higgs mechanism describes the mass generation mechanism via spontaneous symmetry breaking.

2.2 Gauge Principle and Interactions

Discussions in this section are based on the Refs. [45, 46].

2.2.1 $U(1)$ Gauge Transformation and Electromagnetic Interaction

Consider ψ as a spinor. The Lagrangian density $\mathcal{L}$ can be written as

$$\mathcal{L} = i(\hbar c)\overline{\psi}\gamma^\mu\partial_\mu\psi - (mc^2)\overline{\psi}\psi. \tag{2.2.1}$$

The interaction terms are not included in Eq. (2.2.1). According to the gauge principle, the interaction term will be introduced by requiring invariance of the Lagrangian under the local gauge transformation as

$$\psi \to e^{i\theta(x^\nu)}\psi. \tag{2.2.2}$$

As a result of the gauge principle, the interaction term is introduced via the covariant derivative as

$$\partial_\mu \to \mathcal{D}_\mu \equiv \partial_\mu + i\frac{Q}{\hbar c}A_\mu, \tag{2.2.3}$$

where Q is a constant. $A_\mu(x^\nu)$ is a new field which is required to make the Lagrangian invariant and transforms simultaneously with the gauge transformation as

$$A_\mu \to A_\mu - \hbar c\partial_\mu\Lambda(x^\nu), \tag{2.2.4}$$

where $\theta(x^\nu) \equiv Q\Lambda(x^\nu)$. As a result, the Lagrangian with the interaction term is

$$\begin{aligned}\mathcal{L} &= i(\hbar c)\overline{\psi}\gamma^\mu\mathcal{D}_\mu\psi - (mc^2)\overline{\psi}\psi \\ &= [i(\hbar c)\overline{\psi}\gamma^\mu\partial_\mu\psi - (mc^2)\overline{\psi}\psi] - (Q\overline{\psi}\gamma^\mu\psi)A_\mu.\end{aligned} \tag{2.2.5}$$

The last term of Eq. (2.2.5) is the interaction term between spinor field ψ and gauge field A_μ with the coupling constant $-Q$.

It should be noted that the Lagrangian of A_μ with the mass m can be written as

$$\begin{aligned}\mathcal{L} &= -\frac{1}{16\pi}(\partial^\mu A^\nu - \partial^\nu A^\mu)(\partial_\mu A_\nu - \partial_\nu A_\mu) + \frac{1}{8\pi}\left(\frac{mc}{\hbar}\right)^2 A^\nu A_\nu \\ &\equiv -\frac{1}{16\pi}F^{\mu\nu}F_{\mu\nu} + \frac{1}{8\pi}\left(\frac{mc}{\hbar}\right)^2 A^\nu A_\nu. \end{aligned} \tag{2.2.6}$$

which is not invariant under the gauge transformation. Therefore, $m = 0$ is required to keep the Lagrangian invariant under the gauge transformation.

The Lagrangian with the interaction between ψ and A_ν can be written as

$$\mathcal{L} = i(\hbar c)\overline{\psi}\gamma^\mu\partial_\mu\psi - (mc^2)\overline{\psi}\psi - (Q\overline{\psi}\gamma^\mu\psi)A_\mu - \frac{1}{16\pi}F^{\mu\nu}F_{\mu\nu}. \tag{2.2.7}$$

The group formed by $e^{iQ\Lambda(x^\nu)}$ is called $U(1)$ group. It is verified with great precision that Eq. (2.2.7) describes the interaction between the fermion with the charge of Q and photon field A_μ.

2.2.2 $SU(2)$ Gauge Transformation and Weak Interaction

Consider the field with two fermions. Defining the spinor ψ_1 and ψ_2, the Lagrangian without including interaction term can be written as

$$\mathcal{L} = i(\hbar c)\overline{\psi}\gamma^\mu\partial_\mu\psi - c^2 M\overline{\psi}\psi, \tag{2.2.8}$$

where ψ is a doublet formed by two spinor fields as

$$\psi \equiv \begin{pmatrix} \psi_1 \\ \psi_2 \end{pmatrix}, \tag{2.2.9}$$

$$\overline{\psi} \equiv \begin{pmatrix} \overline{\psi_1} & \overline{\psi_2} \end{pmatrix}, \tag{2.2.10}$$

$$M \equiv \begin{pmatrix} m_1 & 0 \\ 0 & m_2 \end{pmatrix}. \tag{2.2.11}$$

In the case of $m_1 = m_2 = m$, we have

$$\mathcal{L} = i(\hbar c)\overline{\psi}\gamma^\mu\partial_\mu\psi - mc^2\overline{\psi}\psi. \tag{2.2.12}$$

The gauge transformation on this Lagrangian can be a $SU(2)$ transformation as

$$\begin{pmatrix} \psi_1' \\ \psi_2' \end{pmatrix} = U \begin{pmatrix} \psi_1 \\ \psi_2 \end{pmatrix}, \tag{2.2.13}$$

where U is

$$U = e^{i(\boldsymbol{\lambda}\cdot\boldsymbol{\tau})}, \tag{2.2.14}$$

with $\boldsymbol{\lambda}$ and $\boldsymbol{\tau}$ being a real vector and the Pauli matrices, respectively. The interaction term is introduced via the covariant derivative by the gauge principle as

$$\begin{aligned}\partial_\mu \to \mathcal{D}_\mu &= \partial_\mu + i\frac{g}{\hbar c}(W_{1\mu}\tau_1 + W_{2\mu}\tau_2 + W_{3\mu}\tau_3) \\ &= \partial_\mu + i\frac{g}{\hbar c}\boldsymbol{W}_\mu\cdot\boldsymbol{\tau}, \end{aligned} \tag{2.2.15}$$

where W is a vector boson of $SU(2)$ doublet. The Lagrangian with the interaction term can be written as

$$\mathcal{L} = [i(\hbar c)\overline{\psi}\gamma^\mu\partial_\mu\psi - c^2 M\overline{\psi}\psi] - g\overline{\psi}\gamma^\mu(\boldsymbol{W}_\mu \cdot \boldsymbol{\tau})\psi. \tag{2.2.16}$$

Again the gauge principle requires massless gauge boson. This problem will be solved by introducing Higgs mechanism, will be discussed in Section 2.3.

2.3 $SU(2)_L \otimes U(1)_Y$ Gauge Transformation and Higgs Mechanism

2.3.1 $SU(2)_L \otimes U(1)_Y$ Gauge Transformation

The electroweak interaction is constructed by imposing $SU(2)_L \otimes U(1)_Y$ gauge invariance (Glashow-Weinberg-Salam theory). The Lagrangian without interaction term can be written as

$$\begin{aligned}\mathcal{L} &= i(\hbar c)\overline{\psi}\gamma^\mu\partial_\mu\psi \\ &= i(\hbar c)(\overline{\psi_L} + \overline{\psi_R})\gamma^\mu\partial_\mu(\psi_L + \psi_R) \\ &= i(\hbar c)[\overline{\psi_L}\gamma^\mu\partial_\mu\psi_L + \overline{\psi_R}\gamma^\mu\partial_\mu\psi_R],\end{aligned} \tag{2.3.1}$$

where a left-handed and right-handed spinor field are written separately for further convenience. The gauge transformation is applied as

$$\psi_L \to e^{i\boldsymbol{\lambda}\cdot\boldsymbol{\tau}}e^{iY_L\Lambda}\psi_L, \tag{2.3.2}$$

$$\psi_R \to e^{iY_R\Lambda}\psi_R, \tag{2.3.3}$$

in which only left-handed spinor field is $SU(2)$ doublet while the right-handed field is singlet. The Y, weak hyper charge, is a quantum number associated with $U(1)$ group. The covariant derivative corresponding to the $SU(2)_L \otimes U(1)$ is written as

$$\partial_\mu \to \mathcal{D}_\mu = \partial_\mu + i\frac{g}{\hbar c}\boldsymbol{W}_\mu \cdot \frac{\boldsymbol{\tau}}{2} + i\frac{g'}{\hbar c}\frac{Y_j}{2}B_\mu, \tag{2.3.4}$$

where g and g' are coupling constants. The Lagrangian with the interaction term can be written as

$$\begin{aligned}\mathcal{L} = \sum_{j=L,R}\left[i(\hbar c)\overline{\psi_j}\gamma^\mu\partial_\mu\psi_j + i(\hbar c)\overline{\psi_j}\gamma^\mu\left(i\frac{g'}{\hbar c}\frac{Y_j}{2}B_\mu\right)\psi_j\right] \\ -\frac{ig}{2}\overline{\psi_L}\gamma^\mu\boldsymbol{W}_\mu \cdot \boldsymbol{\tau}\psi_L - \frac{1}{16\pi}(B^{\mu\nu}B_{\mu\nu} + \boldsymbol{W}^{\mu\nu}\boldsymbol{W}_{\mu\nu}),\end{aligned} \tag{2.3.5}$$

where $B_{\mu\nu} \equiv \partial_\mu B_\nu - \partial_\nu B_\mu$ and $\boldsymbol{W}_{\mu\nu} \equiv \partial_\mu \boldsymbol{W}_\nu - \partial_\nu \boldsymbol{W}_\mu$. However, Eq. (2.3.5) is required as local gauge transformation, the gauge boson masses should be zero. These problems can be resolved by introducing Higgs mechanism.

2.3.2 Higgs Mechanism

Introducing a $SU(2)$ doublet of complex scalar field Φ and the Lagrangian which is invariant under $SU(2)_L \otimes U(1)_Y$ global gauge transformation is written as

$$\Phi = \begin{pmatrix} \Phi_A \\ \Phi_B \end{pmatrix} \equiv \begin{pmatrix} \phi_1 + i\phi_2 \\ \phi_3 + i\phi_4 \end{pmatrix}, \tag{2.3.6}$$

$$\mathcal{L} \equiv \frac{1}{2}(\partial_\mu \Phi^\dagger)(\partial^\mu \Phi) + \frac{1}{2}\mu^2(\Phi^\dagger\Phi) - \frac{1}{4}\lambda^2(\Phi^\dagger\Phi)^2, \tag{2.3.7}$$

where $\phi_1, \phi_2, \phi_3, \phi_4$ are real field, μ and λ are real constant. If we require that the Lagrangian is invariant under $SU(2)_L \otimes U(1)_Y$ local gauge transformation, the Lagrangian can also be written as

$$\mathcal{L} = \frac{1}{2}(\mathcal{D}_\mu \Phi^\dagger)(\mathcal{D}^\mu \Phi) + \frac{1}{2}\mu^2(\Phi^\dagger\Phi) - \frac{1}{4}\lambda^2(\Phi^\dagger\Phi)^2. \tag{2.3.8}$$

In this expression, the term $V(\Phi^\dagger\Phi) \equiv -\frac{1}{2}\mu^2(\Phi^\dagger\Phi) + \frac{1}{4}\lambda^2(\Phi^\dagger\Phi)^2$ can be regarded as a potential of the field Φ. In quantum mechanics, the state of particle is described as the excitation from the ground state. $V(\Phi^\dagger\Phi)$ is calculated as

$$\begin{aligned} V(\Phi^\dagger\Phi) &= -\frac{1}{2}\mu^2(\Phi^\dagger\Phi) + \frac{1}{4}\lambda^2(\Phi^\dagger\Phi)^2 \\ &= \frac{1}{4}\lambda^2\left(\Phi^\dagger\Phi - \frac{\mu^2}{\lambda^2}\right)^2 - \frac{1}{4}\frac{\mu^4}{\lambda^2}. \end{aligned} \tag{2.3.9}$$

From this expression, $V(\Phi^\dagger\Phi)$ is minimum at $\Phi = \mu/\lambda$. After performing a proper gauge transformation, a ground state of Φ can be chosen as

$$\Phi_\mu = \begin{pmatrix} 0 \\ \mu/\lambda \end{pmatrix} \equiv \begin{pmatrix} 0 \\ v \end{pmatrix}. \tag{2.3.10}$$

Defining $h(x^\nu)$ as the excitation from ground state, the potential can be written as

$$\Phi = \begin{pmatrix} 0 \\ v + h(x^\nu) \end{pmatrix}, \tag{2.3.11}$$

thus we have $\Phi^\dagger\Phi = (v+h)^2$. Then, the potential $V(\Phi^\dagger\Phi)$ can be re-written with $h(x)$ as

$$\begin{aligned} V(\Phi^\dagger\Phi) &= \frac{1}{4}\lambda^2\left(\Phi^\dagger\Phi - \frac{\mu^2}{\lambda^2}\right)^2 - \frac{1}{4}\frac{\mu^4}{\lambda^2} \\ &= \frac{1}{4}\lambda^2\left((v+h)^2 - \frac{\mu^2}{\lambda^2}\right)^2 - \frac{1}{4}\frac{\mu^4}{\lambda^2} \\ &= \frac{1}{4}\lambda^2(h^4 + 4h^3v + 4h^2v^2 - v^4). \end{aligned} \tag{2.3.12}$$

where a parameter Y in Eq. (2.3.4) is chosen by foreseeing the theory consistent with the electromagnetic interaction. Therefore, the Lagrangian (2.3.8) can be written by the excitation from the ground state as

$$\mathcal{L} = \frac{1}{2}(\partial_\mu h)(\partial^\mu h) + \frac{1}{8}\left(\frac{g}{\hbar c}\right)^2 [W_\mu \, (W^{\ \mu})^* + (W_\mu^+)^* W^{+\mu}](v+h)^2 \\ + \frac{1}{8}\left(\frac{1}{\hbar c}\right)^2 (-gW_{3\mu} + g'B_\mu)(-gW_3^\mu + g'B^\mu)(v+h)^2 - \frac{1}{4}\lambda^2(h^4 + 4h^3 v + 4h^2 v^2 - v^4). \tag{2.3.13}$$

Since we chose the ground state of $\Phi \neq 0$, the Lagrangian does not preserve gauge symmetry around the ground state. Due to the symmetry breaking, the gauge fields B_μ and $W_{3\mu}$ can be mixed, and generate newly gauge fields A_μ and Z_μ. The relation between these gauge fields is represented as

$$\begin{pmatrix} A_\mu \\ Z_\mu \end{pmatrix} \equiv \begin{pmatrix} \cos\theta_W & \sin\theta_W \\ -\sin\theta_W & \cos\theta_W \end{pmatrix} \begin{pmatrix} B_\mu \\ W_{3\mu} \end{pmatrix}, \tag{2.3.14}$$

where A_μ can be regarded as the photon field as we discussed in $U(1)$ gauge transformation, and Z_μ is the Z boson field. θ_W is called Weinberg angle which is a mixing angle of the B and W and is one of the fundamental parameter of the Standard Model. There are relations among Weinberg angle θ_W, elementary charge e, and coupling constants g and g' as

$$g \sin\theta_W = g' \cos\theta_W = e. \tag{2.3.15}$$

The interaction term $\mathcal{L}_{\text{int}}^{\text{NC}}$ in Eq. (2.3.5) can be written as

$$\mathcal{L}_{\text{int}}^{\text{NC}} = -\sum_{j=L,R} e\overline{\psi_j}\gamma^\mu Q\psi_j A_\mu + \sum_{j=1}^{3} \frac{e}{\sin\theta_W \cos\theta_W}\overline{\psi_j}\gamma^\mu(T_3 - Q\sin^2\theta_W)\psi_j Z_\mu. \tag{2.3.16}$$

where Q and T_3 are electric charge and the third component of $SU(2)_L$ spin, respectively. The electroweak interaction is introduced from common $SU(2)_L \otimes U(1)_Y$ gauge transformation. From Eq. (2.3.13), the mass of W and Z boson can be written as

$$m_{W^\pm} = \frac{\sqrt{\pi}}{c^2} gv, \tag{2.3.17}$$

$$m_Z = \frac{\sqrt{\pi}}{c^2} \frac{1}{\cos\theta_W} gv. \tag{2.3.18}$$

Considering the other remaining terms of Eq. (2.3.13)

$$\mathcal{L} = \frac{1}{2}(\partial_\mu h)(\partial^\mu h) - \frac{1}{2}\left[\frac{c}{\hbar}\left(\sqrt{2}\frac{\hbar}{c}\lambda v\right)\right]^2 h^2 - \lambda^2 h^3 v - \frac{\lambda^2}{4}h^4. \tag{2.3.19}$$

The second term of this equation shows the mass of scalar particle, $m_h = \sqrt{2}\frac{\hbar}{c}\lambda v$, where

v is the vacuum expectation value and $v \sim 246$ GeV. The final terms of Eq. (2.3.13)

$$\mathcal{L} = \frac{1}{8\pi}\left(\frac{m_W c}{\hbar}\right)^2 [W \;\; \mu(W-\mu)^* + W_\mu^+(W+\mu)^*] \left(2\frac{h}{v} + \frac{h^2}{v^2}\right) + \frac{1}{8\pi}\left(\frac{m_Z c}{\hbar}\right)^2 Z_\mu Z^\mu \left(2\frac{h}{v} + \frac{h^2}{v^2}\right) \tag{2.3.20}$$

show the interaction term between gauge boson and Higgs particle.

2.3.3 Mass of Fermions

In general, the Lagrangian of the fermion mass term can be written as

$$\mathcal{L} = -mc^2\overline{\psi}\psi = -mc^2(\overline{\psi_L}\psi_R + \overline{\psi_R}\psi_L). \tag{2.3.21}$$

where ψ_L is the doublet of left-handed for $SU(2)$ transformation $\begin{pmatrix} u_L \\ d_L \end{pmatrix}$, and ψ_R is the singlet like u_R or d_R. Eq. (2.3.21) is not invariant for $SU(2)_L$ gauge transformation. In order to solve this problem, the Standard Model introduces interaction between the Higgs boson and fermion to make the Lagrangian gauge invariant as

$$\begin{aligned}\mathcal{L}_{\text{Yukawa}} = &- c_d \left[(\overline{u_L}\ \overline{d_L}) \begin{pmatrix} \Phi_A \\ \Phi_B \end{pmatrix} d_R + \overline{d_R}(\Phi_A^*\ \Phi_B^*) \begin{pmatrix} u_L \\ d_L \end{pmatrix}\right] \\ &- c_u \left[(\overline{u_L}\ \overline{d_L}) \begin{pmatrix} \Phi_B^* \\ -\Phi_A^* \end{pmatrix} u_R + \overline{u_R}(\Phi_B - -\Phi_A) \begin{pmatrix} u_L \\ d_L \end{pmatrix}\right].\end{aligned} \tag{2.3.22}$$

Then, choosing a ground state as Eq. (2.3.11) so that

$$\mathcal{L}_{\text{Yukawa}} = -(c_d v\overline{d}d + c_u v\overline{u}u + c_d h\overline{d}d + c_u h\overline{u}u), \tag{2.3.23}$$

with using the relations of $\overline{u_L}u_R + \overline{u_R}u_L = \overline{u}u$ and $\overline{d_L}d_R + \overline{d_R}d_L = \overline{d}d$. We have

$$c_d v\overline{d}d = m_d c^2\overline{d}d \tag{2.3.24}$$

$$c_u v\overline{u}u = m_u c^2\overline{u}u, \tag{2.3.25}$$

where m_d and m_u are masses of fermions. The coupling constants, c_u and c_d, are called Yukawa coupling and are proportional to the mass of the fermions. There is no mechanism to determine Yukawa couplings and left as free parameters in the Standard Model.

3 The International Linear Collider and Its Detectors

The International Linear Collider (ILC) is proposed as a next-generation energy frontier machine. In this section, details of the ILC, accelerator components, detectors, and its performance are presented.

3.1 Overview of the International Linear Collider

The ILC is a next-generation electron–positron linear collider. It covers the center-of-mass energy range of 250 - 500 GeV and is extendable to 1 TeV. Both the electron and positron beams are designed to be polarized, which allow precise measurements of the properties of the electroweak interaction in the Standard Model. The details of the machine design are summarized in the ILC Technical Design Report (TDR) [24–28]. Figure 3.1.1 is schematic layout of the ILC.

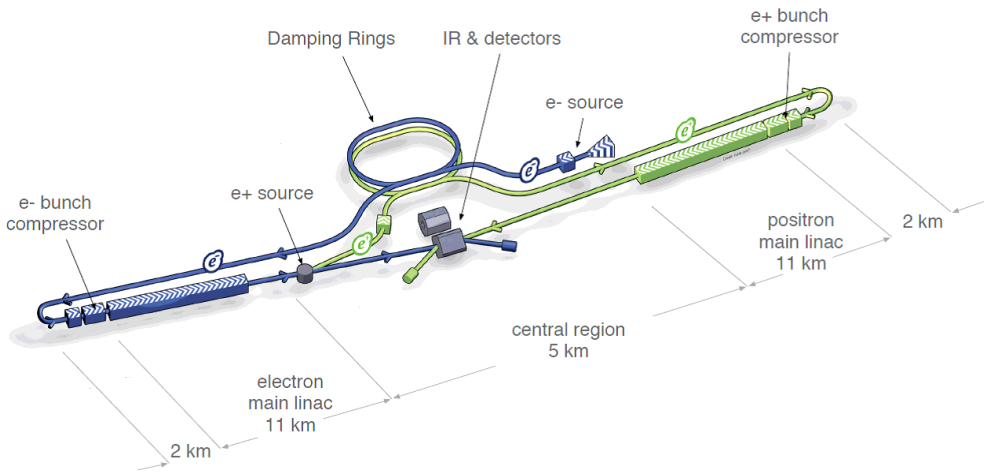

Figure 3.1.1: A schematic layout of the ILC (not scaled) [24].

The ILC is about 31 km long at the first stage. The components of the ILC are following [24, 26, 27]:

- A polarized electron source based on a GaAs photocathode DC gun with a beam polarization of 80%. This beam is accelerated to be 5 GeV and enters to the dumping rings.
- A polarized positron source using a superconducting helical undulator. The positrons are produced by using an electron beam with the energy of 150 - 250 GeV. A beam polarization of the baseline design for positron beam is 30%. An upgrade beam polarization is 60% using a photon collimator. This beam is accelerated to be 5 GeV and enters to the dumping rings. The helical undulator scheme is the baseline design.

- Dumping rings (DR) for the electron beam and the positron beam to reduce emittance. An operating energy of DR is 5 GeV.

- Beam transport systems after the DRs. These components are called Ring To Main Linac (RTML). The RTML consists of five systems, a $\sim$ 15 km long transport line with an operating energy of 5 GeV; betatron and energy collimation systems; a 180° turn-around; spin rotators; and two bunch compressors. A beam is accelerated to be 15 GeV after passing the RTML.

- Two main linacs consist of 1.3 GHz superconducting radio frequency (SCRF) cavities with an average gradient of 31.5 MV/m. These cavities are made of niobium, and have a nine-cell structure as shown in Figure 3.1.2. A beam is accelerated up to 250 GeV at the first stage of the ILC.

- Two Beam Delivery Systems (BDS) which bring the electron and positron beam to the Interaction Point (IP) with the beam crossing angle of 14 mrad. The BDS consists of five components, a section for measuring emittance and matching, trajectory feedback, polarimetry and energy diagnostics; a collimation section to remove beam halo; a final focus system to focus the beam at the IP; an interaction region including detectors; and the extraction lines to transport the beam from IP to a dump.

- Two detector systems with "push-pull" configuration. There are two detector systems for the complementarity and cross-check. These detectors share a single IP of the ILC. A schematic layout of a detector hall for the push-pull configuration is shown in Figure 3.1.3.

Figure 3.1.2: A niobium nine-cell cavity [24].

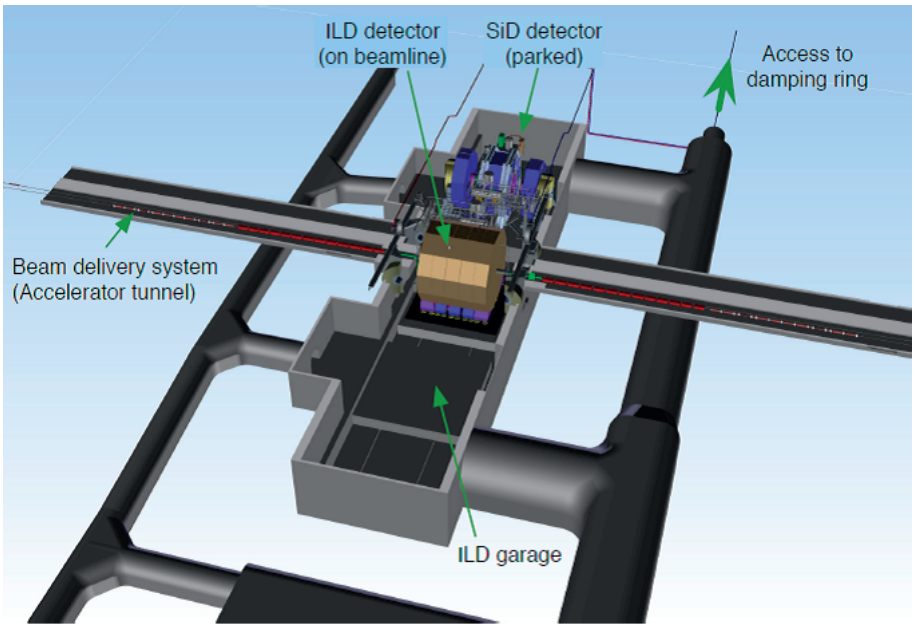

Figure 3.1.3: An example layout of the detector hall for push-pull configuration [24].

The machine parameters of the ILC are shown in Table 3.1.1.

Table 3.1.1: The machine parameters of the ILC [24].

Name		Unit	Baseline 500 GeV machine			1st stage	L upgrade	$E_{\rm CM}$ upgrade	
								A	B
Center-of-mass energy	$E_{\rm CM}$	GeV	250	350	500	250	500	1000	1000
Collision rate	$f_{\rm rep}$	Hz	5	5	5	5	5	4	4
Number of bunches	$N_{\rm b}$		1312	1312	1312	1312	2625	2450	2450
Bunch population	N	$\times 10^{10}$	2.0	2.0	2.0	2.0	2.0	1.74	1.74
Bunch separation	$\Delta t_{\rm b}$	ns	554	554	554	554	366	366	366
Pulse current	$I_{\rm bram}$	mA	5.8	5.8	5.8	5.8	8.8	7.6	7.6
Main linac average gradient	$G_{\rm a}$	MV/m	14.7	21.4	31.5	31.5	31.5	38.2	38.2
Average total beam power	$P_{\rm mean}$	MW	5.9	7.3	10.5	5.9	21.0	27.2	27.2
Estimated AC power	$P_{\rm AC}$	MW	122	121	163	129	204	300	300
RMS bunch length	σ_z	mm	0.3	0.3	0.3	0.3	0.3	0.250	0.225
Electron RMS energy spread	$\Delta p/p$	%	0.190	0.158	0.124	0.190	0.124	0.083	0.085
Positron RMS energy spread	$\Delta p/p$	%	0.152	0.100	0.070	0.152	0.070	0.043	0.047
Electron polarization	P_-	%	80	80	80	80	80	80	80
Positron polarization	P_+	%	30	30	30	30	30	20	20
Horizontal emittance	$\gamma\varepsilon_x$	μm	10	10	10	10	10	10	10
Vertical emittance	$\gamma\varepsilon_y$	nm	35	35	35	35	35	30	30
IP horizontal beta function	β_x^*	mm	13.0	16.0	11.0	13.0	11.0	22.6	11.0
IP vertical beta function	β_y^*	mm	0.41	0.34	0.48	0.41	0.48	0.25	0.33
IP RMS horizontal beam axis	σ_x^*	nm	729.0	683.5	474	729	474	481	335
IP RMS vertical beam axis	σ_x^*	nm	7.7	5.9	5.9	7.7	5.9	2.8	2.7
Luminosity	L	$\times 10^{34}{\rm cm}^{-2}{\rm s}^{-1}$	0.75	1.0	1.8	0.75	3.6	3.6	4.9
Fraction of luminosity in top 1%	$L_{0.01}/L$		87.1%	77.4%	58.3%	87.1%	58.3%	59.2%	44.5%
Average energy loss	$\delta_{\rm BS}$		0.97%	1.9%	4.5%	0.97%	4.5%	5.6%	10.5%
Number of pairs per bunch crossing	$N_{\rm pairs}$	$\times 10^3$	62.4	93.6	139.0	62.4	139.0	200.5	382.6
Total pair energy per bunch crossing	$E_{\rm pairs}$	TeV	46.5	115.0	344.1	46.5	344.1	1338.0	3441.0

3.2 Detector Systems

For the ILC, two detector systems are proposed, the ILD and the SiD. We will discuss the ILD detector. Details of the SiD can be found at Part II of Ref. [28].

The International Large Detector (ILD) is the one of the detector concepts of the ILC. A schematic layout is shown in Figure 3.2.1 and detailed schematic two-dimensional layout is shown in Figure 3.2.2.

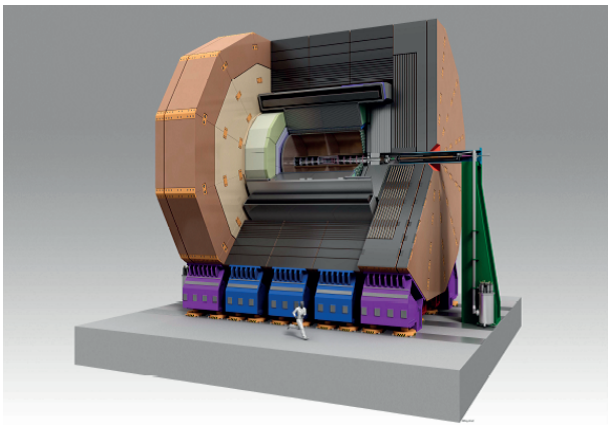

Figure 3.2.1: A schematic layout of the ILD [28].

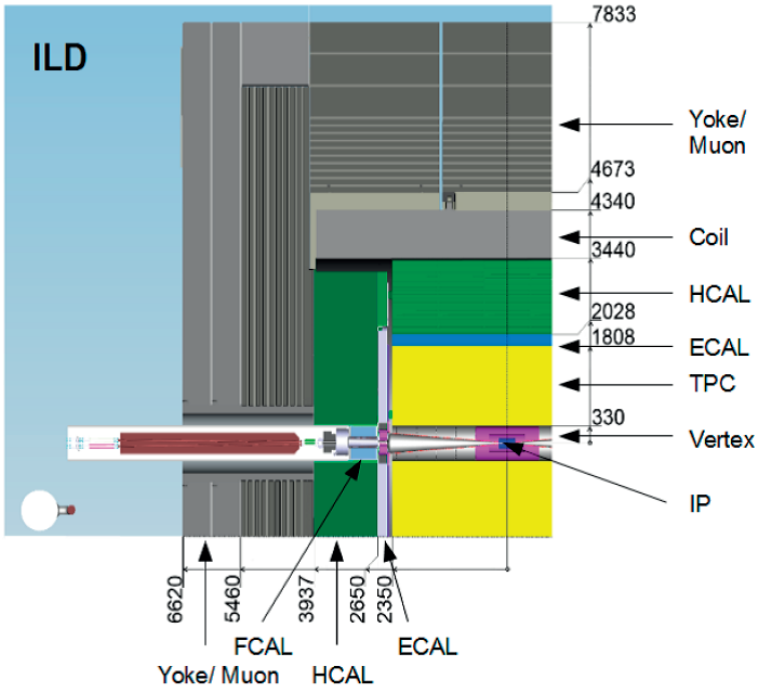

Figure 3.2.2: A two-dimensional schematic layout of the ILD [28].

The ILD is a detector system designed for the Particle Flow Algorithm [47]. The ILD system consists of several detector components; a vertex detector (VTX), silicon tracking systems, a time projection chamber (TPC), an electromagnetic calorimeter (ECAL), a hadronic calorimeter (HCAL), a coil, and a yoke. For the forward region, an FTD, an STD, a LumiCal, an LHCal, and a BeamCal are located.

3.2.1 Vertex Detector

The vertex detector (VTX) is a multi-layer pixel-vertex detector to measure the vertex. VTX is located most inner part of the detector system. The performance goal of VTX is better than $5 \oplus 10/p \sin^{3/2}\theta$ μm for the impact parameter resolution of a track. In order to achieve this, VTX is required to have a spatial resolution near the IP better than 3 μm, a material budget below than 0.15% X_0/layer (X_0: radiation length), a first layer located at a radius of $\sim$ 1.6 cm, and a pixel occupancy not exceeding a few %. VTX has an important role for identification of heavy quarks (charm and bottom). This is the essential point for many ILC physics studies.

The baseline design of VTX is three cylindrical double-sided ladders. VTX covers the radius from 16 mm to 60 mm. An alternative design is five single-sided layers, which covers from 15 mm to 60 mm. Three options are considered for the pixel technology, *i.e.*, CMOS, Fine Pixel CCD (FPCCD), and DEPleted Field Effect Transistor (DEPFET). All layers will be fulfilled with the sensors. The schematic view of VTX geometry is shown in Figure 3.2.3 [48].

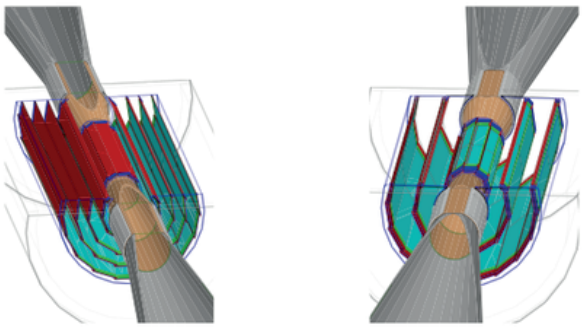

Figure 3.2.3: The geometry of VTX. Left: five single-sided layers, right: three double-sided layers.

3.2.2 Silicon Tracking Systems

A system of silicon strip detectors is located. This system has four components; Silicon Inner Tracker (SIT), Silicon External Tracker (SET), end cap component behind the end plate of the TPC (ETD), and forward tracker (FTD). The location of each detector can be found in Figure 3.2.4 [28].

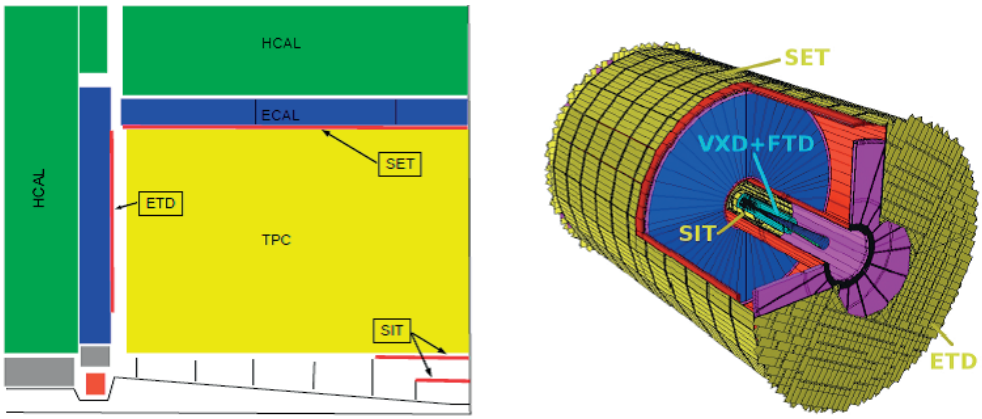

Figure 3.2.4: Left: the locations of SIT, SET, and ETD are shown in this 2D schematic view. Right: a 3D Geant4 [49] simulation description of the silicon tracking systems [28]. ("VXD" means VTX.)

The SIT, SET, and ETD are the central silicon detectors. These give us additional space point information to improve the tracking performance. SIT is located between VTX and TPC, and improves the momentum resolution and reconstruction of low transverse momentum tracks. SET is located between TPC and ECAL, and gives entry points to ECAL. ETD is located between end plate of TPC and end cap of calorimeter system, and gives entry points to the calorimeter. The baseline design for SIT and SET consists of false double-sided silicon microstrips, while single-sided silicon microstrips for ETD. The false double-sided layers are made each of two single-sided strip layers tilted by a small angle with respect to each other. SIT has two such layers and SET has one.

FTD consists of seven tracking disks, and is located between the beam pipe and inner field cage of TPC. The baseline design of first two disks are made by pixels, and others are microstrips. There are three pixel technology options; CMOS, CCD, and DEPFET, as already described at VTX.

3.2.3 Time Projection Chamber

The Time Projection Chamber (TPC) of the ILD is the central tracker to measure the momenta of the tracks precisely, using up to 224 space points per track. TPC also gives us the possibility of dE/dx measurement for the particle identification. The required performance of TPC is following; the point resolution $\sigma_{\rm point}(r\phi) < 100$ μm in overall region, $\sigma_{\rm point}(rz) \simeq 0.4 - 1.4$ mm, dE/dx resolution of $\simeq 5$ %, and momentum resolution of $\sim 1 \times 10^{-4}$ GeV/c at the magnetic field of 3.5 T. The conceptual sketch of TPC is shown in Figure 3.2.5.

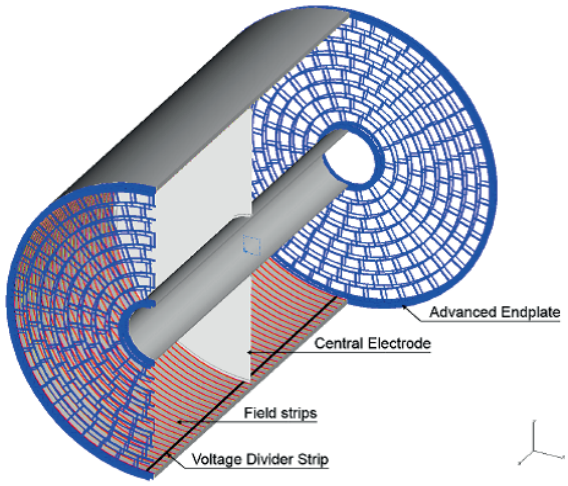

Figure 3.2.5: The conceptual sketch of TPC [28].

For the gas, the so-called T2K gas mixture (Ar 95%-CF_4 3%-isobutane 2%) is considered. Two options are proposed for the system of gas amplification; Micromegas [50] and GEM (Gas Electron Multiplier) [51]. The ionization signals are amplified by this system and collected to readout electronics. The end plate is an assembly of modules containing readout electronics, supply voltages, and cooling.

The LCTPC collaboration [52] is working on the R&D of TPC.

3.2.4 Electromagnetic Calorimeter

The electromagnetic calorimeter (ECAL) is a sampling calorimeter to measure the energy of electrons and photons, made by tungsten absorber layer (radiation length X_0 of 3.5 mm, Molière radius of 9 mm, and interaction length of 99 mm) and silicon layer or scintillator layer. The layout of ECAL and the module are shown in Figure 3.2.6.

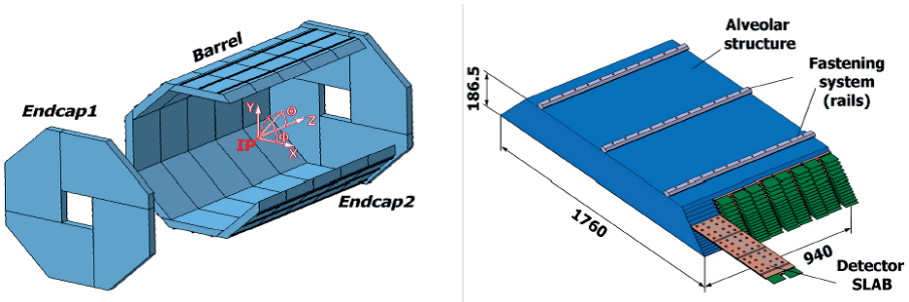

Figure 3.2.6: Left: the layout of ECAL barrel and end caps, right: a module of barrel [48].

In the baseline design of ECAL, 30 readout layers and a thickness of $24X_0$ were chosen. A pad is made by silicon pin diodes and the size is 5×5 mm^2. This ECAL is called SiECAL (Silicon-ECAL). On the other hand, a sensitive layer based on scintillator strips is considered as an alternative option. This is called ScECAL (Scintillator-ECAL).

The CALICE collaboration [53] is working on the R&D of ECAL.

3.2.5 Hadronic Calorimeter

The hadronic calorimeter (HCAL) is a sampling calorimeter to measure the energy of neutral hadrons. The layout of HCAL and module are shown in Figure 3.2.7.

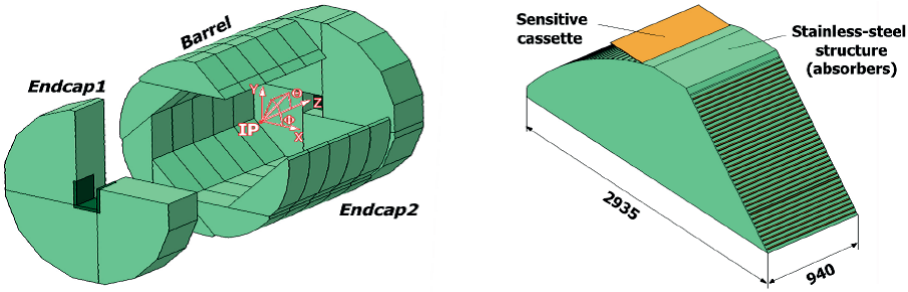

Figure 3.2.7: Left: the layout of HCAL barrel and end caps, right: a module of barrel [48].

HCAL consists of steel absorber (radiation length X_0 of 1.8 cm and hadronic interaction length of 17 cm) and scintillator tiles (AHCAL, Analogue HCAL) or gaseous devices (SDHCAL, Semi-Digital HCAL) as an active medium.

The CALICE collaboration [53] is also working on the R&D of HCAL.

3.2.6 Forward Calorimetry

Some special calorimeters are located in very forward region. They are LHCAL, LumiCal, and BeamCal. Figure 3.2.8 shows the location of each forward detector.

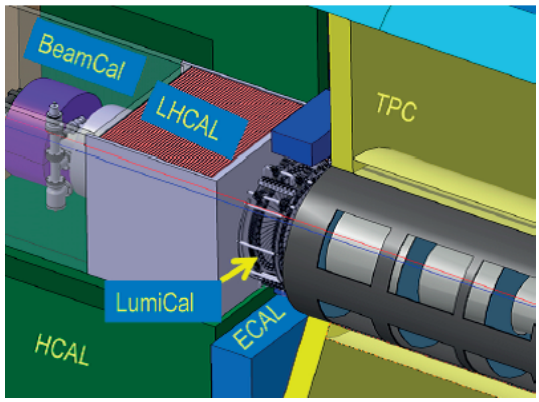

Figure 3.2.8: The location of LHCAL, LumiCal, and BeamCal [28].

LHCAL is a hadronic calorimeter extends the coverage of HCAL to the polar angle. LumiCal is a calorimeter to measure luminosity using Bhabha scattering. BeamCal is a calorimeter for assisting beam tuning and estimating a bunch-by-bunch luminosity using beamstrahlung electron-positron pairs. Both LumiCal and BeamCal are designed as the cylindrical sensor-tungsten sandwich electromagnetic calorimeters [54].

3.2.7 ILD Coil, Yoke System, and Muon System

The coil of the ILD is a superconducting solenoid coil which provides 3.5 T magnetic field in nominal running (with maximum of 4 T capability).

The iron return yoke consists of scintillator strips or Resistive Plate Chambers (RPC). This yoke serves as the main mechanical structure of the ILD, and the same time, behaves as a muon system and tail catcher. The muon system is used for identification of muons, and also has a role of tail catcher, for recovering energy which is leaking out of the back of the calorimeter. Figure 3.2.9 shows the sensitive part of muon system and tail catcher, and Figure 3.2.10 shows the cross section of the ILD magnet.

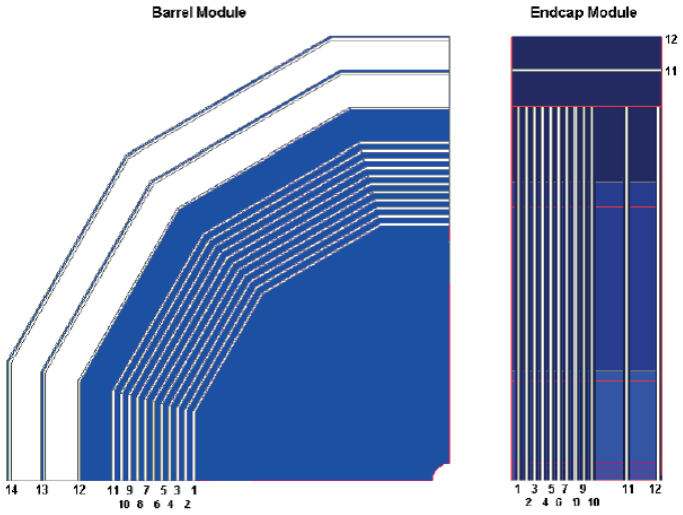

Figure 3.2.9: The sensitive layers of muon system / tail catcher [28].

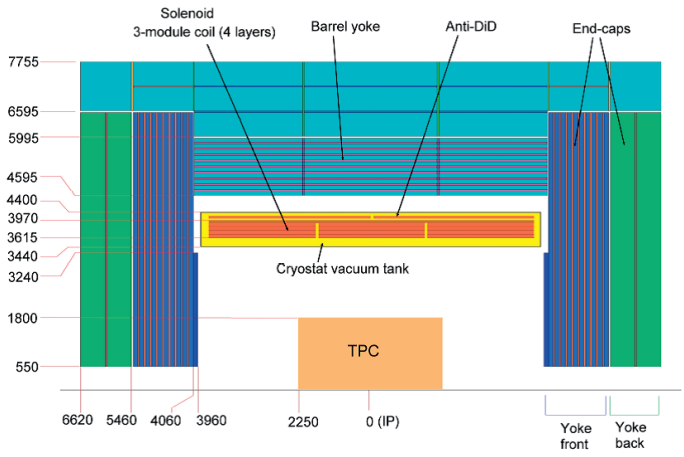

Figure 3.2.10: The cross section of ILD magnet [28].

3.2.8 Particle Flow Algorithm

At the ILC, the separation of W boson and Z boson by reconstructing the mass of these particles is an essential point for physics analysis. Since the mass difference of W and Z boson is about 11 GeV, we need much better mass resolution than 11 GeV. The goal of the ILD is mass resolution comparable to gauge boson width $\sigma_m/m = 2.7\% \sim \ _W/m_W \sim \ _Z/m_Z$ with the hadronic decay of gauge bosons (*i.e.*, $W \to q\overline{q'}$ and $Z \to q\bar{q}$). This goal requires that a jet energy resolution of $\sigma_E/E \lesssim 3.8\%$. For the operation at $\sqrt{s}$ = 500 - 1000 GeV, the typical energy range of a jet is about 150 - 350 GeV. In these cases, the required jet energy resolution is $\sigma_E/E \lesssim 30\%/\sqrt{E}$.

In the traditional way, which combines the energy deposit at ECAL and HCAL, gives poor resolution typically $\gtrsim 55\%/\sqrt{E}$. This is mainly because of the components of jet. About 62% of the components of a jet are charged particles (almost hadrons), $\sim 27\%$ are photons, $\sim 10\%$ are neutral hadrons, and $\sim 1.5\%$ are neutrinos [55]. Thus, approximately 72% particles are measured by HCAL. The performance of HCAL strongly limited the jet energy resolution, and this number is worse than the ILC goal by about factor 2.

On the other hand, the ILD is designed based on the Particle Flow Algorithm (PFA). The main philosophy of the PFA is measuring momenta of charged particles using tracking detectors, while measuring energies of photons and neutral hadrons using calorimeters. In this configuration, HCAL only measures $\sim 10\%$ of all particles in a jet. The crucial point of the PFA is correct assignment of the energy deposits in calorimeter to correct reconstructed particles. This requires a highly granular ECAL and HCAL.

3.3 ILD Performance

The performance of the ILD can be summarized as following.

- tracking efficiency: Figure 3.3.1 shows the case of $t\bar{t} \to 6$ jets at $\sqrt{s}$ = 500 GeV and 1 TeV. The efficiency almost reaches 100% except low momentum tracks ($p < 1$ GeV) and the cases of tracks flight to forward region ($\cos\theta > 0.95$).

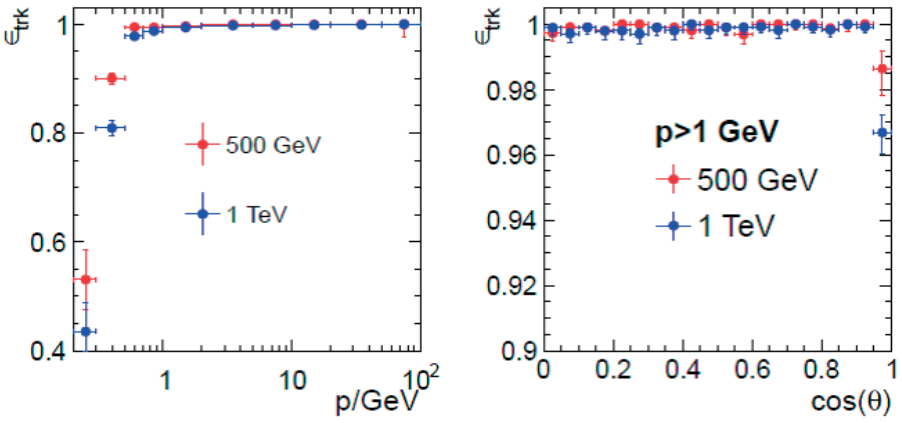

Figure 3.3.1: The tracking efficiency plots for $t\bar{t} \to 6$ jets at $\sqrt{s} = 500$ GeV and 1 TeV, as the function of track momentum in left plot and of $\cos\theta$ in right plot [28].

- momentum resolution: Figure 3.3.2 shows the momentum resolution using single muon events. In the case of $\theta = 30°$, the resolution is better than the goal in overall region. At $\theta = 85°$, all plot points are on or near the goal line.

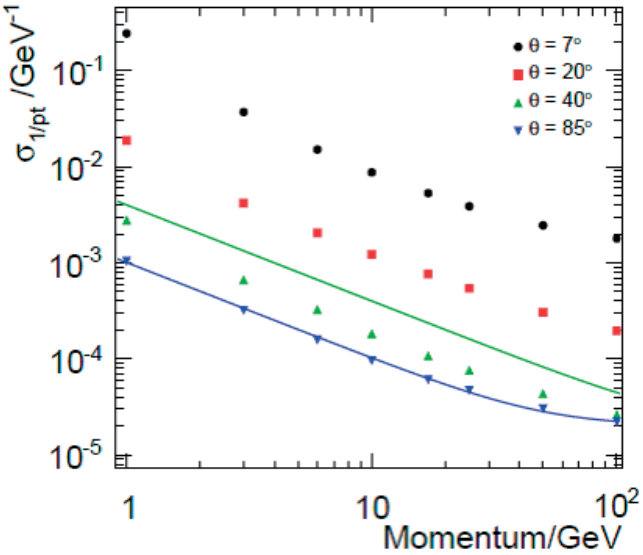

Figure 3.3.2: The transverse momentum resolution as a function of the transverse momentum for different polar angles, using single muon events [28][1]. The lines show $\sigma_{1/p_T} = 2 \times 10^{-5} \oplus 1 \times 10^{-3}/(p_T \sin\theta)$ for $\theta = 30°$ in green and for $\theta = 85°$ in blue.

- impact parameter resolution: Figure 3.3.3 shows the impact parameter resolution using single muon events. In high momentum case such as $p \gtrsim 30$ GeV, it is achieved the requirements.

[1]The green plot points are denote as $\theta = 40°$, but $\theta = 30°$ is true.

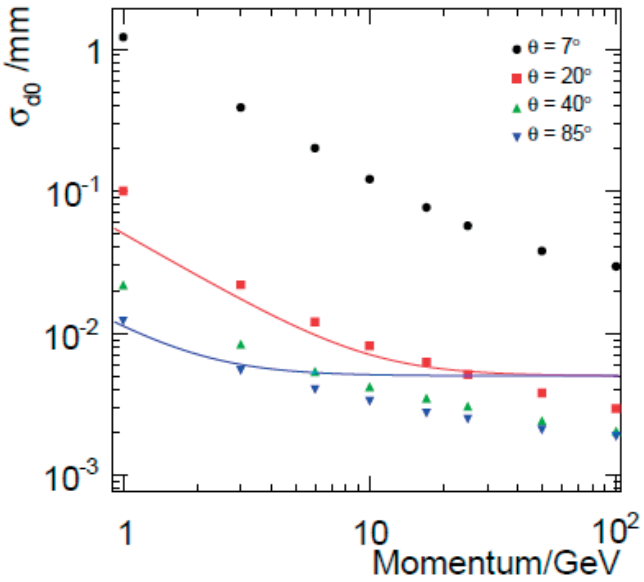

Figure 3.3.3: The impact parameter resolution as a function of the transverse momentum for different polar angles, using single muon events [28][2]. The lines show $\sigma_{r\phi} = 5 \oplus \frac{10}{p \sin^{3/2}\theta} \mu$m for $\theta = 20°$ in red and for $\theta = 85°$ in blue.

- jet energy resolution: Figure 3.3.4 shows the jet energy resolution using the events with Z boson decaying into light quark pairs ($Z \to u\bar{u}, d\bar{d}, s\bar{s}$). The jet energy resolution is better than 3.7% in overall region and all energies greater than 40 GeV, except the region of $|\cos\theta| \sim 1$.

[2]The green plot points are denote as $\theta = 40°$, but $\theta = 30°$ is true.

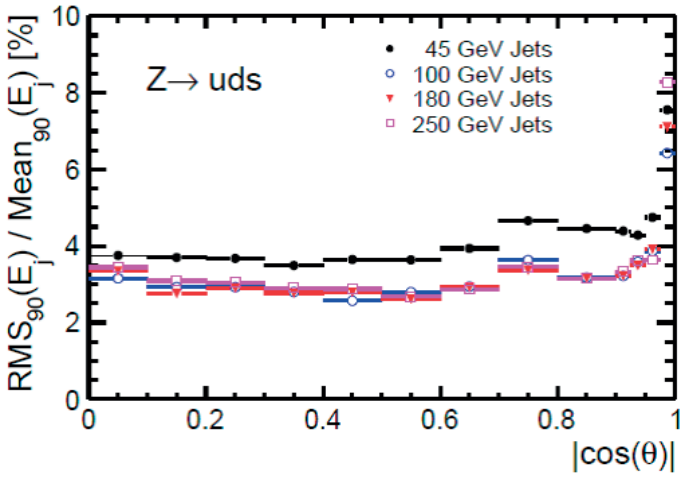

Figure 3.3.4: The jet energy resolution as a function of $|\cos\theta|$, where θ is the thrust axis of the event respect to the beam axis [28].

- flavor tagging performance: Figure 3.3.5 shows the performance of flavor tagging using $Z \to q\bar{q}$ samples at $\sqrt{s} = 91$ GeV and 250 GeV, and $ZZZ \to q\bar{q}q\bar{q}q\bar{q}$ samples at $\sqrt{s} = 500$ GeV and 1 TeV, studied with LCFIPlus package [56]. The LCFIPlus is used for vertex finding, jet finding, and flavor tagging.

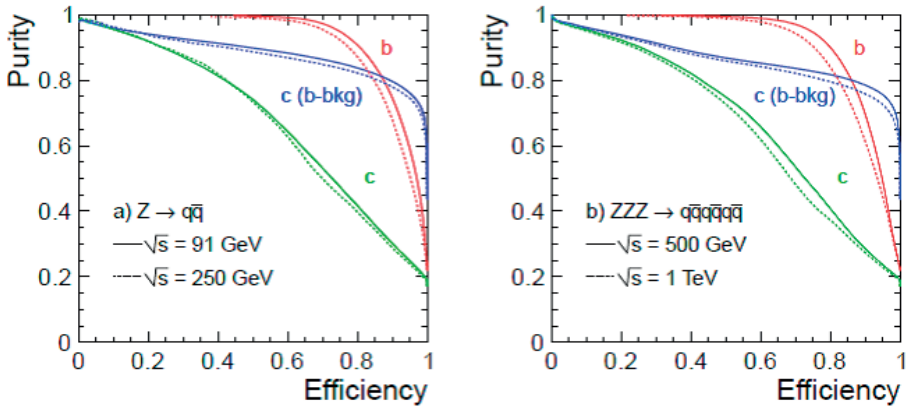

Figure 3.3.5: The performance plots of flavor tagging. Left: $Z \to q\bar{q}$ samples at $\sqrt{s} = 91$ GeV and 250 GeV. Right: $ZZZ \to q\bar{q}q\bar{q}q\bar{q}$ samples at $\sqrt{s} = 500$ GeV and 1 TeV [28].

4 Preparation for Analysis

In this section, details of preparation for the analysis, analysis tools, Monte-Carlo samples, and detector simulations are presented.

4.1 Analysis Settings

In this study, we assumed the sets of $\sqrt{s}$ and integrated luminosity of (250 GeV, 250 fb ^{1}) and (500 GeV, 500 fb ^{1}). These numbers are described as a nominal running scenario of the ILC TDR [28]. We also assumed a Higgs mass of 125 GeV, a branching ratio of Higgs boson decaying into tau pairs (BR($h \to \tau^+\tau$)) of 6.32% [57], and a beam polarization of $P(e\ , e^+) = (-0.8, +0.3)$.

Recently, two papers were published [43,44] about an updated running scenario of the ILC. We will discuss with the case of updated scenario in Section 7.

4.2 Monte-Carlo Samples

4.2.1 Signal Samples

The calculation of cross section and subsequent decay of signal process $e^+e \to f\overline{f}h \to f\overline{f}\tau^+\tau$, where f denotes a fermion, were performed by an event generator [58] using `GRACE` [59, 60]. An event generation was performed by `BASES/SPRING` package [61]. The effect of beamstrahlung was simulated by `GuineaPig` [62], an e^+e beam-beam simulation program, based on the beam parameters by the GDE [63], and implemented to `GRACE` [58]. The initial state radiation was approximately incorporated in an way by the ILC Event Generator Working Group [28,64]. `TAUOLA` [65–67], a library of tau lepton decay, was used for simulating tau decay. In order to handle a spin correlation in the decay of $h \to \tau^+\tau$, `GRACE` was interfaced with `TAUOLA`. `PYTHIA` [68] is a program for hadronization, and used for decaying other short-lived particles and the hadronization. The generated events were stored in STDHEP format [69].

4.2.2 Background Samples

For the background processes, the Monte-Carlo (MC) samples which commonly prepared for the ILC TDR [28] were used for the analysis. These samples were generated by `WHIZARD` [70]. The center-of-mass energies, beam polarizations, and cross sections were listed on the database [71]. `WHIZARD` was used for generating processes as; $e^+e \to 2f$, $e^+e \to 4f$, $e^+e \to 6f$, $e^{\pm}\gamma \to e^{\pm}\gamma$, $e^{\pm}\gamma \to 3f$, $e^{\pm}\gamma \to 5f$, and $e^+e \to f\overline{f}h$. The processes of $e^{\pm}\gamma$ are the interactions between electron/positron beam and beamstrahlung photon. The effects of beamstrahlung and initial state radiation were taken into account in the same way as the signal process. `PYTHIA` and `TAUOLA` were also used for same way as the signal process. Generated events were stored in STDHEP format. The samples of $e^+e \to f\overline{f}h \to f\overline{f}\tau^+\tau$ generated by `WHIZARD` were not used in analysis because current version of `WHIZARD` could not treat the spin correlation in $h \to \tau^+\tau$ decay properly. The hadron backgrounds from $\gamma\gamma$ interactions ($\gamma\gamma \to$ hadron backgrounds), in which photons

were produced by beam–beam interactions were generated based on the cross section model [72] using a phase space particle production model or PYTHIA model.

4.2.3 Detector Simulation and Event Reconstruction

MOKKA [73] was used for the detail detector simulation. A complete description of the detector model with Geant4 [49] was implemented in MOKKA. The ILD model of the version of ILD_o1_v05 which implemented calorimeter options of AHCAL and SiECAL was used in the analysis. The 3D view of ILD_o1_v05 is shown in Figure 4.2.1. SGV fast detector simulation program [74] was used for simulating $e^+e \rightarrow e^+e + 2f$ process (two-photon process) at $\sqrt{s} = 500$ GeV to save CPU time because of its huge cross section. Results of detector simulation were stored in LCIO format [75].

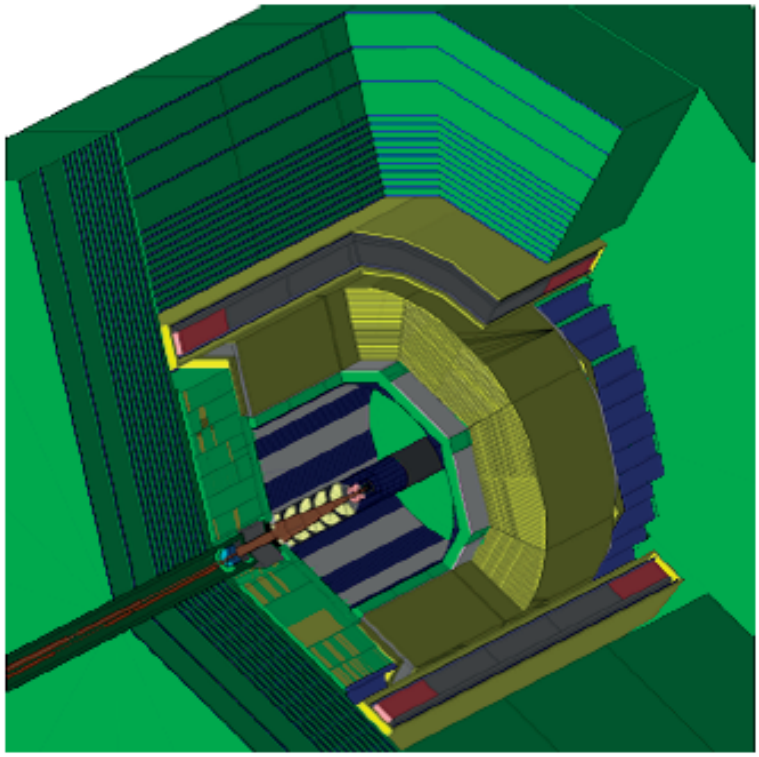

Figure 4.2.1: The 3D view of ILD detector with the model of ILD_o1_v05 [28]. From inside: VTX, SIT, TPC, SET, ECAL, HCAL, Coil, and Yoke. For forward region from inside: FTD, LumiCal, LHCal, and BeamCal.

MARLIN [76] was used for reconstruction and analysis framework. Analysis works were implemented as a processor in MARLIN. The events were reconstructed based on the PFA using PandoraPFA package [47]. There are several additional analysis processors for different analysis mode such as tau reconstruction and jet clustering. Details of algorithm such as tau clustering and jet clustering will be discussed in Sections 5 and 6. The reconstruction and analysis results were stored in ROOT file [77].

The $\gamma\gamma \rightarrow$ hadron backgrounds were overlaid to all MC samples. The average number

of this background was estimated in Ref. [72]. Details will be presented in Sections 5 and 6. In this thesis, we will sometimes call this background as "overlay backgrounds".

4.3 Analysis Optimization

After the reconstruction and analysis, an optimization was performed. All optimizations were to maximize signal significance $S_{\rm sig}$ defined as

$$S_{\rm sig} \equiv \frac{N_S}{\sqrt{N_S + N_B}}, \tag{4.3.1}$$

where $N_S(N_B)$ is the number of remained signal (background) after the analysis.

4.3.1 Multivariate Analysis

A multivariate analysis using TMVA package [78] implemented in ROOT [77] was performed. In this study, the Boosted Decision Tree (BDT) or Gradient Boosted Decision Tree (BDTG) were used for the multivariate analysis. A schematic of Decision Tree is shown in Figure 4.3.1. Starting from "Root node", where a decision is made on which phase space a parameter belongs to. This decision process is repeated depending on the parameters such as number of variables, number of trees, depth of decision trees, and so on. The events are classified as signal or background in final leaf node.

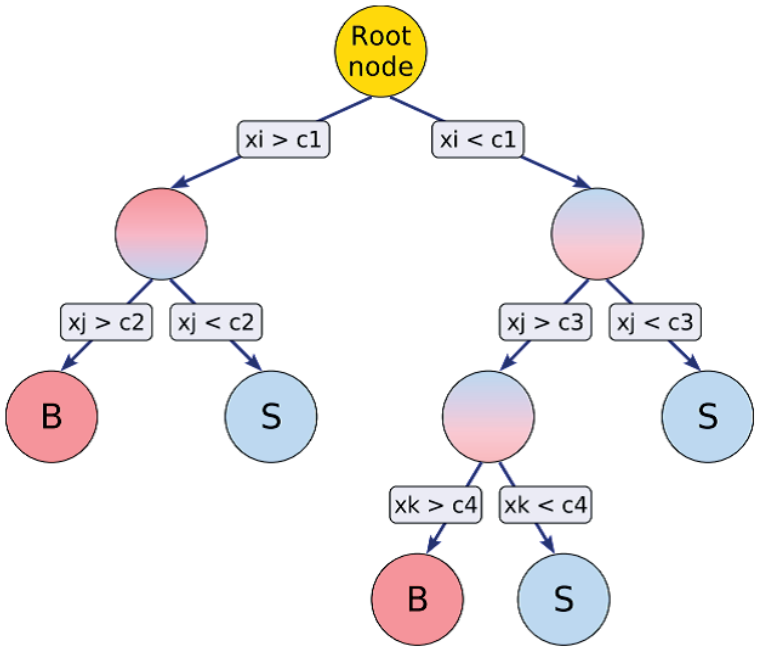

Figure 4.3.1: A schematic view of Decision Tree [79]. The bottom of leaf nodes are labeled with "S" for signal and "B" for background depending on the majority in that node.

In BDT, AdaBoost (adaptive boost) [80, 81] is used as a boosting algorithm, while BDTG using GradBoost (gradient boost) algorithm [79, 82].

In the analysis, half of signal events and half of background events were categorized as training samples, and the other as test samples to avoid the training bias in the event selections. The optimization was performed by both BDT and BDTG, and the better was taken as the final result. The following training parameters were optimized to maximize S_{sig} and avoid overtraining:

- nCuts: number of grid points in variable range used in finding optimal cut in node splitting,
- Shrinkage: learning rate for GradBoost algorithm (only for BDTG),
- MaxDepth: max depth of the decision tree allowed,
- NTrees: number of trees in the forest,
- nEventsMin: minimum number of events of training events required in a leaf node.

It is possible to split the leaf node until it only contains signals or backgrounds, however, such kind of decision tree is strongly overtrained, which simply remember the character of given event samples rather than separating signal and background by their general feature. Therefore, such kind of decision tree should be pruned. In the analysis, the training parameter of nEventsMin is used for pruning, to avoid overtraining.

4.3.2 Cut-based Analysis

The cut-based analysis is a method which applying cuts to reconstructed variables. In this study, the event selection criteria was optimized by the TMVA and the cut-based analysis was performed to understand behavior of variables and to ensure redundancy of the analysis. The results of cut-based analysis for each mode are described in Appendixes B - F.

5 Analysis at Center-of-mass Energy of 250 GeV

In this section, details of analysis at $\sqrt{s} = 250$ GeV will be presented. In this energy, Higgs-strahlung is the dominant production process (see Figure 1.3.1). The signal processes were categorized depending on the decay of Z boson as; $e^+e \to q\bar{q}h$, $e^+e \to e^+e\ h$, $e^+e \to \mu^+\mu\ h$, and $e^+e \to \nu\bar{\nu}h$. In this study, we discuss three analysis modes; $q\bar{q}h$, $e^+e\ h$, and $\mu^+\mu\ h$. As for the $\nu\bar{\nu}h$, we will not discuss in this study because the background rejection is very difficult due to the large ambiguities of missing energy by many neutrinos.

In the analysis, $e^+e \to 2f$, $e^+e \to 4f$, $e^{\pm}\gamma \to e^{\pm}\gamma$, $e^{\pm}\gamma \to 3f$, and $e^+e \to f\bar{f}h$ (except $h \to \tau^+\tau$) were considered for background estimation. They were categorized with the number of fermions in the final states as; two fermions ($2f$), one or three fermions ($1f\_3f$), and four fermions ($4f$). The two-photon processes ($e^+e \to e^+e + 2f$) were categorized as $\gamma\gamma \to 2f$. The number of $\gamma\gamma \to$ hadron backgrounds were estimated as 0.4 per bunch crossing in average at $\sqrt{s} = 250$ GeV [72], and overlaid onto all MC samples.

5.1 Analysis of 250 GeV $e^+e^- \to q\bar{q}h$ Mode

5.1.1 Signal and Backgrounds

The diagram of signal is shown in Figure 5.1.1.

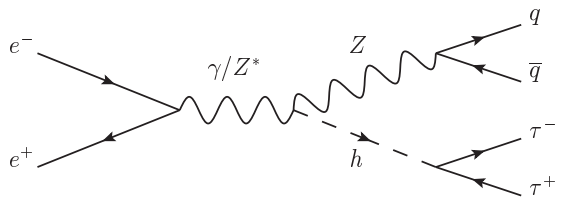

Figure 5.1.1: The diagram of $e^+e \to q\bar{q}h$ signal.

The backgrounds which have the same final state with the signal are irreducible. Figure 5.1.2 left shows the diagram of irreducible background, $e^+e \to ZZ \to q\bar{q}\tau^+\tau$. In addition, the process shown in Figure 5.1.2 right will also be one of the backgrounds due to mis-clustering of taus and/or jets.

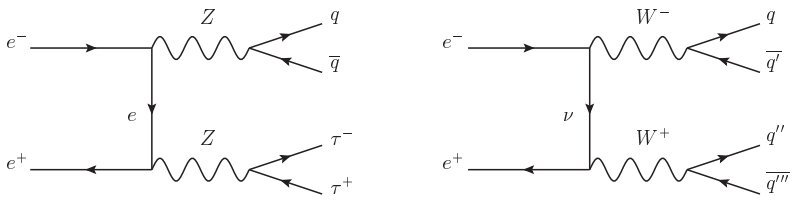

Figure 5.1.2: The example diagram of backgrounds to the $e^+e \rightarrow q\bar{q}h$ signal.

5.1.2 Event Reconstruction

In order to reconstruct the final state of $q\bar{q}\tau^+\tau$ efficiently, the following three steps were applied; (1) tau reconstruction, (2) collinear approximation, (3) jet clustering.

Tau Reconstruction A tau reconstruction algorithm based on a tau mass to find taus in the presence of jet was applied first. The procedures of this algorithm are following;

First, we define the energy of E_{cand} and the momentum $\boldsymbol{P}_{\text{cand}}$ of the tau candidate as

$$E_{\text{cand}} = E_1 + \sum E_i,$$
$$\boldsymbol{P}_{\text{cand}} = \boldsymbol{P}_1 + \sum \boldsymbol{P}_i,$$

where E_1 and $\boldsymbol{P}_1$ are the energy and the momentum of the most energetic track, and E_i and $\boldsymbol{P}_i$ are the energy and the momentum of i-th of other particles that form the tau candidate. The particles forming the tau candidate are chosen in the following way:

1. particles are sorted in the descending order of energy;
2. the highest energy track is temporarily chosen as a tau candidate so that $E_{\text{cand}} = E_1$ and $\boldsymbol{P}_{\text{cand}} = \boldsymbol{P}_1$;
3. the tau candidate is combined with particle i to from an updated tau candidate with $E^{\text{new}}_{\text{cand}} = E_{\text{cand}} + E_i$ and $\boldsymbol{P}^{\text{new}}_{\text{cand}} = \boldsymbol{P}_{\text{cand}} + \boldsymbol{P}_i$, where the particle i is the first in the energy-ordered list of remaining particles that satisfies $\cos\theta_i > 0.99$ and $M^{\text{new}}_{\text{cand}} = \sqrt{E^{\text{new}\,2}_{\text{cand}} - \boldsymbol{P}^{\text{new}\,2}_{\text{cand}}} < 2$ GeV, with θ_i being the angle between $\boldsymbol{P}_{\text{cand}}$ and $\boldsymbol{P}_i$;
4. we repeat step 3, letting $E_{\text{cand}} = E^{\text{new}}_{\text{cand}}$ and $\boldsymbol{P}_{\text{cand}} = \boldsymbol{P}^{\text{new}}_{\text{cand}}$, until all the particles that satisfy the conditions in step 3 are combined to form a tau candidate.

A tau candidate is considered isolated if $E_{\text{cand}} > 3$ GeV, and E_{cone}, the sum of energy of particles within a cone having the cosine of its cone angle greater than 0.95 with the cone axis in the direction of $\boldsymbol{P}_{\text{cand}}$ is smaller than $0.1 \cdot E_{\text{cand}}$. The second condition ensures that the candidate is isolated from other activities. Figure 5.1.3 shows the distribution of E_{cand}, and Figure 5.1.4 shows the distribution of $E_{\text{frac}} \equiv E_{\text{cone}}/E_{\text{cand}}$.

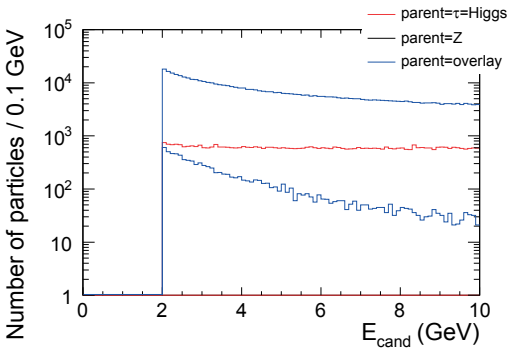

Figure 5.1.3: The distribution of $E_{\rm cand}$. Red, black, and blue histograms show the distribution of particles which parent of seed is Higgs = τ, Z boson, overlay backgrounds, respectively.

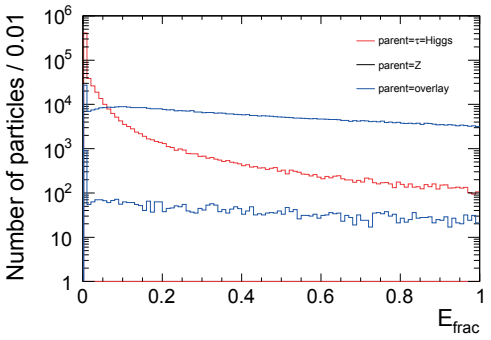

Figure 5.1.4: The distribution of $E_{\rm frac}$. Red, black, and blue histograms show the distribution of particles which parent of seed is Higgs = τ, Z boson, overlay backgrounds, respectively.

The candidate is registered as a 1-prong tau decay, if $N_{(E_{\rm ch}>2{\rm GeV})}$ is 1, where $N_{(E_{\rm ch}>2{\rm GeV})}$ is the number of charged tracks with an energy greater than 2 GeV. The candidate is identified as a 3-prong tau decay if $N_{(E_{\rm ch}>2{\rm GeV})}$ is 3 and the net charge of all charged particles is equal to $+1$ or -1. After finding an isolated tau candidate, those particles that belong to the tau candidate are set aside, and the tau finding algorithm was applied to the remaining particles until there are no remaining charged particles.

The reconstructed efficiencies were;

- reconstruct one τ^+; 70.4%,
- reconstruct one τ^- ; 70.4%,
- reconstruct one τ^+ and one τ^- ; 49.3%.

In the events with reconstructed one τ^+ and one τ^- , the purity was 94.7%. Figure 5.1.5 shows the distribution of tau pair mass $M_{\tau^+\tau^-}$ with opposite charge of tau.

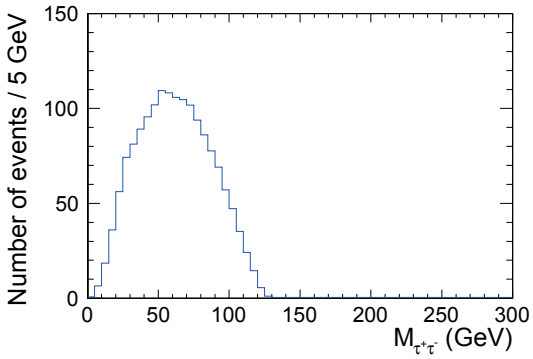

Figure 5.1.5: The distribution of $M_{\tau^+\tau^-}$ of signal process.

Collinear Approximation The collinear approximation [83] was applied to recover momentum of neutrino(s) from tau. To use collinear approximation, two assumptions are needed as following;

- neutrino(s) from a tau are collinear to the visible decay products from that tau,
- the contributions of missing transverse momentum are only come from neutrinos from tau decay.

Since the taus from Higgs boson decay are energetic, it is possible to assume its decay products almost flight same direction. These assumptions are equivalent to assume two taus are going to back-to-back. Detail calculations are written in Appendix A. Figure 5.1.6 shows the distribution of M_{col} with the events which have opposite charge tau pair, where M_{col} is the invariant mass of tau pair system corrected with collinear approximation. It is clear that the original Higgs boson mass of 125 GeV is well reconstructed.

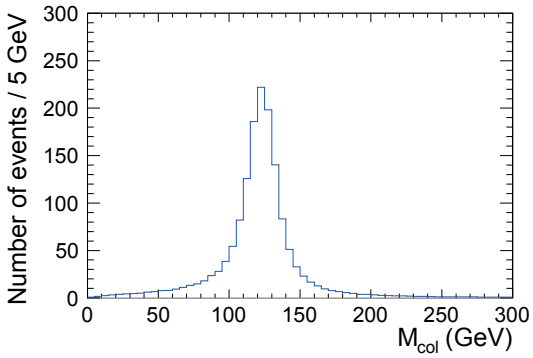

Figure 5.1.6: The distribution of M_{col} of signal process.

Jet Clustering After finishing tau reconstruction, the Durham clustering algorithm [84] was applied for particles which do not belong to tau candidates to force the remaining particles into two jets. The Durham algorithm uses the following dimensionless variable Y_{ij} as

$$Y_{ij} = \frac{2\min[E_i^2, E_j^2](1-\cos\theta_{ij})}{(\sqrt{s})^2}, \tag{5.1.1}$$

where i and j are indexes of particle/jet, E_i and E_j are the energy of i and j, θ_{ij} is the angle between i and j, and $\sqrt{s}$ is the center-of-mass energy, respectively. Calculating Y_{ij} for all possible combinations, and select smallest Y_{ij} and corresponding combination of two particles/jets. That two particles/jets are combined into single jet by summing up the four momenta of i and j. Then repeat above processes until there are remaining two jets for this analysis. Figure 5.1.7 shows the distribution of $M_{q\bar{q}}$ with the events which have reconstructed two jets.

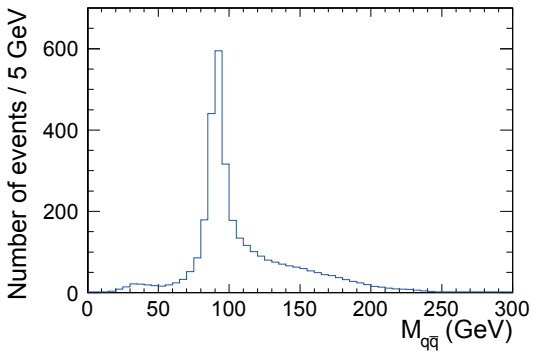

Figure 5.1.7: The distribution of $M_{q\bar{q}}$ of signal process.

5.1.3 Cuts Before Optimization

Before optimizing the selection, the following cuts were applied as the preselection to select events which have a topology consistent to the $q\bar{q}h$ final state;

- number of jets is exactly equal to 2,
- number of τ^+s and τ^- s are exactly equal to 1,
- $N_{\text{track}} \geq 9$, where N_{track} is the number of charged tracks,
- $M_{\text{col}} > 0$ GeV and $E_{\text{col}} > 0$ GeV, where $M_{\text{col}}(E_{\text{col}})$ is the mass (energy) of tau pair system corrected with collinear approximation.

In addition, the following cuts were applied as the basic cuts to suppress trivial backgrounds and enhance signal region;

- $105 < E_{\text{vis}} < 255$ GeV and $M_{\text{vis}} > 95$ GeV, where $E_{\text{vis}}(M_{\text{vis}})$ is the visible energy (visible mass),

- $\sum_i P_{ti} > 40$ GeV, where P_{ti} is the transverse momentum of i-th visible particle,
- thrust < 0.97,
- $60 < E_{q\bar{q}} < 175$ GeV and $35 < M_{q\bar{q}} < 160$ GeV, where $E_{q\bar{q}}(M_{q\bar{q}})$ is the energy (mass) of reconstructed jet pair,
- $\cos\theta_{q\bar{q}} < 0.5$, where $\theta_{q\bar{q}}$ is the angle between reconstructed two jets,
- $E_{\tau^+\tau^-} < 140$ GeV and $5 < M_{\tau^+\tau^-} < 125$ GeV, where $E_{\tau^+\tau^-}(M_{\tau^+\tau^-})$ is the energy (mass) of reconstructed tau pair,
- $\cos\theta_{\tau^+\tau^-} < -0.1$, where $\theta_{\tau^+\tau^-}$ is the angle between reconstructed two taus,
- $30 < E_{\mathrm{col}} < 270$ GeV and $15 < M_{\mathrm{col}} < 240$ GeV,
- $65 < M_{\mathrm{recoil}} < 185$ GeV, where M_{recoil} is the recoil mass against Z boson, can be calculated using the four momentum of reconstructed Z boson and initial state.

All distributions of each variable used for basic cuts are shown in Figure 5.1.8 and Figure 5.1.9. The events passed above all cuts were used for optimization.

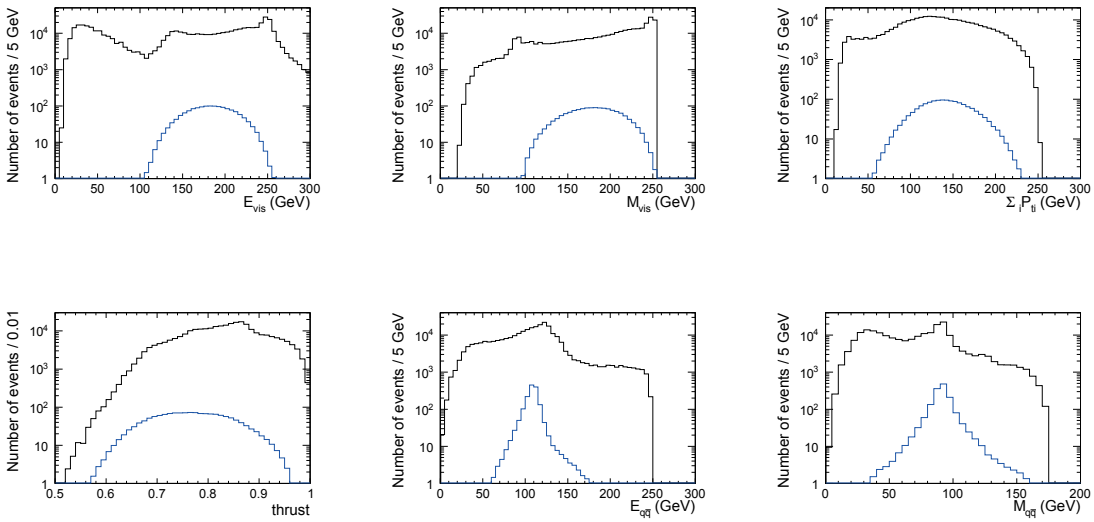

Figure 5.1.8: Distributions of each variable used for basic cuts. Black histograms show the sum of all processes, and blue show signal process.

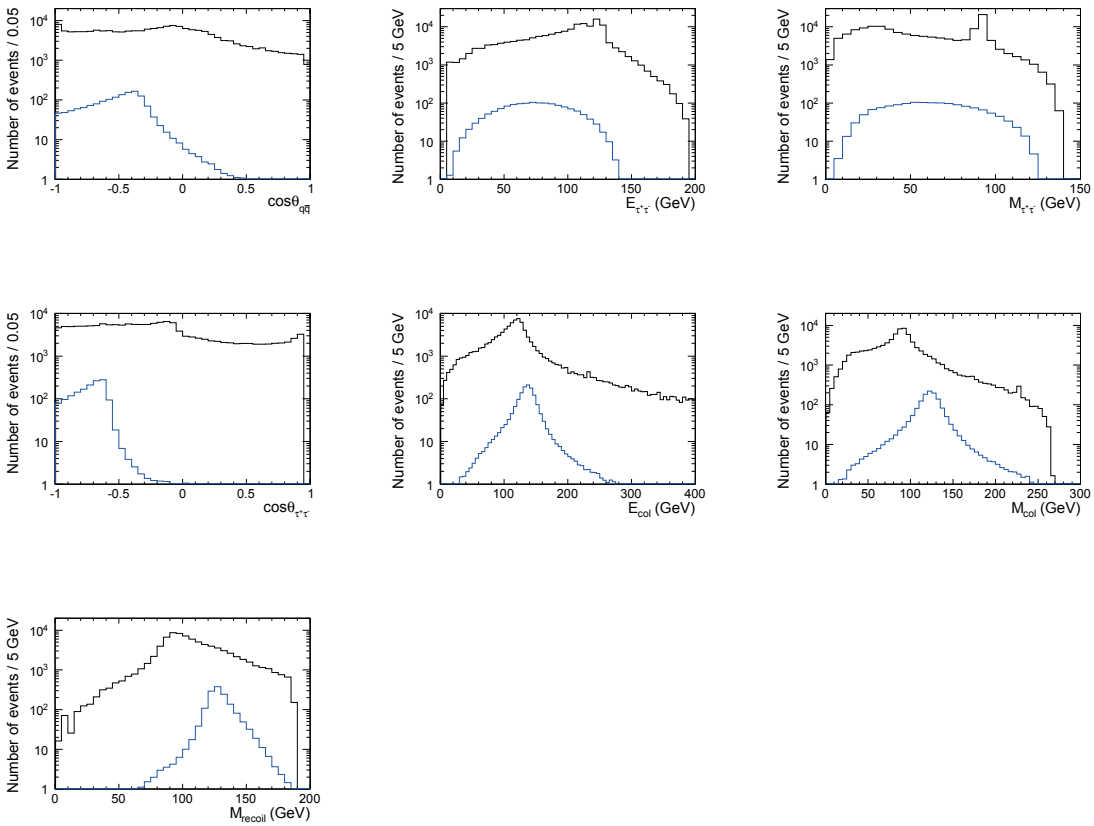

Figure 5.1.9: Distributions of each variable used for basic cuts. Black histograms show the sum of all processes, and blue show signal process.

5.1.4 Multivariate Analysis

A multivariate analysis was performed. All events passed the basic cuts were used. The input variables and training parameters such as nCuts, Shrinkage, MaxDepth, NTrees, and nEventsMin were optimized to extract maximum $S_{\rm sig}$. The optimum training parameters were; nCuts = 55, Shrinkage = 0.29, MaxDepth = 4, NTrees = 300, and nEventsMin = 250. The optimum 16 input variables were;

- $E_{\rm vis}$, P_t, $\cos\theta_{\rm miss}$, where P_t is the magnitude of transverse momentum, and $\theta_{\rm miss}$ is the angle of missing momentum with respect to the beam axis,
- $M_{q\bar{q}}$, $\cos\theta_{q\bar{q}}$, $\cos\theta_Z$, where θ_Z is the production angle of Z boson with respect to beam axis,
- $M_{\tau^+\tau^-}$, $E_{\tau^+\tau^-}$, $\cos\theta_{\tau^+\tau^-}$, $\cos\theta_{\rm acop}$, where $\theta_{\rm acop}$ is the acoplanarity angle between two taus in azimuthal direction minus π,
- $\sum_{\tau^+,\tau^-} \log_{10}|d_0/\sigma(d_0)|$ and $\sum_{\tau^+,\tau^-} \log_{10}|z_0/\sigma(z_0)|$,

- M_{col}, E_{col}, $\cos\theta_{\mathrm{col}}$, where θ_{col} is the Higgs production angle with respect to the beam axis, calculated with using collinear approximation,
- M_{recoil}.

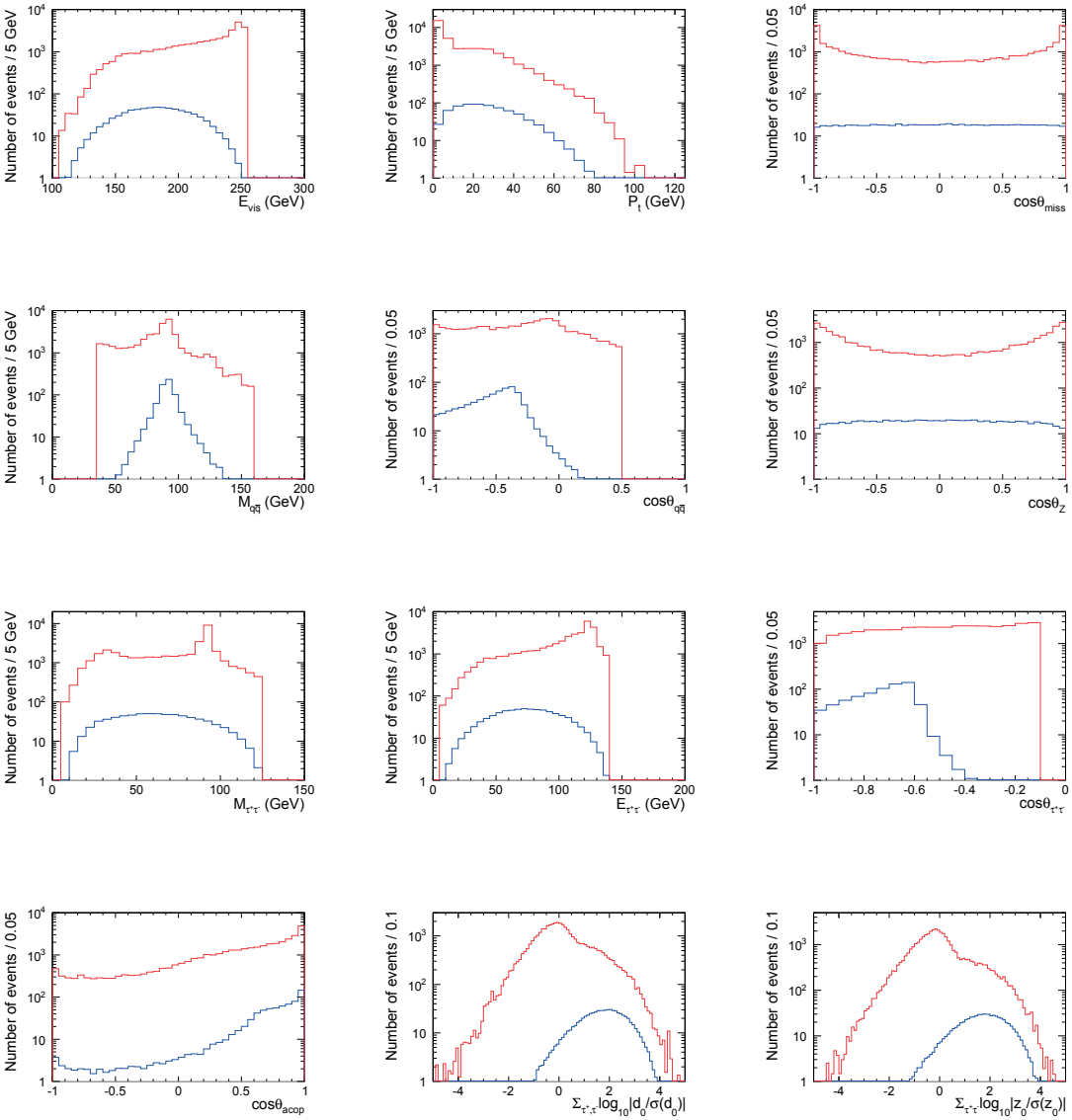

Figure 5.1.10: Distributions of each variable used for multivariate analysis. Blue histograms show the signal processes, and red show background process.

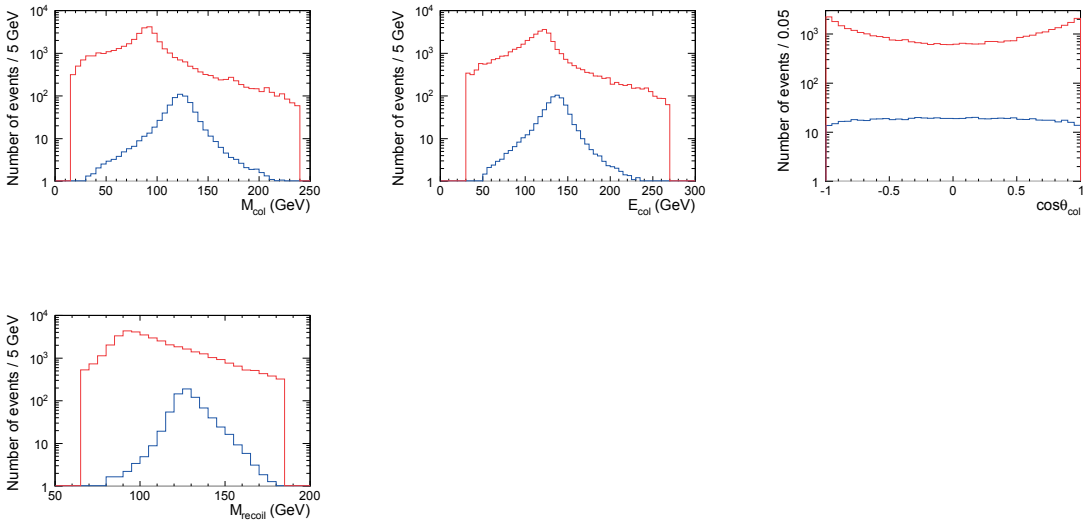

Figure 5.1.11: Distributions of each variable used for multivariate analysis. Blue histograms show the signal processes, and red show background process.

The distribution of TMVA output is shown in Figure 5.1.12.

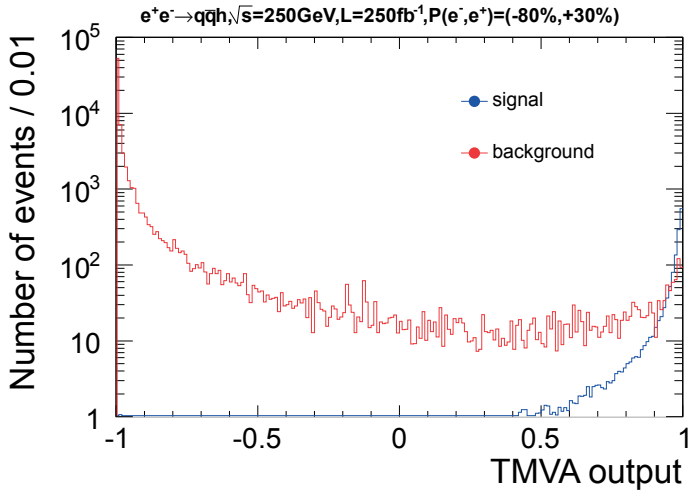

Figure 5.1.12: The distribution of TMVA output for $e^+e \to q\bar{q}h$ 250 GeV analysis.

By applying the cut to TMVA output to maximize $S_{\rm sig}$, 1232 signals and 545 backgrounds were remained. The signal selection efficiency η was 37.1%. $S_{\rm sig}$ and corresponding precision were calculated to be

$$S_{\rm sig} = 29.2,$$
$$\frac{\Delta(\sigma \times {\rm BR})}{(\sigma \times {\rm BR})} = 3.4\%.$$

5.2 Analysis of 250 GeV $e^+e^- \to e^+e^-h$ Mode

5.2.1 Signal and Backgrounds

The diagram of signal of this mode is shown in Figure 5.2.1. The dominant production process of $e^+e\ \ h$ is Higgs-strahlung, and the cross section of ZZ-fusion is negligible as shown in Figure 1.3.1.

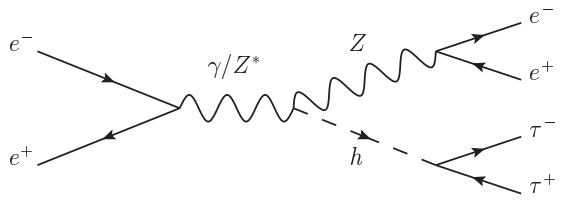

Figure 5.2.1: The diagram of $e^+e\ \ \to e^+e\ \ h$ signal.

Figure 5.2.2 shows the example diagram of irreducible background, $e^+e\ \ \to ZZ \to e^+e\ \ \tau^+\tau\ \ $. Other Z boson decaying such as $Z \to e^+e\ \ , \mu^+\mu\ \ , \tau^+\tau\ \ , \nu\overline{\nu}$ will also be the background processes due to similar final states to the signal.

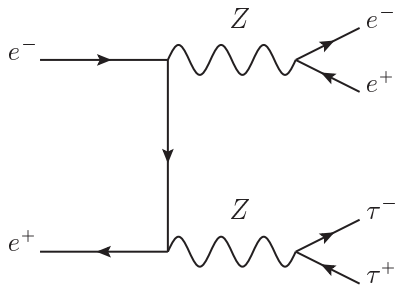

Figure 5.2.2: The example diagram of backgrounds to the $e^+e\ \ \to e^+e\ \ h$ signal.

5.2.2 Event Reconstruction

There were three steps for the event reconstruction of $e^+e\ \ \to e^+e\ \ h$ mode; (1) lepton finding, (2) tau reconstruction, (3) collinear approximation.

Lepton Finding At first, a lepton finding algorithm was applied to reconstruct electron/positron from Z boson. This algorithm was also used for identification of muons. The procedure of this algorithm are;

1. electron/muon finding,
2. tau rejection,
3. recovery process.

To select electrons/muons, the variables of $E_{\mathrm{ECAL}}/(E_{\mathrm{ECAL}} + E_{\mathrm{HCAL}})$ and $(E_{\mathrm{ECAL}} + E_{\mathrm{HCAL}})/P_{\mathrm{track}}$ were used. Figure 5.2.3 and Figure 5.2.4 show the distribution of $E_{\mathrm{ECAL}}/(E_{\mathrm{ECAL}}+E_{\mathrm{HCAL}})$ and $(E_{\mathrm{ECAL}} + E_{\mathrm{HCAL}})/P_{\mathrm{track}}$ in the signal samples of $e^+e\ \ h$ and $\mu^+\mu\ \ h$.

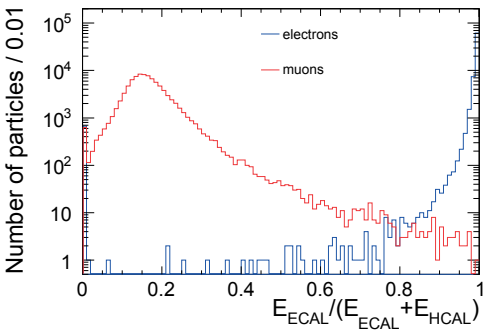

Figure 5.2.3: The distribution of $E_{\mathrm{ECAL}}/(E_{\mathrm{ECAL}} + E_{\mathrm{HCAL}})$ in $e^+e\ \ h$ sample and $\mu^+\mu\ \ h$ sample.

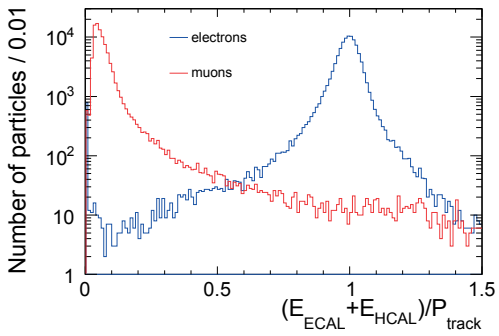

Figure 5.2.4: The distribution of $(E_{\mathrm{ECAL}} + E_{\mathrm{HCAL}})/P_{\mathrm{track}}$ in $e^+e\ \ h$ sample and $\mu^+\mu\ \ h$ sample.

From these, the selection criteria for electron/muon identification (e-ID/μ-ID) were decided as

$$e\text{−ID} : \frac{E_{\mathrm{ECAL}}}{E_{\mathrm{ECAL}} + E_{\mathrm{HCAL}}} > 0.96 \text{ and } \frac{E_{\mathrm{ECAL}} + E_{\mathrm{HCAL}}}{P_{\mathrm{track}}} > 0.6, \tag{5.2.1}$$

$$\mu\text{−ID} : \frac{E_{\mathrm{ECAL}}}{E_{\mathrm{ECAL}} + E_{\mathrm{HCAL}}} < 0.5 \text{ and } \frac{E_{\mathrm{ECAL}} + E_{\mathrm{HCAL}}}{P_{\mathrm{track}}} < 0.6. \tag{5.2.2}$$

The μ-ID will be used in Section 5.3.

The next step is tau rejection. Since now we want reconstruct the particles from Z boson, we need to reject the particles from other origins like tau lepton from Higgs boson. To do this, the impact parameters and E_{charged} were used, because electrons from Higgs boson decaying into tau pairs tend to have larger impact parameter in signal process and overlay backgrounds tend to have smaller energy. Figures 5.2.5 - 5.2.7 show the distribution of $|d_0/\sigma(d_0)|$, $|z_0/\sigma(z_0)|$ and track energy E_{charged} which passed the e-ID criteria, respectively.

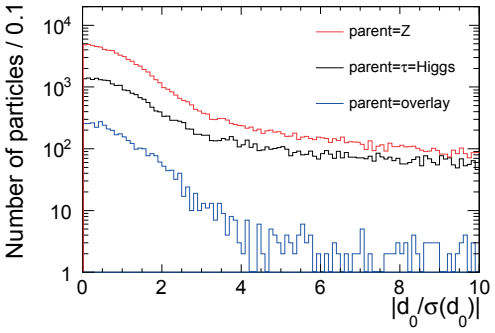

Figure 5.2.5: The distribution of d_0 impact parameter $|d_0/\sigma(d_0)|$.

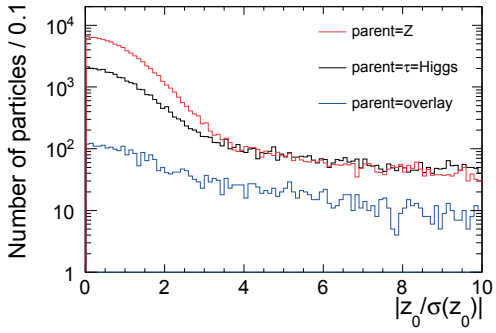

Figure 5.2.6: The distribution of z_0 impact parameter $|z_0/\sigma(z_0)|$.

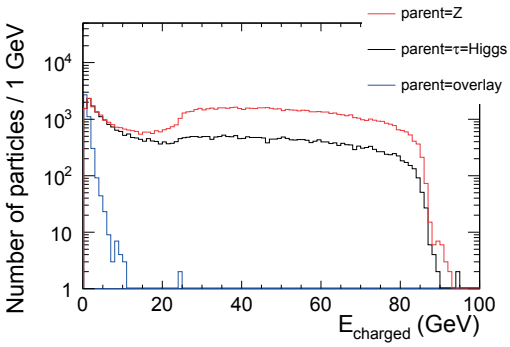

Figure 5.2.7: The distribution of energy of charged particle E_{charged}.

From these, the selection criteria of tau rejection after e-ID were decided as

$$|d_0/\sigma(d_0)| < 6, |z_0/\sigma(z_0)| < 3, E_{\text{charged}} > 10 \text{ GeV}. \tag{5.2.3}$$

The survived particle is regarded as the electron/positron from Z boson.

After the selection, one electron e^- and one positron e^+ were combined as the Z boson. If there were two or more possibilities, a pair of e^- and e^+ which has a nearest invariant mass to 91.19 GeV (M_Z) was selected. The efficiency which correctly reconstruct one e^- and one e^+ was 60.9%.

In final, the recovery process to the lepton was applied to improve mass and energy resolution. This is the process to recover the energy of lepton due to bremsstrahlung and/or final state radiation. For this, the neutral particles which satisfy $\cos\theta > 0.999$ with respect to the lepton were combined to the lepton by adding four momenta of neutral particles to the lepton. Figure 5.2.8 shows the distribution of electron pair mass $M_{e^+e^-}$.

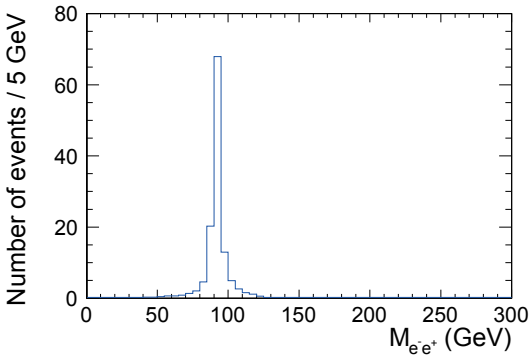

Figure 5.2.8: The distribution of electron pair mass $M_{e^+e^-}$.

Tau Reconstruction After finishing Z boson reconstruction, a tau clustering algorithm was applied for tau reconstruction. The reconstruction procedures of this algorithm are as following;

1. Order all charged tracks from highest energy.
2. Select highest energy track from remaining tracks as a seed of tau.
3. Combine four momenta of neighboring particles which satisfy $\theta < 1.0$ radian to the seed keeping the combined mass of $M_{\text{combine}} < 2$ GeV, where θ is the angle of momentum direction with respect to the seed. The combined object is regarded as the tau candidate and particles belong to that candidate are removed from the tau reconstruction.
4. repeat above processes from step 2 until there are no tau candidates.

There are no selection cuts like the finding algorithm described in Section 5.1, because the event topology is simpler than $e^+e \rightarrow q\bar{q}h$ mode. The most energetic positive candidate and the most energetic negative candidate were combined as a Higgs boson, because the overlay backgrounds tend to have lower energy than Higgs-origin particles. Figure 5.2.9 shows the distribution of tau pair mass $M_{\tau^+\tau^-}$. The efficiency of reconstruction of one or more τ^+ and one or more τ was 94.0%.

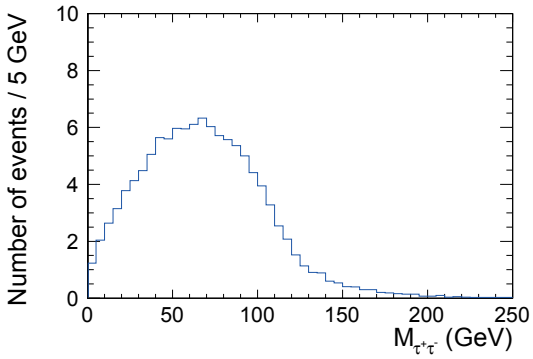

Figure 5.2.9: The distribution of tau pair mass $M_{\tau^+\tau^-}$.

Collinear Approximation The collinear approximation [83] was used to recover the momentum of tau. The assumption and usage are the same as described in Section 5.1. Figure 5.2.10 shows the distribution of tau pair mass with collinear approximation $M_{\rm col}$.

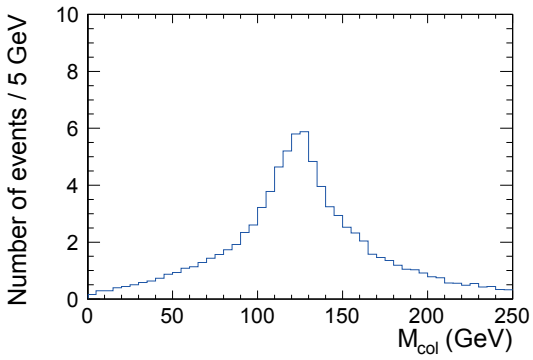

Figure 5.2.10: The distribution of tau pair mass with collinear approximation $M_{\rm col}$.

5.2.3 Cuts Before Optimization

The following cuts were applied as the preselection to select events which have signal topology;

- successfully reconstructed using an electron pair with opposite charge,
- number of τ^+s and τ^- s are greater or equal to 1,
- $N_{\rm tracks} \leq 8$.

In addition, the following cuts were applied as the basic cuts to suppress trivial backgrounds.

- $100 < E_{\rm vis} < 280$ GeV, $85 < M_{\rm vis} < 275$ GeV, and $\sum_i P_{ti} > 35$ GeV,

- $40 < E_{e^+e^-} < 160$ GeV and $10 < M_{e^+e^-} < 145$ GeV, where $E_{e^+e^-}(M_{e^+e^-})$ is the energy (mass) of electron pair,
- $M_{\mathrm{recoil}} > 50$ GeV.

All distributions of each variable used for basic cuts are shown in Figure 5.2.11.

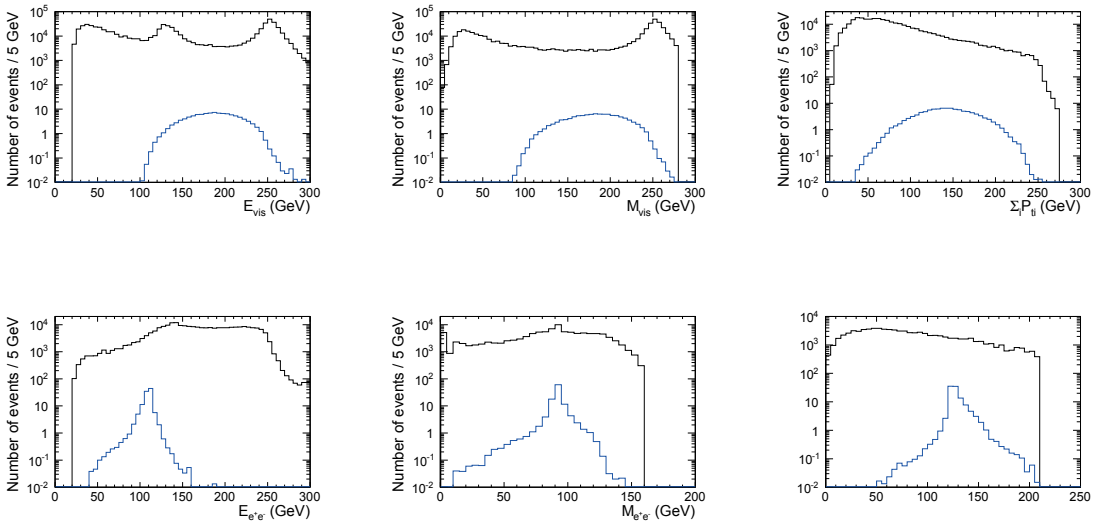

Figure 5.2.11: Distributions of each variable used for basic cuts. Black histograms show the sum of all processes, and blue show signal process.

5.2.4 Multivariate Analysis

The multivariate analysis was performed. Input variables and training parameters were optimized to extract maximum S_{sig}. The optimum training parameters were; nCuts = 60, MaxDepth = 3, NTrees = 350, nEventsMin = 130. The optimum 11 input variables were;

- M_{vis}, E_{vis}, $\cos\theta_{\mathrm{thrustaxis}}$, $\cos\theta_{\mathrm{miss}}$, where $\theta_{\mathrm{thrusttaxis}}$ is the angle of thrust axis with respect to the beam axis,
- $M_{e^+e^-}$,
- $M_{\tau^+\tau^-}$, $\cos\theta_{\tau^+\tau^-}$, $\cos\theta_{\mathrm{acop}}$,
- $\sum_{\tau^+,\tau^-} \log_{10}|d_0/\sigma(d_0)|$, $\sum_{\tau^+,\tau^-} \log_{10}|z_0/\sigma(z_0)|$,
- M_{recoil}.

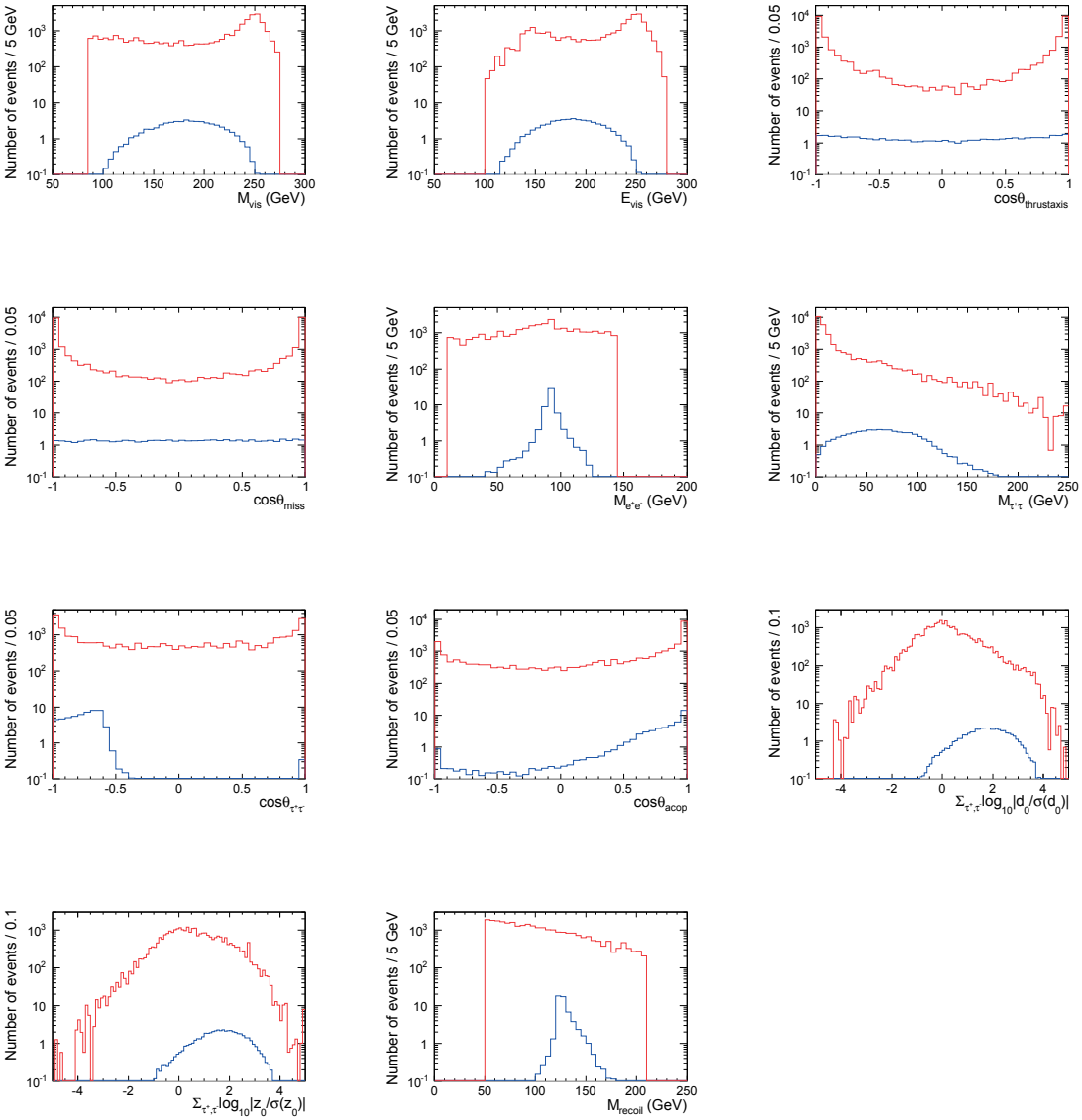

Figure 5.2.12: Distributions of each variable used for multivariate analysis. Blue histograms show the signal processes, and red show background process.

The distribution of TMVA output is shown in Figure 5.2.13.

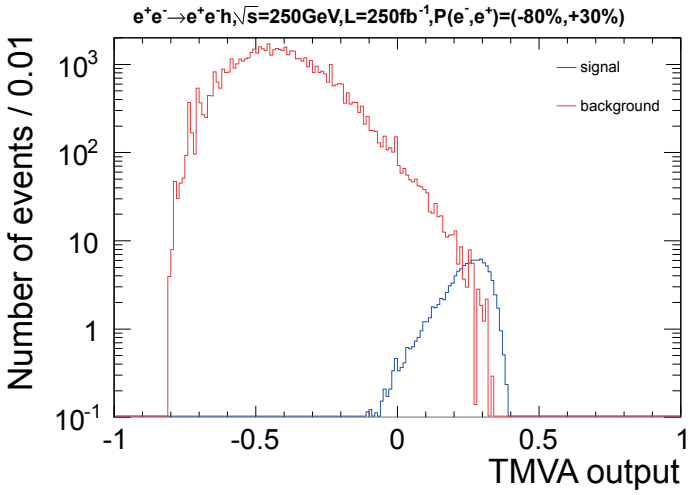

Figure 5.2.13: The distribution of TMVA output for $e^+e^- \to e^+e^- h$ 250 GeV analysis.

By applying the cut to TMVA output to maximize S_{sig}, 76.32 signal events and 45 backgrounds were remained. η was 43.6%. S_{sig} and corresponding precision were calculated as

$$S_{\text{sig}} = 6.9,$$
$$\frac{\Delta(\sigma \times \text{BR})}{(\sigma \times \text{BR})} = 14.4\%.$$

5.3 Analysis of 250 GeV $e^+e^- \to \mu^+\mu^- h$ Mode

5.3.1 Signal and Backgrounds

The diagram of signal of this mode is shown in Figure 5.3.1.

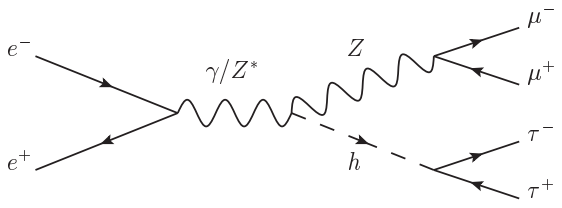

Figure 5.3.1: The diagram of $e^+e^- \to \mu^+\mu^- h$ signal.

Figure 5.3.2 shows the example diagram of irreducible background, $e^+e^- \to ZZ \to \mu^+\mu^-\tau^+\tau^-$. Other Z boson decaying such as $Z \to e^+e^-, \mu^+\mu^-, \tau^+\tau^-, \nu\overline{\nu}$ will also be the background processes due to similar final states to the signal.

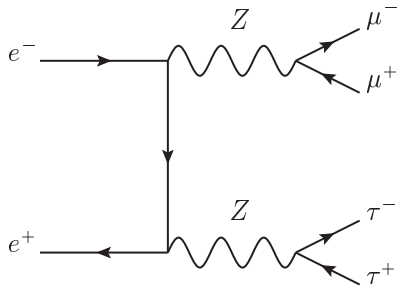

Figure 5.3.2: The example diagram of backgrounds to the $e^+e \to \mu^+\mu\ h$ signal.

5.3.2 Event Reconstruction

There were three steps for reconstruction of $\mu^+\mu\ h$ process; (1) lepton finding, (2) tau reconstruction, (3) collinear approximation.

Lepton Finding At first, the lepton finding algorithm was applied. This is the same algorithm as described in Section 5.2. For selecting muons, the criteria were already shown in Section 5.2. The numbers were as

$$\frac{E_{\mathrm{ECAL}}}{E_{\mathrm{ECAL}} + E_{\mathrm{HCAL}}} < 0.5 \text{ and } \frac{E_{\mathrm{ECAL}} + E_{\mathrm{HCAL}}}{P_{\mathrm{track}}} < 0.6. \tag{5.3.1}$$

The next step is tau rejection, using impact parameters and particle energy. Figures 5.3.3 - 5.3.5 show the distribution of $|d_0/\sigma(d_0)|$, $|z_0/\sigma(z_0)|$ and track energy E_{charged} which passed the μ-ID, respectively.

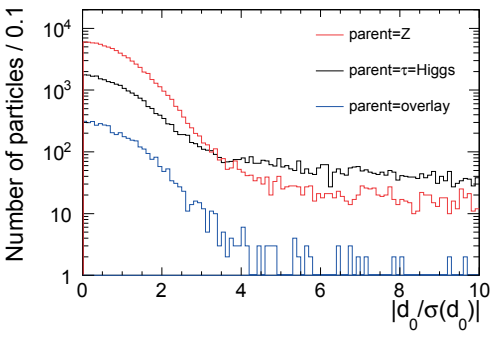

Figure 5.3.3: The distribution of d_0 impact parameter $|d_0/\sigma(d_0)|$.

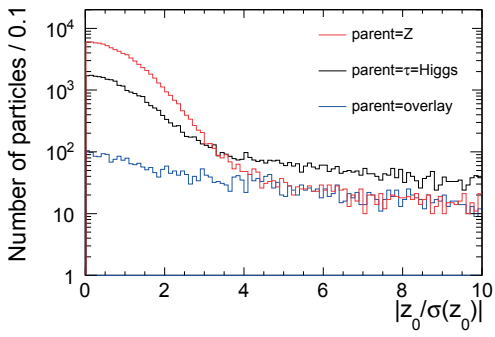

Figure 5.3.4: The distribution of z_0 impact parameter $|z_0/\sigma(z_0)|$.

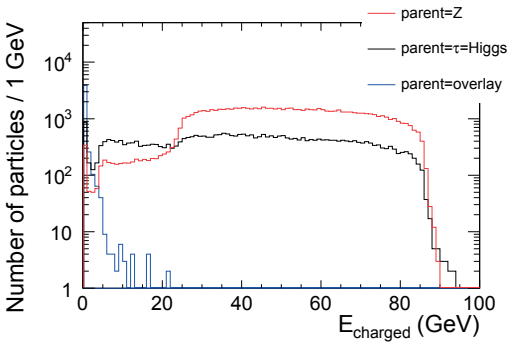

Figure 5.3.5: The distribution of energy of charged particle E_{charged}.

From these, the selection criteria of tau rejection after μ-ID were decided as

$$|d_0/\sigma(d_0)| < 3, |z_0/\sigma(z_0)| < 3, E_{\text{charged}} > 20 \text{ GeV}. \tag{5.3.2}$$

The survived particles are regarded as the muons from Z boson.

After this selection, one μ^- and one μ^+ were combined as the Z boson. If there are two or more possibilities, a pair of μ^- and μ^+ which have nearest invariant mass to 91.19 GeV (M_Z) was selected. The efficiency which correctly reconstruct one μ^- and one μ^+ was 92.4%. In final, the recovery process was applied in the same way as described in Section 5.2. Figure 5.3.6 shows the distribution of muon pair mass $M_{\mu^+\mu^-}$.

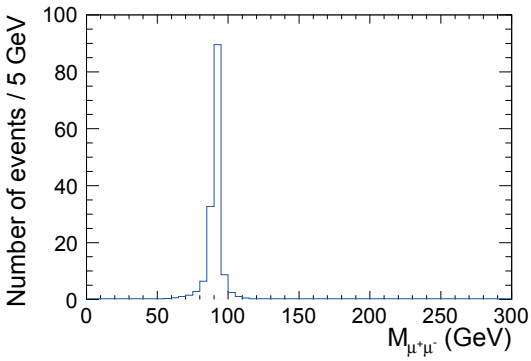

Figure 5.3.6: The distribution of muon pair mass $M_{\mu^+\mu^-}$.

Tau Reconstruction After finishing Z boson reconstruction, the tau clustering algorithm described in Section 5.2 was applied. Figure 5.3.7 shows the distribution of tau pair mass $M_{\tau^+\tau^-}$. The efficiency of reconstruction of one or more τ^+ and one or more τ^- was calculated to be 93.7%.

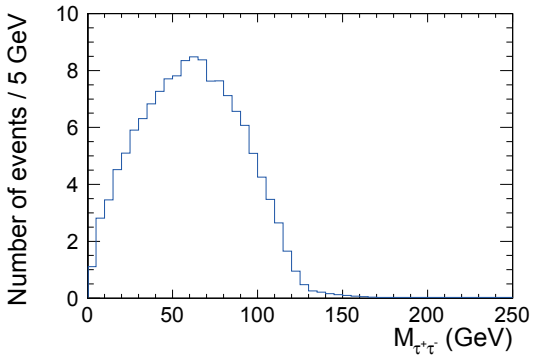

Figure 5.3.7: The distribution of tau pair mass $M_{\tau^+\tau^-}$.

Collinear Approximation The collinear approximation [83] was applied to recover the momentum of tau. Figure 5.3.8 shows the distribution of tau pair mass with collinear approximation $M_{\rm col}$.

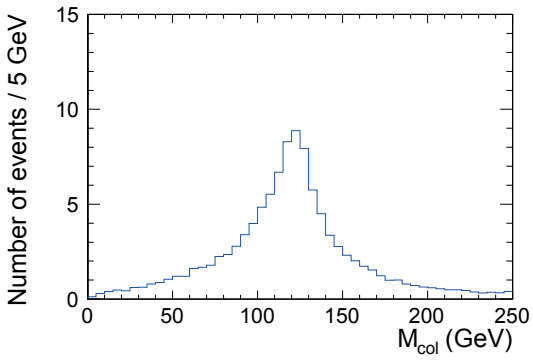

Figure 5.3.8: The distribution of tau pair mass with collinear approximation $M_{\rm col}$.

5.3.3 Cuts Before Optimization

The following cuts were applied as the preselection to select events which have signal topology;

- successfully reconstructed using a muon pair with opposite charge,
- number of τ^+s and τ^- s are greater or equal to 1,
- $N_{\rm tracks} \leq 8$.

In addition, the following cuts were applied as the basic cuts to suppress trivial backgrounds.

- $105 < E_{\rm vis} < 280$ GeV, $85 < M_{\rm vis} < 275$ GeV, and $\sum_i P_{ti} > 35$ GeV,

- $45 < E_{\mu^+\mu^-} < 145$ GeV and $25 < M_{\mu^+\mu^-} < 125$ GeV, where $E_{\mu^+\mu^-}(M_{\mu^+\mu^-})$ is the energy (mass) of muon pair,
- $M_{\tau^+\tau^-} < 170$ GeV,
- $M_{\text{recoil}} > 75$ GeV.

All distributions of each variable used for basic cuts are shown in Figure 5.3.9.

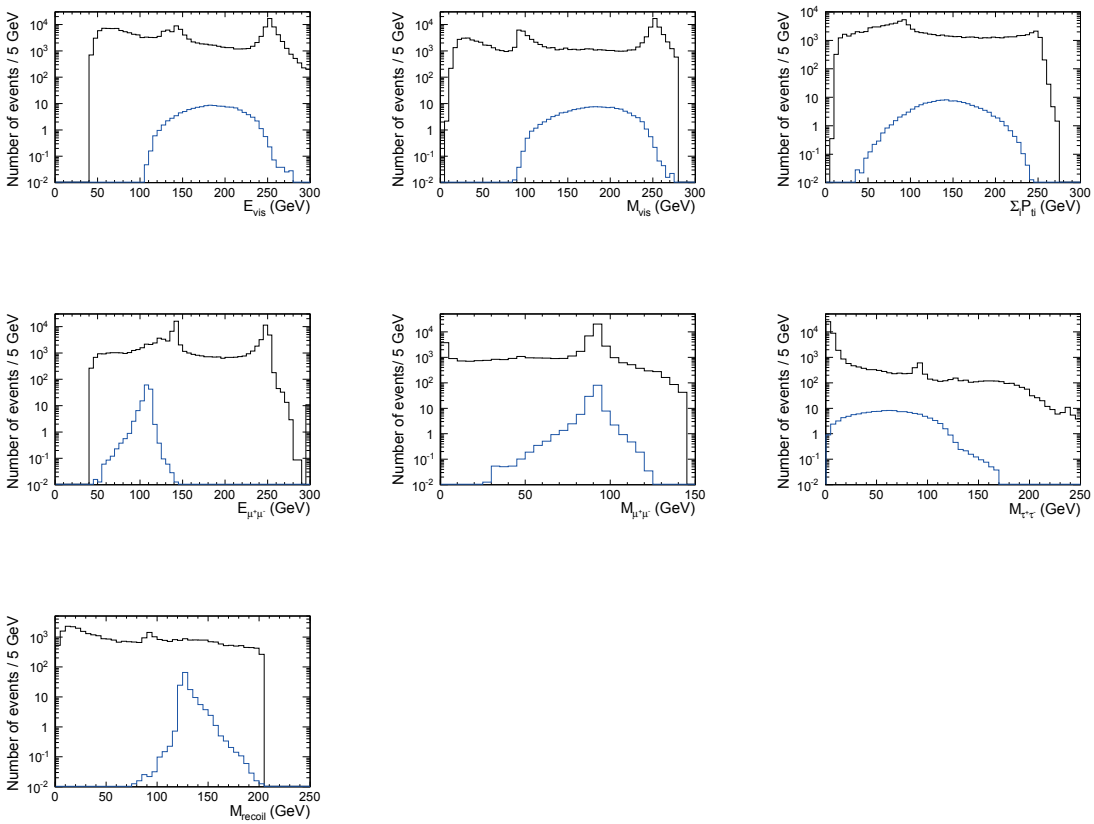

Figure 5.3.9: Distributions of each variable used for basic cuts. Black histograms show the sum of all processes, and blue show signal process.

5.3.4 Multivariate Analysis

The multivariate analysis was performed. Input variables and training parameters were optimized to extract maximum S_{sig}. The optimum training parameters were; nCuts = 50, Shrinkage = 0.11, MaxDepth = 4, NTrees = 350, nEventsMin = 160. The optimum 12 input variables were;

- M_{vis}, E_{vis}, P_t,
- $M_{\mu^+\mu^-}$, $\cos\theta_Z$,
- $M_{\tau^+\tau^-}$, $E_{\tau^+\tau^-}$, $\cos\theta_{\tau^+\tau^-}$,

- $\sum_{\tau^+,\tau^-} \log_{10} |d_0/\sigma(d_0)|$, $\sum_{\tau^+,\tau^-} \log_{10} |z_0/\sigma(z_0)|$,
- M_{col},
- M_{recoil}.

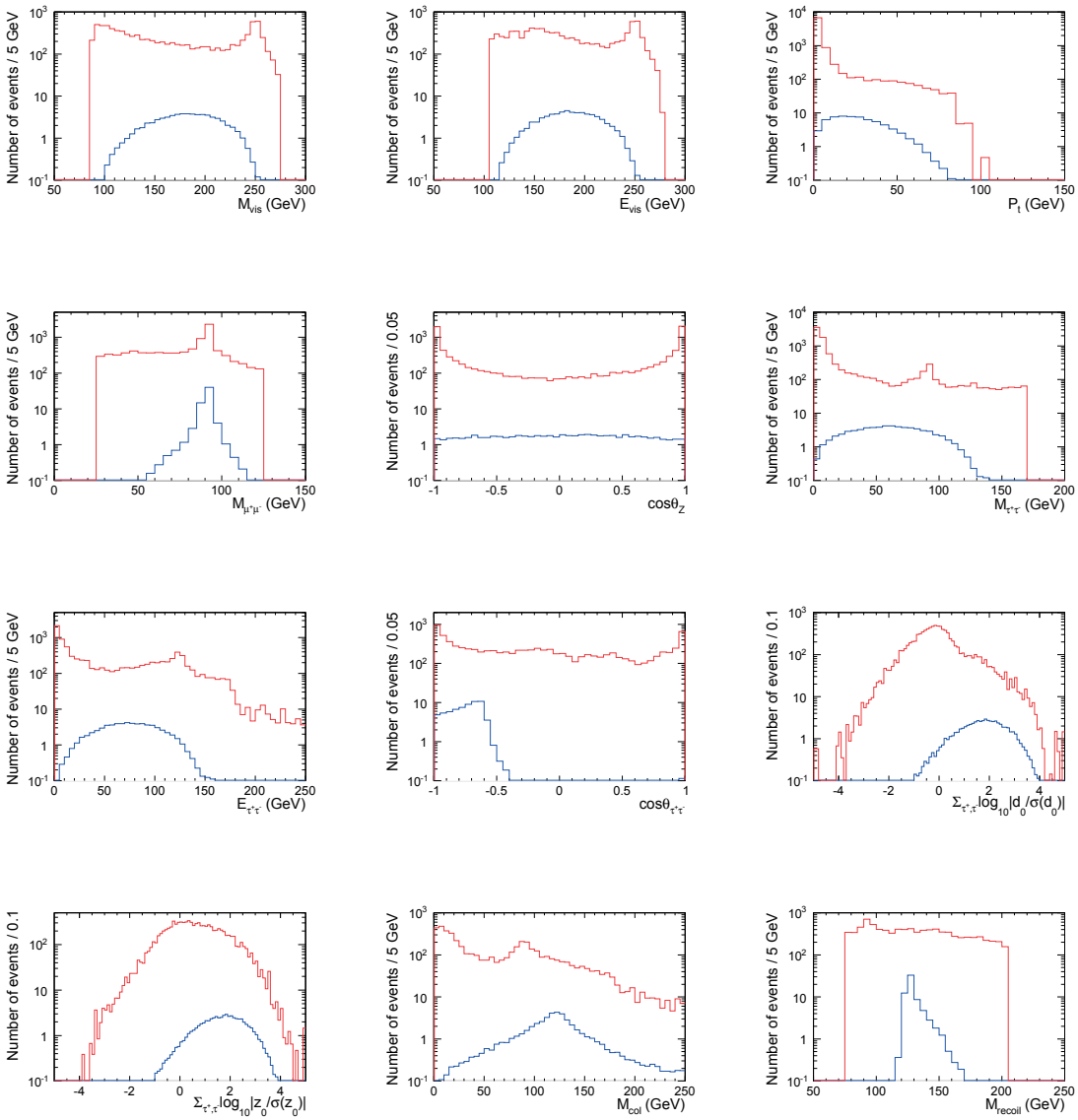

Figure 5.3.10: Distributions of each variable used for multivariate analysis. Blue histograms show the signal processes, and red show background process.

The distribution of TMVA output is shown in Figure 5.3.11.

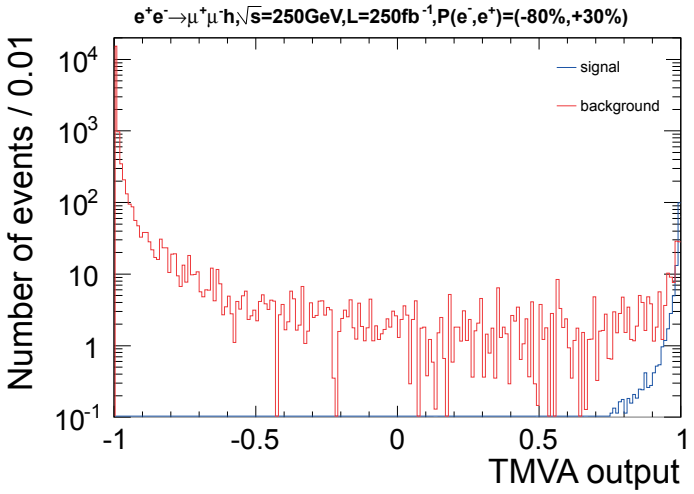

Figure 5.3.11: The distribution of TMVA output for $e^+e \to \mu^+\mu\ h$ 250 GeV analysis.

By applying the cut to TMVA output to maximize $S_{\rm sig}$, 101.94 signal events and 31 background events were remained. η was 61.9%. $S_{\rm sig}$ and corresponding precision were calculated to be as

$$S_{\rm sig} = 8.84,$$
$$\frac{\Delta(\sigma \times {\rm BR})}{(\sigma \times {\rm BR})} = 11.3\%.$$

5.4 Summary of 250 GeV Analysis

In this section, the analyzes for the processes of $e^+e \to q\bar{q}h$, $e^+e \to e^+e\ h$, and $e^+e \to \mu^+\mu\ h$ are discussed. All results are summarized in Table 5.4.1.

Table 5.4.1: Results of $\sqrt{s} = 250$ GeV using multivariate analysis with the integrated luminosity of 250 fb ^{1}.

mode	$\frac{\Delta(\sigma \times {\rm BR})}{(\sigma \times {\rm BR})}$
$q\bar{q}h$	3.4%
$e^+e\ h$	14.4%
$\mu^+\mu\ h$	11.3%

The $q\bar{q}h$ mode is most sensitive channel because we can use high statistics and full information of Z boson and Higgs boson. This mode almost determines the overall precision at $\sqrt{s} = 250$ GeV. The modes of $e^+e\ h$ and $\mu^+\mu\ h$ will contribute slightly. The combined precision of 250 GeV analysis was $\Delta(\sigma \times {\rm BR})/(\sigma \times {\rm BR}) = 3.2\%$.

6 Analysis at Center-of-mass Energy of 500 GeV

In this section, the analysis at $\sqrt{s} = 500$ GeV will be presented. This is the highest energy of the ILC before energy upgrade. At $\sqrt{s} = 500$ GeV, the dominant Higgs production process is WW-fusion, followed by Higgs-strahlung as shown in Figure 1.3.1.

The signal processes were also categorized in the same way as Section 5; $e^+e \to q\bar{q}h$, $e^+e \to e^+e\ h$, $e^+e \to \mu^+\mu\ h$, and $e^+e \to \nu\bar{\nu}h$. In this study, we will discuss the two analysis modes as $q\bar{q}h$ and $\nu\bar{\nu}h$. As for the $e^+e\ h$ and $\mu^+\mu\ h$, we will not discuss in this thesis because of tiny production cross section.

For the background estimation, the samples as; $e^+e \to 2f$, $e^+e \to 4f$, $e^+e \to 6f$, $e^{\pm}\gamma \to 5f$, and $e^+e \to f\bar{f}h$ (except $h \to \tau^+\tau$) were used. They were categorized with the number of fermions in final state as; two-fermions ($2f$), four-fermions ($4f$), five-fermions ($5f$), and six-fermions ($6f$). The two-photon processes of $e^+e \to e^+e + 2f$ and $e^+e \to e^+e + 4f$ were categorized as $\gamma\gamma \to 2f$ and $\gamma\gamma \to 4f$. The number of $\gamma\gamma \to$ hadrons overlay backgrounds were estimated to be 1.7 per bunch crossing [72], and overlaid onto all MC samples.

6.1 Analysis of 500 GeV $e^+e^- \to q\bar{q}h$ Mode

6.1.1 Signal and Backgrounds

The diagrams of signal and possible backgrounds are the same as those of 250 GeV $q\bar{q}h$ case.

6.1.2 Event Reconstruction

In order to reconstruct the final state of $q\bar{q}\tau^+\tau$ efficiently, the following four steps were applied; (1) tau reconstruction, (2) collinear approximation, (3) overlay removal, (4) jet clustering.

Tau Reconstruction The tau finding algorithm described in Section 5.1 was also used to this mode. The procedures are the same as those of 250 GeV analysis, but the selection parameter E_{cand} was changed to greater than 4 GeV. Figure 6.1.1 shows the distribution of E_{cand}, and Figure 6.1.2 shows the distribution of E_{frac}.

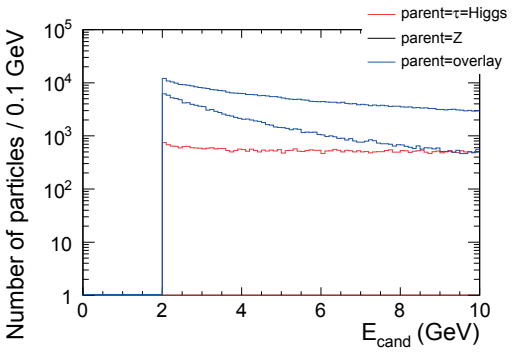

Figure 6.1.1: The distribution of $E_{\rm cand}$. Red, black, and blue histograms show the distribution of particles which parent of seed is Higgs = τ, Z boson, overlay backgrounds, respectively.

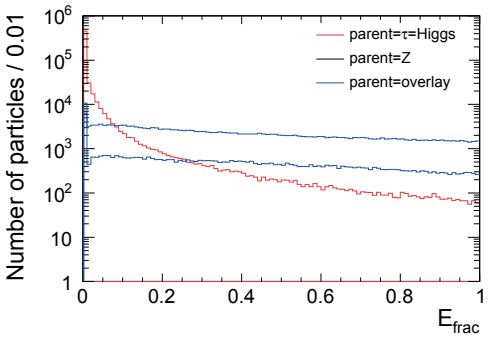

Figure 6.1.2: The distribution of $E_{\rm frac}$. Red, black, and blue histograms show the distribution of particles which parent of seed is Higgs = τ, Z boson, overlay backgrounds, respectively.

The reconstructed efficiencies were;

- reconstruct one τ^+; 73.4%,
- reconstruct one τ^- ; 73.3%,
- reconstruct one τ^+ and one τ^- ; 53.8%.

In the events with reconstructed one τ^+ and one τ^- , the purity was 96.5%. Figure 6.1.3 shows the distribution of tau pair mass $M_{\tau^+\tau^-}$.

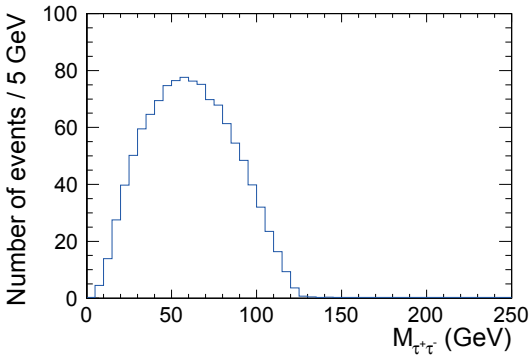

Figure 6.1.3: The distribution of $M_{\tau^+\tau^-}$ of signal process.

Collinear Approximation The collinear approximation [83] was applied to recover the momentum of tau. Figure 6.1.4 shows the distribution of M_{col}. It is clear that the original Higgs boson mass of 125 GeV was well reconstructed.

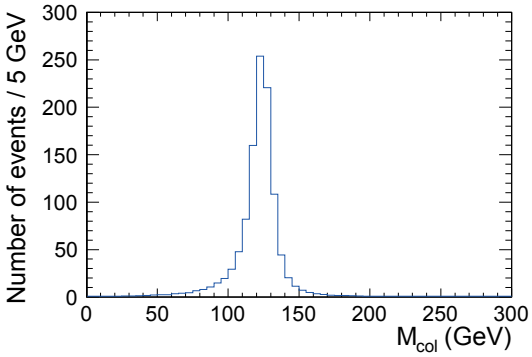

Figure 6.1.4: The distribution of M_{col} of signal process.

Overlay Removal The visible mass of remaining particles after tau reconstruction should be close to Z mass. However due to the significant contribution of $\gamma\gamma \to$ hadron overlay backgrounds, this visible mass shifts to higher mass region. In order to eliminate the overlay backgrounds, the k_T clustering algorithm [85, 86] was applied. The `FastJet` package [87] was used to perform k_T clustering.

The k_T clustering uses the variables d_{ij} and d_{iB} defined as

$$d_{ij} = \min[p_{ti}^2, p_{tj}^2]\Delta R_{ij}^2/R^2, \tag{6.1.1}$$

$$\Delta R_{ij}^2 = (y_i - y_j)^2 + (\phi_i - \phi_j)^2, \tag{6.1.2}$$

$$d_{iB} = p_{ti}^2, \tag{6.1.3}$$

where i and j are indexes of particle/jet, and p_{ti}, y_i, and ϕ_i are transverse momentum, rapidity, and azimuth of i-th particle. R is a generalized jet-radius parameter which

typically used in $R \sim 1$ and necessary to be optimized. The algorithm calculates d_{ij} and d_{iB}, and find the minimum value as $d_{\min}$. If $d_{\min} = d_{ij}$, then the i and j are combined by summing up the four momenta as $P = P_i + P_j$. If $d_{\min} = d_{iB}$, then the particle is regarded as a jet and remove that from the list of remaining particles.

For the optimization of R, the range of R = 0.5 - 1.4 for every 0.1 were studied, and checked the distribution of visible mass after tau reconstruction. Figure 6.1.5 shows the distribution of visible mass of remaining particles and distributions after applying k_T clustering. $R = 0.9$ was chosen as the best because it has highest peak at the Z boson mass.

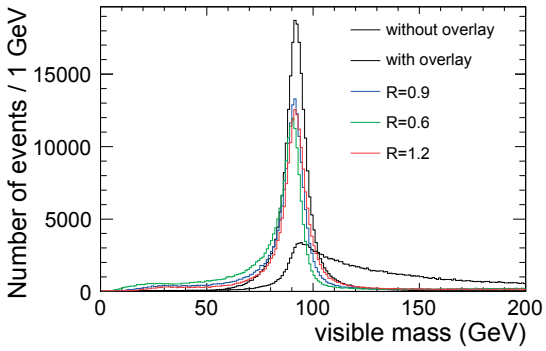

Figure 6.1.5: The distribution of visible mass of remaining particles after Z boson reconstruction. Solid black shows the ideal visible mass, which means there are no overlay particles. Dotted black shows the real distribution of visible mass, affected by overlay particles. Blue, green and red show the visible mass distribution after applying k_T clustering with R of 0.9, 0.6, and 1.2, respectively.

Jet Clustering In final, the Durham clustering algorithm [84] was used to force the remaining particles into two jets. Figure 6.1.6 shows the distribution of $M_{q\bar{q}}$ with the events which have reconstructed two jets.

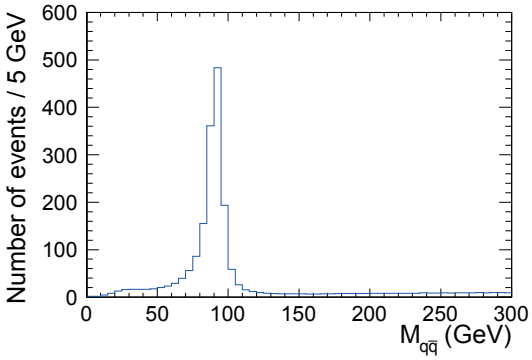

Figure 6.1.6: The distribution of $M_{q\bar{q}}$ of signal process.

6.1.3 Cuts Before Optimization

The following cuts were applied to select events which have signal topology;

- number of jets is exactly equal to 2,
- number of τ^+s and τ^- s are exactly equal to 1,
- $M_{\mathrm{col}} > 0$ and $E_{\mathrm{col}} > 0$.

In addition, the following cuts were applied as the basic cuts to suppress trivial backgrounds;

- $8 \leq N_{\mathrm{tracks}} \leq 70$
- $140 < E_{\mathrm{vis}} < 580$ GeV, $120 < M_{\mathrm{vis}} < 575$ GeV, and $\sum_i P_{ti} > 70$ GeV,
- thrust < 0.98,
- $50 < E_{q\bar{q}} < 380$ GeV and $5 < M_{q\bar{q}} < 350$ GeV,
- $E_{\tau^+\tau^-} < 270$ GeV and $M_{\tau^+\tau^-} < 180$ GeV,
- $\cos\theta_{\tau^+\tau^-} < 0.7$,
- $40 < E_{\mathrm{col}} < 430$ GeV and $M_{\mathrm{col}} < 280$ GeV.

All distributions of each variable used for basic cuts are shown in Figure 6.1.7 and Figure 6.1.8.

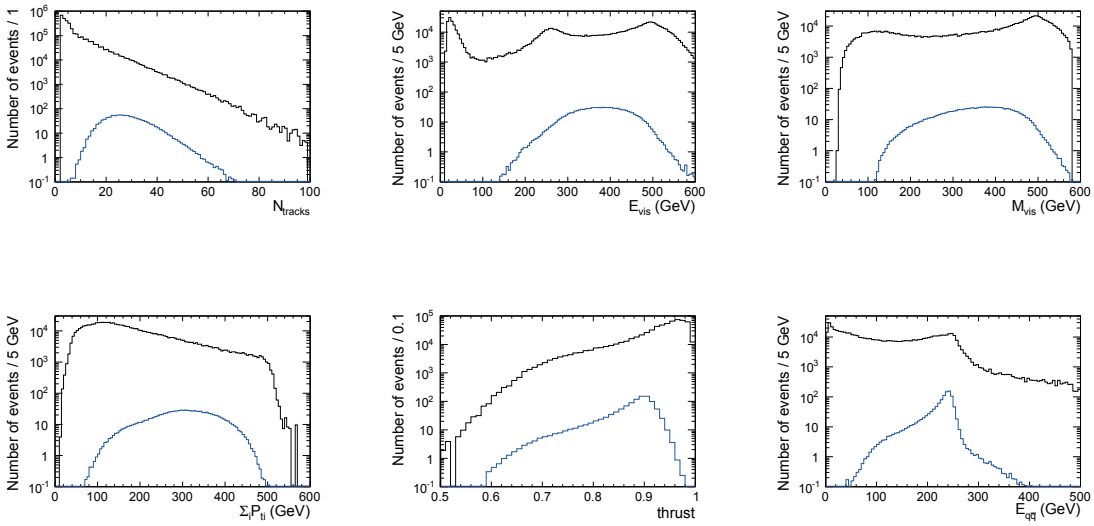

Figure 6.1.7: Distributions of each variable used for basic cuts. Black histograms show the sum of all processes, and blue show signal process.

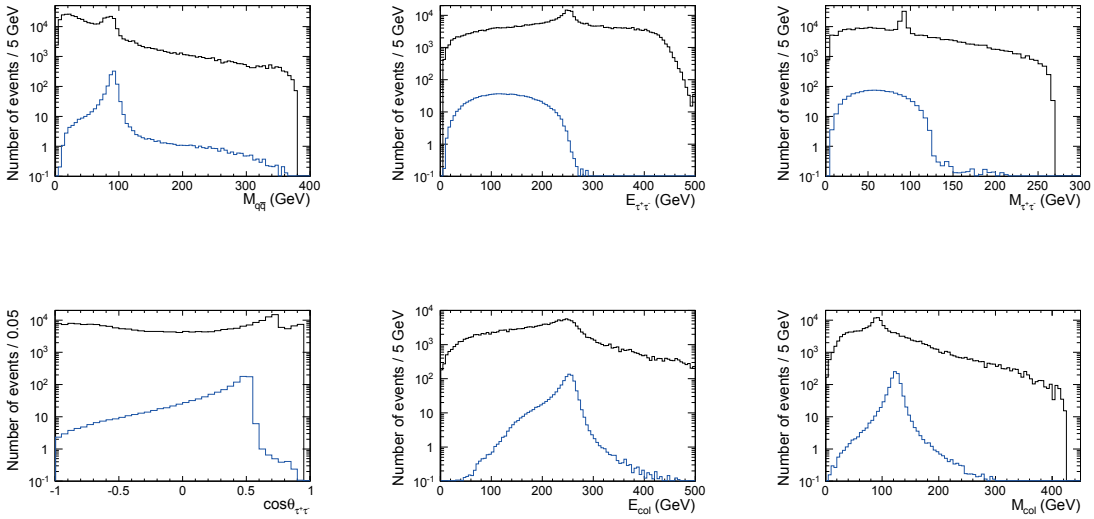

Figure 6.1.8: Distributions of each variable used for basic cuts. Black histograms show the sum of all processes, and blue show signal process.

6.1.4 Multivariate Analysis

The multivariate analysis was performed. Input variables and training parameters were optimized to maximize S_{sig}. The optimum training parameters were; nCuts = 55, Shrinkage = 0.13, MaxDepth = 3, NTrees = 450, nEventsMin = 190. The optimum 14 input variables were;

- E_{vis}, $\sum_i P_{ti}$, P_t,
- $M_{q\bar{q}}$, $E_{q\bar{q}}$, $\cos\theta_{q\bar{q}}$, $\cos\theta_Z$,
- $M_{\tau^+\tau^-}$, $\cos\theta_{\tau^+\tau^-}$,
- $\sum_{\tau^+,\tau^-} \log_{10}|d_0/\sigma(d_0)|$, $\sum_{\tau^+,\tau^-} \log_{10}|z_0/\sigma(z_0)|$,
- M_{col}, E_{col},
- M_{recoil}.

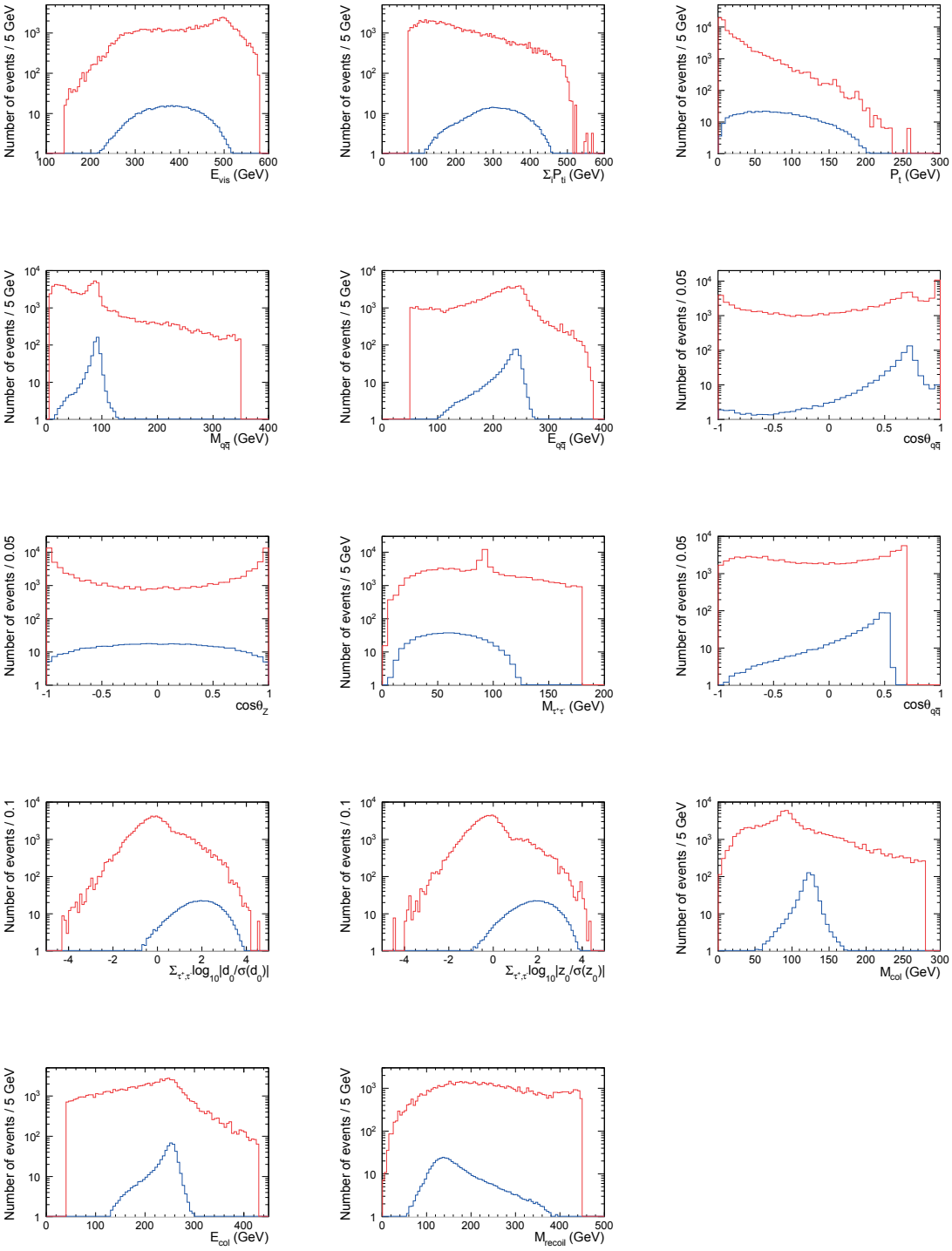

Figure 6.1.9: Distributions of each variable used for multivariate analysis. Blue histograms show the signal processes, and red show background process.

The distribution of TMVA output is shown in Figure 6.1.10.

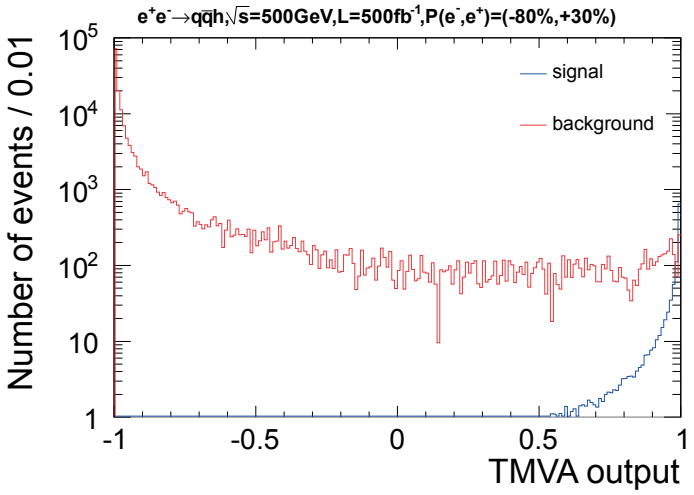

Figure 6.1.10: The distribution of TMVA output for $e^+e \to q\bar{q}h$ 500 GeV analysis.

By applying the cut to TMVA output to maximize $S_{\rm sig}$, 782.1 signal events and 340 background events were remained. η was 36.7%. $S_{\rm sig}$ and the precision was calculated to be as

$$S_{\rm sig} = 23.3,$$
$$\frac{\Delta(\sigma \times {\rm BR})}{(\sigma \times {\rm BR})} = 4.3\%.$$

6.2 Analysis of 500 GeV $e^+e^- \to \nu\bar{\nu}h$ Mode

6.2.1 Signal and Backgrounds

The signal diagrams are shown in Figure 6.2.1. There are two contributions from Higgs-strahlung and WW-fusion.

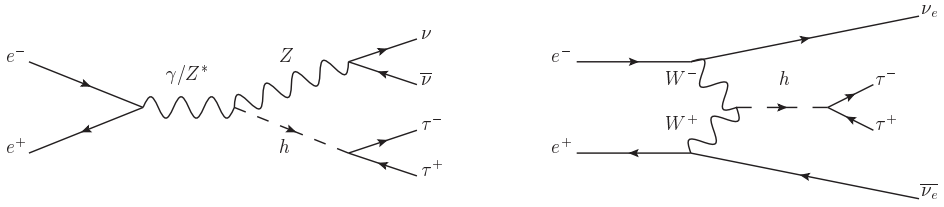

Figure 6.2.1: The diagrams of $e^+e \to \nu\bar{\nu}h$ signal. Left; Higgs-strahlung, right; WW-fusion.

The diagrams of possible backgrounds are shown in Figure 6.2.2. Left and center processes have same final state to the signal, while the right one have similar final state. Due to many neutrinos, two fermion processes would also be the source of background against to the signal.

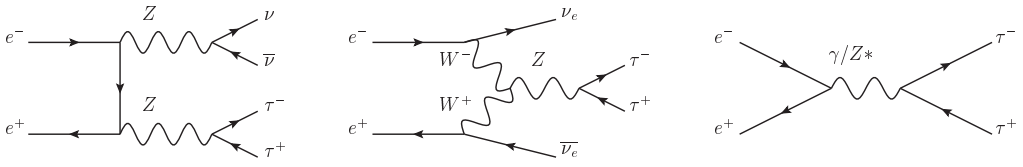

Figure 6.2.2: The diagrams of possible backgrounds against $e^+e \to \nu\overline{\nu}h$ signal.

6.2.2 Event Reconstruction

The tau clustering algorithm described in Section 5.2 was applied. The usage is the same as of the 250 GeV analysis case, except for the clustering angle changed to $\theta < 0.76$ radian. Figure 6.2.3 shows the distribution of tau pair mass $M_{\tau^+\tau^-}$. The efficiency of reconstruction of one or more τ^+ and one or more τ was 81.2%.

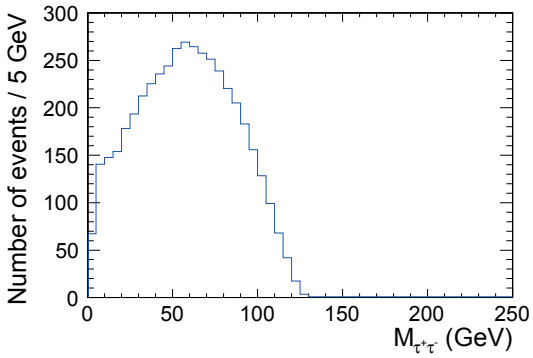

Figure 6.2.3: The distribution of tau pair mass $M_{\tau^+\tau^-}$.

The collinear approximation cannot be applied due to neutrinos not only from tau leptons.

6.2.3 Cuts Before Optimization

The following cuts were applied as the preselection to select events which have signal topology;

- number of τ^+s and τ s are greater or equal to 1,
- $N_{\text{tracks}} \leq 10$.

However, the remaining backgrounds after these preselection were still huge. The most dominant backgrounds at this step were $\gamma\gamma \to 2f$. To suppress them, the following cuts were applied as the preselection 2;

- $N_{P_t>3\text{GeV}} \geq 1$ and $N_{E>5\text{GeV}} \geq 1$, where $N_{P_t>3\text{GeV}}(N_{E>5\text{GeV}})$ is the number of tracks which have the transverse momentum greater than 3 GeV (energy greater than 5 GeV).

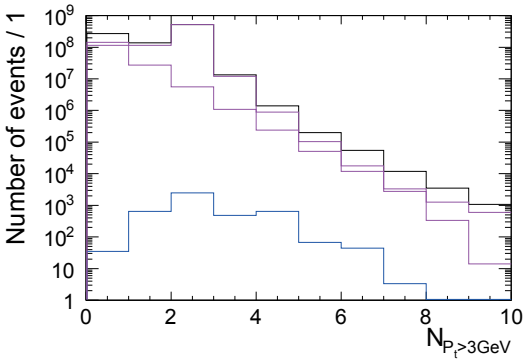

Figure 6.2.4: The distribution of $N_{P_t>3\mathrm{GeV}}$. Black, blue, dotted purple, solid-dotted purple histograms show the summing up of all processes, signal, $\gamma\gamma \to q\bar{q}$, and $\gamma\gamma \to \ell^+\ell^-$, respectively.

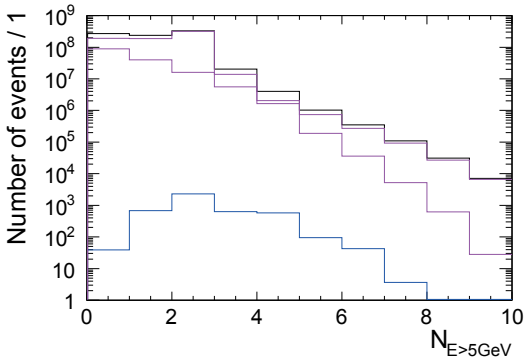

Figure 6.2.5: The distribution of $N_{E>5\mathrm{GeV}}$. Black, blue, dotted purple, solid-dotted purple histograms show the summing up of all processes, signal, $\gamma\gamma \to q\bar{q}$, and $\gamma\gamma \to \ell^+\ell^-$, respectively.

In the processes of $\gamma\gamma \to q\bar{q}$, tracks tend to have lower energy and lower transverse momentum. After applying the cuts, the number of $\gamma\gamma \to q\bar{q}$ processes suppressed by 85%.

Also, the following cuts were applied as the preselection 3;

- $|\cos\theta_{\mathrm{miss}}| < 0.98$ and $\cos\theta_{\mathrm{acop}} < 0.98$.

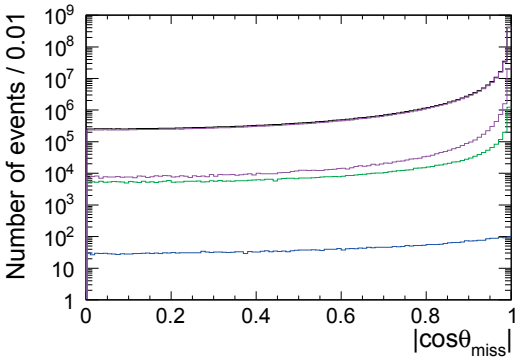

Figure 6.2.6: The distribution of missing momentum angle θ_{miss}. Black, blue, green, dotted purple, solid-dotted purple histograms show the summing up of all processes, signal, $2f$, $\gamma\gamma \to q\bar{q}$, and $\gamma\gamma \to \ell^+\ell^-$, respectively.

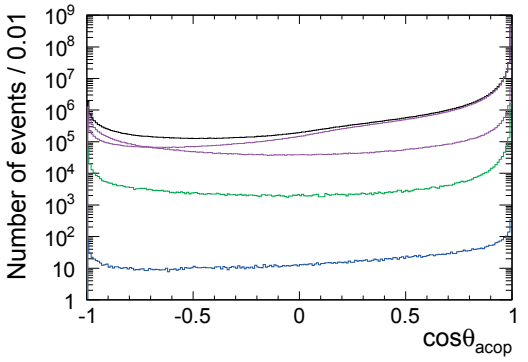

Figure 6.2.7: The distribution of acoplanarity angle of two taus θ_{acop}. Black, blue, green, dotted purple, solid-dotted purple histograms show the summing up of all processes, signal, $2f$, $\gamma\gamma \to q\bar{q}$, and $\gamma\gamma \to \ell^+\ell^-$, respectively.

The cut for θ_{miss} has the separation power for processes which do not contain neutrinos. The acoplanarity cut is useful for back-to-back events in azimuthal direction. This cut

sacrifices the signal events by about 15%, but still very useful to suppress $2f$ and $\gamma\gamma \to 2f$ background processes, especially $\gamma\gamma \to 2f$ processes suppressed by 90%.

In addition, the following cuts were applied as the basic cuts to suppress trivial processes;

- $10 < E_{\rm vis} < 265$ GeV and $5 < M_{\rm vis} < 235$ GeV,
- $M_{\rm inv} > 130$ GeV, where $M_{\rm inv}$ is the invisible mass,
- $\sum_i P_{ti} > 5$ GeV,
- $E_{\tau^+\tau^-} < 240$ GeV and $M_{\tau^+\tau^-} < 130$ GeV,
- $\cos\theta_{\tau^+\tau^-} < 0.8$,
- $\log_{10}|\min[d_0/\sigma(d_0)]| > -2$, where min[] stands for smaller impact parameter between τ^+ and τ^- .

All distributions of each variable used for basic cuts are shown in Figure 6.2.8.

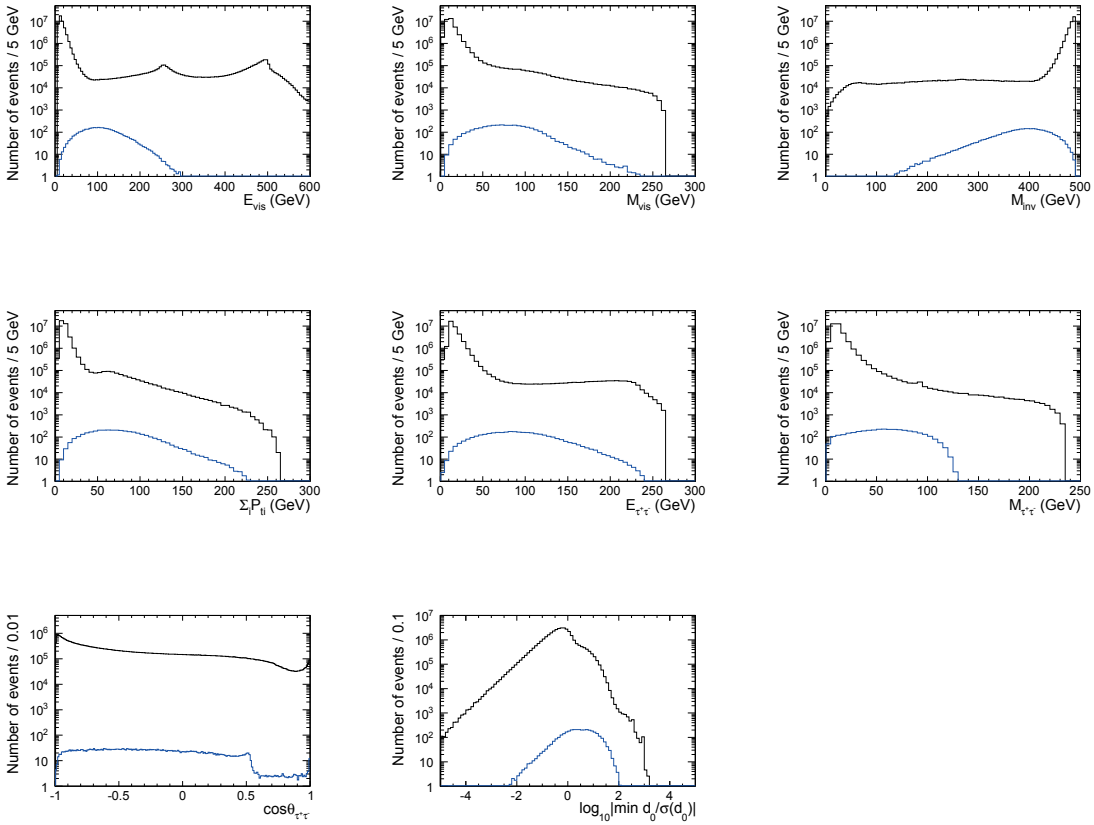

Figure 6.2.8: Distributions of each variable used for basic cuts. Black histograms show the sum of all processes, and blue show signal process.

6.2.4 Multivariate Analysis

The multivariate analysis was performed. Input variables and training parameters were optimized to extract maximum $S_{\rm sig}$. The optimum training parameters were; nCuts = 60, Shrinkage = 0.19, MaxDepth = 3, NTrees = 350, nEventsMin = 370. The optimum 13 input variables were;

- $M_{\rm vis}$, $E_{\rm vis}$,
- $\sum_i P_{ti}$, P_t,
- $N_{E>5{\rm GeV}}$, $N_{P_t>5{\rm GeV}}$, where $N_{P_t>5{\rm GeV}}$ is the number of charged tracks with the transverse momentum greater than 5 GeV,
- $\cos\theta_{\rm thrustaxis}$, $\cos\theta_{\rm miss}$,
- $M_{\tau^+\tau^-}$, $E_{\tau^+\tau^-}$, $\cos\theta_{\tau^+\tau^-}$, $\cos\theta_{\rm acop}$,
- $\log_{10}|\min[d_0/\sigma(d_0)]|$.

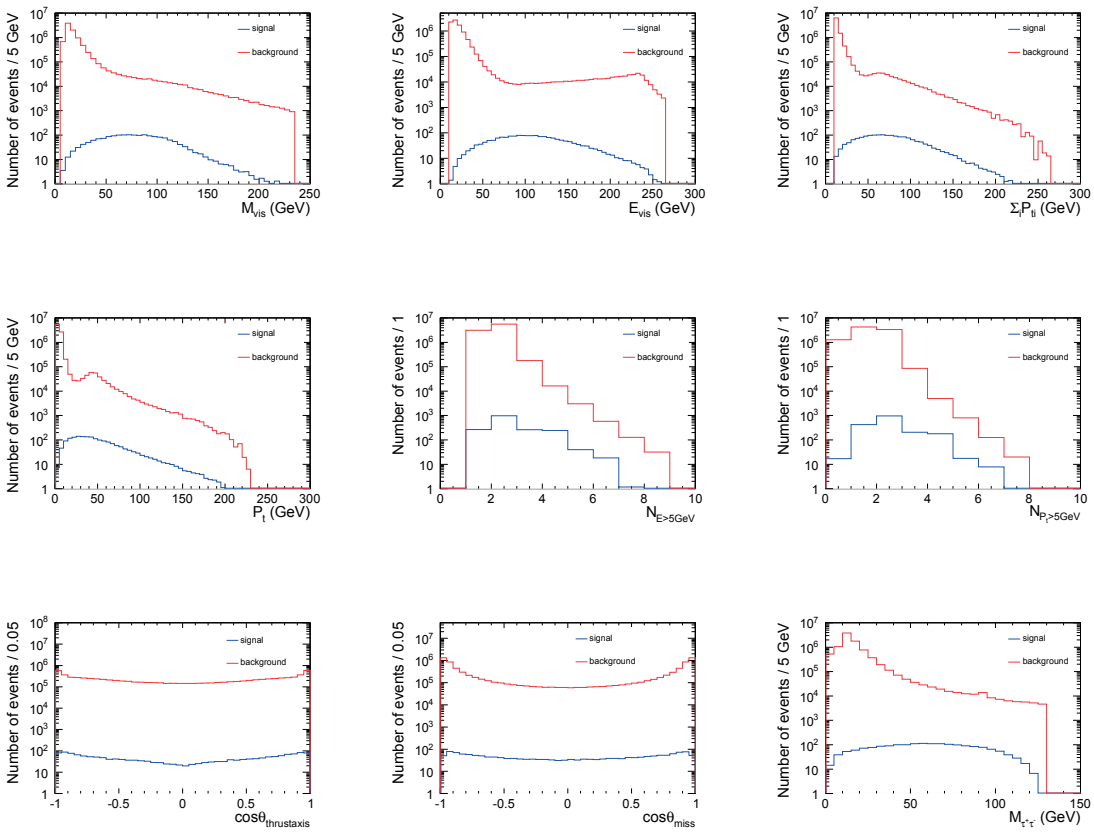

Figure 6.2.9: Distributions of each variable used for multivariate analysis. Blue histograms show the signal processes, and red show background process.

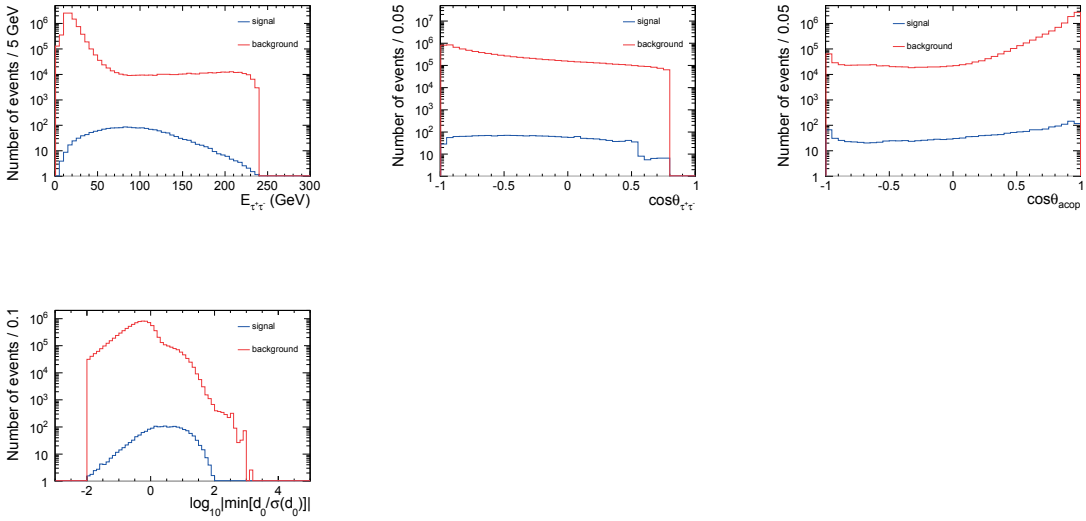

Figure 6.2.10: Distributions of each variable used for multivariate analysis. Blue histograms show the signal processes, and red show background process.

The distribution of TMVA output is shown in Figure 6.2.11.

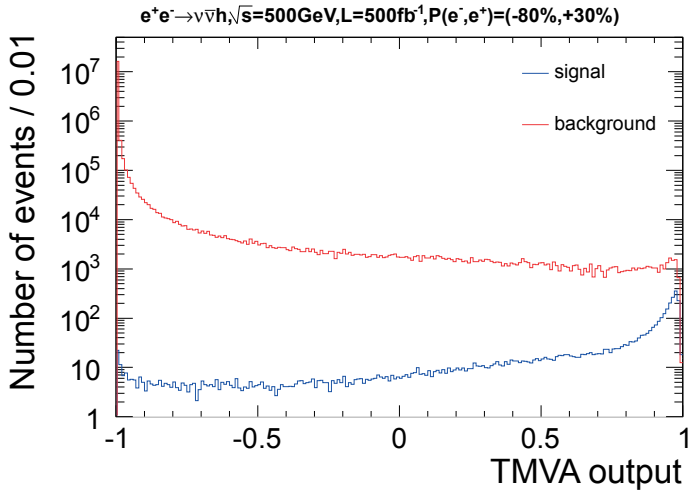

Figure 6.2.11: The distribution of TMVA output for $e^+e^- \to \nu\bar{\nu}h$ 500 GeV analysis.

By applying the cut to TMVA output to maximize $S_{\rm sig}$, 1642 signal events and 1.11×10^4 background events were remained. η was 29.7%. $S_{\rm sig}$ and corresponding precision was calculated to be as

$$S_{\rm sig} = 14.6,$$
$$\frac{\Delta(\sigma \times {\rm BR})}{(\sigma \times {\rm BR})} = 6.9\%.$$

6.2.5 Effect of Interference

As shown in Figure 6.2.1, there are two contributions for the production of signal process. It means that these two processes will interfere with each other. In order to study this effect, we checked the distribution of neutrino pair mass $M_{\nu\bar{\nu}}$ in $\nu\bar{\nu}h$ using MC truth information. Figure 6.2.12 shows the distribution of $M_{\nu\bar{\nu}}$ with no cuts applied.

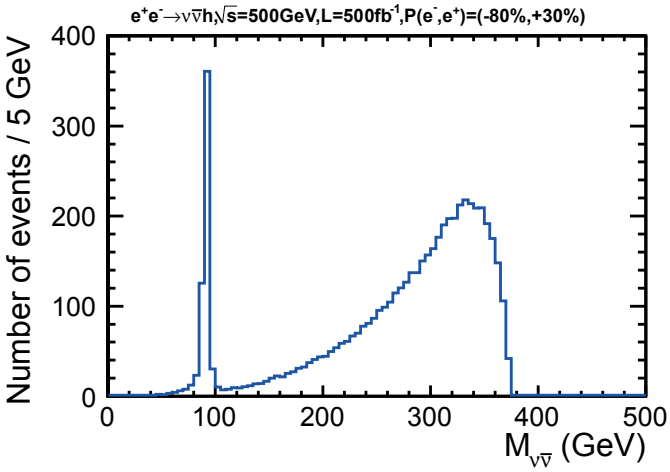

Figure 6.2.12: The distribution of $M_{\nu\bar{\nu}}$ using MC truth information.

We can clearly see the peak around 90 GeV. These events are the Higgs-strahlung events, and other events are WW-fusion events. The effect of interference would be small. From this, the events with $M_{\nu\bar{\nu}} < 120$ GeV are defined as the Higgs-strahlung events, and others are defined as the WW-fusion events. In the remaining signal events after all selection cuts using TMVA, 12.6% events were Higgs-strahlung and 87.4% were WW-fusion events. The acceptance for Higgs-strahlung events were 33.5% and for WW-fusion were 29.2%.

6.3 Summary of 500 GeV Analysis

In this section, we discussed the cases of $e^+e \to q\bar{q}h$ and $e^+e \to \nu\bar{\nu}h$. All results are summarized in Table 6.3.1.

Table 6.3.1: Results of $\sqrt{s} = 500$ GeV using multivariate analysis with the integrated luminosity of 500 fb ^{1}.

mode	$\frac{\Delta(\sigma \times \mathrm{BR})}{(\sigma \times \mathrm{BR})}$
$q\bar{q}h$	4.3%
$\nu\bar{\nu}h$	6.9%

The most sensitive channel was $q\bar{q}h$ mode because we could use full information of Z boson and Higgs boson. The $\nu\bar{\nu}h$ mode contributes significantly using its high statistics.

7 Discussion

The results we discussed in the previous sections, which are summarized in Table 5.4.1 and Table 6.3.1 are based on the nominal running scenario proposed in ILC TDR. Recently, two papers were published which discussed the ILC physics case [43] and running scenario of the ILC [44]. Since integrated luminosities and beam polarization combinations in the running scenarios are different from the nominal running scenario, we will discuss the results based on Refs. [43, 44] in this section.

7.1 ILC Running Scenario

The proposed integrated luminosities and beam polarization combinations in Refs. [43,44] are summarized in Table 7.1.1 and Table 7.1.2.

Table 7.1.1: The proposed integrated luminosities in Refs. [43, 44].

$\sqrt{s}$ (GeV)	initial (fb ^{1})	LumiUP (fb ^{1})	total (fb ^{1})
250	500	1500	2000
350	200	-	200
500	500	3500	4000

Table 7.1.2: Relative sharing of beam polarization combination $(P(e\ ), P(e^+))$ in Refs. [43, 44].

$\sqrt{s}$ (GeV)	$(-0.8, +0.3)$	$(+0.8, -0.3)$	$(-0.8, -0.3)$	$(+0.8, +0.3)$
250	67.5%	22.5%	5%	5%
350	67.5%	22.5%	5%	5%
500	40%	40%	10%	10%

According to the running scenario, the ILC operation starts with $\sqrt{s} = 500$ GeV for 3.7 years, $\sqrt{s} = 350$ GeV for 1.3 years, $\sqrt{s} = 250$ GeV again for 3.1 years, as the initial running phase. After the initial running, a machine modification for luminosity upgrade is planned for 1.5 years. Then, the luminosity upgrade running (LumiUP) will starts at $\sqrt{s} = 500$ GeV for 7.5 years, followed by $\sqrt{s} = 250$ GeV for 3.1 years. The integrated luminosities for actual running scenario and beam polarization combinations are summarized in Table 7.1.3 (for $\sqrt{s} = 250$ GeV and 500 GeV cases only).

Table 7.1.3: Integrated luminosities (in fb ^{1}) for actual running scenario and beam polarization combination. "Nominal": assume TDR nominal running scenario and assumed in this thesis, "initial": assume the running scenario proposed in Refs. [43,44] with initial phase, "full": assume the running scenario proposed in Refs. [43, 44] with initial phase plus LumiUP phase.

$\sqrt{s}$ (GeV)	Scenario	$(-0.8, +0.3)$	$(+0.8, -0.3)$	$(-0.8, -0.3)$	$(+0.8, +0.3)$
250	nominal	250	0	0	0
250	initial	337.5	112.5	25	25
250	full	1350	450	100	100
500	nominal	500	0	0	0
500	initial	200	200	50	50
500	full	1600	1600	400	400

To estimate the precisions with the upgraded scenarios, we assumed that the selection efficiencies are same as those of $(-0.8, +0.3)$ in other beam polarization combinations. The selection efficiency would change if the event topology of the final states depends on the ratio of $S_z = \pm 1$ and 0 in the initial states, where S_z is the spin component of the initial state along the positron beam direction. Nevertheless, this assumption is justified as follows. The $e^+e \to Zh$ process is mediated by the s-channel Z boson exchange with the vector or the axial vector coupling, which forbids the same-sign helicity combinations: $(\pm 1, \pm 1)$ while giving more or less the same angular distributions for the opposite-sign helicity combination: $(\mp 1, \pm 1)$. On the other hand, the WW-fusion proceeds only through the left-right helicity combination: $(-1, +1)$ since the W boson couples only to the left-handed e and the right-handed e^+. For the signal processes, therefore, their angular distributions stay the same for the active (*i.e.*, opposite) helicity combinations, independently of the choice of the beam polarization combinations. The same reasoning applies to the background processes with the s-channel γ/Z exchange or those involving W bosons coupled to the initial state e^+ or e . On the other hand, the processes involving t-channel photon exchange or photon–photon interactions do not forbid the same-sign helicity combinations. However, since the probability of finding an electron and a positron in the same-sign helicity combinations is the same for both the $(-0.8, +0.3)$ and $(+0.8, -0.3)$ polarization combinations, the efficiencies for such background processes with the same-sign helicity combination should also be the same. As long as we do not use the $(\pm 0.8, \pm 0.3)$ polarization combinations, which can barely improve the measurement precisions anyway because of the small corresponding signal cross sections and the relatively small integrated luminosities allocated, it can be reasonably justified that the selection efficiencies will not depend on the choice of the beam polarization combinations. We can then estimate the projected statistical precisions for other scenarios by calculating the number of signal and background events with the production cross sections and the integrated luminosities for individual beam polarization combinations, according to the running scenarios. The results from the estimations are summarized in Table 7.1.4.

Table 7.1.4: The expected precisions for cross section times branching ratio with actual running scenario.

scenario	$\sqrt{s}$ (GeV)	L (fb ^{1})	$q\bar{q}h$	$e^+e\ h$	$\mu^+\mu\ h$	$\nu\bar{\nu}h$	combine
nominal	250	250	3.4%	14.4%	11.3%	—	3.2%
	500	500	4.3%	—	—	6.9%	—
	combine		2.7%	14.4%	11.3%	—	2.6%
	combine		—	—	—	6.9%	6.9%
initial	250	500	2.5%	10.9%	8.7%	—	2.4%
	500	500	4.9%	—	—	9.6%	—
	combine		2.3%	10.9%	8.7%	—	2.1%
	combine		—	—	—	9.6%	9.6%
full	250	2000	1.3%	5.5%	4.3%	—	1.2%
	500	4000	1.7%	—	—	3.4%	—
	combine		1.0%	5.5%	4.3%	—	1.0%
	combine		—	—	—	3.4%	3.4%

7.2 The Precision of Branching Ratio

In previous sections, we discussed the measurement accuracy for the cross section times branching ratio ($\sigma \times$ BR). In this section, we will discuss the precision for the branching ratio. We could extract the precision of the branching ratio by using another result of measuring cross section.

At the ILC, the production cross section of the Higgs boson via Higgs-strahlung can be independently measured by using the recoil mass technique [25, 28, 43]. The cross section of WW-fusion can also be measured by the process of the Higgs boson decays to b quarks [25]. Thus, it is possible to extract the precision of the branching ratio of Higgs boson decaying into tau pairs.

At $\sqrt{s} = 250$ GeV, contributions from WW- and ZZ-fusion are negligible, the Higgs-strahlung only contributes to the production cross section. This cross section is expected to be measured at $\Delta\sigma/\sigma = 2.6\%$ with the nominal running scenario [88] and at a sub-% level with the full running scenario [43]. At $\sqrt{s} = 500$ GeV, both the Higgs-strahlung and WW-fusion contribute to the Higgs boson production, while the contribution of ZZ-fusion is negligible. As for the $\nu\bar{\nu}h$ process, it is possible to estimate contributions from the Higgs-strahlung and WW-fusion separately, but its precision is worse than other modes and is not contribute to the precise measurement. Thus, we do not include $\nu\bar{\nu}h$ mode for estimation of the precision of the branching ratio. The expected precision for the branching ratio of the Higgs boson decaying into tau pairs is $\Delta\text{BR}/\text{BR} = 3.7\%$ with the nominal running scenario assuming $\Delta\sigma/\sigma = 2.6\%$ and will reaches $\Delta\text{BR}/\text{BR} = 1.4\%$ with the full running scenario assuming $\Delta\sigma/\sigma = 1.0\%$.

7.3 Systematic Uncertainty

We investigated the systematic uncertainty from the statistics of MC samples and found sufficiently small even for the full luminosity results, in which the highest precision is required for the analysis. The systematic uncertainty of the luminosity measurement is estimated to be 0.1% or better for the ILC [29], and it is expected not to be significant source of the systematic error. In this study, we did not discuss the systematic uncertainties from the selection criteria caused by the uncertainties of the momentum/energy resolution, tracking efficiency etc. in the analyzes. These are closely related to the detailed design and construction of the detector as well as the beam conditions and should be studied in accordance with these developments.

8 Conclusion

We evaluated the measurement precision of the production cross section times the branching ratio of the Higgs boson decaying into a tau pair at the ILC. We evaluated realistic detection efficiencies fr this process by a full simulation for the ILD detector model. We assumed the Higgs mass of 125 GeV, the branching ratio of BR($h \to \tau^+\tau^-$) = 6.32%. The optimization of event selection criteria was performed to maximize signal significance with the ILC nominal running scenario described in the TDR.

At the center-of-mass energy of 250 GeV, three modes as; $e^+e^- \to q\bar{q}h$, $e^+e^- \to e^+e^-h$, and $e^+e^- \to \mu^+\mu^-h$ were analyzed with the integrated luminosity of 250 fb^{-1}. The obtained precisions for the production cross section times the branching ratio, $\Delta(\sigma \times \mathrm{BR})/(\sigma \times \mathrm{BR})$, were 3.4%, 14.4%, and 11.3%, respectively, using multivariate analysis technique. At the center-of-mass energy of 500 GeV, $e^+e^- \to q\bar{q}h$ and $e^+e^- \to \nu\bar{\nu}h$ were analyzed with the integrated luminosity of 500 fb^{-1}. The obtained precisions for $\Delta(\sigma \times \mathrm{BR})/(\sigma \times \mathrm{BR})$ were 4.6% and 6.9%.

We also discussed improvements of the precisions with a possible luminosity upgrade running scenario. In the full running scenario, in which integrated luminosities of 2000 fb^{-1} at the center-of-mass energy of 250 GeV and 4000 fb^{-1} at the energy of 500 GeV are assumed, the expected measurement accuracy for the cross section times the branching ratio will reach to 1.0%. We also estimated the precisions for the measurement of branching ratio for the Higgs boson decaying into tau pairs by assuming precisions of the production cross section, σ, of the Higgs boson at the ILC, which can be measured independently by the ILC experiment. The expected precision for the branching ratio was estimated to be 3.6% with nominal running scenario assuming $\Delta\sigma/\sigma = 2.6\%$, and to be 1.4% with full running scenario assuming $\Delta\sigma/\sigma = 1.0\%$.

In conclusion, we expect the precision of measurements for the production cross section times the branching ratio of Higgs boson decaying into tau pairs by 2.6% with the nominal ILC running scenario, and it can be 1.0% with the possible luminosity upgrade full running scenario. The expected precisions are smaller or comparable with predictions from typical model of physics beyond the Standard Model, showing that this channel can be a good probe to search for physics beyond the Standard Model. In addition, we presented the results of the study as the production cross section times the branching ratio, separately for the Higgs-strahlung and the WW-fusion process; in a way to give the primary information of the ILC, which can be used as input parameters to the phenomenological studies on beyond the Standard Model.

A Detail Calculation of Collinear Approximation

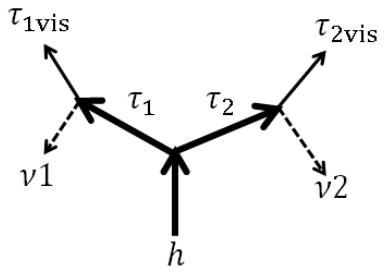

Figure A.0.1: A Higgs boson decaying into a tau pair. In this figure, h means Higgs boson, $\tau_1(\tau_2)$ means tau, $\tau_{1\mathrm{vis}}(\tau_{2\mathrm{vis}})$ means the visible decay products from $\tau_1(\tau_2)$, and $\nu 1(\nu 2)$ means the neutrino(s) from $\tau_1(\tau_2)$, respectively.

Consider the situation as shown in Figure A.0.1, a Higgs boson decaying into a tau pair. Defining a four momentum of visible decay products from τ_1 as $(E_{\mathrm{vis1}}, \boldsymbol{p}_{\mathrm{vis1}})$, and a four momentum of neutrino(s) from τ_1 as $(E_{\nu 1}, \boldsymbol{p}_{\nu 1})$. Also defining four momenta as $(E_{\mathrm{vis2}}, \boldsymbol{p}_{\mathrm{vis2}})$ and $(E_{\nu 2}, \boldsymbol{p}_{\nu 2})$ from τ_2 as the same way of τ_1.

In the collinear approximation, we consider the visible decay products and the neutrino(s) from the same tau are collinear, which means flighting same direction. We can write this situation for τ_1 as,

$$\boldsymbol{p}_{\nu 1} = a\boldsymbol{p}_{\mathrm{vis1}}, \tag{A.0.1}$$
$$\therefore (E_{\nu 1}, \boldsymbol{p}_{\nu 1}) = (E_{\nu 1}, \boldsymbol{p}_{\mathrm{vis1}}), \tag{A.0.2}$$

where a is a coefficient ($a > 0$). Also for τ_2 we have,

$$\boldsymbol{p}_{\nu 2} = b\boldsymbol{p}_{\mathrm{vis2}}, \tag{A.0.3}$$
$$\therefore (E_{\nu 2}, \boldsymbol{p}_{\nu 2}) = (E_{\nu 2}, \boldsymbol{p}_{\mathrm{vis2}}), \tag{A.0.4}$$

where b is a coefficient ($b > 0$). By ignoring the mass of neutrino, we have

$$E_{\nu 1}{}^2 - a^2|\boldsymbol{p}_{\mathrm{vis1}}|^2 = 0 \tag{A.0.5}$$
$$E_{\nu 1}{}^2 = a^2|\boldsymbol{p}_{\mathrm{vis1}}|^2 \tag{A.0.6}$$
$$E_{\nu 1} = a|\boldsymbol{p}_{\mathrm{vis1}}|, \tag{A.0.7}$$

for τ_1. Then we have

$$(E_{\nu 1}, \boldsymbol{p}_{\nu 1}) = (a|\boldsymbol{p}_{\mathrm{vis1}}|, a\boldsymbol{p}_{\mathrm{vis1}}). \tag{A.0.8}$$

Taking same procedures for τ_2, then we have

$$(E_{\nu 2}, \boldsymbol{p}_{\nu 2}) = (b|\boldsymbol{p}_{\mathrm{vis2}}|, b\boldsymbol{p}_{\mathrm{vis2}}). \tag{A.0.9}$$

In the collinear approximation, we also assume that the contributions of transverse missing momentum only comes from the neutrino(s) from tau decay. Considering this we

have

$$p_{\mathrm{mis}_x} = a p_{\tau 1_x} + b p_{\tau 2_x} \tag{A.0.10}$$

$$p_{\mathrm{mis}_y} = a p_{\tau 1_y} + b p_{\tau 2_y}, \tag{A.0.11}$$

because we have relations shown in Eq. (A.0.8) and Eq. (A.0.9). Using Eq. (A.0.10) we have

$$a = \frac{p_{\mathrm{mis}_x} - b p_{\tau 2_x}}{p_{\tau 1_x}}. \tag{A.0.12}$$

Substituting above equation to Eq. (A.0.11), we have

$$p_{\mathrm{mis}_x} = \frac{p_{\mathrm{mis}_x} - b p_{\tau 2_x}}{p_{\tau 1_x}} p_{\tau 1_y} + b p_{\tau 2_y} \tag{A.0.13}$$

$$\therefore b = \frac{p_{\mathrm{mis}_y} p_{\tau 1_x} - p_{\mathrm{mis}_x} p_{\tau 1_y}}{p_{\tau 1_x} p_{\tau 2_y} - p_{\tau 2_x} p_{\tau 1_y}}. \tag{A.0.14}$$

Also from Eq. (A.0.10), we have

$$b = \frac{p_{\mathrm{mis}_x} - a p_{\tau 1_x}}{p_{\tau 2_x}}. \tag{A.0.15}$$

Substituting this equation to Eq. (A.0.11), we have

$$p_{\mathrm{mis}_y} = a p_{\tau 1_y} + \frac{p_{\mathrm{mis}_x} - a p_{\tau 1_x}}{p_{\tau 2_x}} p_{\tau 2_y} \tag{A.0.16}$$

$$\therefore a = \frac{p_{\mathrm{mis}_y} p_{\tau 2_x} - p_{\mathrm{mis}_x} p_{\tau 2_y}}{p_{\tau 1_y} p_{\tau 2_x} - p_{\tau 1_x} p_{\tau 2_y}}. \tag{A.0.17}$$

Combining equations of Eq. (A.0.8), Eq. (A.0.9), Eq. (A.0.14), and Eq. (A.0.17), we can calculate the four momenta of neutrino(s) from tau decay. We then can calculate of four momentum of τ_1, τ_2, and initial Higgs boson by combining τ_1 and τ_2.

B Cut-based Analysis for 250 GeV $e^+e^- \to q\bar{q}h$ Mode

In this section, we will discuss the cut-based analysis for 250 GeV $e^+e \to q\bar{q}h$ mode. The cut-based analysis was performed to extract maximum S_{sig}. Color meanings of all histograms in this section are as following;

- black: summing up all processes,
- blue: signal ($q\bar{q}h, h \to \tau^+\tau$),
- ocher: $q\bar{q}h, h \not\to \tau^+\tau$,
- ash: $\ell^+\ell$ h and $\nu\bar{\nu}h$,
- green: $2f$,

- red: $4f$,
- dashed pink: $1f\_3f$,
- brown: $\gamma\gamma \to 2f$.

The following cuts were applied sequentially.

- $E_{\mathrm{vis}} < 240$ GeV and $|\cos\theta_{\mathrm{miss}}| < 0.98$ for suppressing neutrino-less backgrounds.

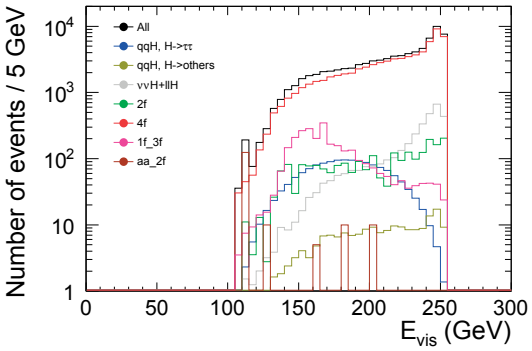

Figure B.0.2: The distribution of visible energy E_{vis}.

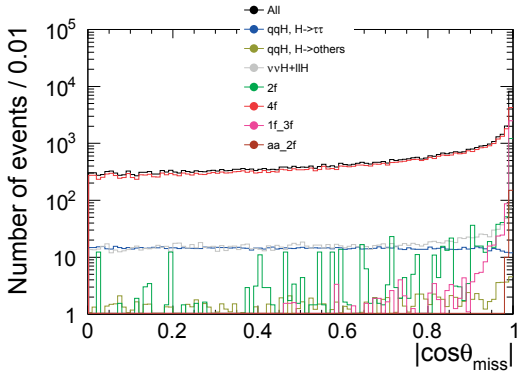

Figure B.0.3: The distribution of missing momentum angle $|\cos\theta_{\mathrm{miss}}|$.

- $E_{q\bar{q}} < 125$ GeV and $M_{q\bar{q}} > 80$ GeV, for selecting the events contain a Z boson.

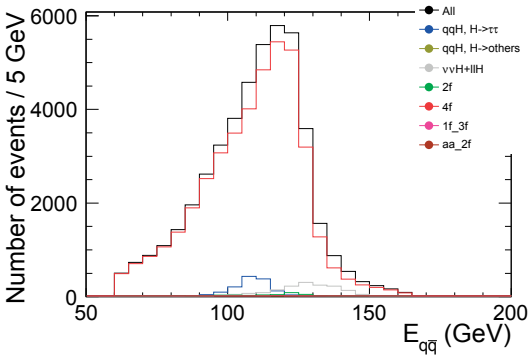

Figure B.0.4: The distribution of jet pair energy $E_{q\bar{q}}$.

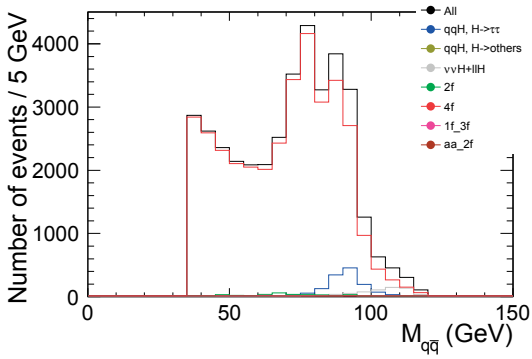

Figure B.0.5: The distribution of jet pair mass $M_{q\bar{q}}$.

- $E_{\tau^+\tau^-} < 130$ GeV, $M_{\tau^+\tau^-} < 115$ GeV, and $\cos\theta_{\tau^+\tau^-} < -0.54$, for selecting tau pair. The energy and mass cut could suppress the tail of backgrounds due to the broad distribution of signal. The angle between taus is very useful for suppressing lots of background processes thanks to the monochromatic signal event topology.

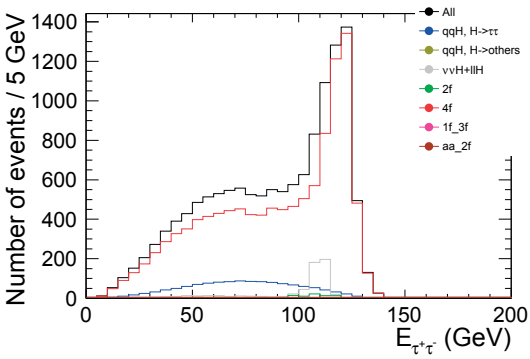

Figure B.0.6: The distribution of tau pair energy $E_{\tau^+\tau^-}$.

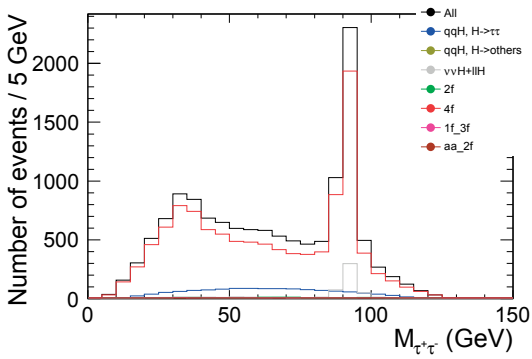

Figure B.0.7: The distribution of tau pair mass $M_{\tau^+\tau^-}$.

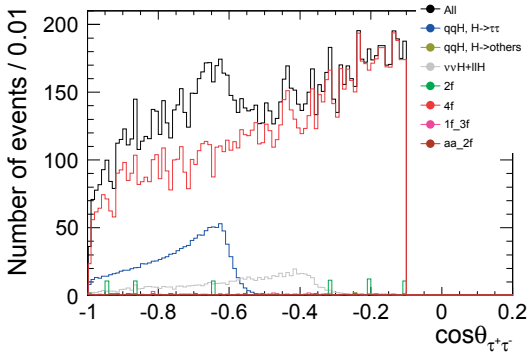

Figure B.0.8: The distribution of angle between two taus $\cos\theta_{\tau^+\tau^-}$.

- $E_{\text{col}} < 210$ GeV and $M_{\text{col}} > 100$ GeV, for selecting Higgs events. M_{col} has better separation power to suppress $4f$ processes which have W boson and/or Z boson.

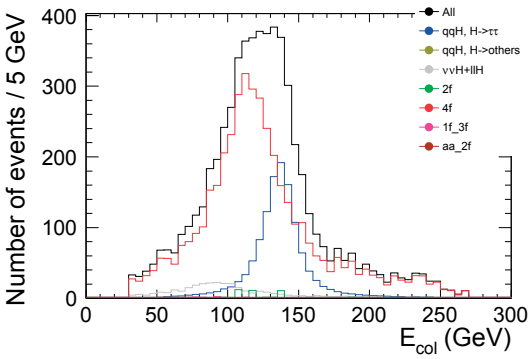

Figure B.0.9: The distribution of tau pair energy with collinear approximation E_{col}.

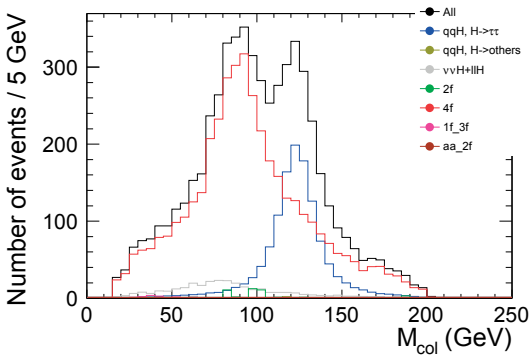

Figure B.0.10: The distribution of tau pair mass with collinear approximation M_{col}.

- $\sum_{\tau^+,\tau^-} \log_{10}|d_0/\sigma(d_0)| > -0.2$ and $\sum_{\tau^+,\tau^-} \log_{10}|z_0/\sigma(z_0)| > -0.4$. Since a tau lepton has longer lifetime, these cuts are useful to suppress backgrounds which not containing tau leptons.

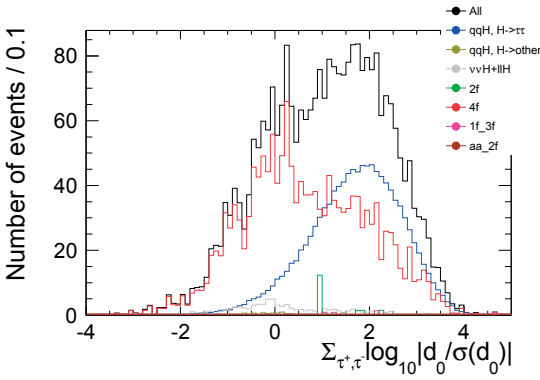

Figure B.0.11: The distribution of d_0 impact parameter $\sum_{\tau^+,\tau^-} \log_{10}|d_0/\sigma(d_0)|$.

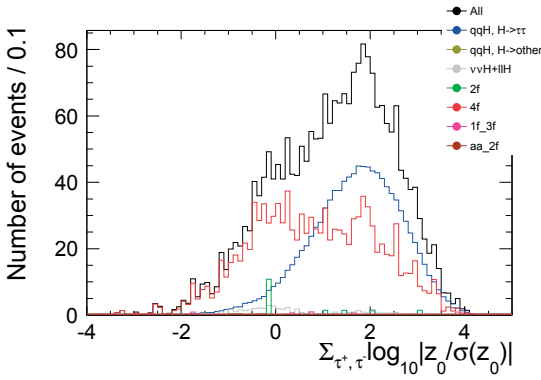

Figure B.0.12: The distribution of z_0 impact parameter $\sum_{\tau^+,\tau^-} \log_{10}|z_0/\sigma(z_0)|$.

- $M_{\text{recoil}} > 113$ GeV, as the final discriminant of this analysis to select Higgs events.

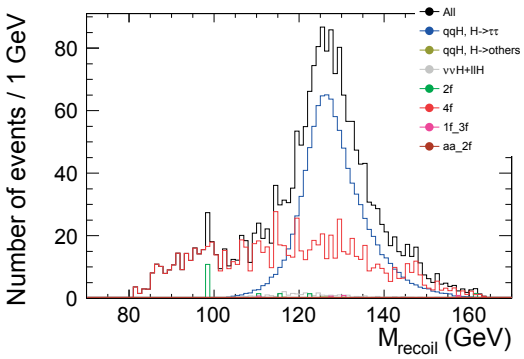

Figure B.0.13: The distribution of recoil mass M_{recoil}.

The cut table of this analysis is shown in Table B.0.1. After the analysis, 1016 signals and 575 backgrounds were remained. The selection efficiency of signal process η was 30.6%. S_{sig} was calculated to be 25.5. This result corresponds to the precision of cross section times branching ratio ($\sigma \times \mathrm{BR}$) as

$$\frac{\Delta(\sigma \times \mathrm{BR})}{(\sigma \times \mathrm{BR})} = 3.9\%.$$

Table B.0.1: The cut table of 250 GeV $q\bar{q}h$ mode with the integrated luminosity of 250 fb ^{1}. "Pre" means preselection cuts and "Basic" means basic cuts, described in Section 5.1.3.

	$q\bar{q}h$ $h \to \tau^+\tau$	$q\bar{q}h$ $h \not\to \tau^+\tau$	$\ell^+\ell^- h$ $\nu\bar{\nu}h$	$2f$	$4f$	$1f\_3f$	$\gamma\gamma \to 2f$	S_{sig}
No cuts	3318	4.920×10^4	2.729×10^4	2.863×10^7	1.021×10^7	2.305×10^8	1.634×10^8	0.160
Pre	1529	671.4	3849	5.877×10^4	2.522×10^5	5.195×10^4	1.617×10^5	2.10
Basic	1451	183.0	3343	2316	6.924×10^4	2861	159.5	5.14
E_{vis}	1435	142.8	1759	1753	4.727×10^4	2753	159.5	6.10
θ_{miss}	1411	134.6	1636	491.0	4.121×10^4	176.6	0	6.65
$E_{q\bar{q}}$	1371	72.73	659.4	354.4	3.505×10^4	141.1	0	7.06
$M_{q\bar{q}}$	1251	62.84	616.6	85.72	1.110×10^4	40.38	0	10.9
$E_{\tau^+\tau^-}$	1248	62.84	616.3	85.72	1.095×10^4	40.38	0	10.9
$M_{\tau^+\tau^-}$	1244	62.68	613.3	85.72	1.086×10^4	40.28	0	10.9
$\theta_{\tau^+\tau^-}$	1234	24.71	307.2	45.69	4277	22.57	0	16.1
E_{col}	1218	22.11	298.5	43.97	4034	21.67	0	16.2
M_{col}	1105	11.52	78.86	17.26	1560	4.000	0	21.0
$d_0/\sigma(d_0)$	1064	7.422	49.18	17.26	1129	4.000	0	22.3
$z_0/\sigma(z_0)$	1037	4.576	35.18	17.26	913.0	3.100	0	23.1
M_{recoil}	1016	3.991	28.98	4.818	534.5	2.450	0	25.5

C Cut-based Analysis for 250 GeV $e^+e^- \to e^+e^-h$ Mode

The cut-based analysis was performed to extract maximum S_{sig}. Color meanings of all histograms in this section are as following;

- black: summing up all processes,
- blue: signal ($e^+e\ \ h, h \to \tau^+\tau\ \ $),
- ocher: $e^+e\ \ h, h \not\to \tau^+\tau\ \ $,
- solid ash: $\mu^+\mu\ \ h$,
- dashed ash: $\tau^+\tau\ \ h$,
- dotted ash: $q\bar{q}h$ and $\nu\bar{\nu}h$,
- green: $2f$,
- red: $4f$,
- dashed pink: $1f\_3f$,
- brown: $\gamma\gamma \to 2f$.

The following cuts were applied;

- $\sum_i P_{ti} > 85$ GeV and $P_t > 5$ GeV. Since in the signal process, produced Z boson and Higgs boson are almost stopping. Therefore, each particle tends to have larger transverse momentum, then the $\sum_i P_{ti}$ will have different distribution between signal and backgrounds. P_t cut is suppressing neutrino-less backgrounds.

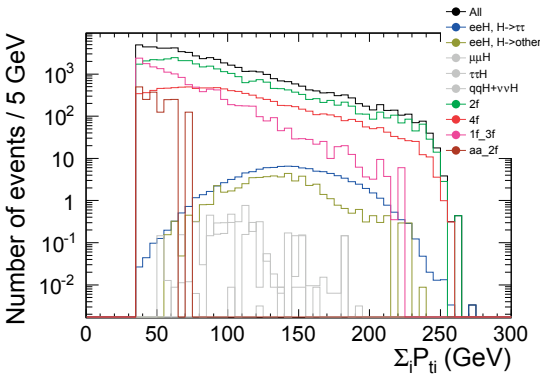

Figure C.0.14: The distribution of sum of the transverse momenta $\sum_i P_{ti}$.

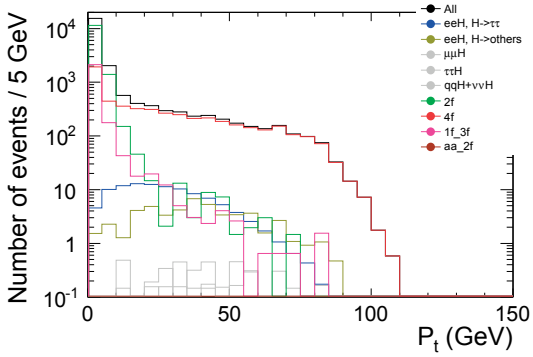

Figure C.0.15: The distribution of transverse momentum P_t.

- $|\cos\theta_{\text{miss}}| < 0.97$, to also suppress neutrino-less events.

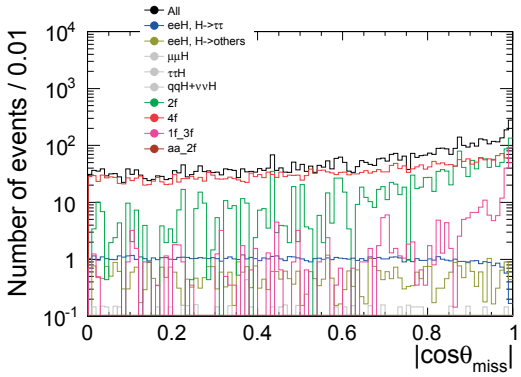

Figure C.0.16: The distribution of missing momentum $|\cos\theta_{\text{miss}}|$.

- $E_{e^+e^-} < 120$ GeV and $85 < M_{e^+e^-} < 110$ GeV, for suppressing backgrounds which not have Z boson.

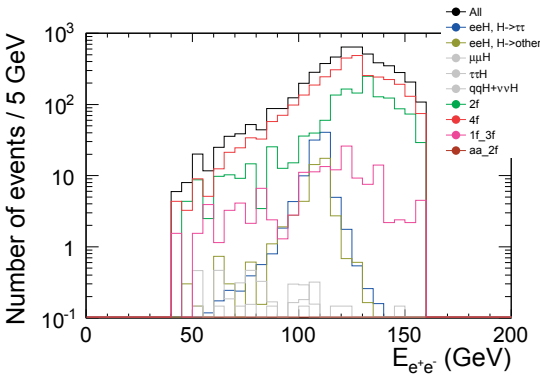

Figure C.0.17: The distribution of electron pair energy $E_{e^+e^-}$.

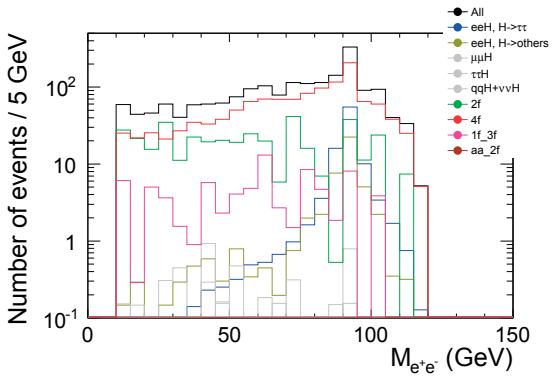

Figure C.0.18: The distribution of electron pair mass $M_{e^+e^-}$.

- $M_{\tau^+\tau^-} > 10$ GeV and $\cos\theta_{\tau^+\tau^-} < -0.55$. The $M_{\tau^+\tau^-}$ can cut the low mass events, and $\cos\theta_{\tau^+\tau^-}$ is very useful for suppressing lots of backgrounds because of the monochromatic signal event topology.

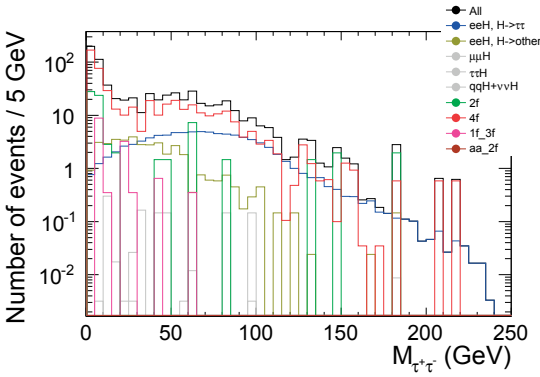

Figure C.0.19: The distribution of tau pair mass $M_{\tau^+\tau^-}$.

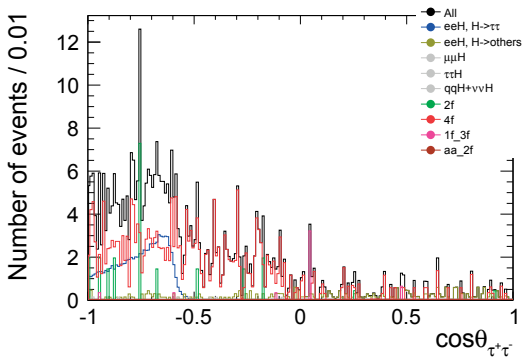

Figure C.0.20: The distribution of angle between two taus $\cos\theta_{\tau^+\tau^-}$.

- $120 < M_{\text{recoil}} < 136$ GeV, as the final discriminant of this analysis to select Higgs events.

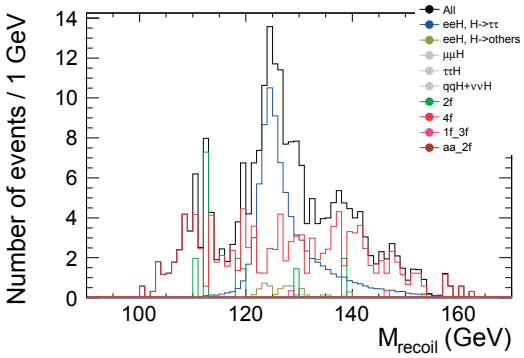

Figure C.0.21: The distribution of recoil mass M_{recoil}.

The cut table of this analysis is shown in Table C.0.2. After the analysis, 69.89 signals and 46 backgrounds were remained. η was 39.9%. S_{sig} was calculated to be $S_{\text{sig}} = 6.49$. This result corresponds to the precision of cross section times branching ratio ($\sigma \times \text{BR}$) as

$$\frac{\Delta(\sigma \times \text{BR})}{(\sigma \times \text{BR})} = 15.4\%.$$

Table C.0.2: The cut table of 250 GeV e^+e h mode with the integrated luminosity of 250 fb ^{1}. "Pre" means preselection cuts and "Basic" means basic cuts, described in section 5.2.3.

	e^+e^-h $h \to \tau^+\tau^-$	e^+e^-h $h \not\to \tau^+\tau^-$	$\mu^+\mu^-h$	$\tau^+\tau^-h$	$q\bar{q}h$ $\nu\bar{\nu}h$	$2f$	$4f$	$1f\_3f$	$\gamma\gamma \to 2f$	S_{sig}
No cuts	175.1	2544	2602	2591	7.190×10^4	2.863×10^7	1.021×10^7	2.305×10^8	1.634×10^8	0.00842
Pre	109.6	54.62	0.471	6.206	3.417	2.215×10^5	3.810×10^4	1.809×10^5	2.673×10^5	0.130
Basic	109.4	54.01	0.468	4.088	1.622	3.334×10^4	9824	1.373×10^4	1866	0.451
$\sum_i P_{ti}$	104.8	51.91	0.468	3.421	1.596	1.309×10^4	5412	2415	0	0.722
P_t	100.2	50.38	0.468	3.395	1.596	1660	3483	290.8	0	1.34
θ_{miss}	98.75	48.40	0.468	3.389	1.450	1388	3301	146.7	0	1.40
$E_{e^+e^-}$	95.93	46.91	0.468	3.236	1.304	387.7	1248	78.62	0	2.22
$M_{e^+e^-}$	86.01	37.64	0.155	0.174	0.801	73.37	486.9	13.80	0	3.25
$M_{\tau^+\tau^-}$	84.02	33.62	0.155	0.171	0.801	21.87	242.1	4.925	0	4.27
$\theta_{\tau^+\tau^-}$	82.63	5.239	0.146	0.012	0.328	16.11	120.8	0.700	0	5.50
M_{recoil}	69.89	4.765	0	0.009	0.173	1.460	39.28	0.350	0	6.49

D Cut-based Analysis for 250 GeV $e^+e^- \to \mu^+\mu^- h$ Mode

The cut-based analysis was performed to extract maximum S_{sig}. Color meanings of all histograms in this section are as following;

- black: summing up all processes,
- blue: signal,
- ocher: $\mu^+\mu^- h, h \not\to \tau^+\tau^-$,
- solid ash: $e^+e^- h$,
- dashed ash: $\tau^+\tau^- h$,
- dotted ash: $q\bar{q}h$ and $\nu\bar{\nu}h$,
- green: $2f$,
- red: $4f$,
- dashed pink: $1f\_3f$,
- brown: $\gamma\gamma \to 2f$.

The following cuts were applied;

- $E_{\text{vis}} < 245$ GeV and $P_t > 5$ GeV. Both cuts are useful to suppress neutrino-less backgrounds.

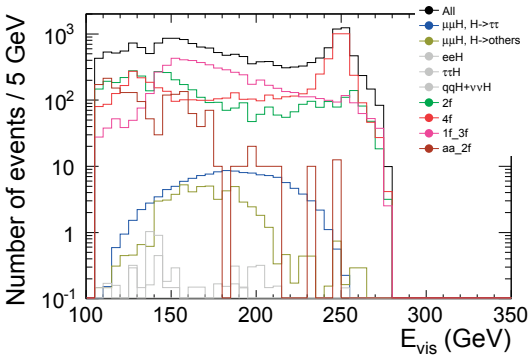

Figure D.0.22: The distribution of visible energy E_{vis}.

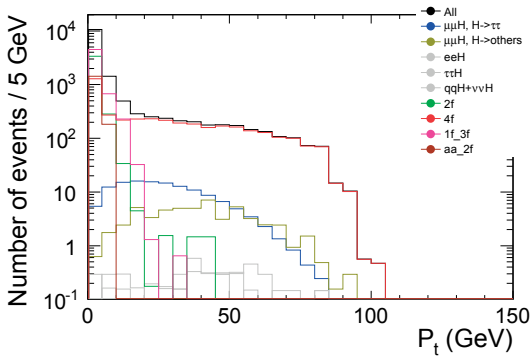

Figure D.0.23: The distribution of transverse momentum P_t.

- $|\cos\theta_{\text{miss}}| < 0.97$, also useful for rejecting neutrino-less backgrounds.

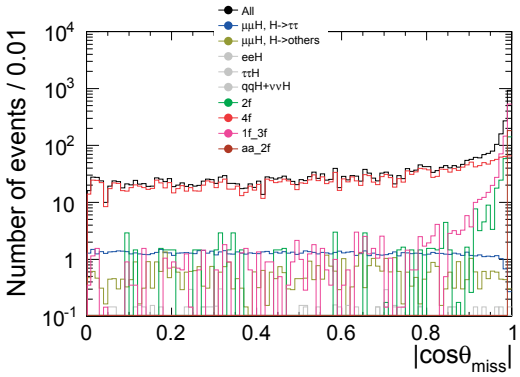

Figure D.0.24: The distribution of missing momentum angle $|\cos\theta_{\text{miss}}|$.

- $E_{\mu^+\mu^-} < 115$ GeV and $65 < M_{\mu^+\mu^-} < 105$ GeV, for selecting events contain a Z boson.

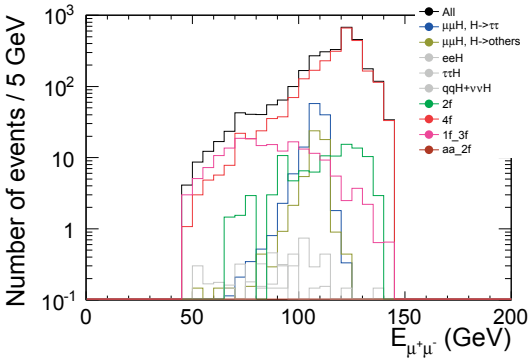

Figure D.0.25: The distribution of muon pair energy $E_{\mu^+\mu^-}$.

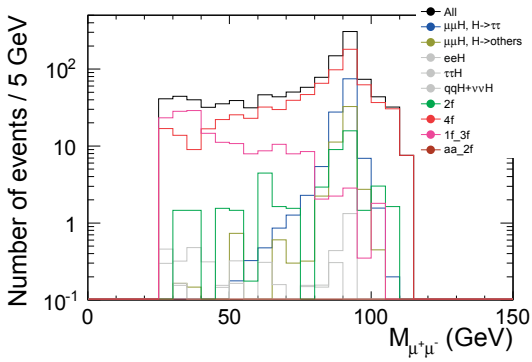

Figure D.0.26: The distribution of muon pair mass $M_{\mu^+\mu^-}$.

- $E_{\tau^+\tau^-} > 15$ GeV, $M_{\tau^+\tau^-} > 10$ GeV, and $\cos\theta_{\tau^+\tau^-} < -0.52$. The energy and mass cuts can suppress some of backgrounds especially low mass events. The cut for $\theta_{\tau^+\tau^-}$ is very useful thanks to the monochromatic signal event topology.

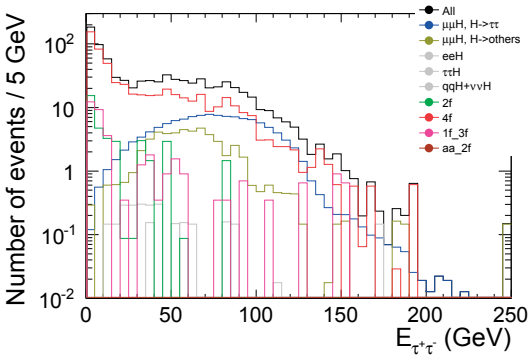

Figure D.0.27: The distribution of tau pair energy $E_{\tau^+\tau^-}$.

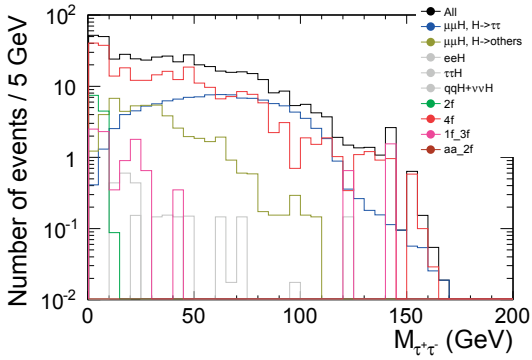

Figure D.0.28: The distribution of tau pair mass $M_{\tau^+\tau^-}$.

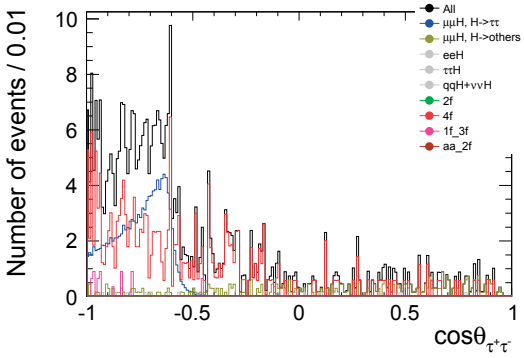

Figure D.0.29: The distribution of angle between two taus $\cos\theta_{\tau^+\tau^-}$.

- $123 < M_{\text{recoil}} < 138$ GeV, as the final discriminant of this analysis to select Higgs boson.

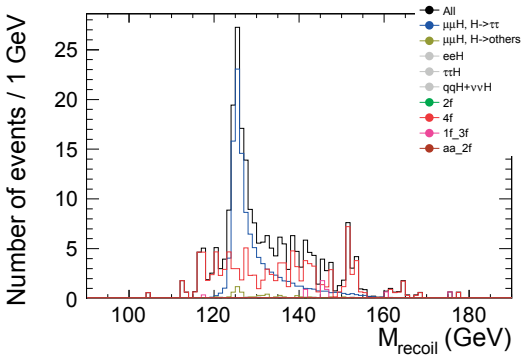

Figure D.0.30: The distribution of recoil mass M_{recoil}.

The cut table of this analysis is shown in Table D.0.3. After the analysis, 98.83 signals and 46 backgrounds were remained. η was 60.0%. $S_{\rm sig}$ was calculated to be $S_{\rm sig} = 8.22$. This result corresponds to the precision of cross section times branching ratio ($\sigma \times \mathrm{BR}$) as

$$\frac{\Delta(\sigma \times \mathrm{BR})}{(\sigma \times \mathrm{BR})} = 12.2\%.$$

Table D.0.3: The cut table of 250 GeV $\mu^+\mu^-h$ mode with the integrated luminosity of 250 fb^{-1}. "Pre" means preselection cuts and "Basic" means basic cuts, described in Section 5.3.3.

	$\mu^+\mu^-h$ $h \to \tau^+\tau^-$	$\mu^+\mu^-h$ $h \not\to \tau^+\tau^-$	e^+e^-h	$\tau^+\tau^-h$	$q\bar{q}h$ $\nu\bar{\nu}h$	$2f$	$4f$	$1f\_3f$	$\gamma\gamma \to 2f$	S_{sig}
No cuts	164.6	2437	2719	2591	7.190×10^4	2.863×10^7	1.021×10^7	2.305×10^8	1.634×10^8	0.00791
Pre	133.0	56.47	1.810	3.310	4.223	6.569×10^4	1.894×10^4	2.287×10^4	8.229×10^4	0.305
Basic	132.8	56.16	1.643	2.456	3.261	4182	6382	5899	1629	0.982
E_{vis}	131.8	54.67	1.626	2.456	3.115	3701	3960	5441	1616	1.08
P_t	126.4	54.04	1.602	2.456	2.822	326.0	2673	935.9	182.3	1.93
θ_{miss}	124.4	52.85	1.455	2.453	2.667	100.5	2480	184.9	0	2.29
$E_{\mu^+\mu^-}$	122.1	51.50	1.455	2.443	2.375	47.80	755.8	169.7	0	3.60
$M_{\mu^+\mu^-}$	120.7	50.44	0.167	0.649	2.074	35.42	558.7	36.16	0	4.26
$E_{\tau^+\tau^-}$	119.0	49.55	0.167	0.649	1.927	12.03	270.1	11.05	0	5.52
$M_{\tau^+\tau^-}$	117.2	44.32	0.167	0.649	1.927	0.088	191.8	6.250	0	6.16
$\theta_{\tau^+\tau^-}$	115.6	5.674	0.018	0.482	0.585	0	116.8	5.250	0	7.39
M_{recoil}	98.83	4.641	0	0.155	0.292	0	40.61	0	0	8.22

E Cut-based Analysis for 500 GeV $e^+e^- \to q\bar{q}h$ Mode

The cut-based analysis was performed to extract maximum S_{sig}. Color meanings of all histograms in this section are as following;

- black: summing up all processes,
- blue: signal,
- ocher: $q\bar{q}h, h \not\to \tau^+\tau^-$,
- ash: $\ell^+\ell^- h$ and $\nu\bar{\nu}h$,
- green: $2f$,
- red: $4f$,
- dashed pink: $5f$,
- brown: $6f$,
- solid purple: $\gamma\gamma \to 2f$,
- dashed purple: $\gamma\gamma \to 4f$.

The following cuts were applied;

- $\sum_i P_{ti} > 205$ GeV and $P_t > 15$ GeV. Both cuts are suppressing neutrino-less backgrounds.

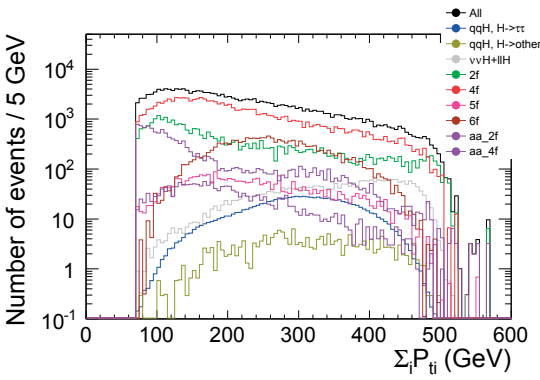

Figure E.0.31: The distribution of transverse momenta $\sum_i P_{ti}$.

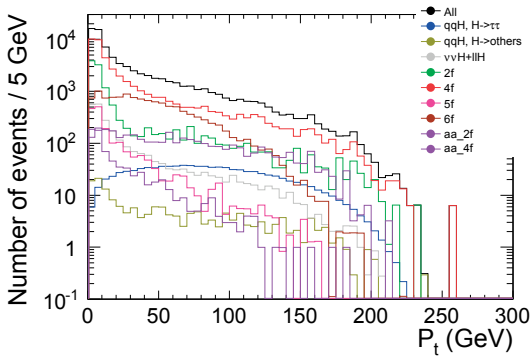

Figure E.0.32: The distribution of transverse momentum P_t.

- thrust < 0.94, for suppressing the backgrounds going to very forward region.

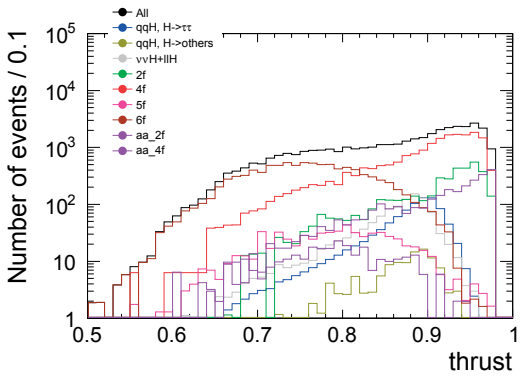

Figure E.0.33: The distribution of thrust.

- $175 < E_{q\bar{q}} < 260$ GeV and $70 < M_{q\bar{q}} < 135$ GeV, for selecting events which have Z boson.

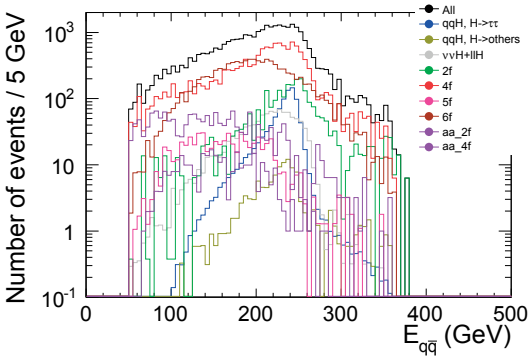

Figure E.0.34: The distribution of energy of jet pair $E_{q\bar{q}}$.

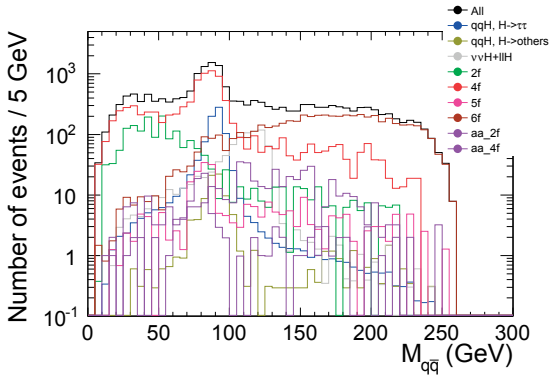

Figure E.0.35: The distribution of mass of jet pair $M_{q\bar{q}}$.

- $M_{\tau^+\tau^-} < 110$ GeV and $\cos\theta_{\tau^+\tau^-} < 0.56$. The tau pair mass cut could suppress the backgrounds distributed around the tail of signal. The angle cut is useful cut thanks to monochromatic signal event topology.

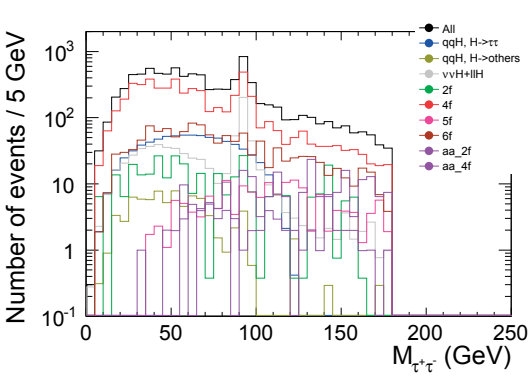

Figure E.0.36: The distribution of mass of tau pair $M_{\tau^+\tau^-}$.

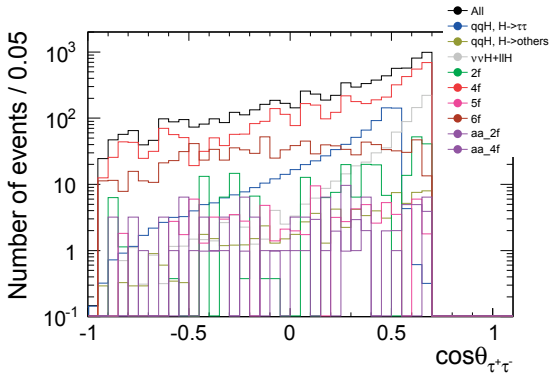

Figure E.0.37: The distribution of angle between two taus $\cos\theta_{\tau^+\tau^-}$.

- $\sum_{\tau^+,\tau^-} \log_{10}|d_0/\sigma(d_0)| > 0.3$, to select the events which have tau leptons.

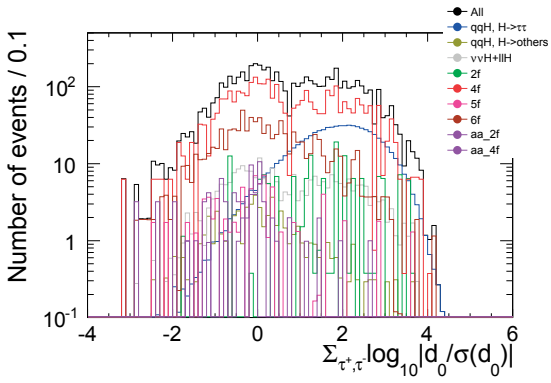

Figure E.0.38: The distribution of d_0 impact parameter $\sum_{\tau^+,\tau^-} \log_{10}|d_0/\sigma(d_0)|$.

- $195 < E_{\text{col}} < 290$ GeV and $110 < M_{\text{col}} < 140$ GeV, as the final discriminant of this analysis to select Higgs events.

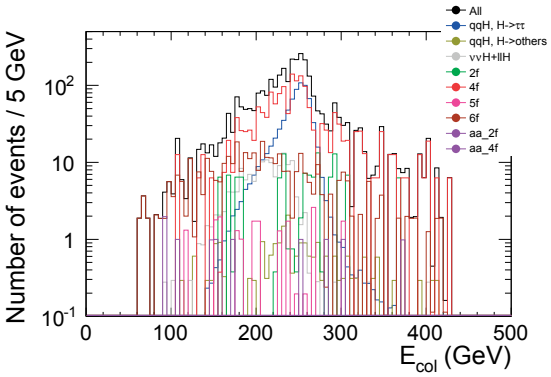

Figure E.0.39: The distribution of energy of tau pair with collinear approximation E_{col}.

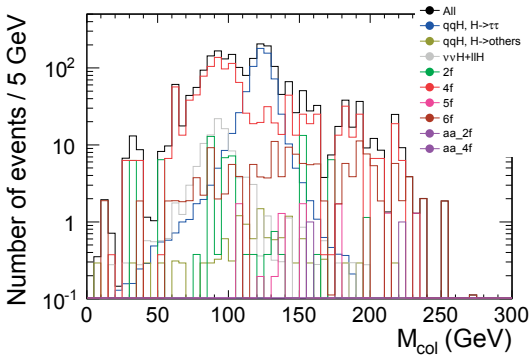

Figure E.0.40: The distribution of mass of tau pair with collinear approximation M_{col}.

The cut table of this analysis is shown in Table E.0.4. After the analysis, 586.4 signals and 175 backgrounds were remained. η was 27.5%. S_{sig} was calculated to be $S_{\mathrm{sig}} = 21.25$. This result corresponds to the precision of cross section times branching ratio ($\sigma \times \mathrm{BR}$) as

$$\frac{\Delta(\sigma \times \mathrm{BR})}{(\sigma \times \mathrm{BR})} = 4.7\%.$$

Table E.0.4: The cut table of 500 GeV $q\bar{q}h$ mode with the integrated luminosity of 500 fb ^{1}. "Pre" means preselection cuts and "Basic" means basic cuts, described in Section 6.1.3.

	$q\bar{q}h$ $h \to \tau^+\tau^-$	$q\bar{q}h$ $h \not\to \tau^+\tau^-$	$\ell^+\ell^-h$ $\nu\bar{\nu}h$	2f	4f	5f	6f	$\gamma\gamma \to$ 2f	$\gamma\gamma \to$ 4f	S_{sig}
No cuts	2131	3.260×10^4	9.397×10^4	1.320×10^7	1.598×10^7	6.876×10^4	5.888×10^5	9.829×10^8	1.041×10^5	0.0669
Pre	1104	409.1	5600	7.696×10^5	5.274×10^5	6705	2.517×10^4	1.868×10^6	1.006×10^4	0.616
Basic	1088	200.1	2688	3.013×10^4	1.012×10^5	3178	1.555×10^4	1.318×10^4	1821	2.65
$\sum_i P_{ti}$	955.5	174.4	2465	1.228×10^4	4.338×10^4	1821	1.209×10^4	3415	734.4	3.44
P_t	914.9	121.1	1059	4001	1.897×10^4	658.5	9608	2903	300.7	4.66
thrust	904.3	120.5	1051	2501	1.360×10^4	648.1	9602	1687	297.7	5.19
$E_{q\bar{q}}$	842.6	94.73	833.2	1683	8633	248.9	5296	439.3	110.0	6.25
$M_{q\bar{q}}$	766.6	77.68	734.4	315.8	5124	154.2	1216	202.4	67.16	8.24
$M_{\tau^+\tau^-}$	756.8	75.60	699.7	256.1	4605	81.84	966.3	72.35	40.50	8.71
$\theta_{\tau^+\tau^-}$	754.0	56.18	259.1	149.4	3020	74.08	879.1	65.94	26.68	10.4
$d_0$sig	703.8	22.59	148.1	116.3	1644	18.59	376.9	0	9.896	12.8
E_{col}	676.2	13.31	101.3	63.81	1153	9.426	157.0	0	1.992	14.5
M_{col}	586.4	4.837	9.029	2.257	128.8	1.678	28.14	0	0	21.3

F Cut-based Analysis for 500 GeV $e^+e^- \to \nu\bar{\nu}h$ Mode

The cut-based analysis was performed to extract maximum $S_{\rm sig}$. Color meanings of all histograms in this section are as following;

- black: summing up all processes,
- blue: signal,
- ocher: $\nu\bar{\nu}h, h \not\to \tau^+\tau^-$,
- solid ash: $q\bar{q}h$ and $\ell^+\ell^- h$,
- green: $2f$,
- dashed red: $4f$ with the final state of $\nu\nu\tau^+\tau^-$,
- solid red: $4f$ with the final state of $\nu\nu\ell^+\ell^-$,
- dashed dark-brown: $4f$ with the final state of $\nu\nu\tau\ell$,
- solid dark-brown: $4f$ with other final states,
- dashed pink: $5f$,
- brown: $6f$,
- dashed purple: $\gamma\gamma \to q\bar{q}$,
- dash-dotted purple: $\gamma\gamma \to \ell^+\ell^-$,
- solid purple: $\gamma\gamma \to 4f$.

The following cuts were applied;

- $E_{\rm vis} < 240$ GeV and $M_{\rm vis} < 155$ GeV, for selecting neutrino-rich events.

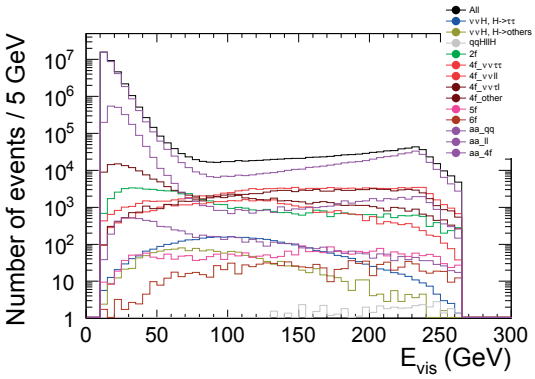

Figure F.0.41: The distribution of visible energy E_{vis}.

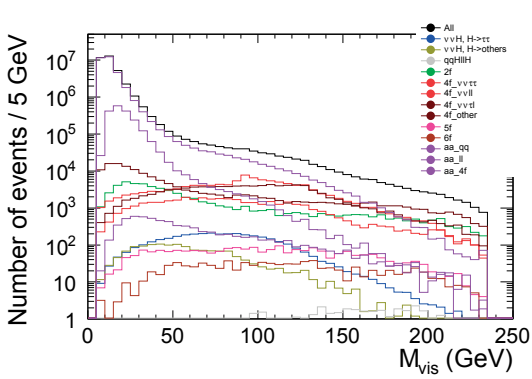

Figure F.0.42: The distribution of visible mass M_{vis}.

- $\sum_i P_{ti} > 30$ GeV and $P_t > 10$ GeV. These cuts can reject the forward events.

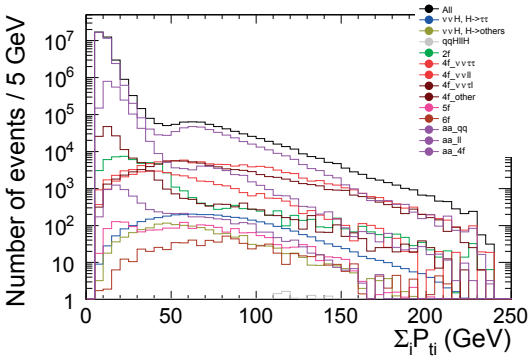

Figure F.0.43: The distribution of transverse momenta $\sum_i P_{ti}$.

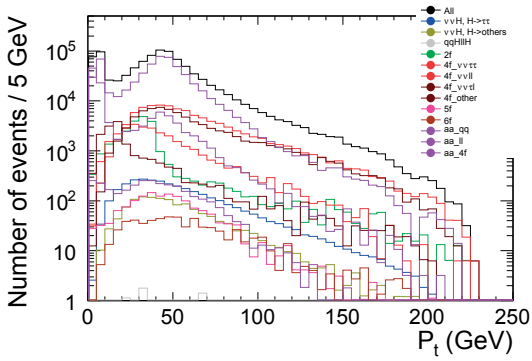

Figure F.0.44: The distribution of transverse momentum P_t.

- Thrust < 0.96 and $|\cos\theta_{\mathrm{thrustaxis}}| < 0.9$. These cuts can also suppress forward events.

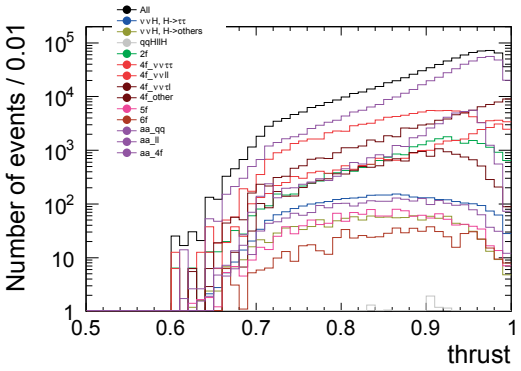

Figure F.0.45: The distribution of thrust.

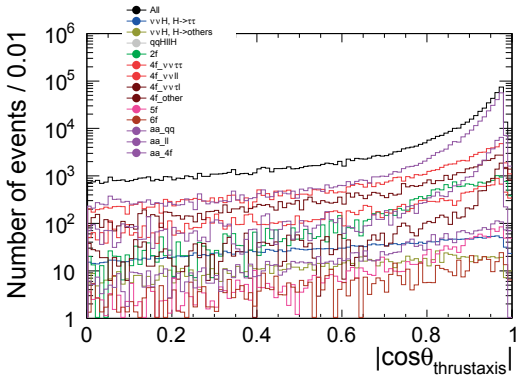

Figure F.0.46: The distribution of thrust axis angle $|\cos\theta_{\text{thrustaxis}}|$.

- $E_{\tau^+\tau^-} > 30$ GeV and $M_{\tau^+\tau^-} < 120$ GeV, for rejecting low mass events or selecting Higgs-like events.

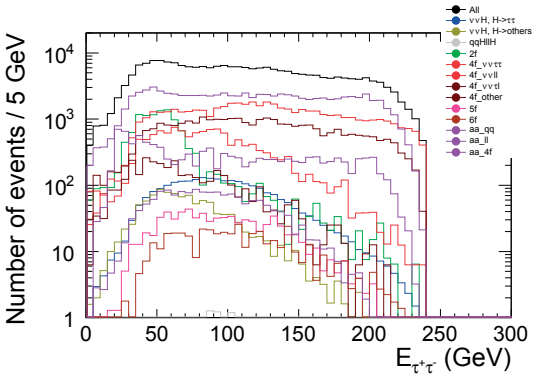

Figure F.0.47: The distribution of tau pair energy $E_{\tau^+\tau^-}$.

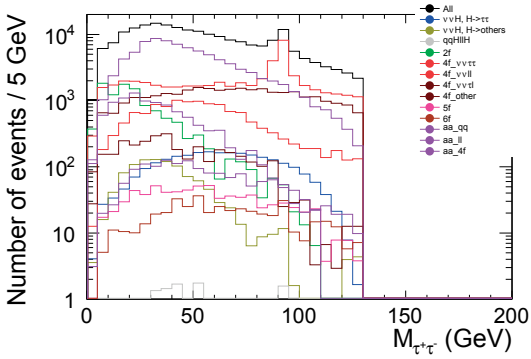

Figure F.0.48: The distribution of tau pair mass $M_{\tau^+\tau^-}$.

- $-0.92 < \cos\theta_{\tau^+\tau^-} < -0.55$ and $\cos\theta_{\text{acop}} < 0.96$. A peak around 0.5 in $\cos\theta_{\tau^+\tau^-}$ is coming from $Zh \to \nu\bar{\nu}\tau^+\tau$, and other broad contribution coming from WW-fusion. $\cos\theta_{\tau^+\tau^-}$ cut helps to suppress some backgrounds. The meaning of $\cos\theta_{\text{acop}}$ is same as did at the preselection.

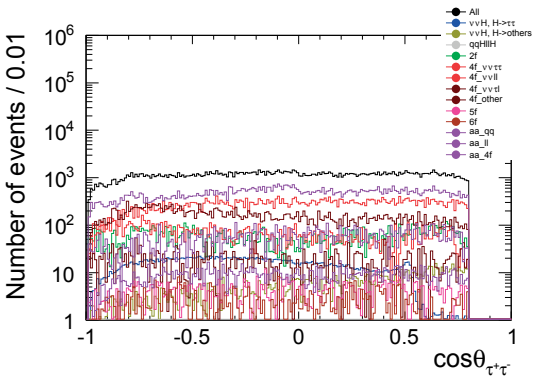

Figure F.0.49: The distribution of angle between two taus $\cos\theta_{\tau^+\tau^-}$.

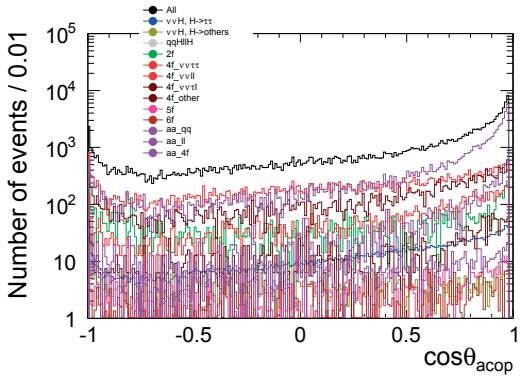

Figure F.0.50: The distribution of acoplanarity angle of taus $\cos\theta_{\text{acop}}$.

- $\log_{10}|\min(d_0/\sigma(d_0))| > 0.4$, as the final discriminant of this analysis to select tau lepton events.

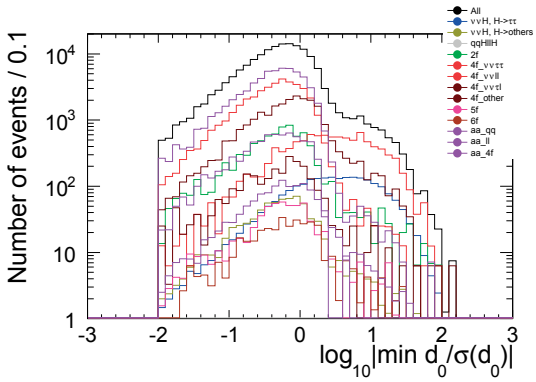

Figure F.0.51: The distribution of d_0 impact parameter $\log_{10}|\min(d_0/\sigma(d_0))|$.

The cut table of this analysis is shown in Table F.0.5. After the analysis, 1252.1 signals and 9195 backgrounds were remained. η was 22.6%. S_{sig} was calculated to be $S_{\text{sig}} = 12.25$. This result corresponds to the precision of cross section times branching ratio ($\sigma \times \text{BR}$) as

$$\frac{\Delta(\sigma \times \text{BR})}{(\sigma \times \text{BR})} = 8.2\%.$$

Table F.0.5: The cut table of 500 GeV $\nu\overline{\nu}h$ mode with the integrated luminosity of 500 fb ^{1}. "Pre", "Pre2", "Pre3" means preselection cuts, preselection 2 cuts, preselection 3 cuts, and "Basic" means basic cuts, respectively, described in Section 6.2.3.

	$\nu\overline{\nu}h$ $h \to \tau^+\tau^-$	$\nu\overline{\nu}h$ $h \not\to \tau^+\tau^-$	$\ell^+\ell^-h$ $q\overline{q}h$	$2f$	$4f$ $\nu\overline{\nu}\tau^+\tau^-$	$4f$ $\nu\overline{\nu}\ell^+\ell^-$	$4f$ $\nu\overline{\nu}\tau\ell$	$4f$ others	$5f$	$6f$	$\gamma\gamma \to q\overline{q}$	$\gamma\gamma \to \ell^+\ell^-$	$\gamma\gamma \to 4f$	$S_{\rm sig}$
No cuts	5534	7.953×10^4	4.363×10^4	1.320×10^7	1.452×10^5	9.450×10^5	6.310×10^5	1.426×10^7	6.895×10^4	5.888×10^5	2.780×10^8	7.111×10^8	1.041×10^5	0.173
Pre	4395	2394	639.4	2.921×10^6	1.070×10^5	6.816×10^5	4.646×10^5	2.336×10^6	1.105×10^4	3262	1.666×10^8	6.412×10^8	3.247×10^4	0.154
Pre2	4343	2239	639.3	2.686×10^6	1.021×10^5	6.617×10^5	4.523×10^5	1.627×10^6	1.059×10^4	3252	2.461×10^7	5.086×10^8	3.005×10^4	0.187
Pre3	3738	2076	520.9	4.310×10^5	7.466×10^4	4.903×10^5	3.199×10^5	5.098×10^5	5630	2719	2.738×10^6	4.865×10^7	1.024×10^4	0.512
Basic	3632	1497	49.48	6.261×10^4	4.163×10^4	1.234×10^5	1.023×10^5	1.514×10^5	2547	992.5	1.972×10^6	3.427×10^7	7455	0.599
$E_{\rm vis}$	3613	1493	40.08	6.120×10^4	4.107×10^4	1.167×10^5	9.723×10^4	1.493×10^5	2366	917.1	1.969×10^6	3.422×10^7	7328	0.597
$M_{\rm vis}$	3529	1473	19.35	5.396×10^4	3.749×10^4	1.085×10^5	8.855×10^4	1.348×10^5	1917	692.4	1.968×10^6	3.421×10^7	6962	0.583
$\sum_i P_{ti}$	3258	1304	19.31	2.421×10^4	3.009×10^4	9.730×10^4	7.998×10^4	1.680×10^4	1474	659.7	1.119×10^5	5.776×10^5	3034	3.35
P_t	3222	1293	19.09	2.300×10^4	2.945×10^4	9.704×10^4	7.981×10^4	1.432×10^4	1413	654.3	4.314×10^4	4.792×10^5	2564	3.66
thrust	2964	1244	18.68	1.895×10^4	1.880×10^4	8.314×10^4	4.929×10^4	1.323×10^4	1342	599.5	3.799×10^4	3.014×10^5	2421	4.07
$\theta_{\rm thrustaxis}$	2505	1077	17.24	1.156×10^4	1.299×10^4	5.189×10^4	3.027×10^4	4024	752.4	440.8	1.280×10^4	8.859×10^4	1603	5.36
$E_{\tau^+\tau^-}$	2466	1022	17.19	1.063×10^4	1.262×10^4	5.122×10^4	2.991×10^4	3241	744.0	437.6	9997	8.613×10^4	1572	5.38
$M_{\tau^+\tau^-}$	2456	1014	17.15	1.063×10^4	1.236×10^4	4.887×10^4	2.840×10^4	3216	732.5	424.6	9997	8.555×10^4	1543	5.42
$\theta_{\tau^+\tau^-}$	2391	724.0	10.07	8320	1.030×10^4	4.104×10^4	2.489×10^4	2636	618.5	386.4	8123	7.146×10^4	1310	5.76
$\theta_{\rm acop}$	2307	712.1	9.864	7856	9865	3.998×10^4	2.391×10^4	2531	596.9	373.0	6992	6.144×10^4	1273	5.81
$d_0$sig	1252	45.77	3.826	475.1	4939	601.1	2242	151.8	38.81	41.12	10.80	553.4	93.40	12.2

References

[1] M. Gell-Mann,
"A schematic model of baryons and mesons",
Phys. Lett. **8** (1964) 214 - 215

[2] H. Fritzsch, M. Gell-Mann, H. Leutwyler,
"Advantages of the color octet gluon picture",
Phys. Lett. B **47** (1973) 365 - 368

[3] David J. Gross, Frank Wilczek,
"Ultraviolet Behavior of Non-Abelian Gauge Theories",
Phys. Rev. Lett. **30** (1973) 1343 - 1346

[4] H. David Politzer,
"Reliable Perturbative Results for Strong Interactions?",
Phys. Rev. Lett. **30** (1973) 1346 - 1349

[5] Sheldon L. Glashow,
"Partial-Symmetries of weak interactions",
Nucl. Phys. **22** (1961) 579 - 588

[6] Steven Weinburg,
"A model of leptons",
Phys. Rev. Lett. **19** (1967) 1264 - 1266

[7] A. Salam in "Elemetary Particle Theory",
S. N., Almqvist, Wiksell, Sand, Stockholm, eds., p 367 (1969)

[8] P. W. Higgs,
"Broken symmetries, massless particles and gauge fields",
Phys. Lett. **12** (1964) 132 - 133

[9] Peter W. Higgs,
"Broken symmetries and the masses of gauge bosons",
Phys. Rev. Lett. **13** (1964) 508 - 509

[10] Peter W. Higgs,
"Spontaneous Symmetry Breakdown without Massless Bosons",
Phys. Rev. **145** (1966) 1156 - 1163

[11] F. Englert, R. Brout,
"Broken symmetry and the mass of gauge vector mesons",
Phys. Rev. Lett. **13** (1964) 321 - 323

[12] G. S. Guralnik, C. R. Hagen, T. W. B. Kibble,
"Global conservation laws and massless particles"
Phys. Rev. Lett. **13** (1964) 585 - 587

[13] Y. Nambu, G. Jona-Lasinio,
"Dynamical Model of Elementary Particles Based on an Analogy with Superconductivity. I",
Phys. Rev. **122** (1961) 345 - 358

[14] Y. Nambu, G. Jona-Lasinio,
"Dynamical Model of Elementary Particles Based on an Analogy with Superconductivity. II",
Phys. Rev. **124** (1961) 246 - 254

[15] `http://home.web.cern.ch/`

[16] ALEPH Collaboration, DELPHI Collaboration, L3 Collaboration, OPAL Collaboration, The LEP Working Group for Higgs Boson Searches,
"Search for the Standard Model Higgs boson at LEP",
Phys. Lett. B **565** (2003) 61 - 75

[17] CDF Collaboration, D0 Collaboration,
"Combination of Tevatron Searches for the Standard Model Higgs Boson in the W^+W^- Decay Mode",
Phys. Rev. Lett. **104** (2010) 061802

[18] The ALEPH, CDF, D0, DELPHI, L3, OPAL, SLD Collaborations, the LEP Electroweak Working Group, the Tevatron Electroweak Working Group, the SLD electroweak heavy flavour groups,
"Precision Electroweak Measurements and Constraints on the Standard Model",
arXiv:0911.2604 [hep-ex] (2009)

[19] The ATLAS Collaboration,
"Observation of a new particle in the search for the Standard Model Higgs boson with the ATLAS detector at the LHC",
Phys. Lett. B **716** (2012) 1 - 29

[20] The CMS Collaboration,
"Observation of a new boson at a mass of 125 GeV with the CMS experiment at the LHC",
Phys. Lett. B **716** (2012) 30 - 61

[21] `http://www.nobelprize.org/nobel_prizes/physics/laureates/2013/`

[22] `http://www.esa.int/Our_Activities/Space_Science/Planck/Planck_reveals_an_almost_perfect_Universe`

[23] Rick S. Gupta, Heidi Rzehak, James D. Wells,
"How well do we need to measure Higgs boson couplings?",
Phys. Rev. D **86**, 095001 (2012)

[24] Ties Behnke *et al.*,
"The International Linear Collider Technical Design Report - Volume 1: Executive Summary",
arXiv:1306.6327 [physics.acc-ph] (2013)

[25] Howard Baer *et al.*,
"The International Linear Collider Technical Design Report - Volume 2: Physics",
arXiv:1306.6352 [hep-ph] (2013)

[26] Chris Adolphsen *et al.*,
"The International Linear Collider Technical Design Report - Volume 3.I: Accelerator R&D in the Technical Design Phase",
arXiv:1306.6353 [physics.acc-ph] (2013)

[27] Chris Adolphsen *et al.*,
"The International Linear Collider Technical Design Report - Volume 3.II: Accelerator Baseline Design",
arXiv:1306.6328 [physics.acc-ph] (2013)

[28] Ties Behnke *et al.*,
"The International Linear Collider Technical Design Report - Volume 4: Detectors",
arXiv:1306.6329 [physics.ins-det] (2013)

[29] D. M. Asner *et al.*,
"ILC Higgs White Paper",
arXiv:1310.0763 [hep-ph] (2013)

[30] Kaustubh Agashe, Roberto Contino, Alex Pomarol,
"The minimal composite Higgs model",
Nucl. Phys. B **719** (2005) 165 - 187

[31] G. C. Branco, P. M. Ferreira, L. Lavoura, M. N. Rebelo, Marc Sher, Joao P. Silva,
"Theory and phenomenology of two-Higgs-doublet models",
Phys. Rept. **516**, 1 (2012)

[32] J. Wess, B. Zumino,
"A lagrangian model invariant under supergauge transformations",
Phys. Lett. B **49**, 52 (1974)

[33] Abdus Salam, J. Strathdee,
"Superfields and Fermi-Bose symmetry",
Phys. Rev. D **11** 1521 (1974)

[34] A. Salam, J. Strathdee,
"Super-symmetry and non-Abelian gauges",
Phys. Lett. B **51**, 353 (1974)

[35] M. Carena, S. Heinemeyer, C. E. M. Wagner, G. Weiglein,
"Suggestions for Improved Benchmark Scenarios for Higgs-Boson Searches at LEP2",
arXiv:hep-ph/9912223 (1999)

[36] Marcela Carena, Howard E. Haber, Heather E. Logan, Stephen Mrenna,
"Distinguishing a minimal supersymmetric standard mdel Higgs boson from the SM Higgs boson at a linear collider",
Phys. Rev. D **65** 055005 (2002)

[37] The ATLAS Collaboration,
"Evidence for the Higgs-boson Yukawa coupling to tau leptons with the ATLAS detector",
JHEP **04** (2015) 117

[38] The CMS Collaboration,
"Evidence for the 125 GeV Higgs boson decaying to a pair of τ leptons", JHEP **05** (2014) 104

[39] The ATLAS and CMS Collaboration,
"Measurements of the Higgs boson production and decay rates and constraints on its couplings from a combined ATLAS and CMS analysis of the LHC pp collision data at $\sqrt{s} = 7$ and 8 TeV",
ATLAS-CONF-2015-044, CMS-PAS-HIG-15-002 (2015)

[40] Markus Klute, Rëmi Lafaye, Tilman Plehn, Michael Rauch, Dirk Zerwas,
"Measuring Higgs couplings at a linear collider",
EPL, **101** (2013) 51001

[41] Marco Battaglia,
"Measuring Higgs Branching Ratios and telling the SM from a MSSM Higgs Boson at the e^+e Linear Collider",
arXiv:hep-ph/9910271 (1999)

[42] Jean-Claude Brient,
"The direct method to measure the Higgs branching ratios at the future e^+e linear collider",
LC Note, LC-PHSM-2002-003 (2002)

[43] Keisuke Fujii *et al.*,
"Physics Case for the International Linear Collider",
arXiv:1506.05992v2 [hep-ex] (2015)

[44] T. Barklow *et al.* [ILC Parameters Joint Working Group],
"ILC Operating Scenarios",
arXiv:1506.07830v1 [hep-ex] (2015)

[45] Hiroaki Aihara,
ISBN:978-4-13-062608-8 (2006)

[46] Yoji Totsuka,
ISBN:978-4000104401 (1992)

[47] M. A. Thomson,
"Particle flow calorimetry and the PandoraPFA algorithm",
Nucl. Instrum. Meth. A **611** (2009) 25 - 40

[48] `http://www.ilcild.org/ild-detector-systems`

[49] S. Agostinelli *et al.*,
"GEANT4 — a simulation toolkit",
Nucl. Instrum. Meth. A **506** (2003) 250 - 303

[50] Y. Giomataris, Ph. Rebourgeard, J. P. Robert, G. Charpak,
"MICROMEGAS: a high-granularity position-sensitive gaseous detector for high particle-flux environments",
Nucl. Instrum. Meth. A **376** (1996) 29 - 35

[51] F. Sauli,
"GEM: A new concept for electron amplification in gas detectors",
Nucl. Instrum. Meth. A **386** (1997) 531 - 534

[52] `http://www.lctpc.org/`

[53] `https://twiki.cern.ch/twiki/bin/view/CALICE/WebHome`

[54] H. Abramowicz *et al*,
"Forward instrumentation for ILC detectors"
JINST **5** (2010) P12002

[55] I. G. Knowles, G. D. Lafferty.
"Hadronization in Z^0 decay",
arXiv:hep-ph/9705217 (1997),
J. Phys. G**23** (1997) 731 - 789

[56] Taikan Suehara, Tomohiko Tanabe
"Status of LCFIPlus",
Talk presented at LCWS12 at Arlington, Texas, USA

[57] S. Heinemeyer, C. Mariotti, G. Passarino, R. Tanaka *et al.*,
"Handbook of LHC Higgs Cross Sections: 3. Higgs Properties",
arXiv:1307.1347 [hep-ph] (2013)

[58] Harumichi Yokoyama's master thesis of the University of Tokyo (2014)

`http://www.icepp.s.u-tokyo.ac.jp/yamashita/archives/yokoyama/master.pdf`

[59] F. Yuasa *et al.*,
"Automatic Computation of Cross Sections in HEP — *Status of GRACE System* —",
Prog. Theor. Phys. Suppl. **138** 18 (2000) (arXiv:hep-ph/0007053)

[60] `http://minami-home.kek.jp/`

[61] S. Kawabata,
"A new Monte Carlo event generator for high energy physics",
Comput. Phys. Commun. **41** (1986) 127 - 153

[62] Daniel Schulte,
"Study of Electromagnetic and Hadronic Background in the Interaction Region of the TESLA Collider",
DESY-TESLA-97-08 (1997)

[63] `http://ilc-edmsdirect.desy.de/ilc-edmsdirect/item.jsp?edmsid=D00000000925325`

[64] M. Skrzypek, S. Jadach,
"Exact and approximate solutions for the electron nonsinglet structure function in QED",
Z. Phys. C **49**, 577 - 584 (1991)

[65] Johann H. Kühn, Zbigniew Wąs,
"TAUOLA — a library of Monte Carlo programs to simulate decays of polarized τ leptons",
Comput. Phys. Commun. **64** (1990) 275 - 299

[66] P. Golonka, B. Kersevan, T. Pierzchała, E. Richter-Wąs, Z. Wąs, M. Worek,
"The tauola-photos-F environment for the TAUOLA and PHOTOS packages, release II",
Comput. Phys. Commun. **174** (2006) 818 - 835

[67] N. Davidson, G. Nanava, T. Przedzinski, E. Richter-Wąs, Z. Wąs,
"Universal interface of `TAUOLA`: Technical and physics documentation",
Comput. Phys. Commun. **183** (2012) 821 - 843

[68] Torbjörn Sjöstrand, Stephen Mrenna, Peter Skands,
"PYTHIA 6.4 physics and manual",
JHEP **05** (2006) 026

[69] Lynn Garren,
"StdHep 5.06.01 Monte Carlo Standardization at FNAL Fortran and C Implementation" (2006),
`http://cepa.fnal.gov/psm/stdhep/`

[70] Wolfgang Kilian, Thorsten Ohl, Jürgen Reuter,
"WHIZARD — simulating multi-particle processes at LHC and ILC",
Eur. Phys. J. C **71** (2011) 1742

[71] `http://www-jlc.kek.jp/jlc/en/ilc-xsec-db`

[72] Pisin Chen, Timothy L. Barklow, Michael E. Peskin,
"Hadron production in $\gamma\gamma$ collisions as a background for e^+e linear colliders",
Phys. Rev. D **49** (1994) 3209 - 3227

[73] P. Mora de Freitas, H. Videau,
"Detector simulation with MOKKA/GEANT4: Present and future",
LC Note, LC-TOOL-2003-010 (2003)

[74] Mikael Berggren,
"SGV 3.0 — a fast detector simulation",
arXiv:1203.0217 [physics.ins-det] (2012)

[75] F. Gaede, T. Behnke, N. Graf, T. Johnson,
"LCIO — A persistency framework for linear collider simulation studies",
arXiv:physics/0306114 [physics.data-an] (2003),
Proceedings of CHEP03

[76] F. Gaede,
"Marlin and LCCD — Software tools for the ILC",
Nucl. Instrum. Meth. A **559** (2006) 177 - 180

[77] Rene Brun, Fons Rademakers,
"ROOT — An Object Oriented Data Analysis Framework",
Proceedings AIHENP'96 Workshop, Lausanne, Sep. 1996,
Nucl. Instrum. Meth. A **389** (1997) 81 - 86,
`http://root.cern.ch/`

[78] P. Speckmayer, A. Höcker, J. Stelzer, H. Voss,
"The Toolkit for Multivariate Data Analysis, TMVA 4",
J. Phys. Conf. Ser. **219** (2010) 032057

[79] A. Hoecker, P. Speckmayer, J. Stelzer, J. Therhaag, E. von Toerne, H. Voss *et al.*,
"TMVA 4 Toolkit for Multivariate Data Analysis with ROOT",
arXiv:physics/0703039 [physics.data-an]

[80] Yoav Freund, Robert E. Schapire,
"A Decision-Theoretic Generalization of On-Line Learning and an Application to Boosting",
J. Comput. Syst. Sci. **55** (1997) 119 - 139

[81] Harris Drucker,
"Improving Regressors using Boosting Techniques",

In D. H. Fisher (Ed.),
proceedings of the fourteenth international conference on machine learning (ICML 1997) (pp. 107115)., Nashville, TN, USA, July 812. Morgan Kaufmann, ISBN 1558604863

[82] Peter J. Huber,
"Robust estimation of a location parameter",
Annals of Mathematical Statistics **35** (1964) 73 - 101

[83] R. K. Ellis, I. Hinchliffe, M. Soldate, J. J. van der Bij,
"HIGGS DECAY TO $\tau^+\tau$ A possible signature of intermediate mass Higgs bosons at high energy hadron colliders",
Nucl. Phys. B **297** (1998) 221 - 243

[84] S. Catani, Yu. L. Dokshitzer, M. Olsson, G. Turnock, B. R. Webber,
"New clustering algorithm for multijet cross sections in e^+e annihilation",
Phys. Lett. B **269** (1991) 432 - 438

[85] S. Catani, Yu. L. Dokshitzer, M. H. Seymour, B. R. Webber,
"Longitudinally-invariant $k_\perp$-clustering algorithms for hadron-hadron collisions",
Nucl. Phys. B **406** (1993) 187 - 224

[86] Stephen D. Ellis, Davison E. Soper,
"Successive combination jet algorithm for hadron collisions",
Phys. Rev. D **48** 3160 (1993)

[87] Matteo Cacciari, Gavin P. Salam, Gregory Soyez,
"FastJet user manual (for version 3.0.1)",
arXiv:1111.6097 [hep-ph] (2011)

[88] Sally Dawson, Andrei Gritsan, Heather Logan, Jianming Qian, Chris Tully, Rick Van Kooten *et al.*,
"Higgs working group report",
arXiv:1310.8361 [hep-ex] (2013)

Acknowledgement

First, I would like to thank my supervisor Prof. Tohru Takahashi (Hiroshima University), for giving me this work and the chance of PhD possible. Second, I would like to thank Dr. Tomohiko Tanabe (The University of Tokyo), Dr. Taikan Suehara (Kyushu University), and Prof. Keisuke Fujii (KEK), who supported most my work. It was impossible to proceed this work without their help. I also would like to thank Dr. Junping Tian (KEK) and Dr. Masakazu Kurata (The University of Tokyo), who helped my work with many discussion.

公表論文

A study of the measurement precision of the Higgs boson decaying into tau pairs at the ILC

Shin-ichi Kawada, Keisuke Fujii, Taikan Suehara, Tohru Takahashi, Tomohiko Tanabe

The European Physical Journal C, **75**:617, pp 1 - 11 (2015)

Eur. Phys. J. C manuscript No.
(will be inserted by the editor)

A study of the measurement precision of the Higgs boson decaying into tau pairs at the ILC

Shin-ichi Kawada[a,1], **Keisuke Fujii**[2], **Taikan Suehara**[3], **Tohru Takahashi**[1], **Tomohiko Tanabe**[4]

[1]Advanced Sciences of Matter (AdSM), Hiroshima University, 1-3-1, Kagamiyama, Higashi-Hiroshima, Hiroshima, 739-8530, Japan
[2]High Energy Accelerator Research Organization (KEK), 1-1, Oho, Tsukuba, Ibaraki, 305-0801, Japan
[3]Graduate School of Science, Kyushu University, 6-10-1, Hakozaki, Higashi-ku, Fukuoka, 812-8581, Japan
[4]International Center for Elementary Particle Physics (ICEPP), The University of Tokyo, 7-3-1, Hongo, Bunkyo-ku, Tokyo, 113-0033, Japan

Received: XXX / Accepted: XXX

Abstract We evaluate the measurement precision of the production cross section times the branching ratio of the Higgs boson decaying into tau lepton pairs at the International Linear Collider (ILC). We analyze various fina states associated with the main production mechanisms of the Higgs boson, the Higgs-strahlung and WW-fusion processes. The statistical precision of the production cross section times the branching ratio is estimated to be 2.6% and 6.9% for the Higgs-strahlung and WW-fusion processes, respectively, with the nominal integrated luminosities assumed in the ILC Technical Design Report; the precision improves to 1.0% and 3.4% with the running scenario including possible luminosity upgrades. The study provides a reference performance of the ILC for future phenomenological analyses.

1 Introduction

After the discovery of the Higgs boson by the ATLAS and the CMS experiments at the LHC [1, 2], the investigation of the properties of the Higgs boson has become an important target of study in particle physics. In the Standard Model (SM), the coupling of the Higgs boson to the matter fermions, *i.e.*, the Yukawa couplings, is proportional to the fermion mass. The Yukawa couplings can deviate from the SM prediction in the presence of new physics beyond the SM. Recent studies indicate that the deviations from the SM could be at the few-percent level if there is new physics at the scale of around 1 TeV [3]. It is therefore desired to measure the Higgs couplings as precisely as possible in order to probe new physics.

In this study, we focus on Higgs boson decays into tau lepton pairs ($h \to \tau^+\tau^-$) at the International Linear Collider (ILC). This decay has been studied by the ATLAS and the CMS experiments, who reported a combined signal yield consistent with the SM expectation, with a combined observed significanc at the level of 5.5σ [4–6]. The purpose of this study is to estimate the projected ILC capabilities of measuring the $h \to \tau^+\tau^-$ decay mode in fina states resulting from the main Higgs boson production mechanisms in e^+e^- collisions. Existing studies on $h \to \tau^+\tau^-$ decays at e^+e^- collisions [7, 8] did not take into account some of the relevant background processes or were based on a Higgs boson mass hypothesis which differs from the observed value, both of which are addressed in this study. We assume the ILC capabilities for the accelerator and the detector as documented in the ILC Technical Design Report (TDR) [9–13] together with its running scenario published recently [14, 15]. The results presented in this paper will be useful for future phenomenological studies.

The contents of this paper are organized as follows. In Section 2, we describe the ILC and the ILD detector concept, and the analysis setup. The event reconstruction and selection at center-of-mass energies of 250 GeV and 500 GeV are discussed in Sections 3 and 4. Section 5 describes the prospects for improving the measurement precision with various ILC running scenarios. We summarize our results in Section 6.

2 Analysis conditions

2.1 International Linear Collider

The ILC is a next-generation electron–positron linear collider. It covers a center-of-mass energy ($\sqrt{s}$) in the range of 250–500 GeV and can be extended to $\sqrt{s} = 1$ TeV. In the ILC design, both the electron and positron beams can be polarized, which allow precise measurements of the properties of the electroweak interaction. The details of the machine

[a]e-mail: s-kawada@huhep.org

Table 1 Typical integrated luminosities L and center-of-mass energies $\sqrt{s}$ of the ILC [9, 14, 15].

Scenario	$\sqrt{s}$ (GeV)	L (fb^{-1})
Nominal	250	250
	500	500
Luminosity upgrade	250	2000
	500	4000

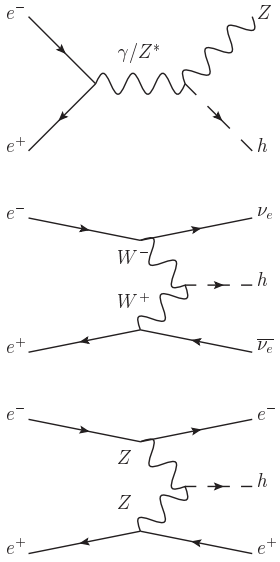

Fig. 1 Diagrams of the main production mechanisms of the Higgs boson in e^+e^- collisions. Top: Higgs-strahlung (Zh) process. Middle: WW-fusion process. Bottom: ZZ-fusion process.

design are summarized in the ILC Technical Design Report (TDR) [9–13].

The ILC aims to explore physics beyond the SM via precise measurements of the Higgs boson and the top quark as well as to search for new particles within its energy reach. The center-of-mass energies and integrated luminosities which are foreseen are summarized in Table 1. The numbers for the nominal running scenario are taken from the ILC TDR [9]. The numbers for scenarios including energy and luminosity upgrades are based on studies in Refs. [14, 15].

2.2 Production and decay of the Higgs boson

Figure 1 shows the diagrams for the main production mechanisms of the Higgs boson in e^+e^- collisions. The cross sections of Higgs boson production calculated by `WHIZARD` [16] with a Higgs mass of 125 GeV are shown in Figure 2, where polarizations of -80% and $+30\%$ for the electron and positron beams are assumed, and initial state radiation is taken into account.

For the calculation of the production cross section and the subsequent decay of the signal processes of $e^+e^- \to f\bar{f}h \to f\bar{f}\tau^+\tau^-$, where f denotes a fermion, we use an event generator based on `GRACE` [17,18]. The effect of beamstrahlung is implemented according to the calculation by `GuineaPig` [19], which simulates e^+e^- beam–beam interactions, with the beam parameters described in the TDR [20]. Initial state radiation is incorporated following the prescription developed by the ILC Event Generator Working Group [13,21]. To handle the spin correlation of tau pairs from the Higgs boson decay, `GRACE` is interfaced with `TAUOLA` [22–25]. The decays of other short-lived particles and the hadronization of quarks and gluons are handled by `PYTHIA` [26].

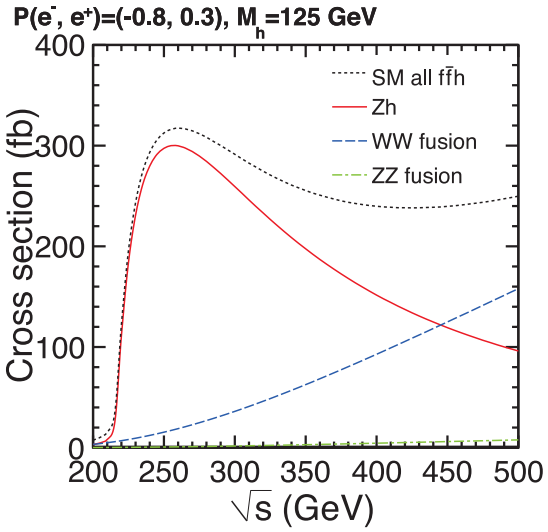

Fig. 2 Cross sections of the Higgs boson production as a function of $\sqrt{s}$ in the electron–positron interaction.

2.3 Background processes

For background processes, we use common Monte-Carlo (MC) samples for SM processes previously prepared for the studies presented in the ILC TDR [13]. The event samples include $e^+e^- \to 2f$, $e^+e^- \to 4f$, $e^+e^- \to 6f$, and $e^+e^- \to f\bar{f}h$. The event generation of these processes is performed with `WHIZARD` [16], in which beamstrahlung, initial state radiation, decay of short-lived particles, and hadronization are taken into account in the same way as described in the previous section for the signal process. The background processes from $\gamma\gamma$ interactions with hadronic fina states, in which photons are produced by beam–beam interactions, are generated on the basis of the cross section model in Ref. [27]. We fin that the interactions between electron or positron beams and beamstrahlung photons, *i.e.*, $e^\pm\gamma \to e^\pm\gamma$, $e^\pm\gamma \to 3f$, and $e^\pm\gamma \to 5f$, have negligible contributions to background.

Table 2 Summary of the performance of the ILD detector model.

Name	Value
Impact parameter resolution	$5 \oplus \frac{10}{p \sin^{3/2}\theta}\,\mu$m
Momentum resolution	$2\times10^{-5} \oplus \frac{1\times10^{-3}}{P_t \sin\theta}$ GeV/c
Jet energy resolution	$\sim \frac{30}{\sqrt{E(\mathrm{GeV})}}$%

2.4 Detector Model

The detector model used in this analysis is the International Large Detector (ILD), which is one of the two detector concepts described in the ILC TDR. It is a general-purpose 4π detector designed for particle fl w analysis[1], aiming at best possible jet energy resolution.

The ILD model consists of layers of sub-detectors surrounding the interaction point. One finds from the innermost to the outer layers, a vertex detector (VTX), a silicon inner tracker (SIT), a time projection chamber (TPC), a silicon envelope tracker (SET), an electromagnetic calorimeter (ECAL), and a hadron calorimeter (HCAL), all of which are put inside a solenoidal magnet providing a magnetic fiel of 3.5 T. The return yoke of the solenoidal magnet has a built-in muon system. The ILD design has not yet been fi nalized. In this analysis, we assume the following configu rations and performance. The VTX consists of three double layers of silicon pixel detectors with radii at 1.6 cm, 3.7 cm and 6 cm. Each silicon pixel layer provides a point resolution of 2.8 μm. The TPC provides up to 224 points per track over a tracking volume with inner and outer radii of 0.33 m and 1.8 m. The SIT and SET are used to improve the track momentum resolution by adding precise position measurements just inside and outside of TPC. The ECAL consists of layers of tungsten absorbers interleaved with silicon layers segmented into 5×5 mm^2 cells, has an inner radius of 1.8 m, and has a total thickness of 20 cm corresponding to 24 radiation length. The HCAL consists of layers of steel absorbers interleaved with scintillator layers segmented into 3×3 cm^2 cells and has an outer radius of 3.4 m corresponding to 6 interaction length. Additional silicon trackers and calorimeters are located in the forward region to assure hermetic coverage down to 5 mrad from the beam line. The key detector performance of the ILD model is summarized in Table 2. Details of the ILD model and the particle fl w algorithm are found in Refs [13, 28].

[1]The particle fl w algorithm aims at achieving the best attainable jet energy resolution by making one-to-one matching of charged particle tracks with calorimetric clusters so as to restrict the use of calorimetric information, which is in general less precise than tracker information, to neutral particles. This requires highly granular calorimeters and a tracking system with high performance pattern recognition for events with high particle multiplicity.

2.5 Detector simulation and event reconstruction

In this study, we assume a Higgs boson mass of 125 GeV, a branching ratio of the Higgs boson decay into tau pairs (BR($h\to\tau^+\tau^-$)) of 6.32% [29], and beam polarizations of -80% and $+30\%$ for the electron and the positron beams, respectively.

We perform a detector simulation with `Mokka` [30], a `Geant4`-based [31] full detector simulator, with the ILD model for all signal and background processes, with the exception of the $e^+e^-\to e^+e^-+2f$ process at $\sqrt{s}=500$ GeV, for which `SGV` fast simulation [32] is used. The event reconstruction and physics analysis are performed within the `MARLIN` software framework [33], in which events are reconstructed using track findin and fittin algorithms, followed by a particle fl w analysis using the `PandoraPFA` package [28].

3 Analysis at the center-of-mass energy of 250 GeV

At $\sqrt{s}=250$ GeV, the Higgs-strahlung ($e^+e^-\to Zh$) process dominates the SM Higgs production, as shown in Figure 2. The WW-fusion and ZZ-fusion cross sections are negligible at this energy. We take into account $e^+e^-\to f\bar{f}h$ (excluding the $h\to\tau^+\tau^-$ signal), $e^+e^-\to 2f$, and $e^+e^-\to 4f$ for the background estimation. The $\gamma\gamma\to$ hadrons background is overlaid onto the MC samples with an average of 0.4 events per bunch crossing [27]. An integrated luminosity of 250 fb^{-1} is assumed for the results in this section.

There are four main signal modes: $e^+e^-\to q\bar{q}h$, $e^+e^-\to e^+e^-h$, $e^+e^-\to\mu^+\mu^-h$, and $e^+e^-\to\nu\bar{\nu}h$. For our $\sqrt{s}=250$ GeV results, we report on the firs three of these modes. We do not quote the results for the $\nu\bar{\nu}h$ mode as we fin that it suffers from background processes with neutrinos in the fina state. We do not analyze the $e^+e^-\to\tau^+\tau^-h$ mode in this study.

3.1 $e^+e^-\to q\bar{q}h$

Reconstruction of isolated tau leptons and the $Z\to q\bar{q}$ decay

For the $q\bar{q}h$ mode, we firs identify the tau leptons using a dedicated algorithm developed for this topology. The algorithm proceeds as follows.

1. The charged particle with the highest energy is chosen as a working tau candidate.
2. The tau candidate is combined with the most energetic particle (charged or neutral) satisfying the following two conditions: the angle θ_i between the particle and the tau candidate satisfie $\cos\theta_i>0.99$; and the combined mass, calculated from the sum of the four momenta of the particle and the tau candidate, does not exceed 2 GeV. The

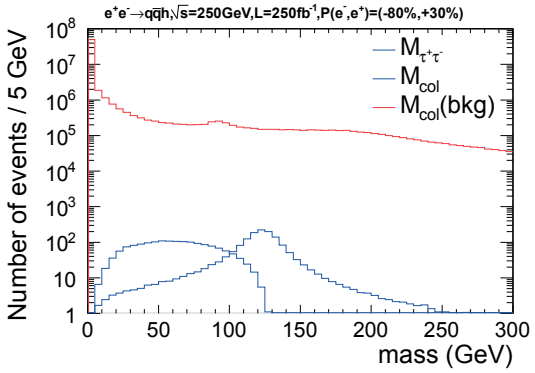

Fig. 3 Distributions of the invariant mass of the reconstructed tau lepton pairs at $\sqrt{s} = 250$ GeV for the $e^+e^- \to q\bar{q}h$ mode. $M_{\tau^+\tau^-}$ and $M_{\rm col}$ stand for the tau pair masses before and after the collinear approximation, respectively, for the signal. $M_{\rm col}$(bkg) is the tau pair mass with the collinear approximation for the background.

four momentum of this particle is then added to that of the tau candidate.

3. Step 2 is repeated until there are no more particles left to combine. The resulting tau candidate is then set aside.
4. The algorithm is repeated from Step 1 until there are no more charged particles left.

A tau candidate is accepted if the number of charged particles with track energy greater than 2 GeV is equal to one or three, the net charge is equal to ± 1, and the total energy is greater than 3 GeV. Furthermore, an isolation requirement is applied as follows. A cone of half-angle θ_c, with $\cos\theta_c = 0.95$, is define around the direction of the tau momentum. The tau candidate is accepted if the energy sum of all particles inside the cone (excluding those forming the tau candidate) does not exceed 10% of the tau candidate energy. We require exactly two fina tau candidates with opposite charges. This results in a selection efficien y of 49.3% for the $q\bar{q}\tau^+\tau^-$ signal events.

After the tau candidates are identified the neutrino energy is recovered by using the collinear approximation [34]. Because tau leptons from a Higgs boson decay are highly boosted, it is reasonable to assume that the tau momentum and the neutrino momentum are nearly parallel. Under this assumption, the energy of the two neutrinos, one from each tau decay, can be solved by requiring that the overall transverse momentum of the event is balanced in two orthogonal directions. The neutrino reconstructed in this way is added to the tau candidate. Figure 3 shows the invariant mass distributions of the tau pairs without ($M_{\tau^+\tau^-}$) and with ($M_{\rm col}$) the collinear approximation for the events containing two tau lepton candidates with opposite charges. With the collinear approximation, a clear peak is visible at 125 GeV for signal events. The $M_{\rm col}$ distribution for background events with the same criteria is also shown.

The Durham jet clustering algorithm [35] is applied to the remaining particles to reconstruct the two jets from the Z boson decay.

Event selection

We perform a pre-selection over the reconstructed events, followed by a multivariate analysis. The pre-selection is designed to reduce background while keeping most of the signal. The events are pre-selected according to the following criteria. The $Z \to q\bar{q}$ candidate and the $h \to \tau^+\tau^-$ candidate are successfully reconstructed. The total number of charged particles is at least 9. The visible energy of the event, $E_{\rm vis}$, lies in the range of 105 GeV $< E_{\rm vis} <$ 255 GeV. The visible mass of the event, $M_{\rm vis}$, is greater than 95 GeV. The sum of the magnitude of the transverse momentum of all visible particles, $P_{t,\rm sum}$, is greater than 40 GeV. The thrust of the event is less than 0.97. The Z candidate dijet has an energy, E_Z, in the range of 60 GeV $< E_Z <$ 175 GeV and has an invariant mass, M_Z, in the range of 35 GeV $< M_Z <$ 160 GeV. The angle between the two jets, θ_{jj}, satisfie $\cos\theta_{jj} < 0.5$. The recoil mass against the Z boson, computed as $M_{\rm recoil} = \sqrt{(\sqrt{s} - E_Z)^2 - |\mathbf{p}_Z|^2}$, is in the range of 65 GeV $< M_{\rm recoil} <$ 185 GeV. The Higgs candidate tau pair before the collinear approximation has an energy, $E_{\tau^+\tau^-}$, less than 140 GeV and an invariant mass, $M_{\tau^+\tau^-}$, in the range of 5 GeV $< M_{\tau^+\tau^-} <$ 125 GeV. The angle between the two tau candidates, $\theta_{\tau^+\tau^-}$, satisfie $\cos\theta_{\tau^+\tau^-} < -0.1$. The tau pair after the collinear approximation has an energy, $E_{\rm col}$, in the range of 30 GeV $< E_{\rm col} <$ 270 GeV and an invariant mass, $M_{\rm col}$, in the range of 15 GeV $< M_{\rm col} <$ 240 GeV.

We use a multivariate analysis using Boosted Decision Trees (BDTs) as implemented in the Toolkit for Multivariate Data Analysis [36] of the ROOT framework [37]. The input variables are

- $E_{\rm vis}$, $P_{t,\rm vis}$, $\cos\theta_{\rm miss}$, where $P_{t,\rm vis}$ is the magnitude of the visible transverse momentum and $\theta_{\rm miss}$ is the angle of the missing momentum with respect to the beam axis;
- M_Z, $\cos\theta_{jj}$, $M_{\rm recoil}$, $\cos\theta_Z$, where θ_Z is the angle of the Z candidate momentum with respect to the beam axis;
- $M_{\tau^+\tau^-}$, $E_{\tau^+\tau^-}$, $\cos\theta_{\tau^+\tau^-}$, $\cos\theta_{\rm acop}$, where $\theta_{\rm acop}$ is the acoplanarity angle between the two tau candidates;
- $\sum_{\tau^+,\tau^-} \log_{10}|d_0/\sigma_{d_0}|$, $\sum_{\tau^+,\tau^-} \log_{10}|z_0/\sigma_{z_0}|$, where d_0/σ_{d_0} and z_0/σ_{z_0} are respectively the transverse and longitudinal impact parameters of the most energetic track in the tau candidate divided by their respective uncertainty estimated from the track fit
- $M_{\rm col}$, $E_{\rm col}$, and $\cos\theta_{\rm col}$, where $\theta_{\rm col}$ is the angle of the Higgs candidate momentum with the collinear approximation measured from the beam axis.

The BDTs are trained using a set of statistically independent signal and background samples. The distribution of the resulting multivariate discriminant is shown in Figure 4. We apply a fina selection on the multivariate discriminant that

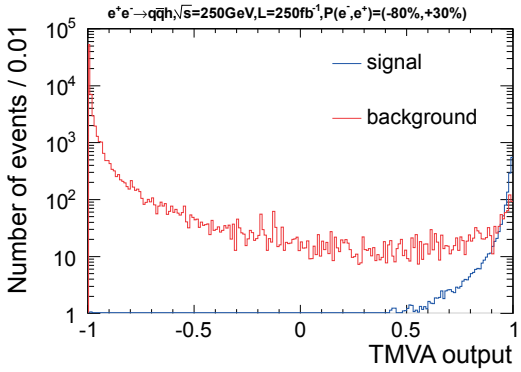

Fig. 4 Distributions of the multivariate discriminant from training Boosted Decision Trees for the $e^+e^- \to q\bar{q}h$ mode, shown for the signal and the total background.

Table 3 Event yields estimated for the $e^+e^- \to q\bar{q}h$ mode at $\sqrt{s} = 250$ GeV, assuming an integrated luminosity of 250 fb^{-1} and beam polarizations of $P(e^-, e^+) = (-0.8, +0.3)$, shown for the signal and the background processes. The signal contribution ($h \to \tau^+\tau^-$) is removed from the $f\bar{f}h$ process. "No cut" is the number of events corresponding to the production cross section times the integrated luminosity. "Preselected" is the number of events after the pre-selection for the multivariate analysis. "Final" is the number of events after the selection on the multivariate discriminant.

	Signal	$f\bar{f}h$	$2f$	$4f$
No cut	3318	7.649×10^4	2.863×10^7	1.736×10^8
Pre-selected	1451	3526	2316	6.940×10^4
Final	1232	22.0	9.3	512.0

maximizes the signal significanc define as $S/\sqrt{S+B}$, where S and B are the number of signal and background events, respectively. The fina selected sample consists of 1232 signal and 543 background events. The estimated event yields before and after the selection are summarized in Table 3. The signal selection efficien y is 37% with a signal signifi cance of 29, which corresponds to a statistical precision of $\Delta(\sigma \times \mathrm{BR})/(\sigma \times \mathrm{BR}) = 3.4\%$.

3.2 $e^+e^- \to e^+e^-h$

Z boson and tau lepton reconstruction

For the e^+e^-h mode, we firs reconstruct the e^+e^- pair that forms a Z boson candidate. A reconstructed particle is identifie as an electron or a positron if its track momentum (P_{trk}) and its associated energy deposits in the ECAL (E_{ECAL}) and HCAL (E_{HCAL}) satisfy the following criteria:

$$E_{\mathrm{ECAL}}/(E_{\mathrm{ECAL}} + E_{\mathrm{HCAL}}) > 0.96,$$
$$(E_{\mathrm{ECAL}} + E_{\mathrm{HCAL}})/P_{\mathrm{trk}} > 0.6.$$

For the particles that are identifie as electrons or positrons, we further require that $|d_0/\sigma_{d_0}| < 6$ and $|z_0/\sigma_{z_0}| < 3$, to reduce the electrons from secondary decays such as the tau lepton decays from the Higgs boson. We also require the track energy to be greater than 10 GeV, which removes the contamination from the $\gamma\gamma \to$ hadron background. The e^+e- pair whose combined mass is closest to the Z boson mass is selected as the Z boson candidate. To improve the mass and energy resolutions, the momenta of nearby neutral particles are added to that of the Z candidate if their angle θ measured from at least one of the $e^\pm$ satisfie $\cos\theta > 0.999$. The fraction of $e^+e^-\tau^+\tau^-$ signal events that survive the Z boson selection is 61%.

We apply a tau findin algorithm to the remaining particles. Compared with the $q\bar{q}h$ mode, the algorithm is simpler due to the absence of hadronic jet activities aside from the tau decays. Starting with the charged particle with the highest energy as a working tau candidate, we defin a cone around its momentum vector with a half-angle of $\theta_c = 1.0$ rad. Particles inside the cone are combined with the tau candidate if the combined mass remains smaller than 2 GeV. The tau candidate is then set aside, and the tau findin is repeated until there are no more charged particles left. The tau candidates are then separated into two categories according to its charge. Within each category, the tau candidate with the highest energy is selected. The chosen $\tau^+\tau^-$ pair forms the Higgs candidate. Finally, the collinear approximation is applied to the selected tau candidates.

Event selection

A pre-selection is applied with the following requirements before proceeding with the multivariate analysis. The $Z \to e^+e^-$ candidate and the $h \to \tau^+\tau^-$ candidate are successfully reconstructed. The total number of charged tracks is 8 or fewer, which ensures statistical independence from the $q\bar{q}h$ mode. The visible energy is in the range of 100 GeV $< E_{\mathrm{vis}} <$ 280 GeV. The visible mass is in the range of 85 GeV $< M_{\mathrm{vis}} <$ 275 GeV. The sum of the magnitude of the transverse momentum of all visible particles, $P_{t,\mathrm{sum}}$, is greater than 35 GeV. The $Z \to e^+e^-$ candidate has an energy in the range of 40 GeV $< E_Z <$ 160 GeV and an invariant mass in the range of 10 GeV $< M_Z <$ 145 GeV. The recoil mass against the Z boson, M_{recoil}, is greater than 50 GeV.

We then apply a multivariate analysis using BDTs using the following input variables:

- M_{vis}, E_{vis}, $\cos\theta_{\mathrm{miss}}$, $\cos\theta_{\mathrm{thrust}}$, where θ_{thrust} is the angle of the thrust axis with respect to the beam axis;
- M_Z, M_{recoil};
- $M_{\tau^+\tau^-}$, $\cos\theta_{\tau^+\tau^-}$, $\cos\theta_{\mathrm{acop}}$;
- $\sum_{\tau^+,\tau^-} \log_{10}|d_0/\sigma_{d_0}|$, and $\sum_{\tau^+,\tau^-} \log_{10}|z_0/\sigma_{z_0}|$.

A fina selection on the multivariate discriminant is applied to maximize the signal significance giving 76.3 signal and 44 background events. The fina signal selection efficien y is 44%. The estimated event yields before and after the selection are summarized in Table 4. The signal significanc is

Table 4 Event yields estimated for the $e^+e^- \to e^+e^-h$ mode at $\sqrt{s} =$ 250 GeV, assuming an integrated luminosity of 250 fb^{-1} and beam polarizations of $P(e^-, e^+) = (-0.8, +0.3)$. Refer to Table 3 for the row definitions

	Signal	$f\bar{f}h$	$2f$	$4f$
No cut	175.1	7.964×10^4	2.863×10^7	1.736×10^8
Pre-selected	109.4	60.2	3.334×10^4	1.169×10^4
Final	76.3	4.2	0	39.9

Table 5 Event yields estimated for the $e^+e^- \to \mu^+\mu^-h$ mode at $\sqrt{s} =$ 250 GeV, assuming an integrated luminosity of 250 fb^{-1} and beam polarizations of $P(e^-, e^+) = (-0.8, +0.3)$. Refer to Table 3 for the row definitions

	Signal	$f\bar{f}h$	$2f$	$4f$
No cut	164.6	7.965×10^4	2.863×10^7	1.736×10^8
Pre-selected	132.8	63.5	4182	8011
Final	101.9	2.2	0	29.0

estimated to be 7.0, corresponding to a statistical precision of $\Delta(\sigma \times \mathrm{BR})/(\sigma \times \mathrm{BR}) = 14.4\%$.

3.3 $e^+e^- \to \mu^+\mu^-h$

Z boson and tau lepton reconstruction

The reconstruction procedure of this mode is similar to that of the e^+e^-h mode, with the electron identificatio replaced by the muon identification The muons are identifie by requiring

$$E_{\mathrm{ECAL}}/(E_{\mathrm{ECAL}} + E_{\mathrm{HCAL}}) < 0.5,$$
$$(E_{\mathrm{ECAL}} + E_{\mathrm{HCAL}})/P_{\mathrm{trk}} < 0.6.$$

We additionally require the identifie muons to satisfy $|d_0/\sigma_{d_0}| <$ 3 and $|z_0/\sigma_{z_0}| < 3$, and to have a track energy greater than 20 GeV. The efficien y for selecting such muon pairs in $\mu^+\mu^-\tau^+\tau^-$ signal events is 92%. The tau lepton reconstruction is the same as in the e^+e^-h mode.

Event selection

The following pre-selection requirements are applied before proceeding with the multivariate analysis. The $Z \to \mu^+\mu^-$ candidate and the $h \to \tau^+\tau^-$ are successfully reconstructed. The total number of charged tracks is 8 or fewer. The visible energy is in the range of 105 GeV $< E_{\mathrm{vis}} <$ 280 GeV. The visible mass is in the range of 85 GeV $< M_{\mathrm{vis}} <$ 275 GeV. The sum of the magnitude of the transverse momentum of all visible particles, $P_{t,\mathrm{sum}}$, is greater than 35 GeV. The $Z \to \mu^+\mu^-$ candidate has an energy in the range of 45 GeV $< E_Z <$ 145 GeV and an invariant mass in the range of 25 GeV $< M_Z <$ 125 GeV. The recoil mass against the Z boson, M_{recoil}, is greater than 75 GeV. The invariant mass of the tau pair system before the collinear approximation, $M_{\tau^+\tau^-}$, is smaller than 170 GeV.

A multivariate analysis with BDTs is applied to the preselected events using the following input variables:

- M_{vis}, E_{vis}, $P_{t,\mathrm{vis}}$;
- M_Z, $\cos\theta_Z$, M_{recoil};
- $M_{\tau^+\tau^-}$, $E_{\tau^+\tau^-}$, $\cos\theta_{\tau^+\tau^-}$, M_{col};
- $\sum_{\tau^+,\tau^-} \log_{10}|d_0/\sigma_{d_0}|$, and $\sum_{\tau^+,\tau^-} \log_{10}|z_0/\sigma_{z_0}|$.

We apply a fina selection on the multivariate discriminant to maximize the signal significance and obtain 101.9 signal and 31 background events. The fina signal selection effi ciency is 62%. The estimated event yields before and after the event selection are shown in Table 5. The signal significance is estimated to be 8.8, corresponding to a statistical precision of $\Delta(\sigma \times \mathrm{BR})/(\sigma \times \mathrm{BR}) = 11.3\%$.

4 Analysis at the center-of-mass energy of 500 GeV

At $\sqrt{s} = 500$ GeV, both the WW-fusion and the Higgs-strahlung processes have sizable contributions to the total signal cross section. We take into account the $e^+e^- \to f\bar{f}h$ (except $h \to \tau^+\tau^-$), $e^+e^- \to 2f$, $e^+e^- \to 4f$, and $e^+e^- \to 6f$ processes as backgrounds. The $\gamma\gamma \to$ hadron background is overlaid onto the signal and background MC samples, assuming an average rate of 1.7 events per bunch crossing [27]. The analysis in this section assumes an integrated luminosity of 500 fb^{-1}. We report our results on the $e^+e^- \to q\bar{q}h$ and $e^+e^- \to \nu\bar{\nu}h$ modes. We do not give results for the $e^+e^- \to e^+e^-h$ and $e^+e^- \to \mu^+\mu^-h$ modes, as they do not contribute significantl to the overall sensitivity due to their small cross sections.

4.1 $e^+e^- \to q\bar{q}h$

Reconstruction of isolated tau leptons and the $Z \to q\bar{q}$ decay

We start with the tau finding following the same procedure described in Section 3.1. We additionally require the tau candidate to have an energy greater than 4 GeV. The energy of the neutrino from tau decays is corrected using the collinear approximation as before, resulting in a clear peak around the Higgs boson mass as can be seen in Figure 5. We fin that 54% of $q\bar{q}\tau^+\tau^-$ signal events survive the requirement of findin exactly one pair of $\tau^+\tau^-$.

The invariant mass of all the particles, except those belonging to the two identifie tau candidates, should be consistent with the Z boson mass; however, a shift to a higher-mass value is observed, due to the presence of non-negligible background particles from $\gamma\gamma \to$ hadron events contaminating signal events. In order to mitigate the effect of these background particles, we use the k_T clustering algorithm [38, 39] implemented in the `FastJet` package [40] with a generalized jet radius of $R = 0.9$. The jets that are formed along

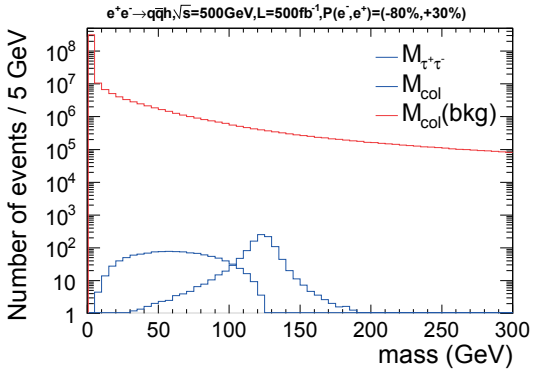

Fig. 5 Distributions of the invariant mass of the reconstructed tau lepton pairs at $\sqrt{s} = 500$ GeV for the $e^+e^- \to q\bar{q}h$ mode. $M_{\tau^+\tau^-}$ and $M_{\rm col}$ stand for the tau pair masses before and after the collinear approximation, respectively, for the signal process. $M_{\rm col}({\rm bkg})$ is the tau pair mass with the collinear approximation for the background processes.

the beam axis are then discarded. The remaining particles are clustered into two jets by using the Durham clustering algorithm to reconstruct the Z boson decay.

Event selection

To facilitate the multivariate analysis, we impose the following pre-selections. The $Z \to q\bar{q}$ candidate and the $h \to \tau^+\tau^-$ candidate are successfully reconstructed. The total number of charged tracks is between 8 and 70. The visible energy of the event is in the range of 140 GeV $< E_{\rm vis} <$ 580 GeV. The visible mass of the event is in the range of 120 GeV $< M_{\rm vis} <$ 575 GeV. The sum of the magnitude of the transverse momentum of all visible particles, $P_{t,{\rm sum}}$, is greater than 70 GeV. The thrust of the event is less than 0.98. The Z candidate dijet has an energy in the range of 50 GeV $< E_Z <$ 380 GeV and has an invariant mass in the range of 5 GeV $< M_Z <$ 350 GeV. The recoil mass against the Z boson is in the range of 40 GeV $< M_{\rm recoil} <$ 430 GeV. The Higgs candidate tau pair before the collinear approximation has an energy, $E_{\tau^+\tau^-}$, less than 270 GeV and an invariant mass, $M_{\tau^+\tau^-}$, less than 180 GeV, and the angle between the two tau candidates satisfie $\cos\theta_{\tau^+\tau^-} < 0.7$. The tau pair after the collinear approximation has an energy in the range of 40 GeV $< E_{\rm col} <$ 430 GeV and an invariant mass, $M_{\rm col}$, which is less than 280 GeV.

A multivariate analysis with BDTs is applied using the following input variables:

- $E_{\rm vis}$, $P_{t,{\rm sum}}$, $P_{\rm vis}$, where $P_{\rm vis}$ is the magnitude of the visible momentum;
- M_Z, E_Z, $\cos\theta_{jj}$, $\cos\theta_Z$, $M_{\rm recoil}$;
- $M_{\tau^+\tau^-}$, $\cos\theta_{\tau^+\tau^-}$, $M_{\rm col}$, $E_{\rm col}$;
- $\sum_{\tau^+,\tau^-} \log_{10}|d_0/\sigma_{d_0}|$, and $\sum_{\tau^+,\tau^-} \log_{10}|z_0/\sigma_{z_0}|$.

After choosing the optimum threshold on the multivariate discriminant to maximize the signal significance we are left with 782 signal and 335 background events. The final signal selection efficiency is 37%. The event yields before and after the selection are summarized in Table 6. The signal significance is found to be 23.4, corresponding to a statistical precision of $\Delta(\sigma \times {\rm BR})/(\sigma \times {\rm BR}) = 4.3\%$.

4.2 $e^+e^- \to \nu\bar{\nu}h$

Tau pair reconstruction

The tau finding algorithm proceeds in the same way as described for the e^+e^-h mode in Section 3.2, except that the half-angle of the cone θ_c around the most energetic track is modified to 0.76 rad. The most energetic positively and negatively charged tau candidates are combined to form a Higgs boson candidate.

Event selection

For the $\nu\bar{\nu}h$ mode, it is necessary to suppress the large background coming from the $e^+e^- \to e^+e^- + 2f$ processes. We apply the following requirements to mitigate this background. A tau lepton pair $\tau^+\tau^-$ is successfully reconstructed. The total number of tracks is less than 10. There is at least one charged track with a transverse momentum greater than 3 GeV and at least one charged track with an energy greater than 5 GeV. The missing momentum angle with respect to the beam axis satisfies $|\cos\theta_{\rm miss}| < 0.98$. The acoplanarity angle between the two tau candidates satisfies $\cos\theta_{\rm acop} <$ 0.98. At this point, 94% of the $e^+e^- \to e^+e^- + 2f$ background is eliminated, while retaining 85% of the signal events.

The following additional pre-selections are applied before the multivariate analysis. The visible energy is in the range of 10 GeV $< E_{\rm vis} <$ 265 GeV. The visible mass is in the range of 5 GeV $< M_{\rm vis} <$ 235 GeV. The missing mass, $M_{\rm miss}$, is greater than 135 GeV. The sum of the magnitude of the transverse momentum of all visible particles, $P_{t,{\rm sum}}$, is greater than 10 GeV. The Higgs candidate tau pair before the collinear approximation has an energy, $E_{\tau^+\tau^-}$, less than 240 GeV and an invariant mass, $M_{\tau^+\tau^-}$, of less than 130 GeV. The angle between the two tau candidates satisfies $\cos\theta_{\tau^+\tau^-} < 0.8$. A requirement on the transverse impact parameter of the tau candidate which gives a smaller value of the two is applied, such that $\min|d_0/\sigma_{d_0}| > 0.01$.

A multivariate analysis with BDTs is applied using the following input variables:

- Number of tracks with energy greater than 5 GeV;
- Number of tracks with transverse momentum greater than 5 GeV;
- $M_{\rm vis}$, $E_{\rm vis}$, $P_{t,{\rm vis}}$, $P_{t,{\rm sum}}$, $\cos\theta_{\rm thrust}$, $\cos\theta_{\rm miss}$;
- $M_{\tau^+\tau^-}$, $E_{\tau^+\tau^-}$, $\cos\theta_{\tau^+\tau^-}$, $\cos\theta_{\rm acop}$;
- $\log_{10}\min|d_0/\sigma_{d_0}|$.

We obtain 1642 signal and 1.11×10^4 background events after optimizing the selection on the multivariate discriminant. The final signal selection efficiency is 30%. The event yields before and after the selection are summarized in Table 7.

Table 6 Event yields estimated for the $e^+e^- \to q\bar{q}h$ mode at $\sqrt{s} = 500$ GeV, assuming an integrated luminosity of 500 fb^{-1} and beam polarizations of $P(e^-, e^+) = (-0.8, +0.3)$. Refer to Table 3 for the row definitions

	Signal	$f\bar{f}h$	$2f$	$4f$	$6f$
No cut	2131	1.266×10^5	1.320×10^7	9.989×10^8	6.929×10^5
Pre-selected	1088	2889	3.013×10^4	1.144×10^5	1.737×10^4
Final	782.1	17.6	1.5	275	41

Table 7 Event yields estimated for the $e^+e^- \to \nu\bar{\nu}h$ mode at $\sqrt{s} = 500$ GeV, assuming an integrated luminosity of 500 fb^{-1} and beam polarizations of $P(e^-, e^+) = (-0.8, +0.3)$. Refer to Table 3 for the row definitions

	Signal	$f\bar{f}h$	$2f$	$4f$	$6f$
No cut	5534	1.232×10^5	1.320×10^7	9.989×10^8	6.929×10^5
Pre-selected	3623	1543	5.957×10^4	1.756×10^7	990.8
Final	1642	65.5	379	1.043×10^4	238

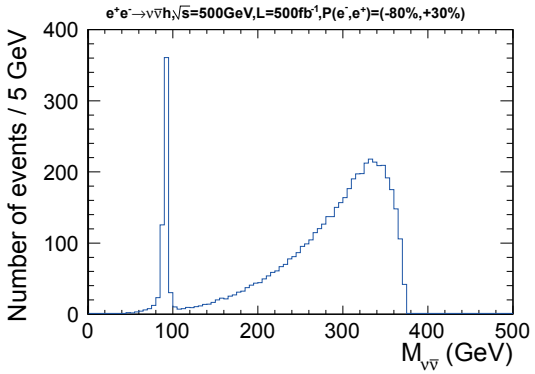

Fig. 6 Distribution of neutrino-pair invariant mass, $M_{\nu\bar{\nu}}$, using event generator information for the $e^+e^- \to \nu\bar{\nu}h$ mode at $\sqrt{s} = 500$ GeV. The effect of detector simulation is not applied.

The signal significanc is 14.5, corresponding to a statistical precision of $\Delta(\sigma \times \mathrm{BR})/(\sigma \times \mathrm{BR}) = 6.9\%$.

In this mode, the $e^+e^- \to Zh \to \nu\bar{\nu}h$ process and the $e^+e^- \to \nu\bar{\nu}h$ process via WW-fusion are expected to be the dominant contributions. The effect of the interference between these two processes is studied using the distribution of the invariant mass of the neutrino pair $M_{\nu\bar{\nu}}$ computed from event generator information as shown in Figure 6. A clear peak around the Z boson mass is visible, with a small contribution underneath it coming from the tail from higher masses, indicating that the interference of the $e^+e^- \to Zh \to \nu\bar{\nu}h$ process and the WW-fusion is small. We hence split the events into two categories based on this generator-level variable, and defin events with $M_{\nu\bar{\nu}} < 120$ GeV as "$e^+e^- \to Zh$" events, and those with $M_{\nu\bar{\nu}} > 120$ GeV as "WW-fusion" events. We fin that the 1642 signal events after the fina selection is composed of 13% $e^+e^- \to Zh$ events and 87% WW-fusion events. The selection effi ciencies for $e^+e^- \to Zh$ and WW-fusion events are 33.5% and 29.2%, respectively.

5 Discussion

5.1 Precision with the ILC running scenarios

We now discuss the prospects of the measurement precision with the ILC running scenarios proposed in Refs. [14, 15] by extrapolating the results presented in the previous sections. Table 8 summarizes the integrated luminosities for various center-of-mass energies and beam polarizations for three different scenarios we consider.

In order to estimate the statistical precision of the cross section times the branching ratio measurements with electron and positron beam polarizations other than $(-0.8, +0.3)$ used in the previous sections, we need to know the corresponding selection efficiencie for the signal and background processes. In the following, we assume the same selection efficiencie obtained in the previous sections for all of these beam polarizations, although in principle the angular distributions of the fina states may depend on the beam polarizations. This assumption is nevertheless justifie as follows. The $e^+e^- \to Zh$ process is mediated by the s-channel Z boson exchange with the vector or the axial vector coupling, which forbids the same-sign helicity states $(\pm 1, \pm 1)$, while giving more or less the same angular distributions for the opposite-sign helicity states $(\mp 1, \pm 1)$. On the other hand, the WW-fusion process proceeds only through the left-right helicity states $(-1, +1)$, since the W boson couples only to the left-handed e^- and the right-handed e^+. For the signal processes, therefore, their angular distributions stay the same for the active (*i.e.* opposite) helicity states, independently of the choice of beam polarizations. The same reasoning applies to the background processes with the s-channel γ/Z exchange or those involving W bosons coupled to the initial state e^+ or e^-. On the other hand, the processes involving t-channel photon exchange or photon-photon interactions do not forbid the same-sign helicity states. However, since the probability of findin an electron and a positron in the same-sign helicity states is the same for both the $(-0.8, +0.3)$

Table 8 Integrated luminosity (in fb^{-1}) for various beam polarizations ($P(e^-), P(e^+)$) at $\sqrt{s} = 250$ GeV and 500 GeV for three running scenarios. "Nominal" is the scenario described in the TDR [9] and used in the main results of this paper. "Initial" and "Full" are the scenarios proposed in Refs. [14, 15].

Scenario	$\sqrt{s}$ (GeV)	$(-80,+30)$	$(+80,-30)$	$(-80,-30)$	$(+80,+30)$	Total
Nominal	250	250	0	0	0	250
	500	500	0	0	0	500
Initial	250	337.5	112.5	25	25	500
	500	200	200	50	50	500
Full	250	1350	450	100	100	2000
	500	1600	1600	400	400	4000

and $(+0.8,-0.3)$ beam polarizations, the efficiencie for such background processes with the same-sign helicity states should also be the same. In our estimation, we do not use the results of the $(\pm 0.8, \pm 0.3)$ beam polarizations, since the signal cross sections are small and the integrated luminosities collected at these beam polarizations are foreseen to be small. Under these assumptions, the selection efficiencie will not depend on the choice of beam polarizations. We can then estimate the projected statistical precision for other scenarios by calculating the number of signal and background events with the production cross sections and the integrated luminosities for individual beam polarizations, according to the running scenarios. The result from this estimation is summarized in Table 9.

5.2 Precision of the $h \to \tau^+\tau^-$ branching ratio

So far, we discussed the precision of the production cross section times the branching ratio, which is the primary information we will obtain from the experiments. Here, we discuss the prospects for measuring the branching ratio itself. At the ILC, the production cross section for the Higgs-strahlung process can be separately measured using the recoil mass technique [10, 13]. The cross section for the WW-fusion process can also be determined by using the branching ratio for the $h \to b\bar{b}$ decay [10]. The obtained cross section values allow us to derive the branching ratio for the $h \to \tau^+\tau^-$ decay.

At $\sqrt{s} = 250$ GeV, the contributions of the WW-fusion and ZZ-fusion processes are negligible. Therefore, we can use the Higgs-strahlung cross section to derive the branching ratio. The Higgs-strahlung cross section σ_{Zh} can be measured to a statistical precision of $\Delta\sigma_{Zh}/\sigma_{Zh} = 2.5\%$ with the nominal TDR running scenario [13]. This improves to a subpercent level with the full running scenario [14].

At $\sqrt{s} = 500$ GeV, both the Higgs-strahlung and the WW-fusion processes contribute to the Higgs boson production, whereas the contribution of the ZZ-fusion process is negligible. For the $e^+e^- \to \nu\bar{\nu}h$ mode, in which both processes are present, it is in principle possible to estimate the contributions from the Higgs-strahlung and the WW-fusion processes separately, as discussed in Section 4.2. However, we do not use this mode here for the estimate. The expected statistical precision of the branching ratio after combining all the modes except the $\nu\bar{\nu}h$ mode is 3.6% for the nominal running scenario. This improves to 1.4% with the full running scenario, where we assume $\Delta\sigma_{Zh}/\sigma_{Zh} = 1.0\%$.

5.3 Systematic uncertainties

The MC statistical uncertainties are found to have negligible impact on the results. The systematic uncertainty in the luminosity measurement has been estimated to be 0.1% or better for the ILC [41] and is not expected to be a significan source of systematic errors. The uncertainties in the selection criteria, such as those caused by the uncertainty in the momentum/energy resolutions and tracking efficiencies are not included in this analysis, since they are beyond the scope of this paper.

6 Summary

We have evaluated the measurement precision of the Higgs boson production cross section times the branching ratio of decay into tau leptons at the ILC. The study is based on the full detector simulation of the ILD model. The dominant Higgs boson production mechanisms were studied at the center-of-mass energies of 250 GeV and 500 GeV, assuming the nominal luminosity scenario presented in the ILC TDR. The analysis results are then scaled up to the running scenarios taking into account realistic running periods and a possible luminosity upgrade.

The results for the various modes and scenarios are summarized in Table 9. In short, the cross section times the branching ratio can be measured with a statistical precision of $\Delta(\sigma \times \mathrm{BR})/(\sigma \times \mathrm{BR}) = 2.6\%$ and 1.0% for the nominal and full running scenarios, respectively. We evaluate the statistical precision of $\mathrm{BR}(h \to \tau^+\tau^-)$ to be 3.6% for the nominal TDR integrated luminosity and 1.4% for the full running scenario, respectively. These results serve to provide primary information on the expected precision of measuring

Table 9 Expected precision of the cross section times the branching ratio $\Delta(\sigma \times \mathrm{BR})/(\sigma \times \mathrm{BR})$, assuming various running scenarios.

Scenario	$\sqrt{s}$ (GeV)	L (fb^{-1})	$q\bar{q}h$	e^+e^-h	$\mu^+\mu^-h$	$\nu\bar{\nu}h$	Combined
Nominal							
$\Delta(\sigma \times \mathrm{BR})/(\sigma \times \mathrm{BR})$	250	250	3.4%	14.4%	11.3%	—	3.2%
	500	500	4.3%	—	—	6.9%	—
	Combined		2.7%	14.4%	11.3%	—	2.6%
	Combined		—	—	—	6.9%	6.9%
Initial							
$\Delta(\sigma \times \mathrm{BR})/(\sigma \times \mathrm{BR})$	250	500	2.5%	10.9%	8.7%	—	2.4%
	500	500	4.9%	—	—	9.6%	—
	Combined		2.3%	10.9%	8.7%	—	2.1%
	Combined		—	—	—	9.6%	9.6%
Full							
$\Delta(\sigma \times \mathrm{BR})/(\sigma \times \mathrm{BR})$	250	2000	1.3%	5.5%	4.3%	—	1.2%
	500	4000	1.7%	—	—	3.4%	—
	combine		1.0%	5.5%	4.3%	—	1.0%
	combine		—	—	—	3.4%	3.4%

Higgs decays to tau leptons at the ILC, which will be useful for future phenomenological studies on physics beyond the SM.

Acknowledgements The authors would like to thank all the members of the ILC Physics Working Group. We thank H. Yokoyama for providing the code for the signal event generator interfacing `GRACE` and `TAUOLA`. This work has been partially supported by JSPS Grants-in-Aid for Science Research No. 22244031 and the JSPS Specially Promoted Research No. 23000002.

References

1. G. Aad *et al.* [ATLAS Collaboration], Phys. Lett. B **716** (2012) 1 - 29
2. S. Chatrchyan *et al.* [CMS Collaboration], Phys. Lett. B **716** (2012) 30 - 61
3. R. S. Gupta, H. Rzehak, J. D. Wells, Phys. Rev. D **86** (2012) 095001
4. G. Aad *et al.* [The ATLAS Collaboration], JHEP **04** (2015) 117
5. S. Chatrchvan *et al.* [The CMS Collaboration], JHEP **05** (2014) 104
6. The ATLAS and CMS Collaborations, ATLAS-CONF-2015-044, CMS-PAS-HIG-15-002 (2015)
7. J.-C. Brient, LC-PHSM-2002-003 (2002)
8. M. Battaglia, arXiv:hep-ph/9910271 (1999)
9. T. Behnke *et al.*, The International Linear Collider Technical Design Report Volume 1: Executive Summary (2013), arXiv:1306.6327 [physics.acc-ph]
10. H. Baer *et al.*, The International Linear Collider Technical Design Report Volume 2: Physics (2013), arXiv:1306.6352 [hep-ph]
11. C. Adolphsen *et al.*, The International Linear Collider Technical Design Report Volume 3.I: Accelerator R&D in the Technical Design Phase (2013), arXiv:1306.6353 [physics.acc-ph]
12. C. Adolphsen *et al.*, The International Linear Collider Technical Design Report Volume 3.II: Accelerator Baseline Design (2013), arXiv:1306.6328 [physics.acc-ph]
13. T. Behnke *et al.*, The International Linear Collider Technical Design Report Volume 4: Detectors (2013), arXiv:1306.6329 [physics.ins-det]
14. K. Fujii *et al.*, arXiv:1506.05992 [hep-ex] (2015)
15. T. Barklow, J. Brau, K. Fujii, J. Gao, J. List, N. Walker, K. Yokoya, arXiv:1506.07830 [hep-ex] (2015)
16. W. Kilian, T. Ohl, J. Reuter, Eur. Phys. J. C **71** (2011) 1742
17. F. Yuasa *et al.*, Prog. Theor. Phys. Suppl. **138** (2000) 18 - 23 (arXiv:hep-ph/0007053)
18. Minami-Tateya web page, `http://www-sc.kek.jp`
19. D. Schulte, DESY-TESLA-97-08 (1997)
20. `http://ilc-edmsdirect.desy.de/ilc-edmsdirect/item.jsp?edmsid=D00000000925325`
21. M. Skrzypek, S. Jadach, Z. Phys. C **49** (1991) 577 - 584
22. H. Yokoyama, Master's thesis at the University of Tokyo (2014)
23. S. Jadach, J. H. Kühn, Z. Wąs, Comput. Phys. Commun. **64** (1991) 275 - 299
24. P. Golonka, B. Kersevan, T. Pierzchała, E. Richter-Wąs, Z. Wąs, M. Worek, Comput. Phys. Commun. **174** (2006) 818 - 835
25. N. Davidson, G. Nanava, T. Przedzinski, E. Richter-Wąs, Z. Wąs, Comput. Phys. Commun. **183** (2012) 821 - 843
26. T. Sjöstrand, S. Mrenna, P. Skands, JHEP **0605** (2006) 026
27. P. Chen, T. L. Barklow, M. E. Peskin, Phys. Rev. D **49** (1994) 3209 - 3227
28. M. A. Thomson, Nucl. Instrum. Meth. A **611** (2009) 25 - 40
29. S. Dittmaier *et al.*, [LHC Higgs Cross Section Working Group], arXiv:1201.3084v1 [hep-ph] (2012)
30. P. Mora de Freitas, H. Videau, LC-TOOL-2003-010 (2003)
31. S. Agostinelli *et al.* [GEANT4 Collaboration], Nucl. Instrum. Meth. A **506** (2003) 250 - 303
32. M. Berggren, arXiv:1203.0217 [physics.ins-det] (2012)
33. F. Gaede, Nucl. Instrum. Meth. A **559** (2006) 177 - 180
34. R. K. Ellis, I. Hinchliffe, M. Soldate, J. J. Van Der Bij, Nucl. Phys. B **297** (1988) 221 - 243
35. S. Catani, Yu. L. Dokshitzer, M. Olsson, G. Turnock, B. R. Webber, Phys. Lett. B **269** (1991) 432 - 438
36. P. Speckmayer, A. Höcker, J. Stelzer, H. Voss, J. Phys. Conf. Ser. **219** (2010) 032057
37. R. Brun, F. Rademakers, Proceedings AIHENP'96 Workshop, Lausanne, Sep. 1996, Nucl. Instrum. Meth. A **389** (1997) 81 - 86, `http://root.cern.ch`
38. S. Catani, Yu. L. Dokshitzer, M. H. Seymour, B. R. Webber, Nucl. Phys. B **406** (1993) 187 - 224
39. S. D. Ellis, D. E. Soper, Phys. Rev. D. **48**, 3160 (1993)
40. M. Cacciari, G. P. Salam, G. Soyez, arXiv:1111.6097v1 [hep-ph] (2011)
41. D. M. Asner *et al.*, arXiv:1310.0763 [hep-ph] (2013)

参考論文

(1) **A conventional positron source for international linear collider**

Tsunehiko Omori, Tohru Takahashi, Sabine Riemann, Wei Gai, Jie Gao, Shin-ichi Kawada, Wanming Liu, Natsuki Okuda, Guoxi Pei, Junji Urakawa, Andriy Ushakov

Nuclear Instruments and Methods in Physics Research Section A, **672**, pp 52 - 56 (2012)

(2) **Feasibility study of the measurement of Higgs pair creation at a photon linear collider**

Shin-ichi Kawada, Nozomi Maeda, Tohru Takahashi, Katsumasa Ikematsu, Keisuke Fujii, Yoshimasa Kurihara, Koji Tsumura, Daisuke Harada, Shinya Kanemura

Physical Review D, **85**, 113009, pp 1 - 7 (2012)

(3) **Development of an intense positron source using a crystal-amorphous hybrid target for linear colliders**

Y. Uesugi, T. Akagi, R. Chehab, O. Dadoun, K. Furukawa, T. Kamitani, S. Kawada, T. Omori, T. Takahashi, K. Umemori, J. Urakawa, M. Satoh, V. Strakhovenko, T. Suwada, A. Variola

Nuclear Instruments and Methods in Physics Research Section B, **319**, pp 17 - 23 (2014)

(4) **Blocking positive ion backflow using a GEM gate: experiment and simulations**

P. Gros, K. Fujii, T. Fusayasu, Y. Kato, S. Kawada, M. Kobayashi, T. Matsuda, O. Nitoh, A. Sugiyama, T. Takahashi, J. Tian, T. Watanabe, R. Yonamine

Journal of Instrumentation, **8**, C11023, pp 1 - 8 (2013)

Proceedings of MPGD2013 (3rd International Conference on Micro Pattern Gaseous Detectors)

(5) **Spatial resolutions of GEM TPC. A novel theoretical formula and its comparison to latest beam test data**
R. Yonamine, K. Fujii, K. Ikematsu, A. Ishikawa, T. Fusayasu, P. Gros, Y. Kato, S. Kawada, M. Kobayashi, T. Matsuda, O. Nitoh, R. D. Settles, A. Sugiyama, T. Takahashi, J. Tian, T. Watanabe
Journal of Instrumentation, **9**, C03002, pp 1 - 15 (2014)
Proceedings of MPGD2013 (3rd International Conference on Micro Pattern Gaseous Detectors)

(6) **Higgs Boson Decays to Tau Pairs at the ILC with ILD Detector**
Shin-ichi Kawada, Keisuke Fujii, Taikan Suehara, Tohru Takahashi, Tomohiko Tanabe
JPS Conference Proceedings, **1**, 013013, pp 1 - 4 (2014)
Proceedings of APPC12 (12th Asia Pacific Physics Conference)

Nuclear Instruments and Methods in Physics Research A 672 (2012) 52–56

Contents lists available at SciVerse ScienceDirect

Nuclear Instruments and Methods in Physics Research A

journal homepage: www.elsevier.com/locate/nima

A conventional positron source for international linear collider

Tsunehiko Omori [a,*], Tohru Takahashi [b], Sabine Riemann [c], Wei Gai [d], Jie Gao [e], Shin-ichi Kawada [b], Wanming Liu [d], Natsuki Okuda [f], Guoxi Pei [e], Junji Urakawa [a], Andriy Ushakov [g]

[a] KEK: High Energy Acceleratoor Research Organization, 1-1 Oho, Tsukuba-shi, Ibaraki 3050801, Japan
[b] Graduate School of Advanced Sciences of Matter, Hiroshima University, 1-3-1 Kagamiyama, Higashi-Hiroshima, 739-8530, Japan
[c] Deutsches Elektronen-Synchrotron, DESY, Platanenallee 6, D-15738 Zeuthen, Germany
[d] Argonne National Laboratory, 9700S. Cass Avenue Argonne, IL 60439, USA
[e] Institute of High Energy Physics, 19B YuquanLu, Shijingshan District, Beijing 100049, China
[f] Department of Physics, Graduate School of Science, The University of Tokyo, 7-3-1 Hongo, Bunkyo-ku, Tokyo 113-0033, Japan
[g] University of Hamburg, Luruper Chaussee 149, D-22607 Hamburg, Germany

ARTICLE INFO

Article history:
Received 29 November 2011
Accepted 10 December 2011
Available online 31 December 2011

Keywords:
ILC
International Linear Collier
Positron source

ABSTRACT

A possible solution to realize a conventional positron source driven by a several-GeV electron beam for the International Linear Collider is proposed. A 300 Hz electron linac is employed to create positrons with stretching pulse length in order to cure target thermal load. ILC requires about 2600 bunches in a train which pulse length is 1 ms. Each pulse of the 300 Hz linac creates about 130 bunches, then 2600 bunches are created in 63 ms. Optimized parameters such as drive beam energy, beam size, and target thickness, are discussed assuming a L-band capture system to maximize the capture efficiency and to mitigate the target thermal load. A slow rotating tungsten disk is employed as positron generation target.

© 2012 Published by Elsevier B.V.

1. Introduction

The International Linear Collier (ILC) [1] is an electron positron linear collider project which employs the superconducting RF acceleration technology in the main linacs. This allows to accelerate high current beams with pulses of 1 ms duration consisting of about 2600 bunches of positrons (electrons), each bunch contains 2×10^{10} positrons (electrons). Such high currents are required to realize the high luminosity, $2\times10^{34}\,\mathrm{cm}^{-2}\,\mathrm{s}^{-1}$ at $E_{CM}=500$ GeV, for the ILC.

However, it is a very challenging issue to design the source for such a high current positron beam. One of biggest risk areas is the thermal load on the positron production target.

The baseline choice of the ILC positron source is the helical undulator scheme. After accelerating the electron beam in the main linac, it passes a 150 m long helical undulator to create a circularly polarized photon beam, and goes to the interaction point [2]. The photon beam hits the production target and generates electron–positron pairs. The positrons are captured, accelerated to 5 GeV, damped, and then accelerated to the collision energy in the main linac. Thus the undulator based positron generation gives interconnection to nearly all sub-systems of the ILC.

Designing and operation of such a large-scale interconnected system is a challenge and strict constraints are given to the positron source and the target heat load by the time structure of the beams. We are constrained to create 2600 bunches in 1 ms, for example. However, it is one advantage of the helical undulator scheme that it provides a polarized positron beam. This advantage will be essential when the LHC will find physics scenarios which can be studied with higher sensitivity if both beams of a electrons–positrons collider are polarized [3].

On the other hand, it could be that the LHC measurements give strong hints to physics scenarios where positron polarization would add only marginal information. Then a conventional unpolarized positron source could be sufficient to reach the physics goal of the ILC. The conventional source suggested in this paper would reduce the thermal load in the positron target by distributing the thermal exposure over the time and using an electron beam with a large cross section. So the risk for the target area can be minimized.

Up to now, only the conventional positron generation scheme has been experienced in real accelerators [4]. With these experiences we are able to control risks in a limited area, that is the target area. The potential risks of the conventional source system are known and could be minimized if used also for the ILC. However, if polarized positrons are required in a later stage of the experiments, the positron source has to be replaced.

The proposed ILC positron source contains risks only in the target area. Therefore, we concentrate to cure these risks in two

* Corresponding author. Tel.: +81 29 8645370; fax: +81 29 8642580.
E-mail address: tsunehiko.omori@kek.jp (T. Omori).

0168-9002/$ - see front matter © 2012 Published by Elsevier B.V.
doi:10.1016/j.nima.2011.12.032

ways: (1) pulse stretching by 300 Hz generation; the proposed scheme creates 2600 bunches in about 60 ms, and (2) optimized drive beam and target thickness parameters.

2. Pulse stretching by 300 Hz generation

The proposed positron source eases the target risk by stretching the pulse length of a bunch-train. The ILC repetition rate, 5 Hz, is rather slow. We have an interval of 200 ms between two pulses. This gives enough time for pulse stretching. A 300 Hz electron linac is employed to create positrons. Since the ILC requires about 2600 bunches in a train of pulse length 1 ms, each pulse of the 300 Hz linac must create about 130 bunches to achieve 2600 bunches in 60 ms.

The positrons created at the source are sent to the damping ring to make the emittance small. In designing the conventional positron source, the authors choose parameters such that they fulfill to requirements of the ILC baseline damping ring. The bunch-to-bunch separation in the damping ring is 6.15 ns, therefore the bunch-to-bunch separation of 6.15 ns in the 300 Hz linac is chosen. In order to avoid instabilities in the damping ring caused by electron clouds, the positron beam has a mini-train structure where about 40 bunches form a mini-train. The gaps of about 100 ns between adjacent mini-trains are the key to prevent instabilities.

The beam structure in the 300 Hz linac is similar. One RF pulse accelerates three mini-trains with inter-mini-train gaps. This package of three mini-trains is named triplet in this article. Each mini-train contains 44 bunches.

In this article, we assume the ILC nominal beam parameters, but with slight modifications. In the original ILC nominal parameter set one RF pulse in the main linac has 2625 bunches. Here, we assume 2640 bunches per pulse.

Fig. 1 shows the schematic view of the 300 Hz scheme. In the ILC, we can employ different bunch structures and pulse structures in the positron source, in the DR, and in the main linac. In the 300 Hz scheme, we employ the triplet mini-train structure in the positron source (Fig. 2) and the mini-train structure in the DR. With 6.15 ns bunch-to-bunch separation and 44 bunches per mini-train, the length of a mini-train is 264 ns. Since a triplet contains three mini-trains, it consists of 132 bunches and we need 20 triplets to form 2640 bunches.

There are gaps of about 100 ns between the mini-trains in a triplet. This triplet structure is required in order to match the bunch timing structure to the fill pattern of DR. Since the triplets are produced by the electron beam they have a repetition rate of 300 Hz. Therefore, we have 3.3 ms between two triplets.

We assume to employ a rotating target made of tungsten alloy. Due to the target rotation, different triplets hit different parts of the target, and the target does not need to survive the impact of 2640 bunches at the same spot. Fig. 3 shows the results of simulations of the instantaneous temperature rise caused by successive triplets impinging on the target; the tangential speeds assumed are (a) 5 m/s, (b) 2 m/s, (c) 1 m/s, and (d) 0.5 m/s. A drive beam energy of 6 GeV and a bunch charge of 3.2 nC are assumed, the spot size of the drive beam at the target is 4 mm (rms) and the target thickness is 14 mm. The choice of the drive beam parameters is discussed later.

As shown in Fig. 3(d), the temperature rise of the target is about 1300 K when we choose 0.5 m/s. Since the melting point of tungsten is 3697 K, a tangential speed of 0.5 m/s is sufficient to tolerate the heat load. The rotation speeds assumed in this article are much less than 100 m/s which is assumed in ILC baseline design. This is one advantage of the 300 Hz scheme. In the simulation, we did not consider cooling of the target. The analysis of the equilibrium temperature for a realistic target design is a future plan.

A flux concentrator is assumed as Adiabatic Matching Device in the capture section. In the 300 Hz scheme, the required pulse

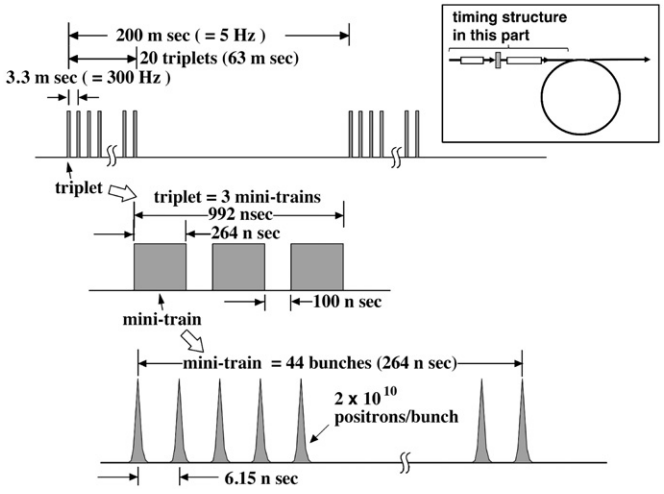

Fig. 2. Timing structure in the positron source and in the booster linac.

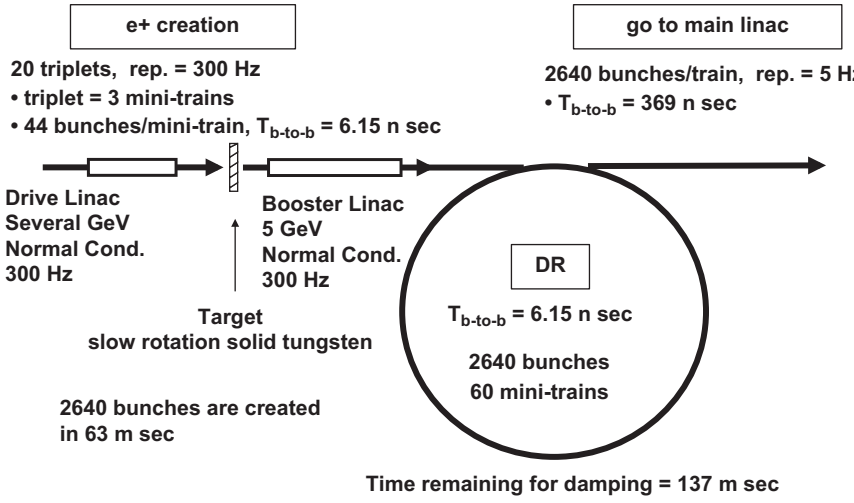

Fig. 1. Schematic view of the 300 Hz scheme.

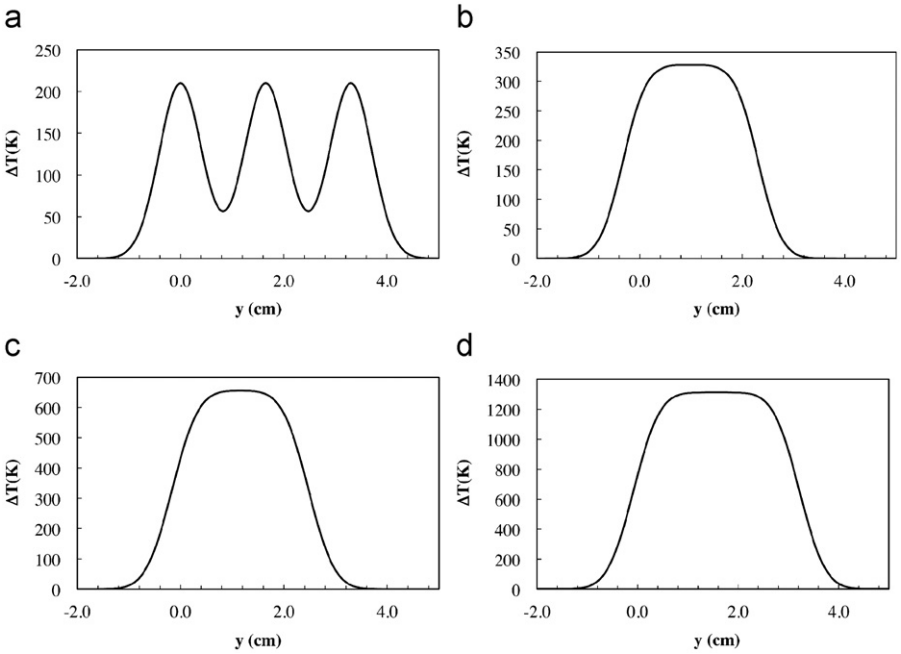

Fig. 3. Instantaneous temperature rise of the target hit by successive triplets. The tangential speeds are (a) 5 m/s after 3 triplets, (b) 2 m/s after 4 triplets, (c) 1 m/s after 8 triplets, and (d) 0.5 m/s after 20 triplets. In the simulation, a drive beam energy of 6 GeV and a bunch charge of 3.2 nC are assumed.

length of the flux concentrator is short; it is about 1 μs. This is the same as that of existing flux concentrators, so the technology is available. Further, the short pulse length allows us to use a high acceleration gradient. The details of the capture system are discussed later.

After the target and capture device, the positron energy is boosted to 5 GeV in a 300 Hz normal conducting linac. A kicker with pulse length of about 1 μs and repetition rate 300 Hz is employed to send the positrons to the DR. One kicker pulse sends a triplet to DR. Also the kicker with 1 μs pulse length can be build with existing technology.

After the damping, bunches are extracted from the DR by a fast kicker, sent to the bunch compressor, and then to the main linac. This part remains the same as in the ILC baseline design with an undulator positron source, the bunch-to-bunch separation is 369 ns after the extraction (Fig. 4).

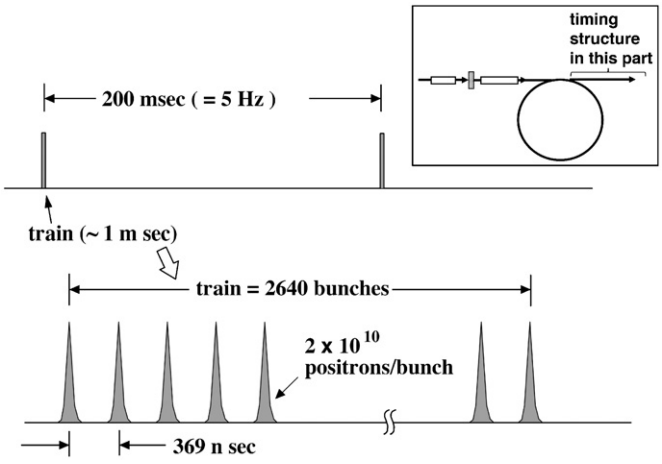

Fig. 4. Time structure after the damping ring.

3. Optimization of drive beam and target parameters.

In order to optimize the parameters for the conventional source, positron yield, peak energy deposit density (PEDD) and total energy deposit in the target were calculated for various combinations of drive beam energy and target thickness. Since PEDD and capture efficiency depend on the transverse size of the drive beam, estimations were also performed for several drive beam sizes. We used Geant 4 for the simulation of positron generation in the target and particle tracking in the subsequent capture section.

Fig. 5 shows the target and the capture section assumed in the analysis. The target material was solid tungsten. An adiabatic matching device (AMD) was assumed as optical matching followed by a L-band pre-accelerator. The longitudinal magnetic field of the AMD is described as

$$Bz(z-z_0) = \frac{B_0}{1+\mu(z-z_0)} + Bsol$$

where $z=0$ is the back end of the tungsten target. The maximum field, B_0, was 7 T and the taper parameter μ was 60.1 m^{-1}. The parameter z_0, a gap between the target and the AMD field, was

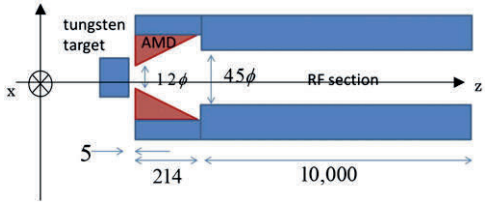

Fig. 5. Layout of the target and positron capture section implemented in the simulation.

assumed 5 mm to accommodate the rotation target. The input aperture of the AMD was 12 mm in diameter. The radial field is calculated according to the prescription described in Ref. [5] as

$$Br(r,z) = -\frac{1}{2}r\frac{\partial B(z)}{\partial z} + \frac{1}{16}r^3\frac{\partial^3 B(z)}{\partial z^3},$$

where r is the transverse distance to the center of the AMD and of the RF section. After the AMD, a RF accelerating field of 1.3 GHz

traveling plane wave with the amplitude of 25 MV/m was applied from $z=219$ to 10219 mm. The aperture of the RF section was assumed to be 45 mm in diameter. In addition to the AMD field, a constant magnetic field $Bsol=0.5$ T was applied in the AMD and RF section, i.e., from $z=5$ to 10129 mm. To calculate the energy deposit in the AMD and RF structures, the outside of the applied fields in lateral direction, indicated by solid areas in Fig. 5, was assumed to be iron while the inner area was air of 10^{-7} Pa to mimic the inside of the accelerator structure.

Simulations were performed by changing the target thickness and the energy of the drive electron beam for beam sizes $\sigma=2.5$ mm and 4.0 mm. Fig. 6(a)–(c) show typical distributions of positrons in the transverse phase space at the input ($z=5$ mm) and output ($z=214$ mm) of the AMD and at the exit of the RF section ($z=10{,}219$ mm). After the tracking simulation, the normalized emittance for Fig. 6(c) is calculated as

$$\gamma\varepsilon_x=\sqrt{\langle x^2\rangle\langle(\gamma x')^2\rangle-\langle x(\gamma x')\rangle}.$$

The twiss parameters for the distribution were obtained:

$$\alpha_x=-\langle x(\gamma x')\rangle/\varepsilon_x$$

$$\beta_x=-\langle x^2\rangle/\varepsilon_x$$

$$\gamma_x=(1+\alpha_x^2)/\beta_x$$

Then, the parameter $A_x\equiv\gamma_x x+2\alpha_x x(\gamma x')+\beta_x(\gamma x')^2$ was calculated for each particle, as well A_y for the y direction. The transverse acceptance of the damping ring was constraint to $A_x+A_y<0.09$ mm. Prior to the estimation of the accepted number of positrons, the phase of the RF field was scanned to maximize the number of positrons.

Fig. 7 shows a typical distribution in the longitudinal phase space at the exit of the RF section after phase optimization. The damping ring acceptance limits the longitudinal phase to ± 25 MeV and ± 3.46 cm of the mean values as indicated in the Fig. 7. Fig. 8 shows a contour plot of the accepted number of positrons within the damping ring acceptance described above for a driving electron beam size of $\sigma=4.0$ mm. Also shown in this figure are the estimated peak temperature rise and the line of the PEDD of 35 J/g, which is the maximum tolerated value estimated by the previous study [5–7]. To determine the PEDD and the peak temperature rise, we assumed the 300 Hz scheme, 132 bunches in a triplet, and a bunch charge of 3.2 nC to accumulate the contributions to both PEDD and peak temperature rise.

Since the time duration which contributes to the target damage is uncertain, we estimated the potential damage due to spatial and temporal concentration of the energy deposit by assuming that all bunches in a triplet in 996 ns contribute equally.

As discussed in the previous section, the time duration of a triplet is shorter than the time of thermal diffusion. But the time between triplets (3.3 ms) is sufficiently long to achieve that each triplet hits a different position of the target rotating with tangential speed of about 5 m/s (see Fig. 3(a)). Even if the tangential speed is lower than 5 m/s, the temperature rise can be acceptable. Fig. 3(d) shows that a tangential speed of 0.5 m/s is acceptable concerning the temperature rise. With 0.5 m/s, the spatial separation of two successive triplets on the target is 1.7 mm, which is smaller than the beam spot size if we employ a beam size larger than 1.7 mm in rms. Since thermal shock waves in the target develop within 1 μs or less, shock waves from successive triplets with 3.3 ms time interval should not be cumulative. If we use the PEDD as a measure of shock wave creation, a tangential speed of 0.5 m/s is acceptable also in this respect.

The actual choice of the tangential speed depends on further optimization and on the engineering design of the target system. Thus we need further studies for the final design of the positron source. The positron yield and the PEDD as function of the size of the driving beam are plotted in Fig. 9. The parameters of the proposed positron source design are summarized in Table 1

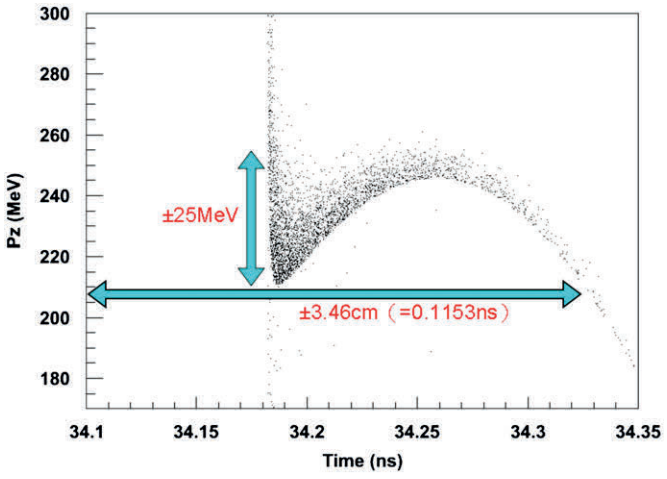

Fig. 7. Longitudinal phase space distribution at the exit of the RF section. The acceptance of the damping ring is indicated by arrows. A drive beam energy of 6 GeV and a beam spot size of 4 mm (rms) on target are assumed.

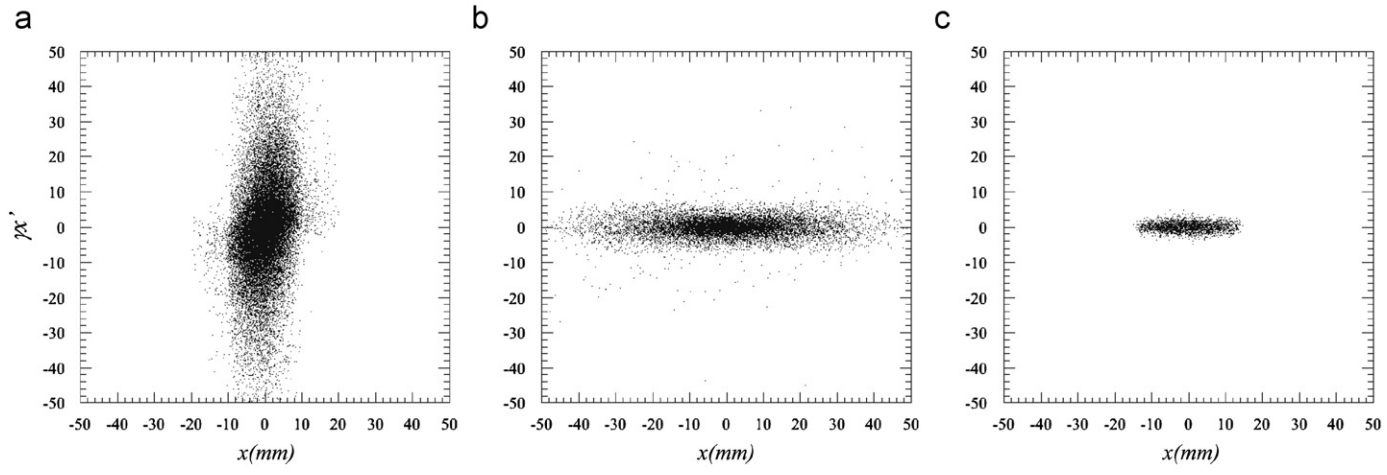

Fig. 6. Transverse phase space distribution of positrons at the entrance of the AMD (a), the exit of the AMD (b) and the exit of the RF section (c). A drive beam energy of 6 GeV and a beam spot size of 4 mm (rms) on the target are assumed.

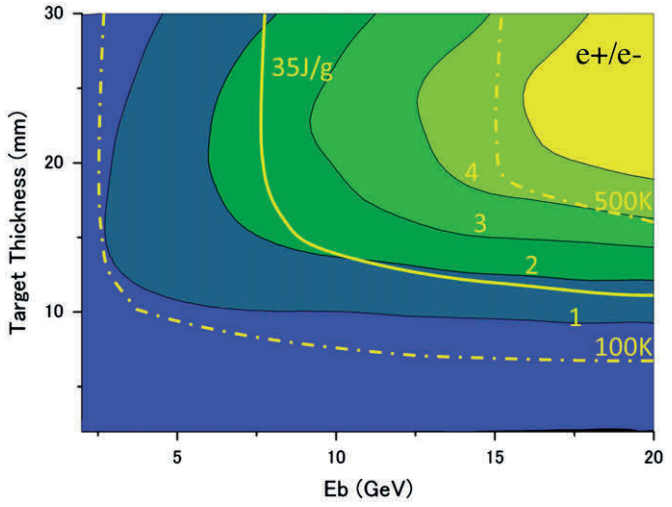

Fig. 8. Number of accepted positrons per incident electron (colored contour) for a driving electron beam size of 4.0 mm. The lines for a PEDD of 35 J/g (solid line) and the peak temperature rise (dot dash line) are also shown. To estimate the PEDD and the peak temperature rise, the contributions of the 132 bunches in a triplet were accumulated; a bunch charge of 3.2 nC was assumed. If we assume that the target will be broken when the PEDD exceeds 35 J/g, the upper-right area above the 35 J/g line is excluded.

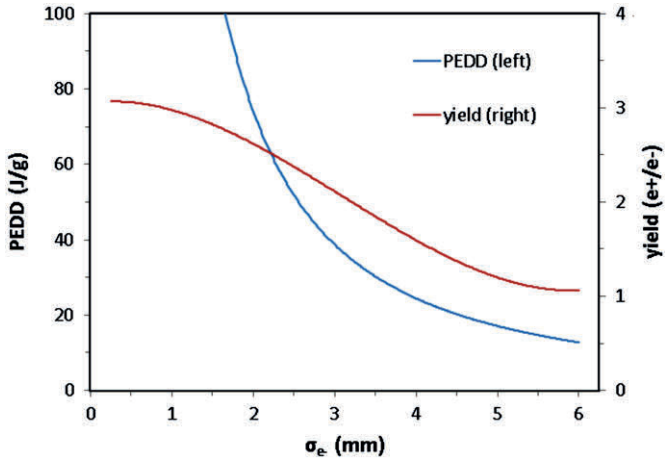

Fig. 9. PEDD (blue, left scale) and positron yield (red, right scale) as a function of drive electron beam size. The drive beam energy is 6 GeV, the bunch charge is 3.2 nC, and the target thickness is 14 mm. We assumed the 300 Hz scheme and 132 bunches in a triplet to accumulate the contributions.

assuming a 6 GeV drive beam of size 4 mm, which hits a tungsten target of 14 mm thickness. The average energies deposited in the target, AMD and RF sections are also shown in the table.

4. Conclusions

A conventional scheme is the only experienced scheme of positron generation in real accelerators. These experiences allow us to contain risk areas of positron generation in a target system. The drawback of the conventional positron source is that it has no capability to provide polarization. We need to replace the positron source when we need a polarized positron beam in future. Although the conventional scheme has such a drawback, it has a significant advantage in the viewpoint of a risk control, which is vitally important in designing a very large system such as ILC. The conventional positron source proposed in this paper largely reduces the risk in target system by pulse stretching, generating about 2600 bunches of positrons by the 300 Hz drive electron beam with optimized beam and target parameters. It cures target thermal issues and enables us to employ a conventional positron generation scheme in the ILC. With respect to the risk control, the conventional scheme could be a suitable solution at the first stage of the ILC project.

Table 1
Parameters and results using a drive electron beam of 6 GeV with beam size 4.0 mm, hitting a target of 14 mm thickness.

Parameters for target and captures		Parameters for the 300 Hz scheme	
Drive beam energy	6 GeV	#Drive e-/bunch	2×10^{10}
Beam size	4.0 mm (rms)	#Bunches/triplet	132 (in 996 ns)
Target material	Tungsten	#Bunches/train	2640 (in 63 ms)
Target thickness	14 mm	Repetition of the trains	5 Hz
Max. AMD field	7 T	Results numbers in () are for the 300 Hz scheme	
Taper parameter	60.1/mm	$e+$yield	$1.6/e^-$
AMD length	214 mm	PEDD in the target	1.04 GeV/cm^3/e^- (22.7 J/g)
Const. field	0.5 T	Energy deposit in the target	823 MeV/e^- (35 kW)
Max. RF field	25 MV/m	Energy deposit in the AMD	780 MeV/e$^-$ (33 kW)
RF frequency	1.3 GHz	Energy deposit in the RF section	470 MeV/e^- (20 kW)

Acknowledgments

We would like to appreciate Dr. M. Kuriki of Hirosima university for his valuable suggestions. We also would like to appreciate Dr. K. Yokoya of KEK, his critical comments were always useful to improve our ideas. Our heartfelt appreciation goes to Dr. L. Rinolfi of CERN and Dr. T. Kamitani of KEK for fruitful discussions. Dr. S. Guiducci of INFN/Frascati gave us constructive comments on the relation between the damping ring design and positron source. We would like to appreciate Dr. J. Rochford of CCLRC/RAL and Dr. I. Bailey of Cockcroft Institute for their help to evaluate target heat issues. We would like to thank valuable discussion with Dr. R. Chehab of University Lyon-1 and Dr. A. Variola of LAL. A part of this research received support of Global COE Program "the Physical Sciences Frontier", MEXT, Japan.

References

[1] ILC-Report-2007-001(2007); ⟨http://www.linearcollider.org/about/Publications/Reference-Design-Report⟩.
[2] V. Bharadwaj, et al., in: Proceedings of 2005 Particle Accelerator Conference, Knoxville, Tennessee, pp. 3230.
[3] G. Moortgat-Pick, et al., Physics Reports 460 (2008) 131–243.
[4] E. Reuter and J. Hodgson, PAC1991 Proceedings pp. 1996–9998, SLAC-PUB-5370.
[5] T. Kamitani and L. Rinolfi, CLIC-NOTE-465 CERN-OPEN-2001-025.
[6] S. Ecklund, SLAC-CN 128 (1981).
[7] NLC Collaboration, SLAC-R-571, 2001.

Feasibility study of the measurement of Higgs pair creation at a photon linear collider

Shin-ichi Kawada,[1,*] Nozomi Maeda,[1] Tohru Takahashi,[1] Katsumasa Ikematsu,[2] Keisuke Fujii,[3] Yoshimasa Kurihara,[3] Koji Tsumura,[4] Daisuke Harada,[5] and Shinya Kanemura[6]

[1]*Graduate School of Advanced Sciences of Matter, Hiroshima University, 1-3-1, Kagamiyama, Higashi-Hiroshima, 739-8530, Japan*
[2]*Department für Physik, Universität Siegen, D-57068, Siegen, Germany*
[3]*High Energy Accelerator Research Organization (KEK), 1-1, Oho, Tsukuba, Ibaraki, 305-0801, Japan*
[4]*Department of Physics, Graduate School of Science, Nagoya University, Furo-cho, Chikusa-ku, Nagoya, 464-8602, Japan*
[5]*Centre for High Energy Physics, Indian Institute of Science, Bangalore, 560012, India*
[6]*Department of Physics, University of Toyama, 3190 Gofuku, Toyama, 930-8555, Japan*

(Received 7 May 2012; published 21 June 2012)

We studied the feasibility of the measurement of Higgs pair creation at a photon linear collider. From the sensitivity to the anomalous self-coupling of the Higgs boson, the optimum $\gamma\gamma$ collision energy was found to be around 270 GeV for a Higgs mass of 120 GeV$/c^2$. We found that large backgrounds such as $\gamma\gamma \to W^+W^-$, ZZ, and $b\bar{b}b\bar{b}$ can be suppressed if correct assignment of tracks to parent partons is achieved and Higgs pair events can be observed with a statistical significance of $\sim 5\sigma$ by operating the photon linear collider for 5 years.

DOI: 10.1103/PhysRevD.85.113009 PACS numbers: 14.80.Bn, 13.90.+i, 14.70.Bh

I. INTRODUCTION

One of the most important events expected in particle physics in the near future is unquestionably the discovery of the Higgs boson. The data from the ATLAS and the CMS experiments at the LHC and the DZero and the CDF experiments at the Tevatron hint at the existence of a light standard-model-like Higgs boson in the mass range of 115–130 GeV$/c^2$ [1–3]. If it is indeed the case, the discovery is expected to be declared within a year or so by the LHC experiments.

In the standard model, the Higgs boson is responsible for giving masses to both gauge bosons and matter fermions, via the gauge and Yukawa interactions, respectively, upon the spontaneous breaking of the electroweak symmetry. However, unlike the gauge interaction, the mechanism of the spontaneous symmetry breaking and the Yukawa interaction has been left untested. As a matter of fact, a Higgs doublet with its wine bottle potential, and its Yukawa coupling to each matter fermion in the standard model are mere assumptions other than being the minimal mechanism to generate the masses of gauge bosons and fermions. In other words, we know essentially nothing, but something must be condensed in the vacuum to give the masses of gauge bosons and fermions. It is well known that the standard model cannot describe everything in the Universe. An example is the existence of the dark matter which occupies about one fourth of the energy density in the Universe. The nonexistence of antimatter is another example. Since the gauge sector of the standard model is well tested, it would be natural to expect that some hints of physics beyond the standard model could be obtained via precise measurements of the Higgs boson properties.

The LHC experiments are likely to discover the standard-model-like Higgs boson. However, their precision is most likely not enough to reveal details of the discovered particle(s) due to high background environments of proton-proton collisions. Thus, precise measurements of the Higgs boson properties by an electron-positron collider and its possible options are crucial to uncover its detailed properties which might go beyond the standard model. The International Linear Collider (ILC) has potential to study the properties of the Higgs boson(s) such as coupling strengths to gauge bosons and matter fermions including the top quark with high precision, thereby opening up a window to physics beyond the standard model [4].

In addition to the e^+e^- collisions, high energy photon-photon collisions are possible at the ILC by converting the electron beam to a photon beam by the inverse Compton scattering [5]. Physics and technical aspects of a photon linear collider (PLC) as an option of the e^+e^- linear collider are described, for instance, in Ref. [6]. A schematic of the PLC is shown in Fig. 1. The Higgs boson

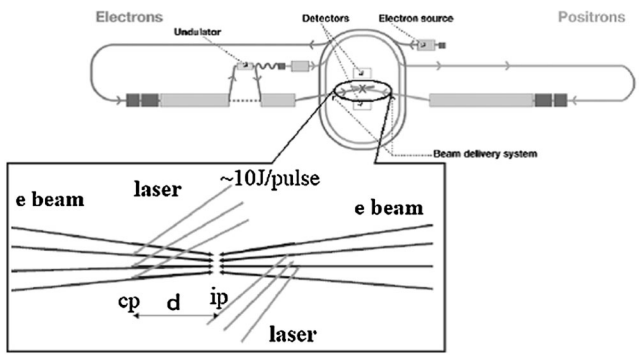

FIG. 1. A schematic of the PLC. The positron beam of the ILC is replaced with an electron beam.

*s-kawada@huhep.org

 © 2012 American Physical Society

properties such as its two-photon decay width and CP properties can be studied in high energy photon-photon interaction, and thus the PLC plays complementary role to the e^+e^- linear collider. It should also be emphasized that the Higgs boson can be singly produced in the s-channel process so that the required electron beam energy is significantly lower than that for the e^+e^- linear collider.

One of the most important observables to be measured in the Higgs sector is its self-coupling, since it directly relates to the dynamics of the Higgs potential, i.e. the mechanism of the spontaneous symmetry breaking. For example, a nonstandard large deviation in the self-coupling can be direct evidence for strong first-order phase transition of the electroweak symmetry in the early Universe [7]. Figures 2(a) and 2(b) show diagrams of processes which involve the self-coupling in $\gamma\gamma$ and e^+e^- interactions. Recently, a prospect for studying the self-coupling at the ILC was reported. According to the study, the self-coupling is expected to be measured with precision of 57% with an integrated luminosity of 2 ab^{-1} at $\sqrt{s} = 500$ GeV [8].

Measurements of the self-coupling at the PLC were discussed by several authors [9–11]. It has been pointed out that contributions of the self-coupling to the cross-section of Figs. 2(a) and 2(b) are different, and measurements in e^+e^- and $\gamma\gamma$ interactions are complementary from a physics point of view. In addition, as a Higgs boson pair is directly produced in the $\gamma\gamma$ interaction, required beam energy is lower, 190 GeV as described later, than that for the e^+e^- interaction. This nature is important when considering energy update scenarios of the ILC.

In Ref. [9], an order-of-magnitude estimation for background processes was presented. However, the cross-section for the W boson pair production is 10^6 orders of magnitude higher than that for the Higgs boson pair production. The backgrounds from $b\bar{b}b\bar{b}$, $b\bar{b}c\bar{c}$, and ZZ production processes are also large and have the same final state as with the Higgs pairs for a low mass Higgs boson, which predominantly decays into $b\bar{b}$. Given the situation, people had been skeptical about the feasibility of the detection of the Higgs pair process at the PLC.

In this work, we studied, for the first time, the Higgs boson pair creation at the PLC extensively with a parameter set of the PLC based on an e^+e^- linear collider optimized for the light Higgs boson of 120 GeV/c^2 and the same detector simulation framework as used for the ILC

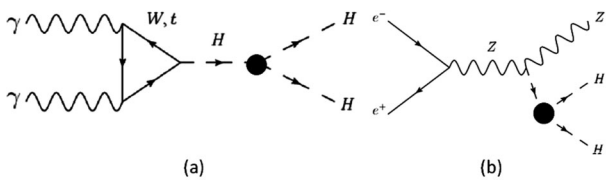

FIG. 2. Diagrams including the Higgs self-coupling, (a) for $\gamma\gamma \to HH$ and (b) for $e^+e^- \to ZHH$. Higgs boson self-coupling occurs at solid circles.

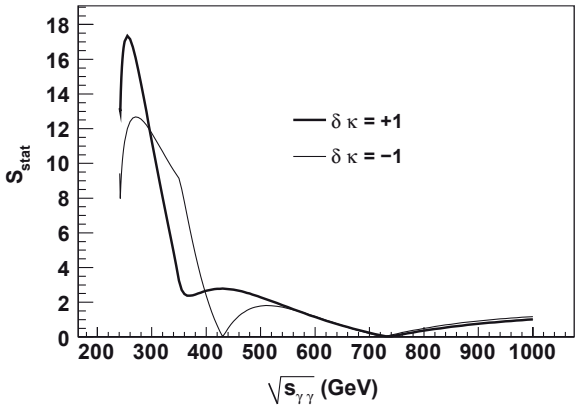

FIG. 3. Statistical sensitivity ($S_{\rm stat}$) as a function of $\gamma\gamma$ collision energy. Bold and thin lines show the $\delta\kappa = +1$ and $\delta\kappa = -1$ cases, respectively.

physics analysis. We report details of the analysis, issues, and prospects for the measurement of the Higgs boson pairs at the PLC.

II. BEAM PARAMETERS

In order to choose parameters for the PLC, we calculated the statistical sensitivity $S_{\rm stat}$ defined as

$$S_{\rm stat} = \frac{|N(\delta\kappa) - N_{\rm SM}|}{\sqrt{N_{\rm obs}}} = \frac{L|\eta\sigma(\delta\kappa) - \eta\sigma_{\rm SM}|}{\sqrt{L(\eta\sigma(\delta\kappa) + \eta_{\rm BG}\sigma_{\rm BG})}}, \quad (1)$$

where $\delta\kappa$ is the deviation of the self-coupling constant from the standard model (SM). The constant of Higgs self-coupling λ can be expressed as $\lambda = \lambda^{\rm SM}(1 + \delta\kappa)$, where $\lambda^{\rm SM}$ is the Higgs self-coupling constant in the standard model. $N(\delta\kappa)$ and $N_{\rm SM}$ are the expected number of events as a function of $\delta\kappa$ and that expected from the standard model. $\sigma(\delta\kappa)$ and $\sigma_{\rm SM}$ are the cross section of the Higgs boson production as a function of $\delta\kappa$ and that of the standard model, while L, η, $\eta_{\rm BG}$, and $\sigma_{\rm BG}$ are the integrated luminosity, the detection efficiency for the signal, the detection efficiency for backgrounds, and the cross section of background processes, respectively. For $\eta = 1$ and $\eta_{\rm BG} = 0$, $S_{\rm stat}$ is written as

TABLE I. The parameters of electron and laser beams based on TESLA optimistic parameters. The polarization of the electron beam was assumed to be 100%.

Parameter	Unit	
Electron beam energy	E_e [GeV]	190
Number of electrons/bunch	$N \times 10^{10}$	2
Longitudinal beam size	σ_z [mm]	0.35
Transverse emittance	$\gamma\varepsilon_{x/y}$ [10^{-6} m · rad]	2.5/0.03
β function @ IP	$\beta_{x/y}$ [mm]	1.5/0.3
Transverse beam size	$\sigma_{x/y}$ [nm]	100/5.7
Laser wavelength	λ_L [nm]	1054
Laser pulse energy	[J]	10
$x = 4\omega E_e/m_e^2$		3.42

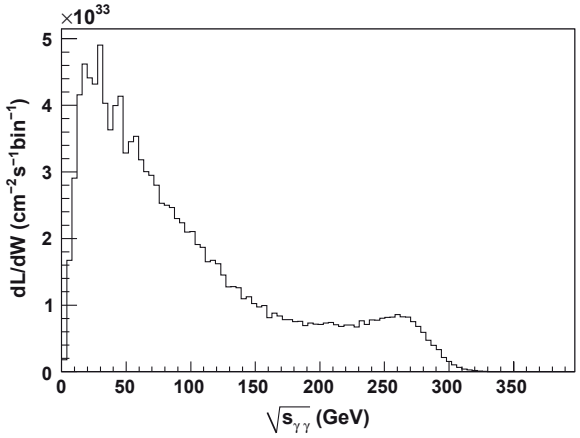

FIG. 4. Luminosity distribution generated by CAIN. Input parameters are shown in Table I.

$$S_{\rm stat} = \sqrt{L}\frac{|\sigma(\delta\kappa) - \sigma_{\rm SM}|}{\sqrt{\sigma(\delta\kappa)}}. \quad (2)$$

Figure 3 plots $S_{\rm stat}$ as a function of the center of mass energy of the $\gamma\gamma$ collision (denoted $\sqrt{s_{\gamma\gamma}}$ hereafter) for the Higgs boson mass of 120 GeV/c^2 with the $\gamma\gamma$ integrated luminosity of 1000 fb^{-1}. The cross section of the signal was calculated according to the formula described in Ref. [10] for the case of $\delta\kappa = +1$ and $\delta\kappa = -1$ as indicated in Fig. 3. From this result, we found the optimum energy to be $\sqrt{s_{\gamma\gamma}} \approx 270$ GeV.

The parameters for the electron and the laser beams are summarized in Table I. It was designed to maximize $\gamma\gamma$ luminosity at $\sqrt{s_{\gamma\gamma}} \approx 270$ GeV based on the TESLA optimistic parameters [12]. The wavelength of the laser was chosen to be 1054 nm, which is a typical wavelength for solid state lasers. The electron beam energy was chosen to maximize $\gamma\gamma$ luminosity around 270 GeV, while keeping the electron beam emittance and the β functions at the interaction point the same as the TESLA parameters. The luminosity distribution was simulated by CAIN [13], as shown in Fig. 4. The $\gamma\gamma$ luminosity in the high energy region ($\sqrt{s_{\gamma\gamma}} > 0.8\sqrt{s_{\gamma\gamma}^{\rm max}}$) was calculated to be 1.2×10^{34} cm^{-2} s^{-1}.

III. SIGNAL AND BACKGROUNDS

Figure 5 shows the cross sections for various processes of $\gamma\gamma$ and e^+e^- collisions as a function of the center of mass energy. The figure indicates that the $\gamma\gamma \to WW$ and $\gamma\gamma \to ZZ$ processes will be the main backgrounds at $\sqrt{s_{\gamma\gamma}} = 270$ GeV because the total cross sections are about 90 pb and 60 fb, respectively, far exceeding that of $\gamma\gamma \to HH$, which was calculated to be 0.19 fb. It should be noted that $\sqrt{s_{\gamma\gamma}} = 270$ GeV is below the threshold of the $\gamma\gamma \to t\bar{t}$ process so that it is not necessary to be considered as a background source.

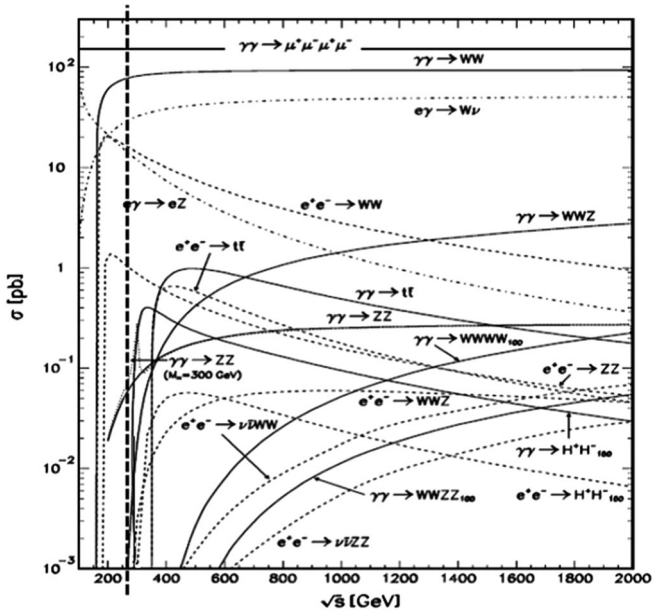

FIG. 5. The cross sections of various standard model processes as a function of collision energy. Solid lines show the $\gamma\gamma$ collision case. The vertical dashed line shows the optimum energy, 270 GeV.

Table II shows the branching ratios of the standard model Higgs boson with a mass of 120 GeV/c^2 [14]. Since the main decay mode of the 120 GeV/c^2 Higgs boson is $H \to b\bar{b}$, we concentrated on the case where both Higgs bosons decay into $b\bar{b}$ in this analysis. This implies that the $\gamma\gamma \to b\bar{b}b\bar{b}$ process must also be considered as a possible background process.

The numbers of events expected for the signal and the backgrounds were calculated from the $\gamma\gamma$ cross sections by convoluting them with the luminosity distribution, as

$$N_{\rm events} = \int \sigma(W_{\gamma\gamma})\frac{dL}{dW_{\gamma\gamma}}dW_{\gamma\gamma}. \quad (3)$$

We used the formula in Refs. [10,11] for the calculation of $\gamma\gamma \to HH$, HELAS [15] for $\gamma\gamma \to WW$, $\gamma\gamma \to ZZ$ code

TABLE II. Branching ratios of the standard model Higgs boson with a mass of 120 GeV/c^2.

Decay mode	Branching ratio
$H \to b\bar{b}$	0.68
$H \to WW^*$	0.13
$H \to gg$	0.071
$H \to \tau\tau$	0.069
$H \to c\bar{c}$	0.030
$H \to ZZ^*$	0.015
$H \to \gamma\gamma$	0.0022
$H \to \gamma Z$	0.0011
$H \to s\bar{s}$	0.000 51
$H \to \mu\mu$	0.000 24

[16,17] with HELAS for $\gamma\gamma \to ZZ$, and GRACE [18] for $\gamma\gamma \to b\bar{b}b\bar{b}$. The numerical integration and subsequent event generation were performed by BASES/SPRING [19]. With this calculation, we expect 16 events/yr for $\gamma\gamma \to HH$, 1.462×10^7 events/yr for $\gamma\gamma \to WW$, and 1.187×10^4 events/yr for $\gamma\gamma \to ZZ$. For $\gamma\gamma \to b\bar{b}b\bar{b}$, 5.194×10^4 events/year is estimated for events with $b\bar{b}$ mass greater than 15 GeV/c^2.

IV. SIMULATION AND ANALYSIS

JLC study framework [20,21] was used as our simulation framework in this study. PYTHIA 6.4 [22] was used for parton shower evolution and subsequent hadronization. For the detector simulation, a fast simulator, QUICKSIM [21], was used instead of a full detector simulation in order to process the huge background samples.

QUICKSIM is, however, fairly detailed and realistic: it smears track parameters with their correlations, vertex detector hits according to given resolution and multiple scattering. It simulates calorimeter signals to individual cells in order to properly take into account their possible overlapping. The calorimeter signals are then clustered and matched to charged tracks, if any, to form particle-flow-like objects to archive the best attainable jet energy resolution (see Ref. [23] for more details).

The detector parameters are summarized in Table III. In the simulation, we assumed a dead cone of a half angle of 7.6° in the forward/backward region of the detector to house the laser optics, the beam pipes, and the masking system [24].

We generated 5×10^4 Monte Carlo events for $\gamma\gamma \to HH$, 7.5×10^7 for $\gamma\gamma \to WW$, 1×10^6 for $\gamma\gamma \to ZZ$, and 1×10^6 for $\gamma\gamma \to b\bar{b}b\bar{b}$, respectively, which are statistically sufficient to assess the feasibility of $\gamma\gamma \to HH$ measurement against the large number of background events.

A. Event selection

First, we applied the forced 4-jet clustering to each event in which the clustering algorithm was applied to each event by changing the clustering parameter until the event is categorized as a 4-jet event. We used the JADE clustering [25] as the clustering algorithm.

Using four-momenta of reconstructed jets, χ_i^2 s ($i = H, W, Z, b\bar{b}$) were calculated for possible jet combinations as

$$\chi_i^2 = \min\left[\frac{(M_1 - M_i)^2}{\sigma_{2ji}^2} + \frac{(M_2 - M_i)^2}{\sigma_{2ji}^2}\right], \quad (4)$$

where M_1 and M_2 are invariant masses of two jets. M_i ($i = H, W, Z, b\bar{b}$) are the masses of the Higgs boson, the W boson, the Z boson, and the invariant mass of $b\bar{b}$ (10 GeV/c^2), respectively. σ_{2ji} ($i = H, W, Z, b\bar{b}$) are their corresponding mass resolutions, and are chosen to be $\sigma_{2jH} = 8$ GeV and $\sigma_{2jW} = \sigma_{2jZ} = \sigma_{2jb\bar{b}} = 6$ GeV, respectively. The "min[]" stands for the operation to choose the minimum out of all the jet combinations.

In order to discriminate b quarks, we used the "nsig" method for the b tagging in this study. Figure 6 illustrates the concept of the "nsig" method. For each track in a reconstructed jet, $N_{\mathrm{sig}} = L/\sigma_L$ was calculated, where L is the distance of closest approach to the interaction point of the track in the plane perpendicular to the beam and σ_L is its resolution. Then $N_{\mathrm{offv}}(a)$, the number of tracks which have $N_{\mathrm{sig}} > a$, is calculated for each jet as a function of a.

Before optimizing event selection criteria, we applied the preselection to reduce the number of background events to a level applicable to the neural network analysis. The criteria for the preselection are

(i) $N_{\mathrm{jet}}(N_{\mathrm{offv}}(3.0) \geq 1) \geq 3$,
(ii) $N_{\mathrm{jet}}(N_{\mathrm{offv}}(3.0) \geq 2) \geq 2$,
(iii) $\beta_{2j} > 0.05$,
(iv) $|\cos\theta_{2j}| < 0.99$,

where $N_{\mathrm{jet}}(N_{\mathrm{offv}}(b) \geq c)$ is the number of jets for which $N_{\mathrm{offv}}(b)$ is greater than or equal to c. β_{2j} is the speed of reconstructed 2-jet which has the least χ_i^2, and θ_{2j} is the angle of reconstructed 2-jet system with respect to the beam axis.

After the preselection, we applied the neural network analysis to optimize the selection criteria. It is a three-layer network with a single output. JETNET [26] was used to train the neural network system which employed the back propagation for the weight optimization.

TABLE III. The detector parameters. p, p_T and E are measured in units GeV. The angle θ is measured from the beam axis.

Detector	Resolution
Vertex detector	$\sigma_b = 7.0 \oplus (20.0/p\sin^{3/2}\theta)$ μm
Drift chamber	$\sigma_{p_T}/p_T = 1.1 \times 10^{-4} p_T \oplus 0.1\%$
ECAL	$\sigma_E/E = 15\%/\sqrt{E} \oplus 1\%$
HCAL	$\sigma_E/E = 40\%/\sqrt{E} \oplus 2\%$

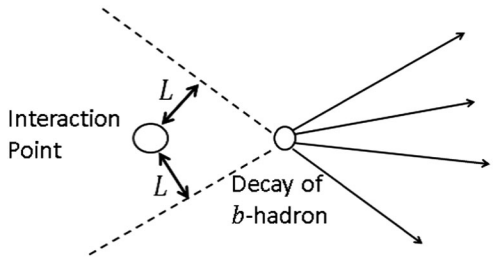

FIG. 6. The concept of "nsig" method. A b hadron is generated at the "interaction point" and decayed at the circle indicated as the "decay of the b hadron." Arrows represent particle tracks. Dotted lines are some of the extrapolated particle tracks towards the interaction point.

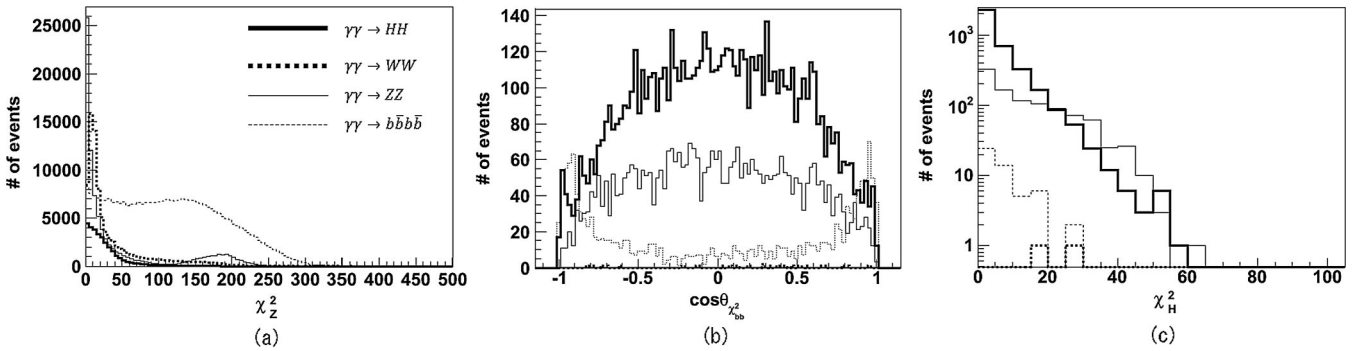

FIG. 7. Typical distributions of neural network input variables: (a) χ^2_Z after the preselection, (b) $\cos\theta_{\chi^2_{b\bar{b}}}$ after the W filter, and (c) χ^2_H after the $b\bar{b}$ filter. Bold solid, bold dotted, thin solid, and thin dotted histograms show the $\gamma\gamma \to HH$ (signal), $\gamma\gamma \to WW$, $\gamma\gamma \to ZZ$, and $\gamma\gamma \to b\bar{b}b\bar{b}$ events, respectively.

For $\gamma\gamma \to WW$ events, inputs to the neural network are χ^2_H, χ^2_Z, the visible energy, $N_{\rm jet}(N_{\rm offv}(3.5) \geq 1)$, $N_{\rm jet}(N_{\rm offv}(3.5) \geq 2)$, the longitudinal momentum, the transverse momentum, the number of tracks, and $Y_{\rm cut}$ of jet clustering. 29 958 signal events and 83 777 background events were used for neural network training with the number of intermediate layers of 18. Figure 7(a) shows the typical distribution of χ^2_Z.

Neural network inputs for $\gamma\gamma \to b\bar{b}b\bar{b}$ analysis are χ^2_H, $\chi^2_{b\bar{b}}$, $\cos\theta_{\chi^2_H}$, $\cos\theta_{\chi^2_{b\bar{b}}}$, the visible energy, the number of tracks, $Y_{\rm cut}$ of jet clustering, thrust (p. 284 of [30]), sphericity (p. 281 of [30]), Y value and (p. 282 of [30]), $\cos\theta_j$, and the largest $|\cos\theta_j|$ of the event, where $\theta_{\chi^2_H(\chi^2_{b\bar{b}})}$ and θ_j are the angle of $H(b\bar{b})$ system and of each jet, with respect to the beam axis. Figure 7(b) shows the distribution of $\cos\theta_{\chi^2_{b\bar{b}}}$ after the W filter. 7756 and 1409 events for the signal and background, respectively, were used with the number of intermediate layers of 34.

For the $\gamma\gamma \to ZZ$ events, we used χ^2_H, χ^2_W, χ^2_Z, the visible energy, the number of tracks, the longitudinal momentum, the energies of the 2-jet systems, $N_{\rm jet}(N_{\rm offv}(3.5) \geq 1)$, and $N_{\rm jet}(N_{\rm offv}(3.5) \geq 2)$ as neural network inputs with 4536 signal and 1189 background events for the training with 20 intermediate layers. Figure 7(c) shows the typical distribution of χ^2_H.

The neural network was trained to maximize statistical significance Σ defined as

$$\Sigma \equiv \frac{N_{\rm signal}}{\sqrt{N_{\rm signal} + N_{\rm BG}}}, \tag{5}$$

where $N_{\rm signal}$ and $N_{\rm BG}$ are the numbers of remaining signal and background events, respectively. To reduce possible systematic effects from the training of the neural network analysis, the performance of the neural network was evaluated by applying the results of the training (weight files) to events generated separately from the training samples. In order to reduce the effect of the statistics of the event samples, we prepared the same number of events for the test sample for each training sample. Table IV shows the summary of event selection with JADE clustering. From Table IV, the statistical significance with the JADE clustering $\Sigma_{\rm JADE}$ was calculated to be

$$\Sigma_{\rm JADE} = 0.922^{+0.045}_{-0.067}\sigma. \tag{6}$$

B. Event selection with an ideal clustering

The result in the previous section indicated that it is necessary to improve the performance of event selection. In order to evaluate the effect of the jet clustering, we

TABLE IV. Cut statistics with JADE clustering. The numbers in the table are the expected numbers of surviving events expected in 5 years. The error on each number is from statistics of the Monte Carlo study.

	$\gamma\gamma \to HH$	$\gamma\gamma \to WW$	$\gamma\gamma \to ZZ$	$\gamma\gamma \to b\bar{b}b\bar{b}$
Expected events	80	7.31×10^7	59 350	259 700
Preselection	47.72 ± 0.28	$81\,312 \pm 282$	5172 ± 18	$80\,002 \pm 144$
Applying W filter	12.27 ± 0.14	24.4 ± 4.9	231.6 ± 3.7	378.1 ± 9.9
Applying $b\bar{b}$ filter	5.867 ± 0.097	$1.95^{+2.6}_{-0.61}$	59.3 ± 1.9	13.2 ± 1.9
Applying Z filter	3.766 ± 0.078	$0^{+1.8}_{-0}$	5.40 ± 0.57	7.5 ± 1.4

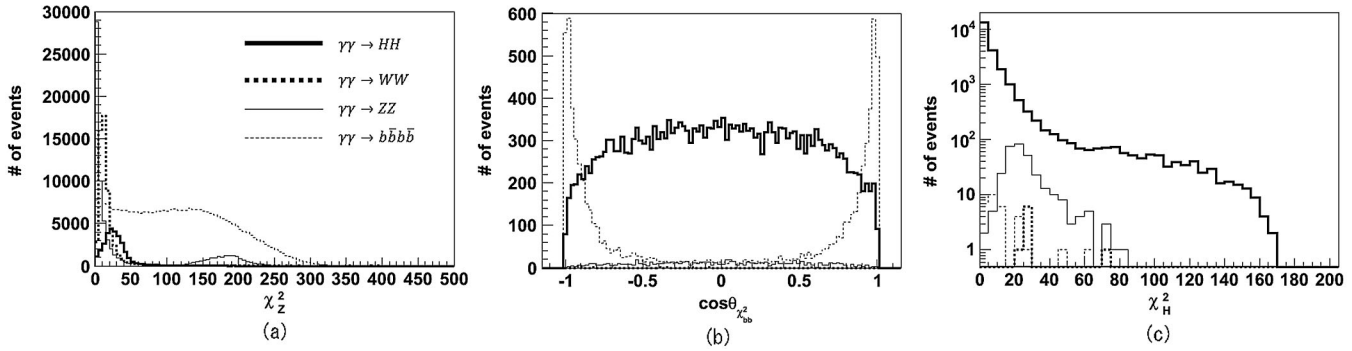

FIG. 8. Typical distributions of input variables in the case of the ideal jet clustering: (a) χ^2_Z after the preselection, (b) $\cos\theta_{\chi^2_{b\bar{b}}}$ after the W filter, and (c) χ^2_H after the $b\bar{b}$ filter. Bold solid, bold dotted, thin solid, and thin dotted histograms show the $\gamma\gamma \to HH$, $\gamma\gamma \to WW$, $\gamma\gamma \to ZZ$, and $\gamma\gamma \to b\bar{b}b\bar{b}$ events, respectively.

applied an "ideal jet clustering" to the $\gamma\gamma \to HH$, $\gamma\gamma \to WW$, and $\gamma\gamma \to ZZ$ events where each track is assigned to its parent (H, W, or Z) by color information obtained from the event generators. The "ideal jet clustering" was not applied to the $\gamma\gamma \to b\bar{b}b\bar{b}$ events since the color singlet combinations were nontrivial for this process. Input variables to the neural network and the number of intermediate layers are the same as the JADE clustering case. As with the previous analysis, the preselection was applied and events that survived the selection cuts were used for the neural network analysis. The number of signal/background events used for the neural network training were 29 152/57 058 for $\gamma\gamma \to WW$, 24 305/6349 for $\gamma\gamma \to b\bar{b}b\bar{b}$, and 22 823/291 for $\gamma\gamma \to ZZ$, respectively. Figures 8(a)–8(c) show the typical distributions of χ^2_Z after the preselection, $\cos\theta_{\chi^2_{b\bar{b}}}$ after the W filter, and χ^2_H after the $b\bar{b}$ filter, respectively. We again applied the results of the neural network training to the event samples which are statistically independent of the training samples. Table V shows the summary of the event selection with the ideal jet clustering. From Table V, the significance Σ_{ideal} was calculated to be

$$\Sigma_{\text{ideal}} = 4.87 \pm 0.13\sigma. \tag{7}$$

This result indicates that $\gamma\gamma \to HH$ would be observed at $\sim 5\sigma$ significance level with the integrated luminosity that corresponds to 5-year operation of the PLC, if the jet clustering performed perfectly.

V. SUMMARY

We studied the feasibility of the measurement of Higgs pair creation at the PLC, which is a possible option of the ILC. The optimum center of mass energy of the $\gamma\gamma$ collision was found to be around 270 GeV for the Higgs boson with a mass of 120 GeV/c^2.

We found that the $\gamma\gamma \to HH$ process can be observed with a statistical significance of about 5σ for the integrated luminosity corresponding to 5 years of the PLC running against the background process which has 10^6 times larger production cross section ($\gamma\gamma \to WW$) than the signal and other backgrounds which have the same final state ($\gamma\gamma \to ZZ$, and $\gamma\gamma \to b\bar{b}b\bar{b}$), if each track could be successfully assigned to parent particles (or partons).

Our analysis showed, for the light Higgs boson, that improvement of the jet clustering technique is crucial to discriminate the backgrounds by invariant mass information rather than to improve the b quark tagging efficiency. This fact is reasonable, because the WW background turned out to be suppressed by a simple b-quark tagging scheme since the W bosons do not decay into b-quark pairs, while the ZZ and $b\bar{b}b\bar{b}$ backgrounds can only be suppressed by their mass differences.

TABLE V. Similar table to Table IV, but with the ideal jet clustering.

	$\gamma\gamma \to HH$	$\gamma\gamma \to WW$	$\gamma\gamma \to ZZ$	$\gamma\gamma \to b\bar{b}b\bar{b}$
Expected events	80	7.31×10^7	59 350	259 700
Preselection	46.64 ± 0.27	55 836 ± 233	4172 ± 16	77 778 ± 142
Applying W filter	40.13 ± 0.25	7.8 ± 2.8	46.3 ± 1.7	1826 ± 22
Applying $b\bar{b}$ filter	36.03 ± 0.24	7.8 ± 2.8	18.5 ± 1.0	7.8 ± 1.4
Applying Z filter	34.68 ± 0.24	4.9 ± 2.2	5.22 ± 0.56	6.0 ± 1.2

For further improvements, vertex information from b-tagging analysis must be taken into account in jet clustering, thus they should be coherently developed. Efforts in this direction are ongoing as a part of the ILC physics study [27,28] and significant improvement could be expected in near future.

This analysis shows the possibility to measure the Higgs boson self-coupling at a lower beam energy than that of the e^+e^- mode and is useful in considering energy upgrade scenarios of the ILC.

ACKNOWLEDGMENTS

The authors would like to thank ILC physics working group [29] for useful discussions, especially Y. Okada for useful theoretical inputs. This work is supported in part by the Creative Scientific Research Grant No. 18GS0202 of the Japan Society for Promotions of Science (JSPS), the JSPS Core University Program, and the JSPS Grant-in-Aid for Science Research No. 22244031, and the JSPS Specially Promoted Research No. 23000002.

[1] The ATLAS Collaboration, Phys. Lett. B **710**, 49 (2012).
[2] The CMS Collaboration, Phys. Lett. B **710**, 26 (2012).
[3] http://www.fnal.gov/pub/presspass/press_releases/2012/Higgs-Boson-20120307.html.
[4] A. Djouadi *et al.*, ILC Reference Design Report Volume 2—Physics at the ILC, 2007, http://www.linearcollider.org/about/Publications/Reference-Design-Report.
[5] I. Ginzburg, G. Kotoki, V. Serbo, and V. Telnov, Pis'ma Zh. Eksp. Teor. Fiz. **34**, 514 (1981); [JETP Lett. **34**, 491 (1982)].
[6] E. Boos *et al.*, Nucl. Instrum. Methods Phys. Res., Sect. A **472**, 100 (2001).
[7] S. Kanemura, Y. Okada, and E. Senaha, Phys. Lett. B **606**, 361 (2005).
[8] J. Tian, slide at the *2011 Linear Collider Workshop of the Americas (ALCPG11)*, (unpublished).
[9] R. Belusevic and G. Jikia, Phys. Rev. D **70**, 073017 (2004).
[10] E. Asakawa, D. Harada, S. Kanemura, Y. Okada, and K. Tsumura, Phys. Lett. B **672**, 354 (2009).
[11] E. Asakawa, D. Harada, S. Kanemura, Y. Okada, and K. Tsumura, Phys. Rev. D **82**, 115002 (2010).
[12] B. Badelek *et al.*, Int. J. Mod. Phys. A **19**, 5097 (2004).
[13] http://www-jlc.kek.jp/subg/ir/Program-e.html.
[14] N. Maeda, K. Fujii, K. Ikematsu, Y. Kurihara, and T. Takahashi, in *Proceedings of the ILC Physics Working Group Meetings at KEK, KEK Proceedings 2009-5*, and also available from http://ccdb5fs.kek.jp/tiff/2009/0925/0925005.pdf.
[15] H. Murayama, I. Watanabe, and K. Hagiwara, KEK Report No. 91-11, 1992, (scanned image available from http://ccdb5fs.kek.jp/cgi-bin/img_index?199124011.
[16] G. J. Gounaris, J. Layssac, P. I. Porfyriadis, and F. M. Renard, Eur. Phys. J. C **13**, 79 (2000).
[17] T. Diakonidis, G. J. Gounaris, and J. Layssac, Eur. Phys. J. C **50**, 47 (2007).
[18] F. Yuasa *et al.*, Prog. Theor. Phys. Suppl. **138**, 18 (2000).
[19] S. Kawabata, Comput. Phys. Commun. **88**, 309 (1995).
[20] K. Abe *et al.*, arXiv:hep-ph/0109166v1.
[21] http://www-jlc.kek.jp/subg/offl/jsf/.
[22] T. Söstrand, S. Mrenna, and P. Skands, J. High Energy Phys. 05 (2006) 026.
[23] R. Yonamine, K. Ikematsu, T. Tanabe, K. Fujii, Y. Kiyo, Y. Sumino, and H. Yokoya, Phys. Rev. D **84**, 014033 (2011).
[24] K. Monig, Acta Phys. Pol. B **37**, 1251 (2006).
[25] W. Bartel *et al.*, Z. Phys. C **33**, 23 (1986).
[26] C. Peterson, T. Rognvaldsson, and L. Lonnblad, Comput. Phys. Commun. **81**, 185 (1994); we used a ROOT-base version of computer code JETNET, http://maxwell.hep.upenn.edu/~neu/root_to_jetnet/rtj.html.
[27] T. Tanabe, T. Suehara, and S. Yamashita, in *International Workshop on Future Linear Colliders (LCWS11), 2011* (unpublished).
[28] T. Suehara, T. Tanabe, S. Yamashita, J. Tian, and K. Fujii, in *International Workshop on Future Linear Colliders (LCWS11)*, 2011 (unpublished).
[29] http://www-jlc.kek.jp/subg/physics/ilcphys/.
[30] V. Barger and R. Phillips, *Collider Physics* (Addison Wesley, Reading, MA, 1987).

Nuclear Instruments and Methods in Physics Research B 319 (2014) 17–23

Contents lists available at ScienceDirect

Nuclear Instruments and Methods in Physics Research B

journal homepage: www.elsevier.com/locate/nimb

Development of an intense positron source using a crystal-amorphous hybrid target for linear colliders

Y. Uesugi [a,*], T. Akagi [a], R. Chehab [e], O. Dadoun [d], K. Furukawa [b], T. Kamitani [b], S. Kawada [a], T. Omori [c], T. Takahashi [a], K. Umemori [b], J. Urakawa [b], M. Satoh [b], V. Strakhovenko [†], T. Suwada [b], A. Variola [d]

[a] Graduate School of Advanced Sciences of Matter, Hiroshima University, 1-3-1 Kagamiyama, Higashi-Hiroshima, Hiroshima 739-8530, Japan
[b] Accelerator Laboratory, High Energy Accelerator Research Organization (KEK), 1-1 Oho, Tsukuba, Ibaraki 305-0801, Japan
[c] Institute of Particle and Nuclear Studies, High Energy Accelerator Research Organization (KEK), 1-1 Oho, Tsukuba, Ibaraki 305-0801, Japan
[d] Laboratoire de l'accélérateur linéaire (LAL), Université Paris–Sud 11, Batiment 200, 91898 Orsay Cedex, France
[e] Institut de Physique Nucléaire de Lyon (IPNL), Université Lyon 1, CNRS/IN2P3, Villeurbanne, France

ARTICLE INFO

Article history:
Received 31 July 2013
Received in revised form 27 October 2013

Keywords:
Positron source
Crystal channeling
Electron and positron linear accelerators

ABSTRACT

In a conventional positron source driven by a few GeV electron beam, a high amount of heat is loaded into a positron converter target to generate intense positrons required by linear colliders, and which would eventually damage the converter target. A hybrid target, composed of a single crystal target as a radiator of intense gamma-rays, and an amorphous converter target placed downstream of the crystal, was proposed as a scheme which could overcome the problem. This paper describes the development of an intense positron source with the hybrid target. A series of experiments on positron generation with the hybrid target has been carried out with a 8-GeV electron beam at the KEKB linac. We observed that positron yield from the hybrid target increased when the incident electron beam was aligned to the crystal axis and exceeded the one from the conventional target with the converter target of the same thickness, when its thickness is less than about 2 radiation length. The measurements in the temperature rise of the amorphous converter target was successfully carried out by use of thermocouples. These results lead to establishment to the evaluation of the hybrid target as an intense positron source.

© 2013 Elsevier B.V. All rights reserved.

1. Introduction

The next-generation linear colliders, such as the International Linear Collider (ILC) [1] and the Compact Linear Collider (CLIC) [2], require a large amount of positrons in short time periods. In particular, the ILC requires a positron beam with the bunch population of 2×10^{10}, the bunch separation of 332 ns and 1,312 bunches in a bunch train with the train repetition rate of 5 Hz. The design luminosity of the order of 10^{34} cm^{-2} s^{-1} equals the value of the KEKB synchrotron [3], which has the highest luminosity in electron-positron colliders. To realize such high luminosity, the ILC requires acceleration and collision of intense electron and positron beams. The detail of the issues and the RD of the ILC is described in [1]. Among those issues, the development of an intense positron source is a key to realize the linear collider.

Conventionally, positrons are generated by impinging an electron beam of a few GeV into a converter target via electromagnetic cascade processes. The converter target is typically a high-Z material such as the tungsten with a thickness of 4–6 radiation lengths, which is nearly equal to the depth of the shower maximum. Since the converter target is easily damaged by the heat load associated with the development the cascade, conventional systems suffer from limitations on the positron yield due to the heat load. The damage of the converter target was quantified under the operating condition of SLC at SLAC National Accelerator Laboratory (formerly Stanford Linear Accelerator Center) [4].

A different approach for generating positrons, which would overcome the heat load problem, is impinging gamma-rays into the converter target instead of electrons. By using combination of initial photons above O (10 MeV) and a thin high-Z material converter target, positrons are produced in the converter target dominantly via electron–positron pair production from initial photons and the energy deposition is reduced. In addition, by keeping the distance between the source of photons and the converter target, the photon beam spot size on the converter target can be increased for relaxing the localized energy deposition. If intensity of the incident gamma-ray is enough and the thickness of the converter target is appropriately chosen, it may be possible to reduce the heat load in the converter target while ensuring the required positron yield. For example, the ILC has adopted the positron source driven by gamma-rays using a long magnetic undulator.

* Corresponding author. Tel.: +81 824247037.
E-mail address: uesg@huhep.org (Y. Uesugi).
† The deceased.

0168-583X/$ - see front matter © 2013 Elsevier B.V. All rights reserved.
http://dx.doi.org/10.1016/j.nimb.2013.10.025

There is a method based on gamma-ray which uses a crystal assisted radiation. It was proposed by R. Chehab and his colleagues at LAL d'Orsay [5], and experimental studies has been carried out with the 1.3-GeV synchrotron in Institute for Nuclear Study, the University of Tokyo [6], at CERN with the experiment WA 103 [7,8] and the KEKB linac at KEK [9]. Simulations have shown [10] that a crystal converter presents the advantage of less energy deposition than the equivalent amorphous converter (giving the same positron yield). However, to avoid significant energy deposition in the crystal, due to large incident beam power, which could affect the available string potential – due to thermal vibrations – a separation between the thin crystal–radiator and the thicker amorphous converter led to the hybrid source scheme. Moreover, using a dipole magnet in between to remove the charged particles is reducing considerably the energy deposition and the peak energy deposition density. This last scheme is considered, here, as the hybrid target. In 2007, the hybrid target scheme was proposed by Chehab, Strakhovenko and Variola [11] as a possible way to generate intense positrons required by CLIC or ILC. In this article, we report results of experimental studies to investigate feasibility of the hybrid target as an intense positron sources.

2. A crystal assisted radiation

When a charged particle enters parallel to a crystal axis or planes in a crystal material, the transverse electric field of the axis or the planes constrains the particle motion in the transverse direction; it is known as the channeling effect. In particular, an electron is captured by the strong field of an atomic string, which is called the axial channeling [12]. The average crystalline potential of an isolated atomic string $U(r)$ is approximately expressed as

$$U(r) = -\frac{Ze^2}{d}\ln\left(1+\frac{3a_{\mathrm{TF}}^2}{r^2}\right), \tag{1}$$

where a_{TF} is the Thomas–Fermi screening radius, Z is the atomic number of the crystal, d is the interatomic spacing in the string, e is the electric charge, and r is the distance from the axis [13]. If the transverse kinetic energy $p_T^2c^2/2E$ of the incident electron with respect to the strings is smaller than the depth $U_0 = |U(0)|$ of the potential and if the entrance point is close enough to a string, the electron is trapped in the potential well and travels along the axis for some distance depending mainly on its energy. The transverse energy of the electron can be written in the form

$$E_T = \frac{p_T^2c^2}{2E} + U(r), \tag{2}$$

where p_T is the transverse component of the electron momentum p, and c is the velocity of light. Considering that p_T is much smaller than p, the incident angle ψ with respect to the axis can be written as $\psi = p_T/p_z$, and we can transpose expression (2) to

$$E_T = \frac{pv}{2}\psi^2 + U(r), \tag{3}$$

where v is the velocity of the electron. The channeled electron, which is in a bound state of $E_T < 0$ moves along a screw-like trajectory about the axial direction as shown in a drawing of Fig. 1. The incident electrons have a critical angle of capture ψ_L, so-called the Lindhard angle:

$$\psi_L = \sqrt{\frac{2U_0}{pv}}. \tag{4}$$

For the crystal axis ⟨1 1 1⟩ of tungsten used in this experiment, the U_0 is 979 eV, and the angle ψ_L is 0.495 mrad at an incident electron energy of 8 GeV.

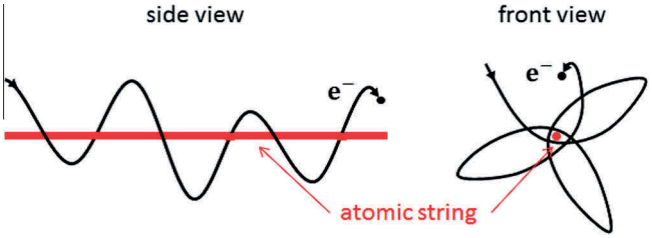

Fig. 1. Drawing of the electron's trajectory in axial channeling.

Channeled electrons emit strong radiation; the *channeling radiation*. The intensity of the radiation is expressed in the form

$$I = \frac{2e^2}{3c^3}\dot{v}_T{}^2\gamma^4, \tag{5}$$

where $\dot{v}_T$ is the transverse acceleration of the electron which moves according to the condition of (3), and $\gamma = 1/\sqrt{1-v^2/c^2}$ [14]. The channeling radiation has much larger intensity and shorter wavelengths than that of a magnetic undulator, due to the strong field of atoms that causes a short period oscillation with the order of some μm in the longitudinal direction and with the an amplitude of the order of an interatomic distance. For the ⟨1 1 1⟩ axis of tungsten with the incident electron energy of 8 GeV, it was found by numerical simulations that the intensity of low energy gamma-rays (⩽30 MeV) is ten times higher than that of nominal bremsstrahlung. Fig. 2 shows the comparison of the photon spectra obtained from a 1.4 mm of tungsten crystal and a 1.4 mm tungsten amorphous converter, the electron energy being 5 GeV.

When electrons enter into the crystal with larger angle than ψ_L, they are no longer trapped by the crystallline potential but are still affected by it. This situation has been discussed in [15]: the radiation becomes synchrotron like, below a critical incidence angle $\psi_0 = U_0/mc^2$, where m is the rest mass of an electron. The angle ψ_0 is 1.92 mrad for $U_0 = 979$ eV which is about four times larger than the critical angle of channeling effect.

There is another effect known as coherent bremsstrahlung, which is the coherent radiation of successive planes or strings. Its spectrum contains regularly spaced peaks given by the interference condition [16,17]. Coherent bremsstrahlung has the spectrum with high-order peaks caused by the condition of interference as

$$\omega_n(\theta) = \frac{v\psi}{d(1-\beta\cos\theta)}2\pi n \quad (n = 1,2,3\ldots), \tag{6}$$

where $\omega_n(\theta)$ is the circular frequency of the photon, θ is the photon emission angle, $\beta = v/c$, and d is the distance between the atoms.

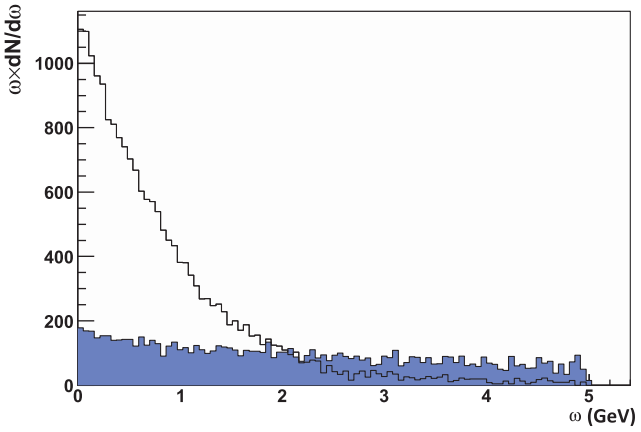

Fig. 2. The comparison of the photon spectra obtained from a 1.4 mm of tungsten crystal (filling white) and a 1.4 mm tungsten amorphous converter (filling check), the electron energy being 5 GeV.

In the conditions of an ultrarelativistic case ($\beta \sim 1 - 1/2\gamma^2$) and forward emitted photons ($\theta = 0$), the expression (6) is approximated to

$$\omega_n(0) = \frac{4\pi c\psi\gamma^2}{d}n. \quad (7)$$

when the energy of incident electrons E is 8 GeV, $\hbar\omega = 4$ GeV ($= E/2$) for $\psi = 2.08$ mrad. Therefore the contribution from coherent bremsstrahlung could be expected up to the energy region around a few GeV in the experiment.

3. Experimental setup and schemes

A series of experiments on positron generation were performed at KEK, Tsukuba, Ibaraki, Japan. A schematic drawing of the hybrid target, which was composed of a single crystal target to produce gamma-rays and an amorphous converter target made of tungsten to generate positrons, is shown in Fig. 3, and the experimental set-up installed in the 3rd switchyard of the KEKB linac [18] is shown in Fig. 4. The KEKB linac delivers single-bunch electron beams with energy of 8 GeV. The beam parameters are given in Table 1. The single crystal target made of tungsten was mounted on the 2-axes goniometer so as to align the crystal axis to the incident electron beam. The thickness of the crystal target was 1 mm and ⟨1 1 1⟩ axis was aligned to the electron beam. The surface mosaicity of this crystal on both sides was measured by an X-ray scattering method was ~ 0.5 mrad. After the crystal target, a sweeping magnet with a length of 800 mm and a magnetic field of 0.96 Tesla was installed to sweep out secondary charged particles generated in the crystal target. Thus, only gamma-rays were directed to the amorphous converter target installed 3313 mm downstream of the crystal target. Five amorphous converter targets of different thicknesses,

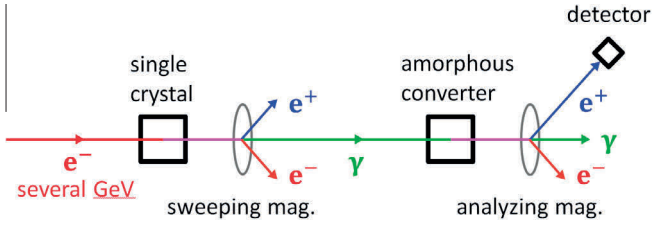

Fig. 3. Construction of the hybrid target using a single crystal target and an amorphous converter target.

Table 1
Properties of the incident electron beam.

Parameter	Value	Unit
Energy	8	GeV
Repetition	50 (max)	Hz
Charge in a pulse	1 (typ), 3 (max)	nC
Bunch length	10 (FWHM)	ps

1.75, 3.5, 5.25, 8 and 18 mm, were mounted on a linear stage to place the converter target of desired thickness on the beam line during the experiment. The particles from the converter target were directed into a vacuum chamber kept at pressure of 10^{-3} Torr. Positrons with momenta of 5, 10 or 20 MeV/c were selected by a magnetic momentum analyzer and led into the detector through collimators. In between the analyzing magnet and the detector, three collimators of aperture of 20 mm were placed to reduce background as well as to improve the momentum resolution. The geometrical acceptance of the detector was 0.22 msr which was defined by the collimator just before the detector. For the data analysis, which is described in Section 4.2, the efficiency of the detector system was evaluated by the simulation which took into account geometrical configuration of all components. The detector comprised lucite Cherenkov counter, its output is proportional to the number of incident positrons to the detector. Thermocouples were stuck on the back surface of two amorphous converter targets (8 and 18 mm) to measure the temperature from which we expect to get information of the heat load on the converter target due to the cascade shower.

The positron yield was investigated in three experimental setup as shown in Fig. 5. The first one was the *conventional* scheme in which the incident electron beam with energy of 8 GeV directly irradiated the amorphous converter target. The second was the *hybrid on axis*, and the last is the *hybrid off axis*. In these schemes, the single crystal target is inserted into the beamline. Charged particles coming out from the crystal were swept out by the sweeping magnet and only photons from the crystal were directed to the amorphous converter target. The crystallographic axis is aligned with the direction of the incident electron beam at the *on axis*, but not at the *off axis* scheme, respectively. Therefore, the enhancement effect by the crystal assisted radiation occurs only in second scheme. In these three schemes, five converter targets with different thicknesses were tested in order to measure the thickness dependence in the generated positron yield. Momentum dependence in the positron yield was also measured with the analyzing magnet.

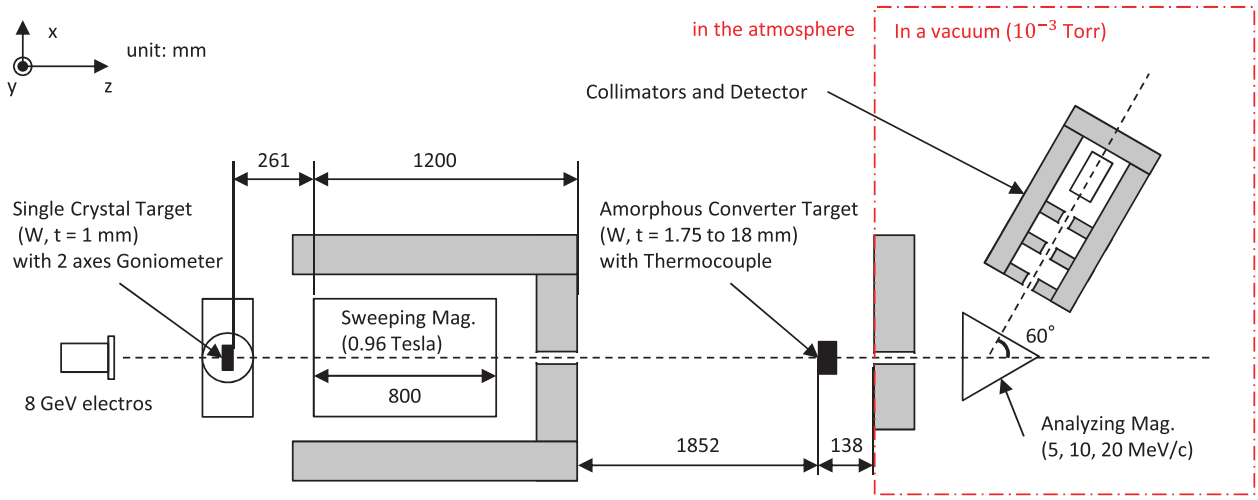

Fig. 4. Layout of the hybrid target and the positron detector system in the experiment in top view.

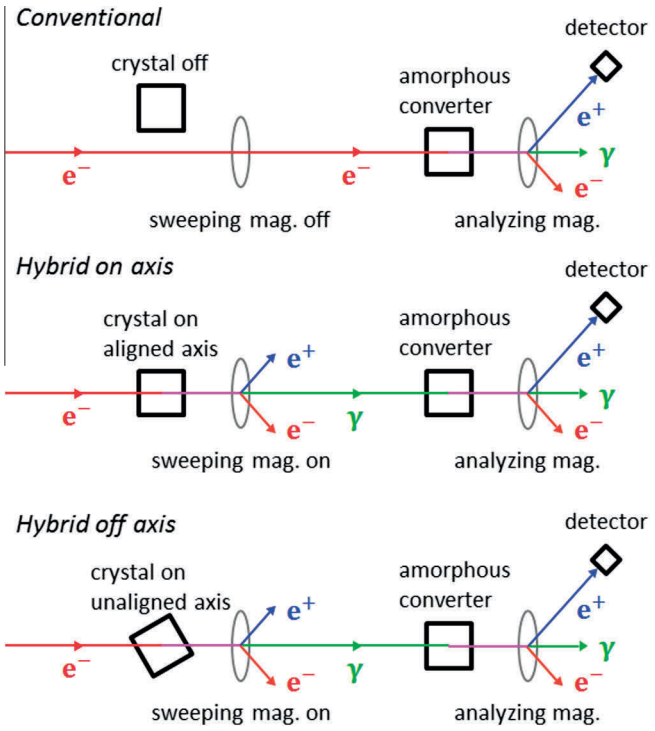

Fig. 5. Three schemes in the target configuration.

Table 2
Transverse spot sizes of the incident electron beam at the positions of the single crystal target and the amorphous converter target.

Target position	σ_x (mm)	σ_y (mm)
Single crystal	0.89 ± 0.01	1.71 ± 0.07
Amorphous converter	1.86 ± 0.03	1.92 ± 0.06

The contribution of the background for the *conventional* scheme were estimated by the data taken without converter targets on the beamline. As for the background estimation in the hybrid schemes, the crystal was removed from the beamline and the sweeping magnet was turned on; only the synchrotron radiation from incident electrons was irradiating the converter target.

Transverse sizes of the incident electron beam on the single crystal target and the amorphous converter target were measured by using a fluorescent screen before and after the experiment. The standard deviation of the two measurements are shown in Table 2. It is found that the profile of the electron beam was elliptic at the single crystal target but almost circular at the converter target. The angular spread of the electron beam was estimated from the beam sizes at the position of the crystal target and the converter target, and were 0.15 mrad for horizontal (x) and 0.030 mrad for vertical (y) directions, respectively.

4. Measurement of the positron yield

4.1. Goniometer angle dependence of the positron production

To confirm the intensity enhancement of the gamma-rays by the crystal, the positron yield was measured while changing relative angle between the crystalline axis ⟨111⟩ and the electron beam axis. The enhancement of the positron yield at the specific angle (*rocking curve*) was observed as shown in Fig. 6. We empirically found that the data can be well fitted by a sum of two Lorentz functions:

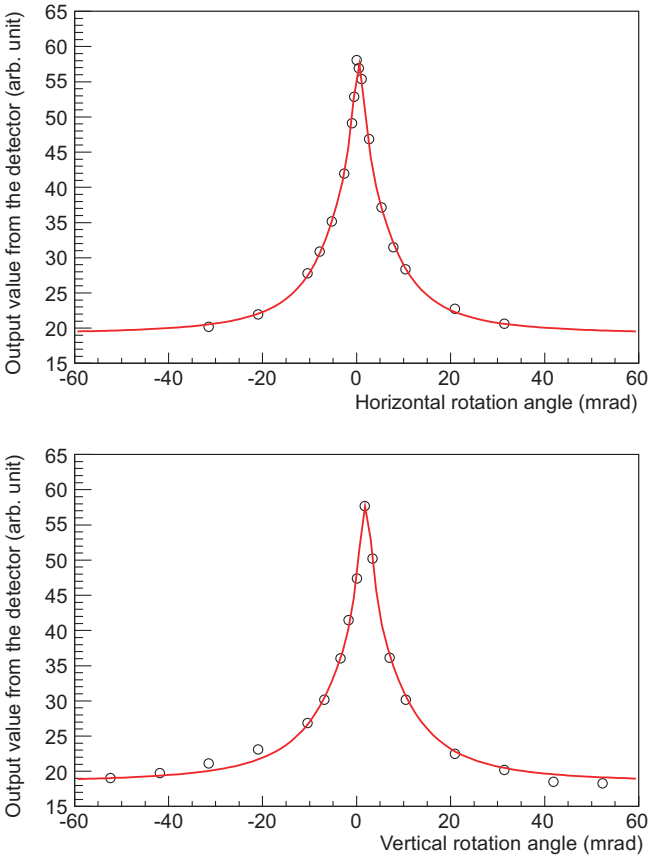

Fig. 6. Goniometer angle dependence of the positron production (*rocking curve*). Top is the result with regards to horizontal rotation, and bottom is that to vertical rotation. When measuring one angle of rotation, the other was being kept equal to zero.

$$f(\theta) = A\frac{\Gamma_1}{(\theta - \langle\theta\rangle)^2 + \Gamma_1^2} + B\frac{\Gamma_2}{(\theta - \langle\theta\rangle)^2 + \Gamma_2^2} + \text{const}, \quad (8)$$

with $A, B, \langle\theta\rangle, \Gamma_1$ and Γ_2 being fitting parameters. The results of the fitting are given in Table 3. The facts that (1) the data were fitted with the sum of the two function and (2) the widths Γ_1 and Γ_2 are wider than the critical angle of the channeling radiation (0.495 mrad) indicates the appreciable contribution of several radiation processes described in Section 2 and associated, in significant part, to above barrier particles.

4.2. Evaluation of the positron yield

To evaluate the experimental data quantitatively, numerical simulations were perfomed by using the GEANT4 (9.4 Patch-01) [19] and the FOT code [20,21]. The FOT simulates electromagnetic interactions taking into account channeling radiation, coherent and incoherent bremsstrahlung, and the transmission of electrons (or positrons) in the crystal. We applied the FOT code to simulate the processes in the crystal for the case of the *hybrid on axis* configuration. The mosaic spread of the crystal was not taken into account in this simulation. For the simulation of the *hybrid off axis* configurations, we put amorphous tungsten of 1-mm thick and used the GEANT4 since processes in the *off axis* case is same with the ones in the amorphous. The positron intensities in the experimental results were normalized with those in the simulations obtained in *conventional* scheme, because it is known that the

Table 3
The results of the fitting in the horizontal and vertical rocking curve.

	A	B	$\langle\theta\rangle$	Γ_1 (mrad)	Γ_2 (mrad)	FWHM
Horizontal	31 ± 11	179 ± 11	0.462 ± 0.058	1.78 ± 0.36	8.4 ± 1.3	$8.7^{+2.5}_{-2.0}$
Vertical	41 ± 13	196 ± 16	1.899 ± 0.087	2.05 ± 0.37	10.1 ± 1.9	$8.9^{+3.3}_{-2.5}$

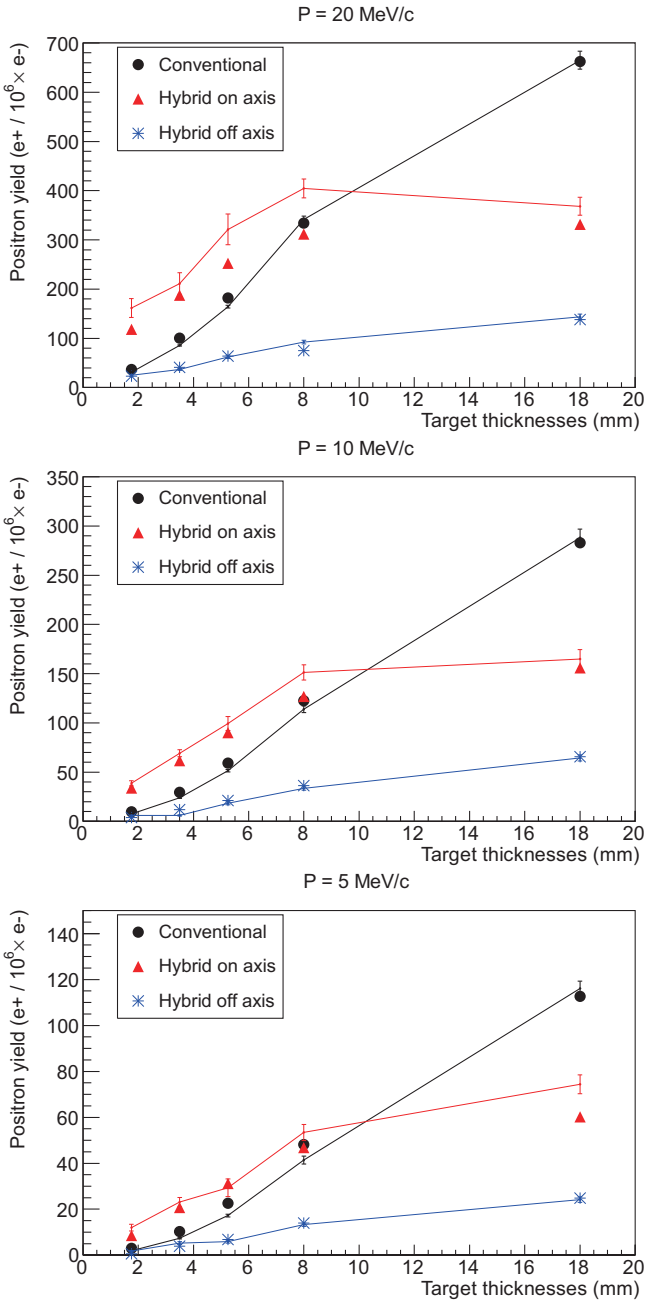

Fig. 7. Comparison of thickness dependences in the positron yield between experimental results and simulations in the analyzed momenta of 20, 10, and 5 MeV/*c*, from the top. On these figures, markers show the experimental data, polygonal lines indicate the simulation, and the vertical axis means the positron yield per million electrons.

GEANT4 is highly reliable in calculation accuracy and reproducibility.

Fig. 7 shows the thickness dependence of the positron yield for the *conventional*, the *hybrid on axis* and the *hybrid off axis* at the momentums of 20, 10 and 5 MeV/*c*, where the experimental data

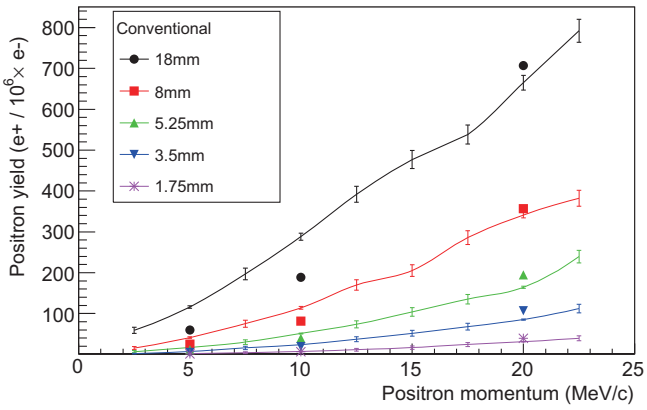

Fig. 8. Momentum dependences in the positron yield in the *conventional* scheme. Here, one normalization constant is used, which is differing from the case of Fig. 7.

were normalized independently for each momentum. In all analyzed momenta, the yields were the greatest at the thickness of 18 mm in the *conventional* scheme. This thickness equals to the shower maximum of electromagnetic cascade for a 8-GeV electron beam and amorphous tungsten. It should be mentioned that the positron yield in the *hybrid on axis* scheme is greater than that of the *conventional* scheme when the thickness of the converter target is thinner than 8 mm. This result comes from a main characteristics of the hybrid target system; i.e. positrons can be directly created via pair creation. In the case of the unaligned crystal axis, that is the *hybrid off axis* scheme, the yield decreases against the *on axis* as discussed in Section 4.1. Comparing the experimental data with the simulations, both results agree with each other on the thickness dependence in the *off axis*. As regards the *on axis* case, the simulation is about 20% larger than the experiment while overall behavior is well reproduced. It indicates that the evaluation of radiation processes in the crystal by FOT needs to be improved for the absolute yield of low energy photons.

The comparison in momentum dependence between experimental results and simulations is shown in Fig. 8 for the *conventional* scheme. Unlike the comparison in Fig. 7, a common normalization factor was used for all momenta. If the acceptance were correctly reproduced, both should have agreed with each other regardless of the analyzed momenta. It was unfortunately found that the simulation did not completely reproduce the experiment in regard to momentum dependence. This would mean that the experimental environment, e.g. the arrangement of collimators, was not reproduced accurately in the simulation. However, it does not directly concern the estimate of FOT because of the high reliableness of GEANT4. The simulation using GEANT4 is actually reproduced with high accuracy in the thickness dependence as shown in Fig. 7.

5. Temperature measurement

Estimation of the heat load in the converter target is an important information to evaluate survivability of the target in the positron source operation. However, the direct measurement of the heat load caused by the electromagnetic shower is not a trivial

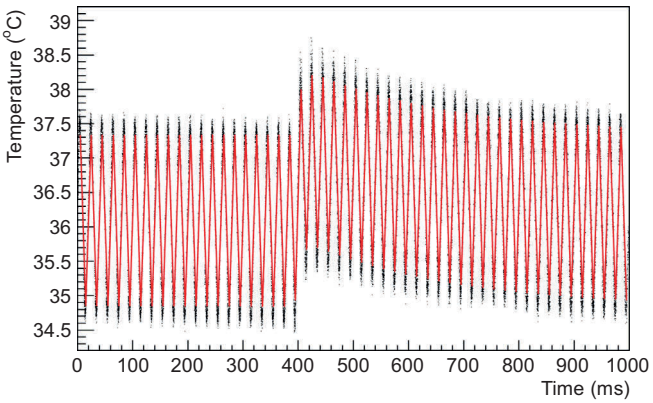

Fig. 9. Time trace in the temperature rise measurement in the condition of the conventional, 18-mm thick amorphous converter target. The 50-Hz noise trace induced from power lines is clearly visible.

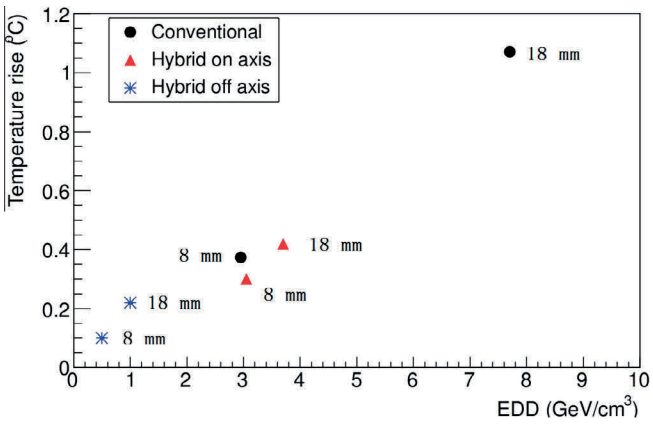

Fig. 10. Correlation plot between the measured amounts of the temperature rise and the calculation results in the EDD.

task. Therefore, simultaneously with the positron yield, we measured temperature of the converter target as an estimation of the heat load.

Type K thermocouples with a sensitive area of 1 mm × 1 mm were used to measure the temperature rise. They were pasted on the back surface of the 8-mm thick and the 18-mm thick amorphous converter targets. Compensating leadwires connected to the thermocouples were laid to the monitoring room. The output from the thermocouple was calibrated with cold-junction compensation and amplified by a thermocouple converter. The signal is recorded with a sampling rate of 1 kHz. After adjusting the position of the thermocouple to the incident electron beam, the temperature rise, synchronized with electron bunches, were measured with the beam repetition rate of 1 Hz. The converters are mounted on the linear stage with the aluminum holders so that the heat was evaluated to the environment (air) directly from the converter or via the holder.

Fig. 9 shows the measured temperature rise in one second corresponding to an irradiation of single–bunch. As is seen from the figure, there was a noise from the 50-Hz power line in the data. To evaluate the temperature variations due to the electromagnetic shower in the converter, the data were fitted with the function $f(t)$ as

$$f(t) = ae^{-(t+\delta+t_0)/\tau_1}\left(1 - e^{-(t+\delta+t_0)/\tau_2}\right) + b\sin\{50 \cdot 2\pi(t+\delta)\} + \text{const}, \quad (9)$$

where $a, \tau_1, \tau_2, t_0, \delta, b$ are the amplitude of temperature rise, decay time and rise time of the temperature, time offset of the temperature rise, overall time offset including 50-Hz noise, and the amplitude of the noise, respectively.

The result of the measurements in regard to three schemes of targets with the 8-mm thick and the 18-mm thick converter targets is shown in Table 4. It was found that the slight temperature rise of 0.1 °C, corresponding to the case of the *hybrid off axis* scheme with the 8-mm thick, was able to be measured using the thermocouple. The decay time constant was sufficiently greater than the resolution time of the measurement instrument. Fig. 10 shows a correlation between the measured temperature rise and the energy deposition density (EDD) at the back end of converter targets computed with a simulation, where the EDD is defined by unit of GeV/cm^3 and is the localized energy deposition in the converter target. It is found that the temperature rise is proportional to the EDD and that the EDD could be evaluated by measuring the variation in the temperature rise measurements.

6. Conclusions

We clearly observed the increase of positron yield when the crystal axis is aligned to the electron beam. The width of the rocking curve was wider than the critical angle of the channeling effect or the angular spread of the incident electron beam, that was consistent with previous experiment indicating appreciable contribution of radiation from other than the channeling effect. This fact is advantageous in practical operation, since it relaxes the precision of the alignment of the crystal target to the electron beam.

Since it has been confirmed that the simulation reproduces the experimental data, one would be able to perform the optimization in designing a positron source with the hybrid target by using the simulation. According to the initial simulation, the angular spread of the positrons from the hybrid target was wider than the conventional target. Because of small angular acceptance of current experimental set up, what we observed in Fig. 7 is a smaller part of the yields for the hybrid target than those for the conventional target. In addition, the tungsten crystal may not be the best choice for the electron–photon converter. Constructing the optimum target and positron capture section by using the simulation may give us the final conclusion of the ability to produce more positrons.

The result of temperature rise measurement gives us basic information about to evaluate the energy deposition in the positron converter target. We need further study to evaluate relation between the measured temperature and energy deposition, however, it will be applicable to any positron target system once it is established.

Table 4
Results of the temperature rise measurement. Each property corresponds to a parameter in the fitting function.

Target scheme	Thickness (mm)	a: Temperature rise (°C)	τ_1: Decay time (ms)	τ_2: Rise time (ms)
Conventional	18	1.071 ± 0.003	332 ± 3	8 ± 1
	8	0.373 ± 0.003	116 ± 1	3 ± 1
Hybrid axis on	18	0.419 ± 0.002	537 ± 1	10 ± 1
	8	0.300 ± 0.002	178 ± 2	2 ± 1
Hybrid axis off	18	0.197 ± 0.004	542 ± 3	7 ± 1
	8	0.095 ± 0.001	144 ± 4	3 ± 1

To evaluate the yield performance in the hybrid target, a simulation including a capture system is planned. To advance designs of the hybrid target, it is important to select the crystal material that gives the highest enhancement in gamma-rays, and to develop the converters with an efficient cooling system. On the temperature measurement, we plan to measure the spatial distribution (s) in the temperature rise measurement with arrayed thermocouples.

Acknowledgment

Authors would like to thank operation crew of the KEKB LINAC for providing excellent beams during the experiment. This work was supported in part by JSPS KAKENHI Grant No. 2540314.

References

[1] The International Linear Collider: Technical Design Report. Available from: <http://www.linearcollider.org>.
[2] M. Aicheler et al., A Multi–TeV Linear Collider Based On CLIC Technology: CLIC Conceptual Design Report, CERN-2012–007, SLAC-R-985, KEK-Report-2012-1, PSI-12-01, JAI-2012-001.
[3] T. Abe et al., Prog. Theor. Exp. Phys. (2013) 03A001.
[4] The NLC collaboration, 2001 Report on the Next Linear Collider: A Report Submitted to Snowmass 2001, SLAC-R-571 (2001) 85–88.
[5] R. Chehab, F. Couchot, A.R. Nyaiesh, F. Richard, X. Artru, 13th IEEE PAC (1989) 283–285.
[6] K. Yoshida et al., Phys. Rev. Lett. 80 (1998) 7.
[7] R. Chehab et al., Phys. Lett. B 525 (2002) 41–48.
[8] X. Artru et al., Nucl. Instr. Meth. B 240 (2005) 762–776.
[9] T. Suwada et al., Phys. Rev. E 67 (2003) 016502.
[10] X. Artru et al., Phys. Rev. Spec. Top. A–B. 6 (2003) 091003.
[11] X. Artru et al., NIM B 266 (2008) 3868–3875.
[12] V.M. Biryukov, Y.A. Chesnokov, V.I. Kotov, Crystal Channeling and Its Application at High-Energy Accelerators, Springer, Berlin, 1997, pp. 27–29.
[13] J. Lindhard, Mat. Fys. Medd. Dan. Vid. Selsk. 34 (1965) 14.
[14] M.A. Kumakhov, Phys. Lett. A 57 (1976) 1.
[15] V.N. Baier, V.M. Katkov, V.M. Strakhovenko, Sov. Phys. JETP. 65 (1987) 4.
[16] M.L. Ter-Mikaelian, High-Energy Eelectromagnetic Processes in Condensed Media, John Wiley & Sons, Inc., New York, 1972, pp. 34–113.
[17] R.V. Vedrinskii, V.S. Malyshevskii, Sov. Phys. JETP. 56 (1982) 3.
[18] M. Akemoto et al., Prog. Theor. Exp. Phys. (2013). 03A002.
[19] S. Agostinelli et al., Nucl. Instr. Meth. A 506 (2003) 250.
[20] X. Artru, NIM B 48 (1990) 278–282.
[21] O. Dadoun, G. Le Meur, F. Touze, A. Variola, X. Artru,R. Chehab, M. Chevallier, V. Strakhovenko, Journal of Physics: Conference Series – IX International Symposium Radiation from Relativistic Electrons in Periodic Structures (RREPS-11), Egham: Royaume–Uni, 2011.

Blocking positive ion backflow using a GEM gate: experiment and simulations

P. Gros[a1] , K. Fujii[b], T. Fusayasu[e], Y. Kato[d], S. Kawada[g], M. Kobayashi[b], T. Matsuda[b], O. Nitoh[f], A. Sugiyama[a], T. Takahashi[g], J. Tian[b], T. Watanabe[c], R. Yonamine[b]

[a]Saga U., Saga, Japan
[b]KEK, IPNS, Tsukuba, Japan
[c]Kogakuin U., Tokyo, Japan
[d]Kinki U., Osaka, Japan
[e]NiAS, Nagasaki, Japan
[f]TUAT, Tokyo, Japan
[g]Hiroshima U., Hiroshima, Japan

Abstract

Positive ion feedback can be problematic in a high precision Time Projection Chamber (TPC) as proposed for the International Linear Collider (ILC). Use of a traditional wire gating device would increase the dead areas in the planned module structure. F. Sauli proposed, in 2006, the use of a Gas Electron Multiplier (GEM) as a gating device. We have measured the electron transparency for a 14 μm thick GEM in a 1T magnetic field. The transparency does not meet the requirement for a TPC at the ILC. We performed a simulation study using Garfield++ to understand the important parameters. Simulations show that a new GEM structure with wider aperture, for example a hexagonal honeycomb structure, can improve the performance as a gate. Results of measurements will be compared to the simulation and the predicted performance of the new GEM structure will be described.

1 Introduction

The Linear Collider Time Projection Chamber (LCTPC), foreseen as the central tracker for one of the International Linear Collider (ILC) detectors,

[1]Corresponding author. E-mail: philippe@hep.phys.saga-u.ac.jp

aims at an unprecedented performance in momentum resolution for this type of detector. This high performance relies strongly on the quality of the electric field in the drift volume. All the different technologies considered for the electron readout in LCTPC will release positive ions into the drift volume during the amplification process. Simulations by K. Fujii [1] have shown that even a very small amount of backdrift ions will produce significant field distortions in the drift volume. Fortunately, the train structure of the electron bunches in ILC allows the use of a gating device. During the readout period (1 ms of bunch-train crossing), the readout amplification will produce a cloud of positive ions extending about 10 mm from the readout plane. These ions have to be neutralised during the 200 ms period between the crossings.

Several gating solutions are considered. The use of a GEM foil, as suggested by F. Sauli [2], is particularly adapted to the module structure of the LCTPC readout plane. The challenge of this type of gating system is to keep a good electron transparency when the gate is open. We will first describe the experimental tests done with such a GEM gating device. We will then show how these results can be reproduced in simulations using Garfield++. Finally, we will show simulation results for gate concepts with higher electron transparency.

2 Experimental tests

2.1 Transparency measurements

F. Sauli showed direct measurements of electron transparency of a GEM gate with different applied voltages [2]. We reproduced the same kind of measurement with a thin GEM gate (14 μm), with 90 μm holes and 140 μm pitch. This measurement was done using a ^{55}Fesource and the simple setup described in fig. 1. In a simple TPC, we measured the charge peaks from X-rays converted in the gas above and below the gate. The ratio of the charge measured will correspond to the effective electron transmission of the gate.

The measured electron transmission in the so-called T2K gas (Ar:CF_4:iC_4H_{10}, 95:3:2), with a 1 T magnetic field is shown in fig. 2. A maximum is observed around 10V, but the enhancement is not very significant, and the transparency remains below 40%.

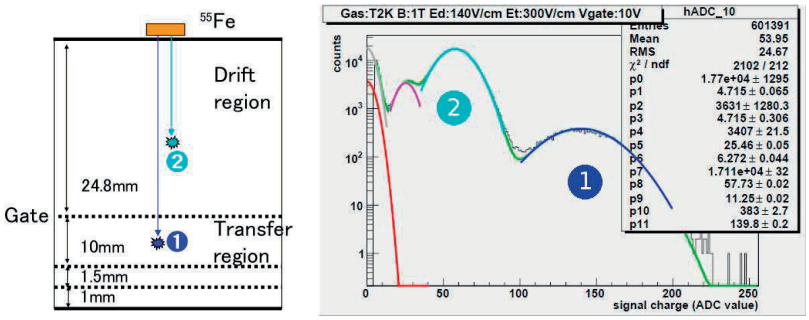

Figure 1: Sketch of the gate transmission test. We measure at the same time signals produced above the gate (2) and below (1). An example of measured spectrum is shown on the right. The ratio of the two peaks positions gives the electron transmission.

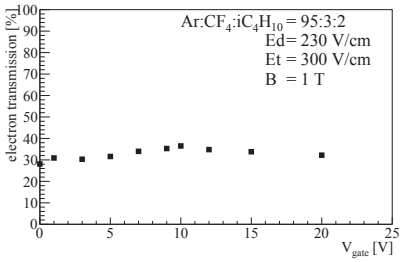

Figure 2: Measured electron transmission as a function of the voltage applied to the GEM gate. A maximum is observed at 10V.

2.2 Effective transparency measurement

In the TPC, the important factor for the space resolution is the effective number of collected electrons N_{eff}, which represents the amount of information from the original ionisation. This value factors in different effects in the TPC, in particular the gain fluctuations in the readout system [3]. We must therefore make sure that the gate does not induce extra fluctations in the system. To check that no extra information was lost in the gate, a measurement of N_{eff} was performed.

Resolution measurements were done for different drift distance using the MPTPC [4], a small 10×10 cm^2 TPC. From this measurement, we could extract N_{eff} with and without the gating GEM, as shown in fig. 3. The loss of about 50% of N_{eff} observed is consistent with the direct transparency measurements. This will correspond to a 30% loss in space resolution, which is not good enough for the performance requirements of the LCTPC.

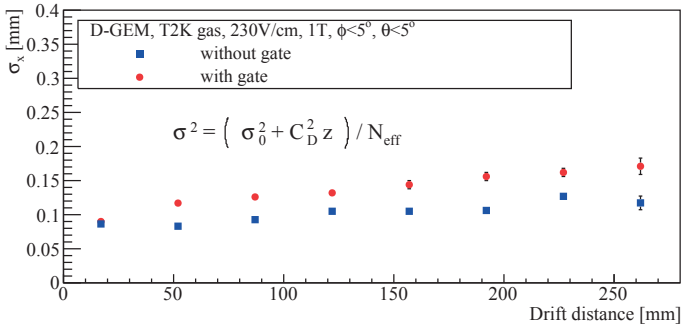

Figure 3: Space resolution measurements with and without gate. The resolution is clearly worse with the gate. At large drift distance, a ratio close to $\sqrt{2}$ indicates a transparency of 50%.

3 Simulation

3.1 Simulation software

To understand the previous results, and investigate the possibilities to improve the gate performance, we did microscopic simulations using Garfield++ [5]. The field calculations were done with the finite elements program ANSYS[2] [6].

The software describes the microscopic behaviour of single electrons in the gas volume. We simply generate individual electrons above the GEM hole (in the drift region), and see whether they arrive below the gate (in the transfer region) or somewhere on the gate. The electrons are generated randomly 250 μm above the GEM, and collected 100 μm below.

In the simulation, we can separate the transmission efficiency into two components [7]:

Collection efficiency is defined as the proportion of electrons reaching the GEM hole ($\epsilon_{coll} = N_{hole}/N_{drift}$). It depends mainly on the geometrical aperture of the GEM, the electric field in the hole (relative to the drift field) and the magnetic field.

Extraction efficiency is defined as the proportion of electrons in the GEM that will reach the transfer region ($\epsilon_{extr} = N_{trans}/N_{hole}$). It depends on the electric field in the GEM hole (relative to the transfer field). It also depends on the thickness of the GEM and the electron diffusion (i.e. the gas properties).

[2]ANSYS v14.0 Release

The transmission is the product of these two values:

$$T = N_{trans}/N_{drift} = \epsilon_{coll} \times \epsilon_{extr} \quad (1)$$

We must maximise these two values simultaneously. In particular, the two components have an opposite dependence with the electric field in the GEM hole (i.e. the GEM voltage).

3.2 Description of experimental results

In a first step, we checked that the simulations give a correct description of the experimental data. Fig. 4 compares experimental and simulated electron transparency in Ar:iC$_4$H$_{10}$ (90:10), with a low drift field (50 V/cm) and relatively high transfer field (300 V/cm). In that case, a clear maximum appears around 3 V, which is very well described by the simulation. It is interesting to notice that the simulation does not require the tuning of any parameter.

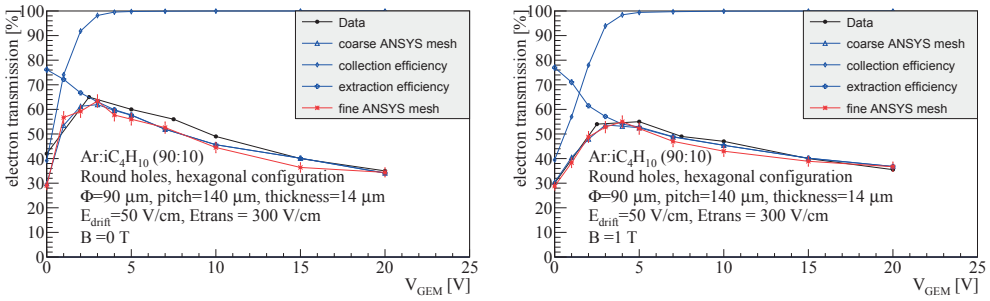

Figure 4: Simulation of the electron transmission for a 14 μm thick GEM gate. The Garfield++ simulation gives a good description of the data both with and without magnetic field. ANSYS gives an accurate field description even for a coarse meshing, which greatly increases the computing speed.

We observe that the maximum can be explained by the collection efficiency increasing (and saturating) very fast, while the extraction efficiency decreases slowly. When the magnetic field is on, the collection efficiency increases more slowly (because the electrons follow the magnetic field lines), but the extraction efficiency becomes slightly larger (because of the reduced diffusion). In both cases, we observed that the collection efficiency is close to the geometrical aperture of the GEM (in this case 37%) for very low voltages. This is consistent with the fact that this configuration has an almost uniform electric field on the drift side of the gate ($E_{hole} \approx E_{drift}$).

The collection efficiency seems to be the operating parameter, especially in a magnetic field. We can try to improve it by increasing the GEM aperture.

4 Simulation of a large aperture gate

4.1 GEM geometry

In this section, we propose to simulate a GEM geometry with a maximised aperture. For this we introduce a hexagonal honeycombed structure as shown in fig. 5. This structure offers an 81% aperture. The electric field was calculated in ANSYS for one sector of the GEM, using symmetric boundaries. The Garfield++ simulation uses these symmetries to extrapolate the field to the whole space.

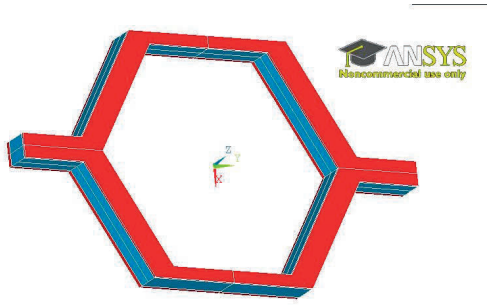

Figure 5: GEM geometry simulated. Only one sector is used for field calculations, using symmetries.

4.2 Closing voltages

Fig. 6 shows that even with large holes, such gating GEMs can offer a high ion suppression for a small applied voltage (under 20V). It is important to notice that due, to their low mobility, the magnetic field has very little influence on the ions trajectories, and can be ignored.

4.3 Electron transmission

We calculated the simulated transmission efficiency for different values of the GEM thickness and of the transfer field. Fig. 7 shows that without magnetic field, the influence of these parameters is as expected. We can see that even with this very large aperture, and very thin structure, a high transfer field is needed to reach a transparency above 70%. Such a high transfer field will make it difficult to have a good field configuration in the amplification system. It will probably make it impossible to reach the same N_{eff} as with a normal

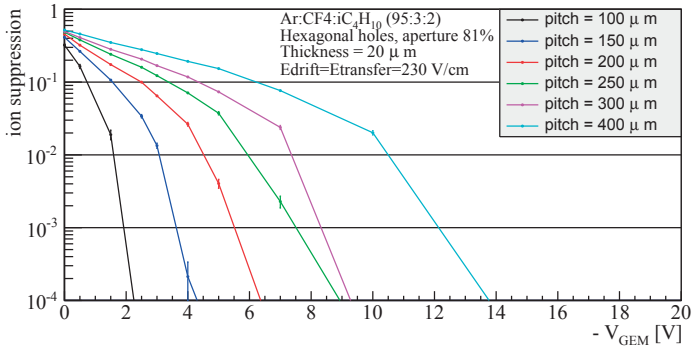

Figure 6: Ion transmission for different GEM voltages. A suppression of several orders of magnitude can be obtained with low voltages, even for wide holes.

drift field, therefore transferring the transparency issue to the amplification region.

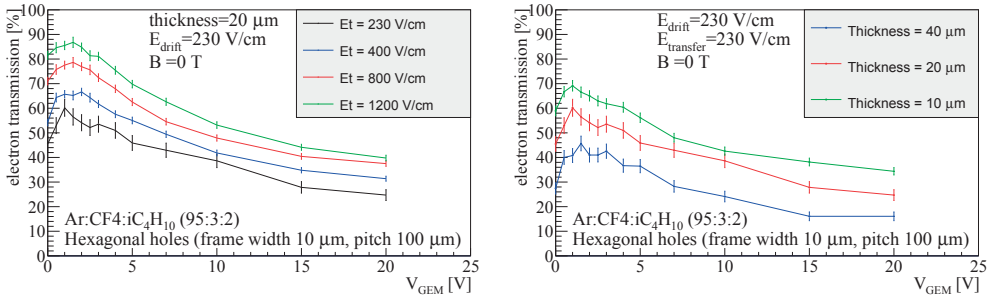

Figure 7: Simulated electron transmission for different transfer fields and different GEM thicknesses. A maximum appears around 2 V, but high transparency can only be achieved in the most extreme configuration.

With the large magnetic field of ILD (3.5 T), and the large corresponding $\omega\tau$ in the T2K gas, the behaviour changes. In that case the electrons trajectories mostly follow the magnetic field lines. In fig. 8, we see that in these conditions, the transfer field has little influence on the transparency. Additionally, the low transverse diffusion allows to achieve good transparency with relatively thick GEMs.

4.4 Distortions

For production reasons, it will be easier to have a wider frame, and therefore, for the same aperture, larger holes. We already saw in sect. 4.2 that the

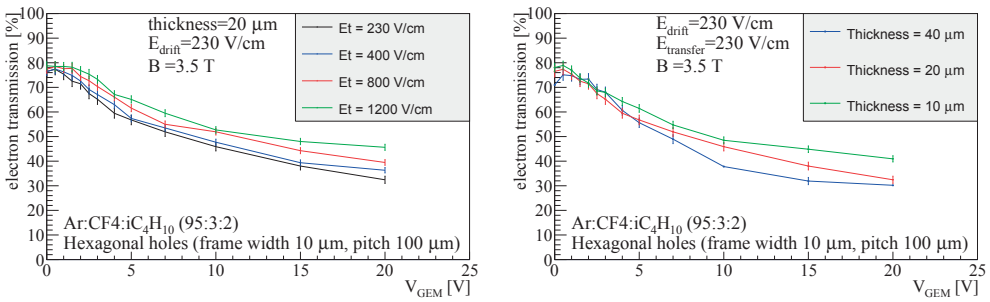

Figure 8: Simulated electron transmission for different transfer fields and different GEM thicknesses, in a 3.5T transverse magnetic field. Due to the high $\omega\tau$, the transfer field and thickness have little influence on the transparency. A transmission efficiency close to the geometrical aperture of the GEM can always be achieved for low voltage.

closing voltage, will increase, but remain reasonable for large holes.

With larger GEM structure, we have to make sure that the position information of each electron is not lost. In fig. 9, we see that for low GEM voltage, the distortions of the electic field are small, and the resulting smearing is negligible compared to diffusion. A small radial displacement can be seen at the edge of the GEM hole, which comes simply from the electron absorption on the GEM.

If some voltage is applied to the GEM, the electrons are displaced to the centre of the GEM hole, and rotate along the edge of the hole due to $E \times B$ effect. In that case, there would be a loss of space resolution, but this regime is already excluded due to the low electron transparency.

5 Conclusion

The LCTPC needs to minimise the ion back flow, and the ILC running scheme allows the use of a gating system. An ion gating device with thin GEMs has been tested experimentally, but does not meet the electron transparency requirements of the LCTPC. Simulations with Garfield++ can explain these results and show that in the high magnetic field of ILD, the dominating parameter of a GEM gate is the geometrical aperture. This leaves some freedom to adjust parameters to satisfy other constraints of the system.

The challenge remains in the production of such a GEM with suitable mechanical properties. This might be possible with large holes and relatively thick GEMs. In particular, the thickness of the metal layers can be increased to provide strength without affecting too much the transparency.

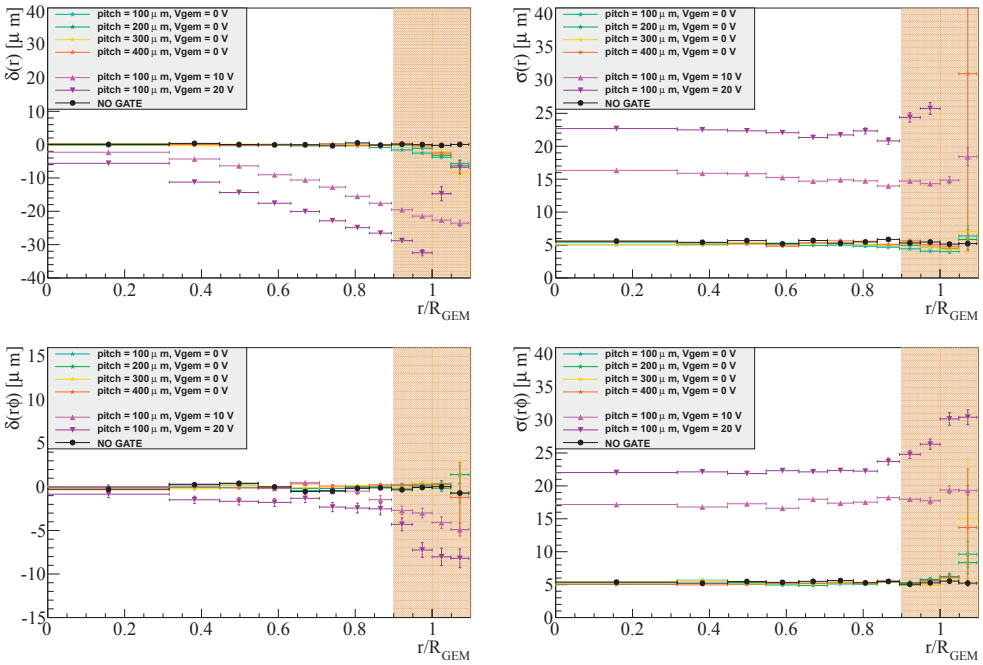

Figure 9: Electron displacement in the GEM hole for different hole sizes, keeping an 81% aperture. On top is the displacement along the hole radius and on the bottom the displacement along the edge of the hole. On the left is the systematic displacement on the right the position smearing. The coordinates are adjusted for the hexagonal geometry to be similar to cylindrical, and normalised to the size of the hole. Without voltage applied to the GEM, the distortions are negligible compared to diffusion. If a tension is applied, the electrons are displaced towards the center of the hole and along the edge of the hole due to $E \times B$ effect, as expected.

As an alternative solution, the LCTPC R&D collaboration is investigating the possibility of using a traditional wire gate.

Acknowledgements

This work was supported by the grant-in-aid for specially promoted research no.23000002 of the Japan Society of Promotion of Science.

References

[1] K. Fujii, LCTPC collaboration meeting presentation, http://ilcagenda.linearcollider.org/getFile.py/access?contribId=3&sessionId=8&resId=0&materialId=slides&confId=5504

[2] F. Sauli, L. Ropelewski, P. Everaerts, Nucl. Instrum. Meth. A 560: 269-277, 2006

[3] Arogancia et al,, Nucl. Instrum. Meth. A 602: 403-414, 2009

[4] K. Ackermann *et al.*, Nucl. Instrum. Meth. A 623 (1): 141-143, 2010

[5] R. Veenhof *et al.*, http://garfieldpp.web.cern.ch/garfieldpp/

[6] http://ansys.com

[7] M. Killenberg *et al.*, Nucl. Instrum. Meth. A 498: 369-383, 2003

Preprint typeset in JINST style - HYPER VERSION

Spatial Resolutions of GEM TPC

A Novel Theoretical Formula and its Comparison to Latest Beam Test Data

R. Yonamine[a*], K. Fujii[a], K. Ikematsu[b], A. Ishikawa[c], T. Fusayasu[d], P. Gros[e], Y. Kato[f], S. Kawada[g] M. Kobayashi[a], T. Matsuda[a], O. Nitoh[h], R.D. Settles[i], A. Sugiyama[e], T. Takahashi[g], J. Tian[a], T. Watanabe[j]

[a] *High Energy Accelerator Research Organization (KEK), 1-1 Oho, Tsukuba 305-0801, Japan*
[b] *Siegen U., Walter-Flex-Str.3, 57068 Siegen, Germany*
[c] *Tohoku U., 6-3 Aoba Aramaki, Sendai 980-8578, Japan*
[d] *Nagasaki Institute of Applied Science (NiAS), 536 Abamachi, Nagasaki 851-0193, Japan*
[e] *Saga U., 1 Honjomachi, Saga 840-8502, Japan*
[f] *Kinki U., 3-4-1 Kowakae, Higashi-Osaka 577-8502, Japan*
[g] *Hiroshima U., 1-3-1 Kagamiyama, Higashi-Hiroshima 739-8530, Japan*
[h] *Tokyo U. of Agriculture and Technology (TUAT), 2-24-16 Nakamachi, Koganei 184-8588, Japan*
[i] *Max Planck Institute for Physics, Föhringer Ring 6, 80805 Munich, Germany*
[j] *Kogakuin U., 1-24-2 Nishi-Shinjuku, Shinjuku 163-8677, Japan*
E-mail: yonamine@post.kek.jp

ABSTRACT: Unprecedented charged particle momentum resolution is required for precision Higgs studies at the International Linear Collider (ILC), which in turn demands as many as 200 sampling points with a high spatial resolution of 100 microns or better if we are to adopt a TPC for the central tracker. We discuss a novel theoretical resolution formula for a GEM-readout TPC, which is applicable to inclined tracks as opposed to the previous formula which is valid only for normal incidence. The formula identifies key factors that determine the spatial resolution and helps optimize the readout pad geometry and High Voltage settings for a given gas mixture. The formula is compared to the latest beam test results for a LC TPC Large prototype.

KEYWORDS: TPC; MPGD; GEM; spatial resolution.

*Corresponding author.

Contents

1. Introduction

The International Linear Collider (ILC) is proposed as the best suited accelerator to investigate the electroweak symmetry breaking [1]. The ILD is a detector concept proposed as one of the two detectors for the ILC. The ILD concept is optimized for particle flow analysis (PFA) [2, 3] aiming at measuring every particle in the event, charged and neutral, with the best possible precision. This goal is achieved by reconstructing charged particles in the tracker, photons in the electromagnetic calorimeter (ECAL), and neutral hadrons in the ECAL and hadronic calorimeter (HCAL).

The central component of the ILD tracker is a Time Projection Chamber (TPC) which provides up to 224 precise measurements along the track of a charged particle. The point resolution and double-hit resolution, which are moderate when compared to silicon detectors, are compensated by continuous tracking. The TPC presents a minimum amount of material as required for the best calorimeter performance.

In order to achieve unprecedented performance with the ILD-TPC, it is important to establish a guiding principle for the development. One of the most important guiding principles is the spatial resolution of TPC. Our group has developed an analytic formula of spatial resolution for tracks which make 90° to a pad row, called “right angle tracks”, in order to understand how the spatial

resolution is determined in the TPC, and succeeded in understanding the behavior of our measured data [4, 5, 6]. In this paper, we have developed a new analytic formula which is applicable to tilted tracks. We will see that this new formula has one additional term compared to the right angle formula, and find that this additional term will consistently vanish in the new formula for the right angle tracks.

2. Charge Centroid Method

Pad Coordinate The readout pads, whose width is w and height is h, are arranged in a row to measure the x- coordinate (azimuthal direction) with charge centroid method, the y-coordinate (radial direction) from the pad row number, and the z-coordinate from the drift time. Figure 1 shows a schematic view of the pad rows.

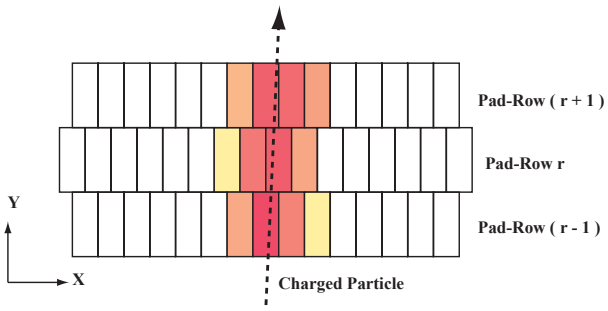

Figure 1. An enlarged illustration showing arrangement of the readout pads. We measure x coordinate at each pad row with the charge centroid method (hit reconstruction).

Charge on a Given Pad The sum of charge contributions to pad a from seed electrons originating from N primary ionizations followed by secondary ionizations resulting in M_i electrons for i-th primary ionization:

$$Q_a = \sum_{i=1}^{N} \sum_{j=1}^{M_i} G_{ij} F_a(\tilde{x} + y_i \tan\phi + \Delta x_{ij}) R(y_i + \Delta y_{ij}) + \Delta Q_a, \tag{2.1}$$

with G_{ij} being the gas gain for seed electron (ij), $F_a(x_{ij})$ being the response function of pad a in the pad row direction (PRF) and $R(y_{ij})$ being the response function in the direction normal to the pad row for seed electron (ij) arriving at $(x_{ij}, y_{ij}) := (\tilde{x} + y_i \tan\phi + \Delta x_{ij}, y_i + \Delta y_{ij})$, $\tilde{x}$ being the x-coordinate of a track at half the height of the pad row in question, y_i being y-coordinate of i-th cluster along the track with the origin at half the height of pad row in question, Δx_{ij} and Δy_{ij} being x- and y- displacements due to diffusion in the drift volume, and ΔQ_a being the electronic noise on pad a. Notice that the track in question has been regarded as a straight line (good approximation locally) and parametrized as $x = \tilde{x} + y \tan\phi$ and hence i-th primary ionization is at $(x_i, y_i) = (\tilde{x} + y_i \tan\phi, y_i)$. The charge centroid with the pad row is given by $\overline{x} = \sum_a (aw Q_a) / \sum_a Q_a$.

Probability Distribution Function for Charge Centroid The probability distribution for the charge centroid is given by

$$
\begin{aligned}
P(\overline{x};\tilde{x}) \;=\; & \sum_{N=1}^{\infty} P_{PI}(N) \prod_{i=1}^{N} \left[\int_{-\frac{\Delta Y}{2}}^{+\frac{\Delta Y}{2}} \frac{dy_i}{\Delta Y} \sum_{M_i=1}^{\infty} P_{SI}(M_i) \right. \\
& \left. \prod_{j=1}^{M_i} \left(\int_{-\infty}^{+\infty} d\Delta y_{ij} P_D(\Delta y_{ij};\sigma_d) \int_{-\infty}^{+\infty} d\Delta x_{ij} P_D(\Delta x_{ij};\sigma_d) \int d\left(\frac{G_{ij}}{\overline{G}}\right) P_G\left(\frac{G_{ij}}{\overline{G}};\theta\right) \right) \right] \\
& \times \int d\Delta Q_a \, P_E(\Delta Q_a;\sigma_E) \, \delta\left(Q_a - \sum_{i=1}^{N}\sum_{j=1}^{M_i} G_{ij} F_a(x_{ij}) R(y_{ij}) - \Delta Q_a \right) \delta\left(\overline{x} - \frac{\sum_a awQ_a}{\sum_a Q_a} \right),
\end{aligned}
\tag{2.2}
$$

with P_{PI} being the primary ionization statistics , P_{SI} being the secondary ionization statistics, P_D being the diffusion , P_G being gain fluctuation , and P_E being noise fluctuation. y_i indicates the y-position of i-th cluster, ΔY represents the range in which electrons may arrive at the pad row in question, G_{ij} ($\overline{G}$) is the gas gain for the seed electron specified by i,j (average), θ in P_G is Polya parameter, and ΔQ_a is an electric noise with $\langle \Delta Q_a \rangle_E = 0$ and $\langle \Delta Q_a^2 \rangle_E = \sigma_E^2$. Notice that $\sum_a Q_a \simeq \sum_{i=1}^{N} \sum_{j=1}^{M_i} G_{ij} R(y_{ij})$ [1].

Variance of Charge Centroid Since the probability distribution $P(\overline{x};\tilde{x})$ depends on the true location of the track $\tilde{x}$, we average over $\tilde{x}$ to define the spatial resolution $\sigma_{\overline{x}}$:

$$
\sigma_{\overline{x}}^2 := \int_{-1/2}^{+1/2} d\left(\frac{\tilde{x}}{w}\right) \int d\overline{x} \, P(\overline{x};\tilde{x}) \, (\overline{x}-\tilde{x})^2. \tag{2.3}
$$

3. Spatial Resolution Formula

Substituting the above expressions we can obtain a general formula (see Appendix A), which is not convenient to understand its physical meanings. To obtain a more useful form, we need an approximation that the width of the pad response function in the direction perpendicular to pad rows can be ignored compared with the pad length, h. Under this assumption, we can approximate $R(y_{ij})$ as

$$
R(y_{ij}) \simeq H_0\left(\frac{h}{2}+y_{ij}\right) H_0\left(\frac{h}{2}-y_{ij}\right)
$$

with H_0 being the step function. Under this assumption we can set $R(y_{ij}) = 1$ as long as y_{ij} moves within the acceptance ($-h/2 \le y \le +h/2$) of the pad row in question. The approximation is then

[1]

$$
\begin{aligned}
\sum_a Q_a \;&=\; \sum_{i=1}^{N}\sum_{j=1}^{M_i} G_{ij} \sum_a F_a(x_{ij}) R(y_{ij}) + \sum_a \Delta Q_a \\
&=\; \sum_{i=1}^{N}\sum_{j=1}^{M_i} G_{ij} R(y_{ij}) + \sum_a \Delta Q_a \\
&\simeq\; \sum_{i=1}^{N}\sum_{j=1}^{M_i} G_{ij} R(y_{ij}),
\end{aligned}
$$

where we used the sum rule : $\sum_a F_a(x_{ij}) = 1$.

tantamount to making the following replacement [2] :

$$\prod_{j=1}^{M_i}\left(\int_{-\infty}^{+\infty} dy_{ij}\, P_D(y_{ij}-y_i;\sigma_d)\right) = \prod_{j=1}^{M_i}\left(\int_{-\infty}^{+\infty} dy_{ij}\, P_D(y_{ij}-y_i;\sigma_d)\,[R(y_{ij})+(1-R(y_{ij}))]\right) \tag{3.1}$$

$$\to [\eta(y_i)+(1-\eta(y_i))]^{M_i} = \sum_{k_i=0}^{M_i} {}_{M_i}C_{k_i}\,\eta(y_i)^{k_i}(1-\eta(y_i))^{M_i-k_i}, \tag{3.2}$$

where we have defined

$$\eta(y_i) := \int_{-\infty}^{+\infty} dy_{ij}\, P_D(y_{ij}-y_i;\sigma_d)\,R(y_{ij}). \tag{3.3}$$

We can take $\eta(y_i)$ as the probability that an electron in i-th cluster is accepted in the pad row in question. Notice that now $\sum_a Q_a$ can be simply given by $\sum_{i=1}^{N}\sum_{j=1}^{k_i} G_{ij}$.

Substituting all the components, we can reduce Eq.(2.3) to a simple expression:

$$\sigma_{\tilde{x}}^2 = A(z,\phi)+\frac{1}{N_{eff}}B(z)+C(\sigma_E)+\frac{1}{\hat{N}_{eff}}D(\phi), \tag{3.4}$$

where

$$\begin{aligned}
A(z,\phi) &:= \int_{-1/2}^{+1/2} d\left(\frac{\tilde{x}}{w}\right)\left(\sum_a (aw)\left\langle\langle F_a\rangle_{\Delta x}^{y}\right\rangle_y - \tilde{x}\right)^2,\\
B(z) &:= \int_{-1/2}^{+1/2} d\left(\frac{\tilde{x}}{w}\right)\left\langle\left(\sum_a (aw)\,F_a - \sum_a (aw)\,\langle F_a\rangle_{\Delta x}\right)^2\right\rangle_{\Delta x},\\
C(\sigma_E) &:= \left(\frac{\sigma_E}{\overline{G}}\right)^2\left\langle\frac{1}{N^2}\right\rangle_N\sum_a (aw)^2,\\
D(\phi) &:= \frac{h^2\tan^2\phi}{12},
\end{aligned} \tag{3.5}$$

$$N_{eff} := \left[\left\langle\sum_{i=1}^{N} k_i\left\langle\left(\frac{G_i}{\sum_{i=1}^{N}k_iG_i}\right)^2\right\rangle_G^{\sum_{i=1}^{N}k_i}\right\rangle_{N,k}\right]^{-1}, \tag{3.6}$$

$$\begin{aligned}
\hat{N}_{eff} := \frac{h^2\tan^2\phi}{12}&\left[\int_{-1/2}^{+1/2} d\left(\frac{\tilde{x}}{w}\right)\right.\\
&\left.\times\left\langle\sum_{i=1}^{N}\left\langle\left(\sum_a (aw)\,\langle F_a\rangle_{\Delta x}^{y}-\sum_a (aw)\left\langle\langle F_a\rangle_{\Delta x}^{y}\right\rangle_y^k\right)^2\right\rangle_y^k\left\langle\left(\frac{\sum_{j=1}^{k_i}G_{ij}}{\sum_{i=1}^{N}\sum_{j=1}^{k_i}G_{ij}}\right)^2\right\rangle_G^{k,\sum_{i=1}^{N}k_i}\right\rangle_{N,k}\right]^{-1}.
\end{aligned} \tag{3.7}$$

[2] The first term, $R(y_{ij})$, in the square bracket of Eq.(3.1) restricts y_{ij} to be in the acceptance of the pad row in question, where $R(y_{ij})=1$ under our assumption, thereby corresponding to the case in which the electron specified by (i,j) arrives on the pad row. On the other hand, the second term, $\big(1-R(y_{ij})\big)$, is zero when y_{ij} is within the pad row's acceptance, thereby corresponding to the case where the electron (i,j) does not arrive on the pad row.

The brackets represent integration or summation over the variables indicated by subscripts. The superscripts show dependent variables after integration or summation. The A term represents the systematic error of the charge centroid method as known as S-shape systematics or hodoscope effect. Interestingly the B term is exactly the same as the one for right angle tracks [5, 6]. This can be shown using a relation (see Appendix C):

$$\begin{aligned}
&\int_{-1/2}^{+1/2} d\left(\frac{\tilde{x}}{w}\right) \left\langle \left(\sum_a (aw) F_a(\tilde{x} + y\tan\phi + \Delta x) - \sum_a (aw) \left\langle F_a(\tilde{x} + y\tan\phi + \Delta x) \right\rangle_{\Delta x}^{y} \right)^2 \right\rangle_{\Delta x}^{y} \\
&= \int_{-1/2}^{+1/2} d\left(\frac{\tilde{x}}{w}\right) \left\langle \left(\sum_a (aw) F_a(\tilde{x} + \Delta x) - \sum_a (aw) \left\langle F_a(\tilde{x} + \Delta x) \right\rangle_{\Delta x} \right)^2 \right\rangle_{\Delta x} . \qquad (3.8)
\end{aligned}$$

As we will see in Eq.(3.17), $\hat{N}_{eff}$ can be reduced to a simpler form for practical application.

Figure 2 shows sample calculation results of $\sigma_{\tilde{x}}^2$ for a diffusion constant of $C_D = 95\ \mu\mathrm{m}/\sqrt{\mathrm{cm}}$, track angle of $\phi = 2^\circ$, the average number of primary clusters of $\overline{N} = 38$ /cm. The cluster size distribution for pure argon data[8] is used.

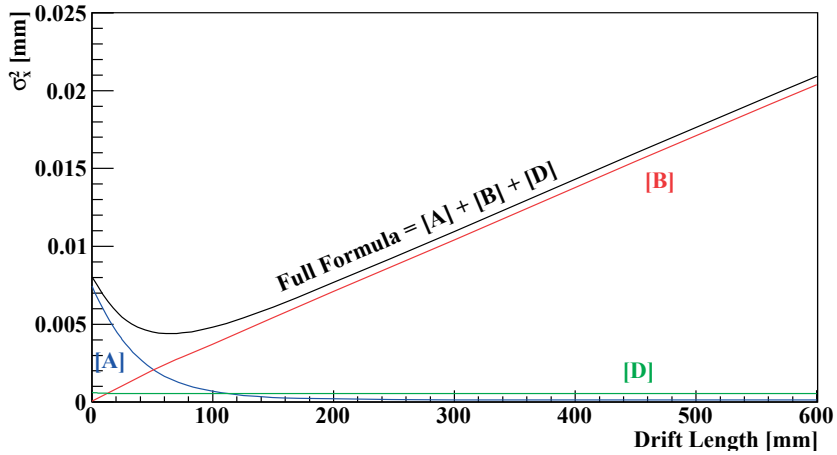

Figure 2. The black line is the analytic formula, the blue line is the A term, the red line is the B term, and the green line is the D term . The electronic noise term C is neglected.

N_{eff} corresponds to the effective number of seed electrons. In order to compare this with N_{eff} in the case of right angle tracks [4, 5, 6], let us use the approximation:

$$\overline{G} \simeq \frac{\sum_{i=1}^{N} k_i G_i}{\sum_{i=1}^{N} k_i}, \qquad (3.9)$$

we can then reduce the N_{eff} formula in Eq.(3.6) to

$$N_{eff} \simeq \left[\left\langle \frac{1}{\sum_{i=1}^{N} k_i} \right\rangle_{N,k} \left\langle \left(\frac{G}{\overline{G}} \right)^2 \right\rangle_{G} \right]^{-1} . \qquad (3.10)$$

This is exactly the same as what we expect for the right angle track case.

We will see the physical meaning of $\hat{N}_{eff}$ in the asymptotic formula later.

The point is that N_{eff} and $\hat{N}_{eff}$ defined here are almost independent of drift length in practice, e.g. ILD-TPC in which σ_d/h will not exceed 0.2 under a strong magnetic field [7] , and therefore these variables can be taken as key parameters of spatial resolution of gaseous detectors (Fig. 3). In the case of finite track angle ϕ, N_{eff}, and $\hat{N}_{eff}$ scale as $1/\cos\phi$ due to the length of track segment in each pad row.

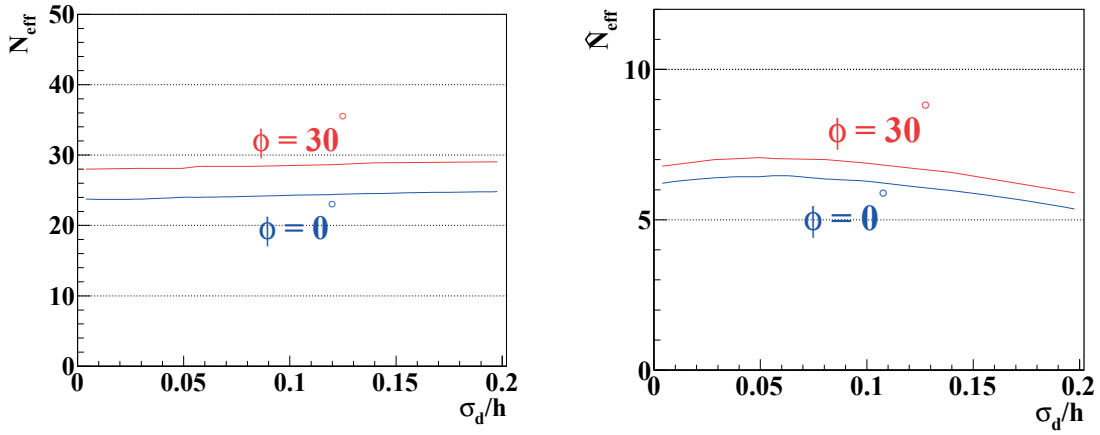

Figure 3. Sample calculation of N_{eff} (left) and $\hat{N}_{eff}$ (right) using (3.6) and (3.16) as a function of diffusion normalized with pad row height: σ_d/h. The blue line corresponds to $\phi = 0°$ and the red line corresponds to $\phi = 30°$. We assumed the pad row height of 5.26 mm, the Polya parameter $\theta = 0.5$, and the average number of primary clusters of $\overline{N} = 38$/cm. The cluster size distribution for pure argon data[8] is used.

Asymptotic Formula Let's think about the region where $\sigma_d/w > 1$ and $\sigma_d/h \ll 1$, which is actually approximately satisfied in most of drift region for practical application (e.g. ILD-TPC) and also give a useful expression to understand physical meanings. In this approximation, the average coordinate coincides exactly with the primary cluster position:

$$\sum_a (aw)\langle F_a(x_{ij})\rangle^{y_i}_{\Delta x_{ij}} \approx \tilde{x} + y_i \tan\phi, \tag{3.11}$$

$$\sum_a (aw)\langle\langle F_a(x_{ij})\rangle^{y_i}_{\Delta x_{ij}}\rangle_{y_i} \approx \tilde{x}. \tag{3.12}$$

These replacements make the A term, the B term, and $\hat{N}_{eff}$ simpler. The A term vanishes in this approximation as we expect. The B term can be written as

$$\int_{-1/2}^{+1/2} d\left(\frac{\tilde{x}}{w}\right) \left\langle \left(\sum_a (aw) F_a(\tilde{x}+\Delta x) - \tilde{x}\right)^2 \right\rangle_{\Delta x}, \tag{3.13}$$

which is independent of Δx. Using a relation given in Appendix D and the fact that the first-order term of Δx vanishes in the integration over Δx,

$$\int_{-1/2}^{+1/2} d\left(\frac{d\tilde{x}}{w}\right) \left\langle \left(\sum_a (aw) F_a(\tilde{x}+\Delta x) - (\tilde{x}+\Delta x) + \Delta x\right)^2 \right\rangle_{\Delta x}$$

$$
\begin{aligned}
&= \int_{-1/2}^{+1/2} d\left(\frac{d\tilde{x}}{w}\right) \left\langle \left(\sum_a (aw) F_a(\tilde{x}+\Delta x) - (\tilde{x}+\Delta x)\right)^2 + 2\Delta x \left(\sum_a (aw) F_a(\tilde{x}+\Delta x) - (\tilde{x}+\Delta x)\right) + \Delta x^2 \right\rangle_{\Delta x} \\
&= \int_{-1/2}^{+1/2} d\left(\frac{d\tilde{x}}{w}\right) \left\langle \left(\sum_a (aw) F_a(\tilde{x}) - \tilde{x}\right)^2 + 2\Delta x \left(\sum_a (aw) F_a(\tilde{x}) - \tilde{x}\right) + \Delta x^2 \right\rangle_{\Delta x} \\
&= \int_{-1/2}^{+1/2} d\left(\frac{d\tilde{x}}{w}\right) \left\langle \left(\sum_a (aw) F_a(\tilde{x}) - \tilde{x}\right)^2 + \Delta x^2 \right\rangle_{\Delta x} \\
&= \int_{-1/2}^{+1/2} d\left(\frac{d\tilde{x}}{w}\right) \left(\sum_a (aw) F_a(\tilde{x}) - \tilde{x}\right)^2 + \left\langle \Delta x^2 \right\rangle_{\Delta x} \\
&= A(0,0) + \sigma_D^2(z), \qquad (3.14)
\end{aligned}
$$

where we used

$$
A(0,0) \;=\; \int_{-1/2}^{+1/2} d\left(\frac{d\tilde{x}}{w}\right) \left(\sum_a (aw) F_a(\tilde{x}) - \tilde{x}\right)^2 . \qquad (3.15)
$$

See more details in Appendix F.
Using Eqs.(3.11),(3.12), Eq.(3.7) can be reduced to

$$
\begin{aligned}
\hat{N}_{eff} &\approx \frac{h^2}{12} \left[\left\langle \sum_{i=1}^{N} \left\langle y_i^2 \right\rangle_y^k \left\langle \left(\frac{\sum_{j=1}^{k_i} G_{ij}}{\sum_{i=1}^{N} \sum_{j=1}^{k_i} G_{ij}} \right)^2 \right\rangle_G^{k_i,\, \sum_{i=1}^{N} k_i} \right\rangle_{N,k} \right]^{-1} \\
&\approx \frac{h^2}{12} \left[\left\langle y^2 \right\rangle_y \left\langle \sum_{i=1}^{N} \left\langle \left(\frac{\sum_{j=1}^{k_i} G_{ij}}{\sum_{i=1}^{N} \sum_{j=1}^{k_i} G_{ij}} \right)^2 \right\rangle_G^{k_i,\, \sum_{i=1}^{N} k_i} \right\rangle_{N,k} \right]^{-1} \qquad (3.16) \\
&\sim \left[\left\langle \sum_{i=1}^{N} \left\langle \left(\frac{\sum_{j=1}^{k_i} G_{ij}}{\sum_{i=1}^{N} \sum_{j=1}^{k_i} G_{ij}} \right)^2 \right\rangle_G^{k_i,\, \sum_{i=1}^{N} k_i} \right\rangle_{N,k} \right]^{-1}, \qquad (3.17)
\end{aligned}
$$

where we used $\langle y^2 \rangle_y \simeq h^2/12$ in the last line. This can be regarded as the effective number of primary clusters for the D term. To see this more clearly, let us make the following bold assumption:

$$
\overline{\hat{G}} := \left\langle \sum_{j=1}^{k_i} G_{ij} \right\rangle \;\sim\; \frac{\sum_{i=1}^{N} \left(\sum_{j=1}^{k_i} G_{ij} \right)}{N} \;=\; \frac{\sum_{i=1}^{N} \hat{G}_i}{N},
$$

which is by no means a good approximation in most cases (where N is not so large). We then have

$$
\hat{N}_{eff} \;\sim\; \left[\left\langle \frac{1}{N} \right\rangle_N \left\langle \left(\frac{\hat{G}}{\overline{\hat{G}}} \right)^2 \right\rangle_{\hat{G}} \right]^{-1}, \qquad (3.18)
$$

which has exactly the same form as the definition of N_{eff}, where the role of individual electrons are replaced by that of individual primary clusters. This indicates that $\hat{N}_{eff}$ should be significantly smaller than N_{eff}.

We can write the asymptotic formula as:

$$
\sigma_{\overline{x}}^2 \;\approx\; \frac{(A(0,0) + C_D^2 z)}{N_{eff}} + \frac{h^2 \tan^2 \phi}{12 \hat{N}_{eff}}
$$

$$= \sigma_0^2 + \frac{C_D^2}{N_{eff}} z + \frac{h^2}{12\hat{N}_{eff}} \tan^2\phi, \tag{3.19}$$

where we defined $\sigma_0^2 \equiv A(0,0)/N_{eff}$.

4. Comparison with Data

Figure 4 shows the squared spatial resolutions σ_x^2 as a function of the drift length, for data taken with different track angles, different gas mixtures using our small/large prototype TPCs [9, 10, 11, 12]. We overlayed our analytic formula to the data. Notice that in these plots, we do not fit the data but we calculated the resolutions using some input parameters such as the average number of primary clusters, the diffusion constants, the pad response functions. We estimated the input parameters of the analytic formula from the $\phi \simeq 0$ data, and then used these parameters to plot the $\phi \simeq 10^\circ$ case. From these results we can see that the analytic formula is consistent with our measured data.

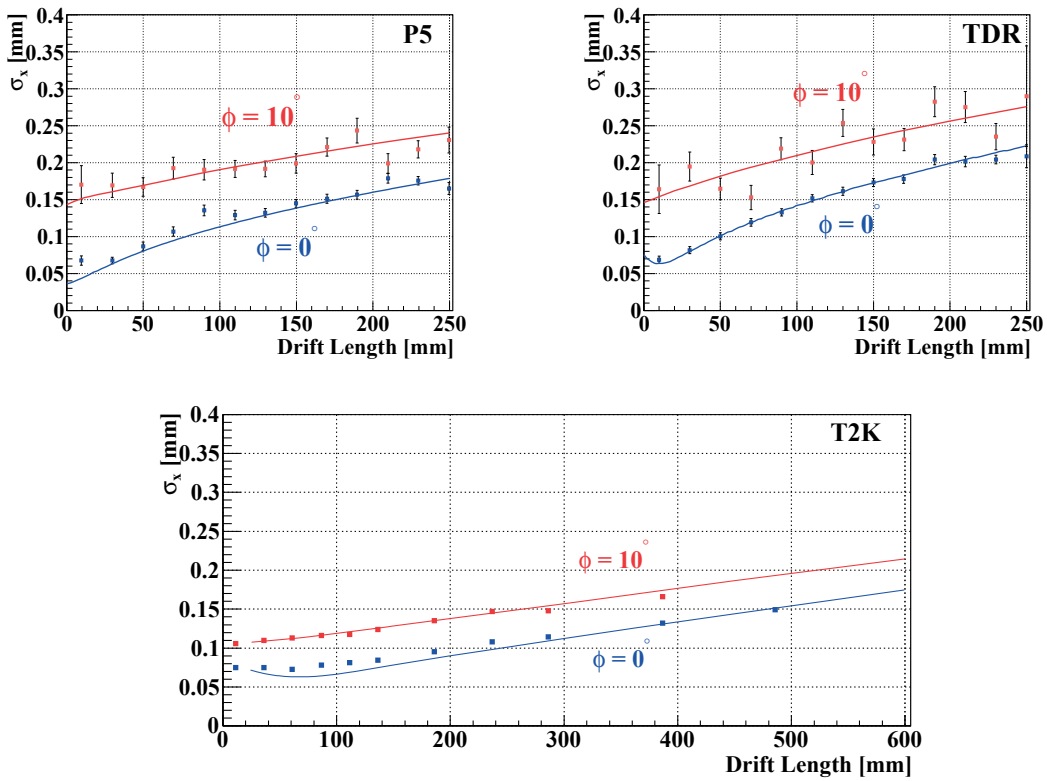

Figure 4. Spatial resolution as a function of drift length. (Top-Left) P5 gas (Ar-CH_4 (95:5)) with a small prototype TPC, (Top-Right) TDR gas (Ar-CH_4-CO_2 (93:5:2)) with a small prototype TPC, (Bottom) T2K gas (Ar-CF_4-$isoC_4H_{10}$ (95:3:2)) with a large prototype TPC. Colors indicate the track angles (Blue : $\phi = 0^\circ$, Red : $\phi = 10^\circ$). Lines show calculation and dots show the measured spatial resolutions. The applied magnetic field is 1 T.

5. Conclusion

We have developed an analytic formula for the spatial resolution as part of our TPC R&D. The formula is applicable to arbitrary incident angles. Compared with the conventional Monte Carlo method, the analytic formula has many advantages. By examining physical meanings of each term of the formula, we can identify what factor mainly contributes to the spatial resolution, which help us find a way to improve the spatial resolution. The important point is that the spatial resolution is characterized by the basic parameters such as the pad size, C_d, PRF, N_{eff}, and $\hat{N}_{eff}$, which are obtained from either measured data or simulation.

Acknowledgments

This work is partly supported by Grant-in-Aid for Creative Research No.18GS0202 and Grant-in-Aid for Specially Promoted Research No. 23000002 by Japan Society for Promotion of Science (JSPS). We thank for valuable discussions and support from the LCTPC collaboration members.

A. General expression for spatial resolution

$$
\begin{aligned}
\sigma_{\tilde{x}}^2 \simeq & \int_{-1/2}^{+1/2} d\left(\frac{\tilde{x}}{w}\right) \sum_{N=1}^{\infty} P_{PI}(N) \prod_{i=1}^{N} \left[\int_{-\frac{\Delta Y}{2}}^{+\frac{\Delta Y}{2}} \frac{dy_i}{\Delta Y} \sum_{M_i=1}^{\infty} P_{SI}(M_i) \right. \\
& \left. \prod_{j=1}^{M_i} \left(\int_{-\infty}^{+\infty} d\Delta y_{ij} P_D(\Delta y_{ij};\sigma_d) \int_{-\infty}^{+\infty} d\Delta x_{ij} P_D(\Delta x_{ij};\sigma_d) \int d\left(\frac{G_{ij}}{\overline{G}}\right) P_G\left(\frac{G_{ij}}{\overline{G}};\theta\right) \right) \right] \\
& \times \left\{ \frac{\sum_a (aw) \sum_{i=1}^{N} \sum_{j=1}^{M_i} G_{ij} F_a(x_{ij}) R(y_{ij})}{\sum_{i=1}^{N} \sum_{j=1}^{M_i} G_{ij} R(y_{ij})} - \tilde{x} \right\}^2 \\
& + \int_{-1/2}^{+1/2} d\left(\frac{\tilde{x}}{w}\right) \sum_{N=1}^{\infty} P_{PI}(N) \prod_{i=1}^{N} \left[\int_{-\frac{\Delta Y}{2}}^{+\frac{\Delta Y}{2}} \frac{dy_i}{\Delta Y} \sum_{M_i=1}^{\infty} P_{SI}(M_i) \right. \\
& \left. \prod_{j=1}^{M_i} \left(\int_{-\infty}^{+\infty} d\Delta y_{ij} P_D(\Delta y_{ij};\sigma_d) \int_{-\infty}^{+\infty} d\Delta x_{ij} P_D(\Delta x_{ij};\sigma_d) \int d\left(\frac{G_{ij}}{\overline{G}}\right) P_G\left(\frac{G_{ij}}{\overline{G}};\theta\right) \right) \right] \\
& \times \int d\Delta Q_a P_E(\Delta Q_a;\sigma_E) \left\{ \frac{\sum_a (aw) \Delta Q_a}{\sum_{i=1}^{N} \sum_{j=1}^{M_i} G_{ij} R(y_{ij})} \right\}^2,
\end{aligned}
$$

where y_i indicates the y-position of i-th cluster, ΔY represents the range in which electronics may arrive at the pad row in question, G_{ij} ($\overline{G}$) is the gas gain for the seed electron specified by i,j (average), θ in P_G is Polya parameter, and ΔQ_a is an electric noise with $\langle \Delta Q_a \rangle_E = 0$ and $\langle \Delta Q_a^2 \rangle_E = \sigma_E^2$.

By changing one of the integration variables from Δy_{ij} to $y_{ij} = y_i + \Delta y_{ij}$, we obtain

$$
\begin{aligned}
\sigma_{\tilde{x}}^2 \simeq & \int_{-1/2}^{+1/2} d\left(\frac{\tilde{x}}{w}\right) \sum_{N=1}^{\infty} P_{PI}(N) \prod_{i=1}^{N} \left[\int_{-\frac{\Delta Y}{2}}^{+\frac{\Delta Y}{2}} \frac{dy_i}{\Delta Y} \sum_{M_i=1}^{\infty} P_{SI}(M_i) \right. \\
& \left. \prod_{j=1}^{M_i} \left(\int_{-\infty}^{+\infty} dy_{ij} P_D(y_{ij} - y_i;\sigma_d) \int_{-\infty}^{+\infty} d\Delta x_{ij} P_D(\Delta x_{ij};\sigma_d) \int d\left(\frac{G_{ij}}{\overline{G}}\right) P_G\left(\frac{G_{ij}}{\overline{G}};\theta\right) \right) \right]
\end{aligned}
$$

$$\times \left\{ \frac{\sum_a (aw) \sum_{i=1}^{N} \sum_{j=1}^{M_i} G_{ij} F_a(\tilde{x} + y_i \tan\phi + \Delta x_{ij}) R(y_{ij})}{\sum_{i=1}^{N} \sum_{j=1}^{M_i} G_{ij} R(y_{ij})} - \tilde{x} \right\}^2$$

$$+ \sum_{N=1}^{\infty} P_{PI}(N) \prod_{i=1}^{N} \left[\int_{-\frac{\Delta Y}{2}}^{+\frac{\Delta Y}{2}} \frac{dy_i}{\Delta Y} \sum_{M_i=1}^{\infty} P_{SI}(M_i) \right.$$
$$\left. \prod_{j=1}^{M_i} \left(\int_{-\infty}^{+\infty} dy_{ij} P_D(y_{ij} - y_i; \sigma_d) \int d\left(\frac{G_{ij}}{\overline{G}}\right) P_G\left(\frac{G_{ij}}{\overline{G}}; \theta\right) \right) \right]$$
$$\times \sigma_E^2 \sum_a (aw)^2 \left\{ \frac{1}{\left(\sum_{i=1}^{N} \sum_{j=1}^{M_i} G_{ij} R(y_{ij}) \right)^2} \right\}, \tag{A.1}$$

where $\tilde{x}$, Δx_{ij}, and Q_E integrations, which are trivial for the second term (the electronic noise term), have been carried out. The quantity sandwiched by the braces in the second term is the inverse square of the total charge, $Q := \sum_a Q_a$, collected by the pad row in question. The summations over N and M_i and the integrations over dy_i, dy_{ij}, and G_{ij} mean that the average of this quantity should be taken:

$$\left\langle \frac{1}{Q^2} \right\rangle_{G,\Delta y, M_i, y_i, N} := \sum_{N=1}^{\infty} P_{PI}(N) \prod_{i=1}^{N} \left[\int_{-\frac{\Delta Y}{2}}^{+\frac{\Delta Y}{2}} \frac{dy_i}{\Delta Y} \sum_{M_i=1}^{\infty} P_{SI}(M_i) \right.$$
$$\left. \prod_{j=1}^{M_i} \left(\int_{-\infty}^{+\infty} dy_{ij} P_D(y_{ij} - y_i; \sigma_d) \int d\left(\frac{G_{ij}}{\overline{G}}\right) P_G\left(\frac{G_{ij}}{\overline{G}}; \theta\right) \right) \right]$$
$$\times \left\{ \frac{1}{\left(\sum_{i=1}^{N} \sum_{j=1}^{M_i} G_{ij} R(y_{ij}) \right)^2} \right\}. \tag{A.2}$$

With this definition we can now express the contribution from the electronic noise to the spatial resolution as

$$\sigma_{\tilde{x},E}^2 := \sigma_E^2 \sum_a (aw)^2 \left\langle \frac{1}{Q^2} \right\rangle_{G,\Delta y, M_i, y_i, N}. \tag{A.3}$$

Let us again move on to further reducing the first term of Eq.(A.1). We will drop the electronic noise contribution in what follows, for notation economy. The spatial resolution formula then becomes

$$\sigma_{\tilde{x}}^2 \simeq \int_{-1/2}^{+1/2} d\left(\frac{\tilde{x}}{w}\right) \sum_{N=1}^{\infty} P_{PI}(N) \prod_{i=1}^{N} \left[\int_{-\frac{\Delta Y}{2}}^{+\frac{\Delta Y}{2}} \frac{dy_i}{\Delta Y} \sum_{M_i=1}^{\infty} P_{SI}(M_i) \right.$$
$$\left. \prod_{j=1}^{M_i} \left(\int_{-\infty}^{+\infty} dy_{ij} P_D(y_{ij} - y_i; \sigma_d) \int_{-\infty}^{+\infty} d\Delta x_{ij} P_D(\Delta x_{ij}; \sigma_d) \int d\left(\frac{G_{ij}}{\overline{G}}\right) P_G\left(\frac{G_{ij}}{\overline{G}}; \theta\right) \right) \right]$$
$$\times \left\{ \frac{\sum_a (aw) \sum_{i=1}^{N} \sum_{j=1}^{M_i} G_{ij} F_a(\tilde{x} + y_i \tan\phi + \Delta x_{ij}) R(y_{ij})}{\sum_{i=1}^{N} \sum_{j=1}^{M_i} G_{ij} R(y_{ij})} - \tilde{x} \right\}^2.$$

Notice here that Δx_{ij} appears only through F_a, which motivates us to define

$$\langle F_a \rangle_{\Delta x}^{y_i} := \int_{-\infty}^{+\infty} d\Delta x_{ij} P_D(\Delta x_{ij}; \sigma_d) F_a(\tilde{x} + y_i \tan\phi + \Delta x_{ij})$$

$$\langle F_a F_b \rangle_{\Delta x}^{y_i} := \int_{-\infty}^{+\infty} d\Delta x_{ij} P_D(\Delta x_{ij};\sigma_d)\, F_a(\tilde{x}+y_i\tan\phi+\Delta x_{ij})\, F_b(\tilde{x}+y_i\tan\phi+\Delta x_{ij}), \quad \text{(A.4)}$$

where y_i dependence indicated as a superfix vanishes if $\tan\phi = 0$. With these defined the above equation for the spatial resolution reduces to

$$\begin{aligned}
\sigma_{\tilde{x}}^2 \simeq & \int_{-1/2}^{+1/2} d\left(\frac{\tilde{x}}{w}\right) \sum_{N=1}^{\infty} P_{PI}(N) \prod_{i=1}^{N} \left[\int_{-\frac{\Delta Y}{2}}^{+\frac{\Delta Y}{2}} \frac{dy_i}{\Delta Y} \sum_{M_i=1}^{\infty} P_{SI}(M_i) \right. \\
& \left. \prod_{j=1}^{M_i} \left(\int d\left(\frac{G_{ij}}{\overline{G}}\right) P_G\left(\frac{G_{ij}}{\overline{G}};\theta\right) \int_{-\infty}^{+\infty} dy_{ij}\, P_D(y_{ij}-y_i;\sigma_d) \right) \right] \\
& \times \left\{ \frac{\sum_{a,b}(abw^2) \sum_{i=1}^{N} \left[\langle F_a F_b \rangle_{\Delta x}^{y_i} - \langle F_a \rangle_{\Delta x}^{y_i} \langle F_b \rangle_{\Delta x}^{y_i} \right] \sum_{j=1}^{M_i} (G_{ij} R(y_{ij}))^2}{\left(\sum_{i=1}^{N} \sum_{j=1}^{M_i} G_{ij} R(y_{ij}) \right)^2} \right. \\
& \left. + \left(\frac{\sum_a (aw) \sum_{i=1}^{N} \langle F_a \rangle_{\Delta x}^{y_i} \sum_{j=1}^{M_i} G_{ij} R(y_{ij})}{\sum_{i=1}^{N} \sum_{j=1}^{M_i} G_{ij} R(y_{ij})} - \tilde{x} \right)^2 \right\}. \quad \text{(A.5)}
\end{aligned}$$

B. Theorem 1

The pad response function $F_a(\tilde{x})$ satisfies the following equation with pad width w:

$$F_a(\tilde{x}+w) = F_{a-1}(\tilde{x}). \quad \text{(B.1)}$$

Proof:

We can write the pad response function with arbitrary distribution P as follows:

$$F_a(\tilde{x}) := \int_{(a-\frac{1}{2})w}^{(a+\frac{1}{2})w} dx P(x-\tilde{x}), \quad \text{(B.2)}$$

then

$$\begin{aligned}
F_a(\tilde{x}+w) &= \int_{(a-\frac{1}{2})w}^{(a+\frac{1}{2})w} dx P(x-\tilde{x}-w) \\
&= \int_{(a-1-\frac{1}{2})w}^{(a-1+\frac{1}{2})w} dx' P(x'-\tilde{x}) \\
&= F_{a-1}(\tilde{x}). \quad \text{(B.3)}
\end{aligned}$$

C. Theorem 2

If

$$\begin{aligned}
& F_a(\tilde{x}+w) = F_{a-1}(\tilde{x}), \\
& \sum_a F_a(\tilde{x}) = 1 \\
& \int d\Delta x P(\Delta x) = 1, \quad \text{(C.1)}
\end{aligned}$$

then

$$\begin{aligned}
&\int_{-1/2}^{+1/2} d\left(\frac{\tilde{x}}{w}\right) \int d\Delta x P(\Delta x) \left[\sum_a (aw) F_a(\tilde{x}+\Delta x) - \sum_a (aw) \int d\Delta x' P(\Delta x') F_a(\tilde{x}+\Delta x')\right]^2 \\
&= \int_{-1/2}^{+1/2} d\left(\frac{\tilde{x}}{w}\right) \int d\Delta x P(\Delta x) \\
&\qquad \times \left[\sum_a (aw) F_a(\tilde{x}+\varepsilon+\Delta x) - \sum_a (aw) \int d\Delta x' P(\Delta x') F_a(\tilde{x}+\varepsilon+\Delta x')\right]^2 . \qquad \text{(C.2)}
\end{aligned}$$

Proof:

Our goal is to prove

$$\begin{aligned}
&\frac{d}{d\varepsilon} \int_{-1/2+\varepsilon}^{+1/2+\varepsilon} d\left(\frac{\tilde{x}}{w}\right) \int d\Delta x P(\Delta x) \\
&\qquad \times \left[\sum_a (aw) F_a(\tilde{x}+\Delta x) - \sum_a (aw) \int d\Delta x' P(\Delta x') F_a(\tilde{x}+\Delta x')\right]^2 = 0. \qquad \text{(C.3)}
\end{aligned}$$

With the fundamental theorem of calculus, we have

$$\frac{d}{d\varepsilon} \int_{\alpha+\varepsilon}^{\beta+\varepsilon} d\xi F(\xi) = F(\beta+\varepsilon) - F(\alpha+\varepsilon), \qquad \text{(C.4)}$$

and the left-hand side of Eq.(C.3) can be modified using Theorem 1 in shape as

$$\begin{aligned}
&\frac{d}{d\varepsilon} \int_{-1/2+\varepsilon}^{+1/2+\varepsilon} d\left(\frac{\tilde{x}}{w}\right) \int d\Delta x P(\Delta x) \left[\sum_a (aw) F_a(\tilde{x}+\Delta x) - \sum_a (aw) \int d\Delta x' P(\Delta x') F_a(\tilde{x}+\Delta x')\right]^2 \\
&= \int d\Delta x P(\Delta x) \times \\
&\quad \left[\left\{\sum_a (aw) F_a(\frac{1}{2}w+\varepsilon w+\Delta x) - \sum_a (aw) \int d\Delta x' P(\Delta x') F_a\left(\frac{1}{2}w+\varepsilon w+\Delta x'\right)\right\}^2 \right. \\
&\qquad \left. - \left\{\sum_a (aw) F_a(-\frac{1}{2}w+\varepsilon w+\Delta x) - \sum_a (aw) \int d\Delta x' P(\Delta x') F_a\left(-\frac{1}{2}w+\varepsilon w+\Delta x'\right)\right\}^2\right] \\
&= \int d\Delta x P(\Delta x) \times \\
&\quad \left[\sum_a (aw) \left\{F_a(\frac{1}{2}w+\varepsilon w+\Delta x) - F_a(-\frac{1}{2}w+\varepsilon w+\Delta x)\right\} \right. \\
&\qquad \left. - \sum_a (aw) \int d\Delta x' P(\Delta x') \left\{F_a\left(\frac{1}{2}w+\varepsilon w+\Delta x'\right) - F_a\left(-\frac{1}{2}w+\varepsilon w+\Delta x'\right)\right\}\right] \times \\
&\quad \left[\sum_a (aw) \left\{F_a(\frac{1}{2}w+\varepsilon w+\Delta x) + F_a(-\frac{1}{2}w+\varepsilon w+\Delta x)\right\} \right. \\
&\qquad \left. - \sum_a (aw) \int d\Delta x' P(\Delta x') \left\{F_a\left(\frac{1}{2}w+\varepsilon w+\Delta x'\right) + F_a\left(-\frac{1}{2}w+\varepsilon w+\Delta x'\right)\right\}\right] \\
&= \int d\Delta x P(\Delta x) \times \\
&\quad \left[\sum_a (aw) \left\{F_a(\frac{1}{2}w+\varepsilon w+\Delta x) - F_{a-1}(\frac{1}{2}w+\varepsilon w+\Delta x)\right\}\right.
\end{aligned}$$

$$
\begin{aligned}
&\quad -\sum_a (aw)\int d\Delta x' P(\Delta x')\left\{F_a\left(\frac{1}{2}w+\varepsilon w+\Delta x'\right)-F_{a-1}\left(\frac{1}{2}w+\varepsilon w+\Delta x'\right)\right\}\Bigg]\times\\
&\Bigg[\sum_a (aw)\left\{F_a(\frac{1}{2}w+\varepsilon w+\Delta x)+F_a(-\frac{1}{2}w+\varepsilon w+\Delta x)\right\}\\
&\quad -\sum_a (aw)\int d\Delta x' P(\Delta x')\left\{F_a\left(\frac{1}{2}w+\varepsilon w+\Delta x'\right)+F_a\left(-\frac{1}{2}w+\varepsilon w+\Delta x'\right)\right\}\Bigg]\\
&=\int d\Delta x P(\Delta x)\times\\
&\Bigg[\left\{\sum_a (aw)F_a(\frac{1}{2}w+\varepsilon w+\Delta x)-\sum_a (a-1)wF_{a-1}(\frac{1}{2}w+\varepsilon w+\Delta x)+w\right\}\\
&\quad -\int d\Delta x' P(\Delta x')\left\{\sum_a (aw)F_a\left(\frac{1}{2}w+\varepsilon w+\Delta x'\right)-\sum_a (a-1)wF_{a-1}\left(\frac{1}{2}w+\varepsilon w+\Delta x'\right)+w\right\}\Bigg]\times\\
&\Bigg[\sum_a (aw)\left\{F_a(\frac{1}{2}w+\varepsilon w+\Delta x)+F_a(-\frac{1}{2}w+\varepsilon w+\Delta x)\right\}\\
&\quad -\sum_a (aw)\int d\Delta x' P(\Delta x')\left\{F_a\left(\frac{1}{2}w+\varepsilon w+\Delta x'\right)+F_a\left(-\frac{1}{2}w+\varepsilon w+\Delta x'\right)\right\}\Bigg]\\
&=\int d\Delta x P(\Delta x)\ \left(w-\int d\Delta x' P(\Delta x')w\right)\\
&\quad \Bigg[\sum_a (aw)\left\{F_a(\frac{1}{2}w+\varepsilon w+\Delta x)+F_a(-\frac{1}{2}w+\varepsilon w+\Delta x)\right\}\\
&\quad -\sum_a (aw)\int d\Delta x' P(\Delta x')\left\{F_a\left(\frac{1}{2}w+\varepsilon w+\Delta x'\right)+F_a\left(-\frac{1}{2}w+\varepsilon w+\Delta x'\right)\right\}\Bigg]\\
&=0. \qquad \text{(C.5)}
\end{aligned}
$$

D. Theorem 3

If

$$
\begin{aligned}
&F_a(\tilde{x}+w)=F_{a-1}(\tilde{x}),\\
&\sum_a F_a(\tilde{x})=1\\
&\int d\Delta x P(\Delta x)=1, \qquad \text{(D.1)}
\end{aligned}
$$

then

$$
\int_{-1/2}^{+1/2} d\left(\frac{\tilde{x}}{w}\right)\left(\sum_a (aw)F_a(\tilde{x}+\Delta x)-(\tilde{x}+\Delta x)\right)^n=\int_{-1/2}^{+1/2} d\left(\frac{\tilde{x}}{w}\right)\left(\sum_a (aw)F_a(\tilde{x})-\tilde{x}\right)^n \qquad \text{(D.2)}
$$

Proof:

Using g in theorem of Appendix E, our goal is to prove

$$
\frac{d}{d\varepsilon}\int_{-1/2}^{+1/2} d\left(\frac{\tilde{x}}{w}\right) g(\tilde{x}+\varepsilon)=0. \qquad \text{(D.3)}
$$

$$
\frac{d}{d\varepsilon}\int_{-1/2}^{+1/2} d\left(\frac{\tilde{x}}{w}\right) g(\tilde{x}+\varepsilon)\ =\ \frac{d}{d\varepsilon}\int_{-1/2-\varepsilon}^{+1/2-\varepsilon} d\left(\frac{\tilde{x}'}{w}\right) g(\tilde{x}')
$$

$$= \frac{d}{d\varepsilon}\int_{-1/2-\varepsilon}^{+1/2-\varepsilon} d\left(\frac{\tilde{x'}}{w}\right) g(\tilde{x'}). \tag{D.4}$$

With the fundamental theorem of calculus, we have

$$\frac{d}{d\varepsilon}\int_{\alpha+\varepsilon}^{\beta+\varepsilon} d\xi F(\xi) = F(\beta+\varepsilon) - F(\alpha+\varepsilon). \tag{D.5}$$

Then Eq.(D.4) becomes

$$\begin{aligned} g\left(\frac{1}{2}w-\varepsilon w\right) - g\left(-\frac{1}{2}w-\varepsilon w\right) &= g\left(\frac{1}{2}w-\varepsilon w\right) - g\left(-\frac{1}{2}w-\varepsilon w+w\right) \\ &= 0, \end{aligned} \tag{D.6}$$

where we used theorem 4 in the last line.

E. Theorem 4

When we define g with an arbitrary number n as follows:

$$g(\tilde{x}) := \left(\sum_a (aw)F_a(\tilde{x}) - \tilde{x}\right)^n, \tag{E.1}$$

the following equation is satisfied:

$$g(\tilde{x}+w) = g(\tilde{x}) \tag{E.2}$$

if

$$\begin{aligned} &F_a(\tilde{x}+w) = F_{a-1}(\tilde{x}), \\ &\sum_a F_a(\tilde{x}) = 1, \\ &\int d\Delta x P(\Delta x) = 1. \end{aligned} \tag{E.3}$$

Proof:

$$\begin{aligned} g(\tilde{x}+w) &= \left(\sum_a (aw)F_a(\tilde{x}+w) - (\tilde{x}+w)\right)^n \\ &= \left(\sum_a (aw)F_{a-1}(\tilde{x}) - (\tilde{x}+w)\right)^n \\ &= \left(\sum_a ((a-1)w+w)F_{a-1}(\tilde{x}) - (\tilde{x}+w)\right)^n \\ &= \left(\sum_{a-1} (a-1)wF_{a-1}(\tilde{x}) - \tilde{x}\right)^n \\ &= g(\tilde{x}) \end{aligned} \tag{E.4}$$

F. $A(0,0)$ in the B term

We find the constant term ($A(0,0)$) in the B term in Eq.(3.15) coincide with the $z \to 0$ limit of the A term:

$$\begin{aligned}
\lim_{z\to 0}[A] &= \lim_{\sigma_d\to 0}\int_{-1/2}^{+1/2} d\left(\frac{\tilde{x}}{w}\right)\left(\sum_a (aw)\left\langle F_a(\tilde{x}+\Delta x)\right\rangle_{\Delta x} - \tilde{x}\right)^2 \\
&= \lim_{\sigma_d\to 0}\int_{-1/2}^{+1/2} d\left(\frac{\tilde{x}}{w}\right)\left(\sum_a (aw)\int_{-\infty}^{+\infty}\frac{d\Delta x}{\sqrt{2\pi}\sigma_d}\exp\left[-\frac{1}{2}\left(\frac{\Delta x}{\sigma_d}\right)^2\right]F_a(\tilde{x}+\Delta x) - \tilde{x}\right)^2 \\
&= \int_{-1/2}^{+1/2} d\left(\frac{\tilde{x}}{w}\right)\left(\sum_a (aw)\lim_{\sigma_d\to 0}\int_{-\infty}^{+\infty}\frac{d\Delta x}{\sqrt{2\pi}\sigma_d}\exp\left[-\frac{1}{2}\left(\frac{\Delta x}{\sigma_d}\right)^2\right]F_a(\tilde{x}+\Delta x) - \tilde{x}\right)^2 \\
&= \int_{-1/2}^{+1/2} d\left(\frac{\tilde{x}}{w}\right)\left(\sum_a (aw)\int_{-\infty}^{+\infty} d\Delta x\,\delta(\Delta x)F_a(\tilde{x}+\Delta x) - \tilde{x}\right)^2 \\
&= \int_{-1/2}^{+1/2} d\left(\frac{\tilde{x}}{w}\right)\left(\sum_a (aw)F_a(\tilde{x}) - \tilde{x}\right)^2 .
\end{aligned}$$

This is why we express the constant term as $A(0,0)$.

References

[1] *ILC Technical Design Report*, *http://www.linearcollider.org/ILC/Publications/Technical-Design-Report*.

[2] Jean-Claude Brient and Henri Videau, *The calorimetry at the future e+ e- linear collider*, `hep-ex/0202004v1` (2002).

[3] M. A. Thomson, *Particle Flow Calorimetry and the PandoraPFA Algorithm*, *Nucl. Instrum. Meth.* **A 611** (2009) 25.

[4] M. Kobayashi, *An estimation of the effective number of electrons contributing to the coordinate measurement with a TPC*, *Nucl. Instrum. Meth.* **A 562** (2006) 136.

[5] D.C. Arogancia et al., *Study in a beam test of the resolution of a Micromegas TPC with standard readout pads*, *Nucl. Instrum. Meth.* **A 602** (2009) 403.

[6] M. Kobayashi et al., *Cosmic ray tests of a GEM-based TPC prototype operated in Ar-CF4-isobutane gas mixtures*, *Nucl. Instrum. Meth.* **A 641** (2011) 37.

[7] M. Kobayashi, *An estimation of the effective number of electrons contributing to the coordinate measurement with a TPC : II*, *Nucl. Instrum. Meth.* **A 729** (2013) 273.

[8] Fischle Hansjorg and Heintze Joachim and Schmidt Bernhard, *Experimental determination of ionization cluster size distributions in counting gases*, *Nucl. Instrum. Meth.* **A 301** (1991) 202.

[9] M. Kobayashi et al., *Performance of MPGD-based TPC prototypes for the linear collider experiment*, *Nucl. Instrum. Meth.* **A 581** (2007) 265.

[10] K. Ackermann et al., *Cosmic Ray Tests of the Prototype TPC for the ILC Experiment*, arXiv:0905.2655 (2009).

[11] K. Ackermann et al., *A study with a small prototype TPC for the international linear collider experiment*, *Nucl. Instrum. Meth.* **A 623** (2010) 141.

[12] R. Yonamine on behalf of LCTPC collaboration, *R & D of MPGD-readout TPC for the International Linear Collider experiment* , 2012 *JINST* **7** C06011.

Higgs Boson Decays to Tau Pairs at the ILC with the ILD Detector

Shin-ichi Kawada[1], Keisuke Fujii[2], Taikan Suehara[3], Tohru Takahashi[1] and Tomohiko Tanabe[4]

[1]*Advanced Sciences of Matter, Hiroshima University, Hiroshima 739-8530, Japan*
[2]*High Energy Accelerator Research Organization, Ibaraki 305-0801, Japan*
[3]*Department of Physics, Tohoku University, Miyagi 980-8578, Japan*
[4]*International Center for Elementary Particle Physics, The University of Tokyo, Tokyo 113-0033, Japan*

E-mail: s-kawada@huhep.org

(Received July 15, 2013)

The investigation of the Higgs boson, especially the verificatio of the mass generation mechanism, is one of the most important themes for particle physics after the discovery of the Higgs boson. To achieve this, the International Linear Collider (ILC) is proposed as a next generation electron-positron collider. We evaluate the measurement accuracy of the Higgs branching ratio into tau pairs at the ILC with a full simulation of the ILD detector concept. We assume a center-of-mass energy of $\sqrt{s}$ = 250 GeV, beam polarizations of $P(e^-, e^+) = (0.8, +0.3)$, and an integrated luminosity of 250 fb^{-1}. We obtain the measurement accuracy $\Delta(\sigma \cdot \mathrm{Br})/(\sigma \cdot \mathrm{Br}) = 3.5$ % for a Higgs boson mass of M_h = 120 GeV. The result scaled to M_h = 125 GeV is estimated to be 4.2 %.

KEYWORDS: Higgs boson, International Linear Collider (ILC)

1. Introduction

After the discovery of the Higgs boson [1, 2], the investigation of that particle has become one of the most important problems for the particle physics, especially the verificatio of the mass generation mechanism. In the Standard Model (SM), the Yukawa coupling of matter fermions with the Higgs boson is proportional to the fermion mass. If there exists new physics beyond the SM, the coupling constant will deviate from the SM prediction. The deviation from the SM is estimated as a few-percent level if no additional new particles are to be found at the LHC [3]. This motivates the precise measurement of the Higgs coupling constants. Moreover, the Higgs branching ratio to tau pairs is an excellent probe for testing new physics effects in the Yukawa coupling because of the relatively small uncertainty in the tau mass. This is not the case for the hadronic Higgs decays.

Searches for Higgs decays into a tau pair at the LHC are not yet sensitive to observe these decays. ATLAS and CMS report a local significanc of 1.1 and 2.9 standard deviations, respectively, from the background-only hypothesis for a Higgs boson of mass 125 GeV using the full 7 and 8 TeV dataset [4, 5]. With 300 fb^{-1} data, it is estimated that the signal strength could be measured to 5-15% [6, 7]. The branching ratio cannot be extracted in a model-independent way at the LHC.

The International Linear Collider (ILC) is proposed as a next generation accelerator, which can measure the properties of Higgs boson precisely. The ILC is an electron-position collider, providing a clean environment ideal for precision measurement. The ILC Technical Design Report is published in June 2013 [8–11].

The International Large Detector (ILD) and the Silicon Detector (SiD) are being developed as detector concepts for the ILC. The ILD consists of a vertex detector, a time projection chamber, an

electromagnetic calorimeter (ECAL), a hadronic calorimeter (HCAL), a return yoke, muon systems, and forward components. Details of the ILD concept can be found in Ref. [11].

We evaluate the measurement accuracy of the branching ratio Br($h \to \tau^+\tau^-$) assuming a center-of-mass energy $\sqrt{s} = 250$ GeV at the ILC using the ILD detector model for the full simulation. In this proceeding, we describe the results obtained with $M_h = 120$ GeV under these conditions, and also give the rescaled results for $M_h = 125$ GeV.

2. Signal, Background, and Simulation Framework

At $\sqrt{s} = 250$ GeV, the main Higgs production process is via the Higgs-strahlung process ($e^+e^- \to Zh$). There are several final states depending on the decay mode of the Z boson as illustrated in Fig. 1. The Z decay mode most sensitive to the measurement of Br($h \to \tau^+\tau^-$) at $\sqrt{s} = 250$ GeV is the $Z \to q\bar{q}$ mode because it offers high statistics. We describe the details of the analysis of the $Z \to q\bar{q}$ mode in this study. The analysis of other processes can be found in Ref. [12].

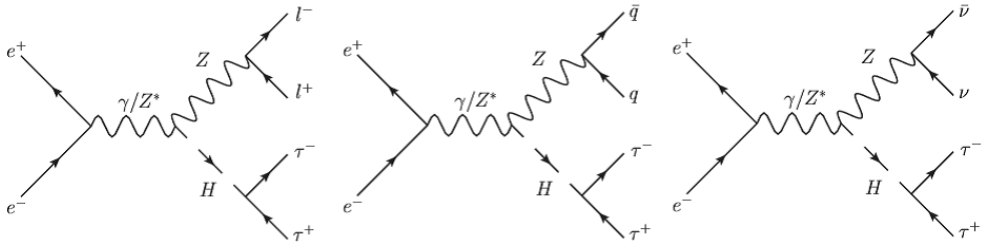

Fig. 1. The signal processes: $Z \to \ell^+\ell^-$ mode (left), $Z \to q\bar{q}$ mode (middle), and $Z \to \nu\bar{\nu}$ mode (right).

The cross section of $e^+e^- \to Zh$ with $Z \to q\bar{q}$ is 19.8 fb. The possible background processes to this signal are $q\bar{q}q\bar{q}$, $q\bar{q}\ell^+\ell^-$, and $q\bar{q}\ell\nu$, which are generated via $e^+e^- \to W^+W^-$ or ZZ. Another possible source of background is the $e^+e^- \to Zh$ process with $Z \to \ell^+\ell^-$ and $h \to q\bar{q}$. Figure 2 shows the diagrams for the background processes.

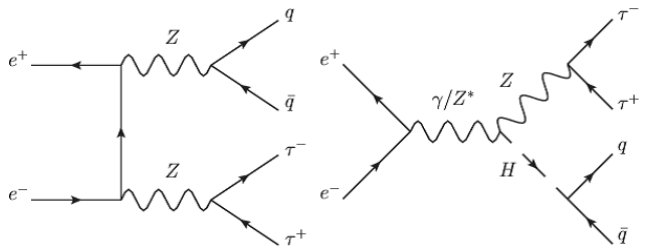

Fig. 2. The diagrams of background processes: $q\bar{q}\tau^+\tau^-$ via $e^+e^- \to ZZ$ (left) and $q\bar{q}\tau^+\tau^-$ via $e^+e^- \to Zh$ (right).

We perform a full detector simulation using Mokka [13], based on Geant4 [14] full simulation, with the ILD detector model (ILD_00 model). TAUOLA [15] is used for the simulation of tau decays.

We use signal and background samples assuming $\sqrt{s} = 250$ GeV, which were generated in the context of the Letter of Intent process of ILC detectors [16]. We assume a Higgs mass of $M_h = 120$ GeV, a branching ratio Br($h \to \tau^+\tau^-$) = 8.0 % assumed by PYTHIA [17], an integrated luminosity $\int L\,dt = 250$ fb^{-1}, and beam polarizations of $P(e^-, e^+) = (-0.8, +0.3)$.

3. Analysis Method and Result

For the $Z \to q\bar{q}$ mode, we reconstruct taus from Higgs boson first followed by the reconstruction of Z boson. We begin by applying a tau finde to all the objects. This tau finde searches for charged particle with the highest energy in the event and attaches to it the neighboring particles ($\cos\theta_{\rm cone} > 0.98$) with the requirement that the combined mass is less than 2 GeV. The combined objects are regarded as the tau jets. The soft charged particles in the tau jet, with an energy less than 2 GeV, are detached one by one from the smallest energy until the number of tracks becomes 1 or 3, and the total charge in the tau jet becomes ± 1. This process is repeated until there are no more tracks with an energy larger than 2 GeV.

After the tau reconstruction, we apply the collinear approximation [18] to reconstruct the tau pair mass. In this approximation, it is assumed that the tau decay products, both visible ones and neutrinos, are collinear, and that the contribution to the missing transverse momentum comes only from the neutrinos. Figure 3 shows the distribution of the tau pair invariant mass with the collinear approximation for the signal process.

After the tau reconstruction, we apply the jet finde with the Durham algorithm [19] for the remaining objects to form two jets, which are used to reconstruct the Z boson.

The event selection is applied to the samples as summarized in Table I. Figure 4 shows the distribution of the recoil mass $M_{\rm recoil}$ against the Z boson. Since the initial four-momentum is known to good precision at the ILC, the four-momentum of the Z boson can be used to calculate the four-momentum of the recoil object. We select events in the region of 112 GeV $< M_{\rm recoil} <$ 160 GeV.

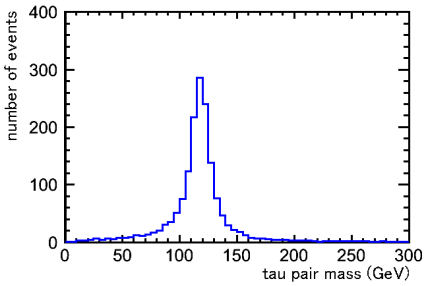

Fig. 3. The distribution of the tau pair mass with the collinear approximation for the signal process.

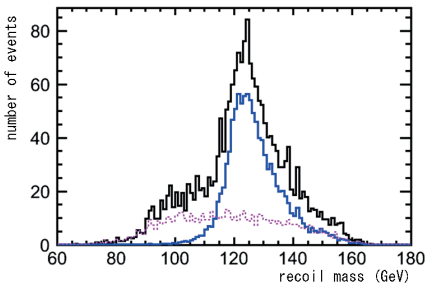

Fig. 4. The recoil mass distribution. Black, blue, and dotted purple histograms show the sum of all processes, the signal process, and the $e^+e \to q\bar{q}\tau^+\tau$ background process, respectively.

After the event selection, 1026 signal events and 554.4 background events remain. The signal significanc is calculated to be 25.8 standard deviations. This corresponds to a measurement accuracy of $\Delta(\sigma \cdot {\rm Br})/(\sigma \cdot {\rm Br}) = 3.9$ %. The results scaled to $M_h = 125$ GeV is calculated to be 4.2 %, where the branching ratio ${\rm Br}(h \to \tau^+\tau)$ of 6.32 % is assumed [20].

4. Conclusions

We estimate the measurement accuracy of the branching ratio of $h \to \tau^+\tau$ using full detector simulation at the ILC. We assume a center-of-mass energy of $\sqrt{s} = 250$ GeV, a Higgs mass of $M_h = 120$ GeV, and a branching ratio ${\rm Br}(h \to \tau^+\tau) = 8.0$ %, beam polarizations of $P(e^+, e) = (0.8, +0.3)$, and integrated luminosity of $\int L\, dt = 250$ fb ^{1}. We obtain a statistical significanc of 25.8 standard deviations (s.d.) from the $Z \to q\bar{q}$ mode. Combining our analysis of the other Z

Table I. Summary of event statistics in the $Z \to q\bar{q}$ mode assuming $\int L\,dt = 250$ fb ^{1}. The variables are define as follows: visible energy ($E_{\rm vis}$), cosine of the missing momentum angle ($\theta_{\rm miss}$), Z candidate mass (M_Z), Z candidate energy (E_Z), angle between the tau candidates ($\theta_{\tau^+\tau}$), transverse impact parameter significanc of the leading track in the tau jet (σ_{d_0}), longitudinal impact parameter significanc of the leading track in the tau jet (σ_{z_0}), mass of the tau pair ($M_{\tau^+\tau}$), energy of the tau pair ($E_{\tau^+\tau}$), mass of the tau pair with collinear approximation ($M_{\rm col}$), and energy of the tau pair with collinear approximation ($E_{\rm col}$). A detailed description can be found in Ref. [12].

Cut	Signal	$e^+e \to q\bar{q}\tau^+\tau$	$e^+e \to q\bar{q}\tau\nu$	$q\bar{q}\ell^+\ell$	Other SM backgrounds
No cut	4233	4.169×10^4	1.326×10^6	3.563×10^5	1.495×10^{10}
Preselection	1647	1.161×10^4	4.948×10^4	6.378×10^4	2.584×10^7
Number of tracks	1644	1.146×10^4	4.806×10^4	6.059×10^4	6.566×10^5
$E_{\rm vis}$	1607	1.107×10^4	4.693×10^4	2.106×10^4	3.642×10^5
$\cos\theta_{\rm miss}$	1572	1.021×10^4	4.415×10^4	8315	1.273×10^5
M_Z	1440	8674	3288	4987	1.181×10^4
E_Z	1429	7857	3061	4797	1.048×10^4
$\cos\theta_{\tau^+\tau}$	1386	2001	1154	1468	4242
σ_{d_0}	1338	1928	1044	854.9	2675
σ_{z_0}	1287	1845	883.4	408.2	1596
$M_{\tau^+\tau}$	1286	1837	883.4	349.1	1557
$E_{\tau^+\tau}$	1282	1836	883.4	324.7	1546
$M_{\rm col}$	1065	616.9	137.0	72.83	240.6
$E_{\rm col}$	1062	612.1	93.52	71.27	171.0
Recoil mass	1026	366.3	43.34	57.07	87.73

decay modes, which are shown to yield 8.0 (8.8) s.d. for the $Z \to e^+e$ ($Z \to \mu^+\mu$) mode [12], the combined result corresponds to a measurement accuracy of $\Delta(\sigma \cdot \mathrm{Br})/(\sigma \cdot \mathrm{Br}) = 3.5$ %. The results scaled to $M_h = 125$ GeV is estimated to be $\Delta(\sigma \cdot \mathrm{Br})/(\sigma \cdot \mathrm{Br}) = 4.2$ %. It is expected that combining measurements at other center-of-mass energies will improve these results.

References

[1] G. Aad *et al.* [ATLAS Collaboration], Phys. Lett. B **716**, 1 (2012) [arXiv:1207.7214 [hep-ex]].
[2] S. Chatrchyan *et al.* [CMS Collaboration], Phys. Lett. B **716**, 30 (2012) [arXiv:1207.7235 [hep-ex]].
[3] R. S. Gupta, H. Rzehak and J. D. Wells, Phys. Rev. D **86**, 095001 (2012) [arXiv:1206.3560 [hep-ph]].
[4] ATLAS Collaboration, ATLAS-CONF-2012-160 (2012)
[5] CMS Collaboration, CMS PAS HIG-13-004 (2013)
[6] ATLAS Collaboration, "Physics at a High-Luminosity LHC with ATLAS," ATL-PHYS-PUB-2013-007 (2013)
[7] CMS Collaboration, "CMS at the High-Energy Frontier. Contribution to the Update of the European Strategy for Particle Physics," CMS-NOTE-2012-006; CERN-CMS-NOTE-2012-006 (2012).
[8] International Linear Collider Technical Design Report — Volume 1 Executive Summary (2013)
[9] International Linear Collider Technical Design Report — Volume 2 Physics (2013)
[10] International Linear Collider Technical Design Report — Volume 3 Accelerator (2013)
[11] International Linear Collider Technical Design Report — Volume 4 Detectors (2013)
[12] S. Kawada, K. Fujii, T. Suehara, T. Takahashi, T. Tanabe, LC-REP-2013-001 (2013)
[13] P. Mora de Fretias, H. Videau, LC-TOOL-2003-010 (2003)
[14] S. Agostinelli *et al.* [GEANT4 Collaboration], Nucl. Instrum. Meth. A **506**, 250 (2003).
[15] S. Jadach, J. H. Kühn, Z. Was, Comput. Phys. Commun. **64**, (1991) 275 - 299
[16] ILD Concept Group, "International Large Detector — Letter of Intent" (2010)
[17] T. Sjöstrand, S. Mrenna, P. Skands, J. High Energy Phys. 0605, 025 (2006)
[18] R. K. Ellis, I. Hinchliffe, M. Soldate, J. J. van der Bij, Nucl. Phys. B **297** (1988) 221 - 243
[19] S. Catani, Y. L. Dokshitzer, M. Olsson, G. Turnock, B. R. Webber, Phys. Lett. B **269** (1991) 432 - 438
[20] LHC Higgs Cross Section Working Group, arXiv:1201.3084v1 [hep-ph]